

Modeling of Sodium-ion Batteries

Citation for published version (APA):

Chayambuka, K. H. (2022). *Modeling of Sodium-ion Batteries*. [Phd Thesis 1 (Research TU/e / Graduation TU/e), Electrical Engineering]. Technische Universiteit Eindhoven.

Document status and date:

Published: 29/03/2022

Document Version:

Publisher's PDF, also known as Version of Record (includes final page, issue and volume numbers)

Please check the document version of this publication:

- A submitted manuscript is the version of the article upon submission and before peer-review. There can be important differences between the submitted version and the official published version of record. People interested in the research are advised to contact the author for the final version of the publication, or visit the DOI to the publisher's website.
- The final author version and the galley proof are versions of the publication after peer review.
- The final published version features the final layout of the paper including the volume, issue and page numbers.

[Link to publication](#)

General rights

Copyright and moral rights for the publications made accessible in the public portal are retained by the authors and/or other copyright owners and it is a condition of accessing publications that users recognise and abide by the legal requirements associated with these rights.

- Users may download and print one copy of any publication from the public portal for the purpose of private study or research.
- You may not further distribute the material or use it for any profit-making activity or commercial gain
- You may freely distribute the URL identifying the publication in the public portal.

If the publication is distributed under the terms of Article 25fa of the Dutch Copyright Act, indicated by the "Taverne" license above, please follow below link for the End User Agreement:

www.tue.nl/taverne

Take down policy

If you believe that this document breaches copyright please contact us at:

openaccess@tue.nl

providing details and we will investigate your claim.

Modeling of Sodium-ion Batteries

PROEFSCHRIFT

ter verkrijging van de graad van doctor aan de Technische Universiteit Eindhoven, op gezag van de rector magnificus prof.dr.ir. F.P.T. Baaijens, voor een commissie aangewezen door het College voor Promoties, in het openbaar te verdedigen op donderdag 29 maart 2022 om 13:30 uur

door

Kudakwashe Hilary Chayambuka

geboren te Harare, Zimbabwe

Dit proefschrift is goedgekeurd door de promotoren en de samenstelling van de promotiecommissie is als volgt:

voorzitter:	prof.dr. K. A Williams
1 ^e promotor:	prof.dr.ir. P.H.L. Notten
copromotor:	dr. D.L. Danilov
leden:	prof.dr. R.-A. Eichel (RWTH Aachen) dr. M. Safari (Universiteit Hasselt) prof.dr.ir. J.G. Slootweg
adviseur:	ir. G. Mulder (EnergyVille, VITO)

Het onderzoek of ontwerp dat in dit proefschrift wordt beschreven is uitgevoerd in overeenstemming met de TU/e Gedragscode Wetenschapsbeoefening.

Table of Contents

List of Abbreviations.....	IV
List of Symbols	VII
Chapter 1 Introduction to sodium-ion batteries.....	1
1.1 Why Sodium-ion batteries (SIBs)	2
1.2 State-of-the-art SIB technology.....	3
1.3 The objective of this thesis.....	4
1.4 Outline of this thesis.....	6
References	8
Chapter 2 From Li-Ion Batteries toward Na-Ion Chemistries.....	11
2.1 Introduction	12
2.2 Physical properties of sodium and lithium	14
2.3 The shared history of sodium- and lithium-ion batteries.....	15
2.4 Comparison between sodium- and lithium-ion batteries.....	20
2.4.1 Physical features.....	21
2.4.2 Energy density, Power and Cyclability	21
2.4.3 Safety.....	24
2.4.4 Cost	26
2.5 Sodium-ion battery materials and electrochemical properties.....	26
2.5.1 Anode materials.....	28
2.5.2 Cathode materials	32
2.5.3 Electrolytes.....	34
2.6 SIB technology trend and outlook.....	36
2.7 Conclusions	38
References	39
Chapter 3 An Experimental and Modeling study of Sodium-ion Battery Electrolytes.....	53
3.1 Introduction	54
3.2 Theoretical background for conductivity measurements.....	55
3.3 Experimental	58
3.3.1 Preparation of electrolytes	58
3.3.2 Conductivity measurements	59
3.3.3 Viscosity measurements	60
3.3.4 AEM calculations	61
3.4 Results and discussion.....	63
3.4.1 Comparison between experimental data and AEM results.....	63

3.4.2 Walden analysis.....	67
3.4.3 Comparison of Na-ion and Li-ion battery electrolytes	70
3.4.4 Preferential ion solvation (PIS) – why some electrolyte combinations fail	72
3.4.5 Optimization of 1 M NaPF ₆ EC _x :PC _{1-x} electrolytes	75
3.5 Conclusions	76
References	78
Chapter 4 Modeling the Diffusion mechanism in Spherical electrode particles.....	83
4.1 Introduction	84
4.2 Modeling solid-state diffusion using analytical methods	87
4.2.1 Derivation of the modified-PSS method	88
4.3 Modeling solid-state diffusion using numerical methods.....	91
4.3.1 Derivation of the hybrid BECV method.....	93
4.3.2 Solving the coupled system of equations	97
4.3.3 Grid spacing	99
4.4 Results and discussion.....	100
4.4.1 Results of the analytical solution method.....	100
4.4.2 Results of the numerical solution method	103
4.5 Conclusions	108
References	110
Chapter 5 Determination of diffusion coefficients and charge transfer rate constants by GITT ...	113
5.1 Introduction	114
5.2 Experimental	118
5.3 Model	119
5.4 Results and discussion.....	123
5.5 Conclusions	129
References	130
Chapter 6 Experimental determination of SIB Modeling parameters	133
6.1 Introduction	134
6.2 Experimental	135
6.2.1 Electrodes	137
6.2.2 Electrolyte	138
6.2.3 Physical property analyses	138
6.2.4 Electrochemical testing	139
6.2.5 Determination of electrode parameters using GITT	140
6.2.6 Full cell cycling	141
6.3 Results and discussion.....	142
6.3.1 Physical analyses.....	142
6.3.2 Na/NVPF half-cell	146

6.3.3 Na//HC half-cell	147
6.3.4 GITT measurements	149
6.3.5 Complete batteries	155
6.4 Conclusions	164
References	166
Chapter 7 Physics-based SIB model and validation.....	171
7.1 Introduction	172
7.2 Description of the system components.....	173
7.3 Model description.....	175
7.3.1 Mass transport in electrode particles	175
7.3.2 Electrode kinetics model	176
7.3.3 Current distribution	177
7.3.4 Electrolyte potential and mass distribution	178
7.3.5 Relation between bulk transport properties and porous electrode properties	180
7.3.6 Modeling interfaces.....	181
7.3.7 Battery voltage	182
7.4 Parameter identification and optimization.....	184
7.5 Results and discussion.....	188
7.6 Conclusions	203
References	204
Chapter 8 Summary and outlook.....	209
Acknowledgements	213
List of Publications	218
Curriculum Vitae.....	221

List of Abbreviations

AEM	Advanced Electrolyte Model
ARC	Accelerating rate calorimetry
BECV	Backward Euler control volume method
BMS	Battery management system
CC	Constant current
CE	Counter electrode
CEA	Alternative Energies and Atomic Energy Commission
CNRS	National Center for Scientific Research
CPE	Constant phase element
CV	Constant voltage
CVM	Control volume method
DEC	Diethyl carbonate
DMC	Dimethyl carbonate
DME	1,2 Dimethoxyethane
DoD	Depth-of-discharge
EC	Ethylene carbonate
EES	Electrical energy storage
EIS	Electrochemical impedance spectroscopy
EMF	Electrode equilibrium potential
ESW	Electrochemical stability window
FDM	Finite difference method
FEM	Finite element method
FMPSS	Fast modified pseudo-steady state
FS-5P	Freudenberg Viledon FS 2226E - Lydall Solupor 5P09B
FVM	Finite volume method
GA	Genetic algorithm
GITT	Galvanostatic intermittent titration technique
HBECV	Hybrid backward Euler control volume method
HC	Hard carbon

IoP-CAS	Institute of Physics Chinese Academy of Sciences
IP	Ion pair
LCO	LiCoO_2
LFP	LiFePO_4
LIB	Lithium Ion Battery
LMO	LiMn_2O_4
MAL	Mass action law
MPSS	Modified pseudo-steady state
Na-RE	Na reference electrode
NaS	Sodium-sulfur
NASICON	Sodium Superionic Conductor
NCA	$\text{LiNi}_{1-x-y}\text{Co}_x\text{Al}_y\text{O}_2$
NMC	$\text{LiNi}_{1-x-y}\text{Mn}_x\text{Co}_y\text{O}_2$
NMMMO	$\text{NaNi}_{1-x-y-z}\text{M}_x^1\text{M}_y^2\text{M}_z^3\text{O}_2$
NMO	$\text{Na}_{0.44}\text{MnO}_2$
NNFM	$\text{NaFe}_{0.4}\text{Mn}_{0.3}\text{Ni}_{0.3}\text{O}_2$
NVP	$\text{Na}_3\text{V}_2(\text{PO}_4)_3$
NVPF	$\text{Na}_3\text{V}_2(\text{PO}_4)_2\text{F}$
OCV	Open-circuit voltage
P2D	Pseudo two-dimensional
PBA	Prussian blue analogs
PC	Propylene carbonate
PDE	Partial differential equation
PIS	Preferential ion solvation
PITT	Potentiostatic intermittent titration technique
PSS	Pseudo-steady state
RE	Reference electrode
RS2E	French network for electrochemical energy storage
SEI	Solid electrolyte interface
SDL	Scaled diffusion length

SEM	Scanning electron microscopy
SHE	Standard hydrogen electrode
SIB	Sodium Ion Battery
SOC	State-of-charge
SSCV	Slow scan rate cyclic voltammetry
TDMA	Tridiagonal matrix algorithm
TI	Triple ion
WE	Working electrode
XRD	X-ray diffraction
ZEBRA	Zeolite Battery Research Africa

List of Symbols

Please note that the list below is for symbols used from Chapters 1 to 4. Parameters used in Chapters 5 to 7 are listed in each chapter.

Symbol	Description	Unit
c	Molality concentration	mol kg^{-1}
c_i^*	Molarity concentration of species i	mol l^{-1}
c_{max}	Maximum concentration of intercalated species	mol m^{-3}
c_s	Concentration of the intercalated species	mol m^{-3}
$c_{s,0}$	Initial concentration of the intercalated species	mol m^{-3}
\hat{C}_{theo}	Theoretical capacity of the electrode material	mAh g^{-1}
D_1	Solid-state diffusion coefficient	$\text{m}^2 \text{s}^{-1}$
D_1^{ref}	Reference diffusion coefficient	$\text{m}^2 \text{s}^{-1}$
e	Elementary charge	C
E_a	Activation energy	J mol^{-1}
F	Faraday constant	C mol^{-1}
J	Flux of species at the surface of the particle	$\text{mol m}^{-2} \text{s}^{-1}$
$K_{1,T}$	The 1 st temperature-dependent coefficient at temperature T	$\text{S m}^8 \text{mol}^{-3}$
$K_{2,T}$	The 2 nd temperature-dependent coefficient at temperature T	$\text{S m}^{3.5} \text{mol}^{-1.5}$
$K_{3,T}$	The 3 rd temperature-dependent coefficient at temperature T	$\text{S m}^2 \text{mol}^{-1}$
K_{cell}	Cell constant for electrolyte conductivity measurements	m^{-1}
L	Inductance	H
M	Number of non-zero positive roots	-
Q	Constant phase element capacitance parameter	F m^{-2}
R	Universal gas constant	$\text{J K}^{-1} \text{mol}^{-1}$
r	Radial distance from the center of the particle	m
R_0	Radius of the active particles	m
R_e	Ionic resistance in the electrolyte bulk	Ω
r_i	Stokes' radius of the i^{th} ionic species	m

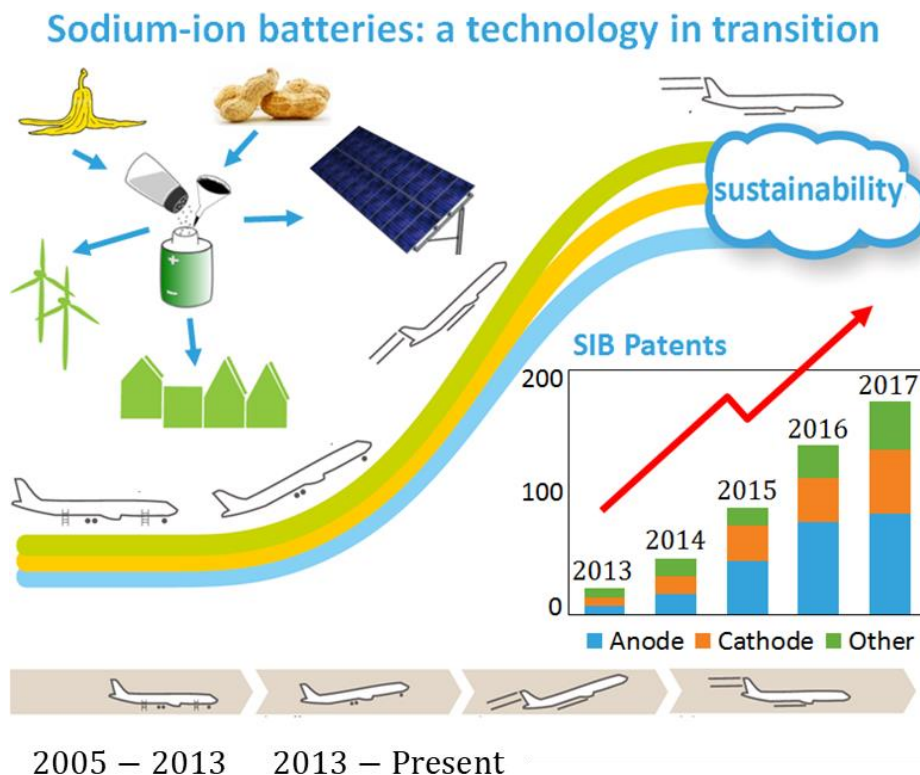
T	Temperature	K
t	Time	s
Y	Admittance	S
Y_{mod}	Modulus of the admittance	S
Z	Total impedance	Ω
z_i	Charge number i^{th} ionic species	-
α	Constant phase element exponent parameter	-
β	A constant which is inversely proportional to the Stokes' radii	$C^2 \text{ mol}^{-1} \text{ m}^{-1}$
κ	Electrolyte conductivity	$S \text{ m}^{-1}$
Λ	Molar conductivity	$S \text{ cm}^2 \text{ mol}^{-1}$
λ_m	Non-zero positive real roots	-
μ_∞	Limiting viscosity at infinite temperature	Pa s
μ	Dynamic viscosity	Pa s
σ	Ionic conductivity	$S \text{ m}^{-1}$
ω	Frequency of the applied alternating signal	rad s^{-1}

CHAPTER 1

INTRODUCTION TO SODIUM-ION BATTERIES

Abstract

The demand for electrochemical energy storage technologies is rapidly increasing due to the increasing supply of renewable energy sources in the grid and the concomitant need for battery energy storage. Although the properties of batteries are ideal for most electrical energy storage applications, the ability of the current lithium-ion battery (LIB) technology to scale-up and match this overwhelming demand remains uncertain, given the technology's resource constraints. Sodium-ion batteries (SIBs) are a different class of batteries with similar performance characteristics to LIBs. Because SIBs are composed of earth-abundant elements, they can be used to assemble utility-scale batteries sustainably. Over the last decade, phenomenal progress has been realized in the SIB technology in preparation for the commercialization of SIBs.



1.1 Why Sodium-ion batteries (SIBs)

Despite an unrivaled commercial success in consumer electronics and recently in battery electric vehicles, lithium-ion batteries (LIBs) remain too expensive for stationary, large-scale, electrical energy storage (EES). In addition, there are justifiable concerns regarding the resource challenges of LIB raw materials [1,2]. Historically, the technology of choice for such EES applications is pumped-hydro which is the dominant technology. As of 2017, pumped-hydro accounted for over 95 % of the total rated power globally (data derived from the US DOE, global energy storage database) [3,4]. However, the number of new pumped-hydro installations has been dwindling due to the technology's specific geographic and geological requirements [5]. Therefore, a technological incentive is to find alternative EES options that are installation flexible, cost-effective, energy-efficient and environmentally benign, to match the rapid growth in intermittent renewable energy sources.

The properties of electrochemical energy storage technologies are, in general, ideal for grid-scale EES applications. LIBs, in particular, can respond rapidly to load changes, have a high energy density combined with an excellent coulombic efficiency, exhibit low standby losses, and have modular designs which facilitate up-scaling [5,6]. Yet, faced with the aforementioned resource constraints and adverse ecological hazards upon disposal (due to toxic elements), the prospects of LIBs to meet large-scale EES demands remain uncertain [5]. The needs and challenges outlined above have motivated the search for alternative, scalable EES technologies composed of cheap, abundant, and environmentally benign materials to match the performance and economic success of LIBs.

Given the relative abundance of elemental sodium compared to lithium in the earth's crust (see **Fig. 1.1**), and the low electrochemical potential of Na (-2.71 V vs. the standard hydrogen electrode, SHE), which is only 330 mV above that of Li, rechargeable batteries based on sodium hold great promise to meet large-scale EES demands. For example, high-temperature ZEBRA cells based on the Na//NiCl₂ system and sodium-sulfur cells have already demonstrated the potential of sodium-based electrochemical energy storage [7,8]. These batteries have already been commercialized for stationary and automotive applications [9–12]. However, their major disadvantage is a high operating temperature of approximately 300°C, which conjures safety hazards and reduces the round-trip energy efficiency of the cells [10,12]. Therefore, a room-

temperature SIB is the most realistic option to match the performance characteristics of state-of-the-art LIBs and meet the future sustainability goals.

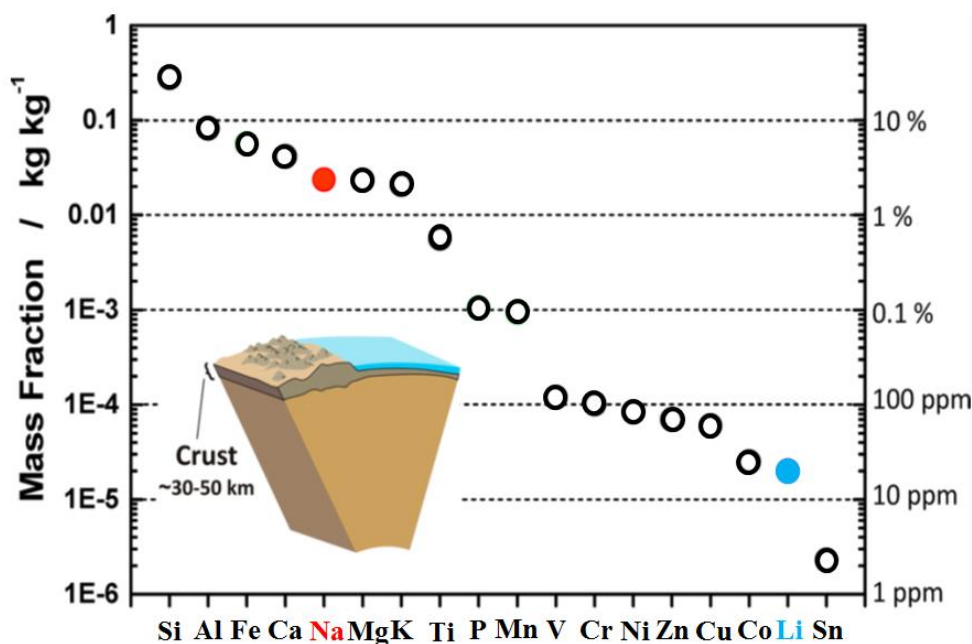


Fig. 1.1. The abundance of elements in the earth's crust. The energy-carrying elements for comparison are highlighted in red for Na and blue for Li. Image adapted from Ref. [13].

1.2 State-of-the-art SIB technology

Although SIBs are not expected to compete with LIBs for energy density, they are expected to leverage their resource abundance and present a price-competitive and sustainable alternative. This advantage is especially desirable in large MWh stationary EES applications, wherein the weight and footprint of the battery are tolerated [14]. In addition, this will alleviate resource constraints on LIBs once LIB production ramps up to meet the demands of e-mobility and grid storage applications. A reliable supply of SIBs would thus stabilize raw material costs and supply chains. In this envisioned roadmap, the SIBs play a complementary role to the LIB technology as opposed to a competitive one.

Fig. 1.2 shows several prototype SIB cells which have been produced to date. From a distance, these cells are indistinguishable from state-of-the-art LIBs. Both chemistries use the same cylindrical and pouch cell designs. The internal electrodes are also similar because SIBs and LIBs are manufactured from the same assembly lines. Therefore, SIBs have often been heralded as drop-

in replacements for LIBs [15]. These technological advances are the reason why the commercialization of the SIB technology is expected to be successful.

Although a number of SIB cells have been manufactured in the traditional form factors of rechargeable batteries, no manufacturer has been able to commercialize SIB cells to date. The current technology can therefore be described as being in a consolidation/growth stage and is moving from successful pilot projects and proof of concepts toward a commercial product. This also means now is an opportune time to focus on improving SIB cell design features, with the aim to enhance performance and reduce costs. This endeavor can therefore benefit from physics-based models which have the ability to predict the performance of the cells and optimize designs quickly.

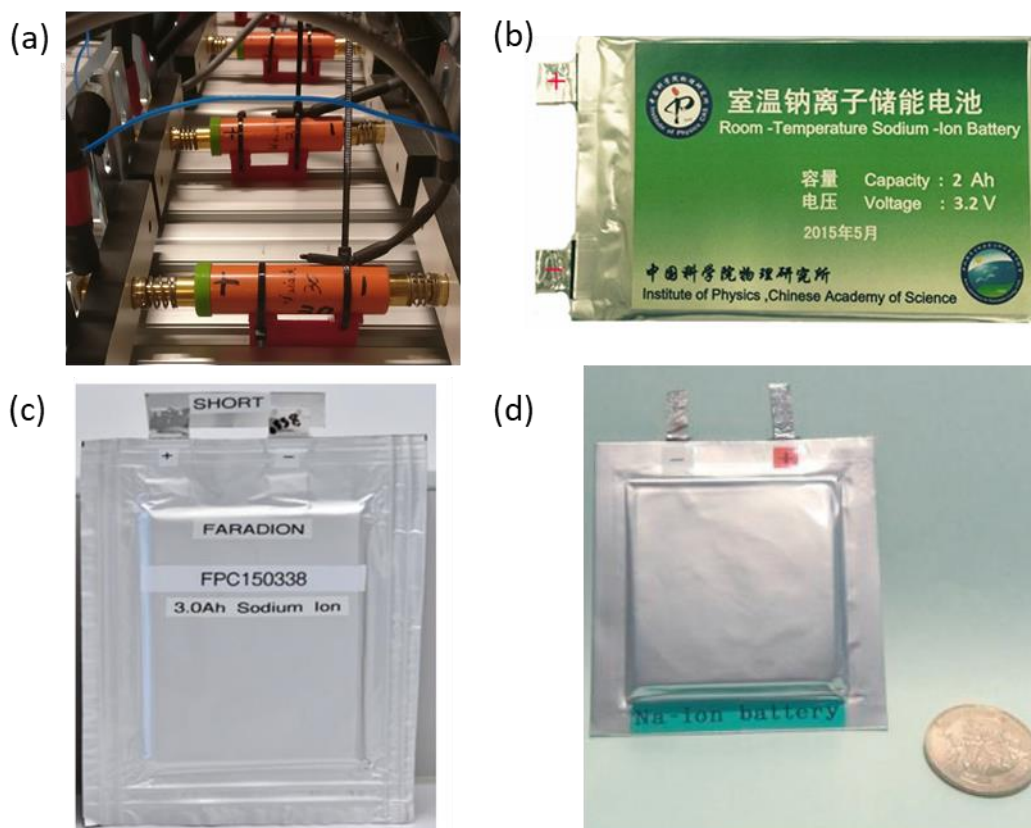


Fig. 1.2. Prototype SIB cells from NAIADES (a), the Chinese Academy of Science (b), Faradion (c), and Sumitomo Chemical (d). (a) Image of SIB cells in EnergyVille, Genk (b) Reproduced with permission [16]. Copyright 2016, The Electrochemical Society (c) Reproduced with permission [17]. Copyright 2017, Faradion. (d) Reproduced with permission [18]. Copyright 2013, Sumitomo Chemical Co., Ltd.

1.3 The objective of this thesis

Fast and accurate physics-based simulation models are needed to accelerate the development and commercialization of the SIB technology. Such models are crucial during the cell design phase, in order to optimize features for specific power, energy density and minimizing internal energy losses. This knowledge reduces the number of experimental trial and error steps which are materially expensive and time-consuming.

Several physics-based models have existed in literature. The "porous electrode theory", proposed by Newman and co-workers, became the first to gain universal acceptance because it involved fewer assumptions about porous electrodes [19]. This model framework is also called the pseudo-two-dimensional (P2D) battery model because the concentration inside electrode particles is resolved along the particle radius and for particles at different positions. However, several modifications to the Newman battery model are expedient to accurately model the new intercalation chemistry of SIBs. These include a revisit to the electrolyte transport theory and the assumptions used in the intercalation dynamics. In addition, optimized solution schemes for solving the coupled system of equations are necessary to efficiently resolve the multi-physics and multi-scale phenomena involved in SIBs.

A P2D model is a rigorous approach because it captures phenomena at different length and time scales. **Fig. 1.3** illustrates the length and time scales of the various phenomena involved in battery models. At the lower end of the spectrum are the molecular scale models, which determine the thermodynamic properties of the materials. These include electrolyte properties and electrode potentials. At the high end of the spectrum, there are battery pack models which investigate the effect of multiple neighboring battery cells and modules on the electric power distribution. The P2D model, however, focuses on the phenomena occurring at the length and time scale of the electrode particles and battery cell. Therefore, the P2D model captures transport processes occurring inside the electrode particles and the macroscopic scale behavior of the complete battery cell.

This thesis presents the development of a P2D model of SIBs based on the experimental electrochemical data and physics-based equations for transport and reaction kinetics. The P2D model developed, accounts for the various kinetic and transport processes within porous SIB electrodes. This feature increases model accuracy and allows the investigation of internal limiting phenomena which cannot be ascertained by experiments alone. The model is furthermore validated

by experimental results from one of the most commercially promising SIBs. This allows the SIB P2D model to be used as a tool to improve cell designs, benchmark new chemistries and further develop the SIB technology.

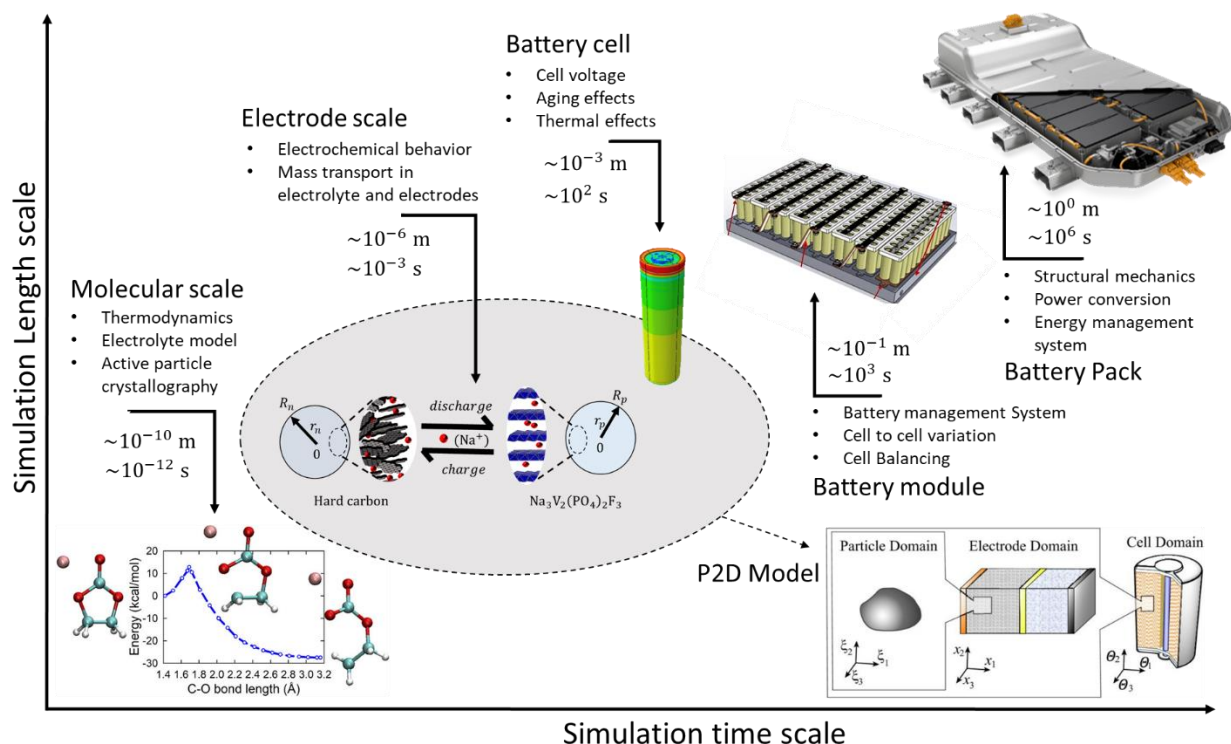


Fig. 1.3. Illustration of the different length and time scales considered in battery simulations. The molecular scale, the electrode scale, the battery cell dimension, the battery module dimension, and the battery pack dimension are indicated. The P2D model resolves phenomena occurring at the time and length scale of the electrodes and battery cell.

1.4 Outline of this thesis

This thesis is organized in a series of Chapters that outline the steps necessary to develop an experimentally validated P2D model of SIBs. The Chapters are also arranged in increasing length scale of the phenomena investigated, starting with the molecular scale properties of SIB electrolytes and ending with the full cell SIB model.

Chapter 2 presents a review of rechargeable batteries based on lithium and sodium. This Chapter explains the historical development of SIBs and LIBs from the perspective of the

technological driving forces which have shaped the modern-day battery landscape. Furthermore, the different active materials used in SIBs are presented to benchmark their relative properties in terms of electrode voltage and gravimetric capacity.

Chapter 3 describes the modeling and experimental validation of SIB electrolytes. In this work, SIB electrolyte properties of conductivity and viscosity are determined using experiments and statistical mechanics model results. The advantage of such a combined model and experimental approach is that extensive properties of electrolytes can be further elucidated. Parameters such as diffusion coefficients and transference numbers are thus deduced and used as inputs in the P2D model.

Chapter 4 presents the modeling of particle scale mass transport. Two methods are presented to resolve the concentration profiles in spherical active particles efficiently. The choice of the appropriate method depends on the functional form of the diffusion coefficient. In the case of a constant diffusion coefficient, an analytical approach is described, while in the case of concentration-dependent diffusion coefficient, a numerical method is presented. These methods are later used in the P2D model of SIBs.

Chapter 5 extends on the work presented in Chapter 4 through the use of a P2D half-cell model and experiments to determine the diffusion coefficients and kinetic parameters of SIB active particles. This work revisits previous, simplified approaches used for this purpose and explains why they are misleading. It is shown that validated parameters can be obtained using the developed P2D half-cell model and experiments. These parameters are later used in the P2D full cell model of SIBs.

Chapter 6 presents experiments performed on half-cell and full cell SIBs to derive parameters necessary for the full cell P2D model. Measurements of the particle sizes and electrode thickness are shown, which are used to define the geometrical properties of the model. It is likewise necessary to determine the equilibrium potential and capacity of the active materials. These experimental deductions reduce the number of unknown model parameters and result in a representative P2D model.

The full cell P2D model is then finally presented in Chapter 7 of this thesis. This model includes the parameters determined from the previous chapters and is validated by the experiments from Chapter 6. A unique feature of this model validation is that it is based on individual electrode potentials and not on the full cell voltage profile. This feature demonstrates the utility of the P2D

model in determining internal battery states. In addition, properties such as the electrolyte concentration profiles and reaction rate distribution are presented, which cannot be easily deduced by direct empirical methods. Finally, a Ragone plot of the cell performance is shown, which can benchmark the performance of state-of-the-art SIBs against other electrical energy storage technologies.

Chapter 8 then presents a summary of the main findings in this thesis and an outlook to address the remaining challenges toward SIB commercialization. Future research challenges in the field of modeling and design of SIBs are further outlined and possible solutions are discussed.

References

- [1] L. Wang, Y. Lu, J. Liu, M. Xu, J. Cheng, D. Zhang, G. John, A Superior Low-Cost Cathode for a Na-Ion Battery, *Angew. Chem. Int. Ed.* **52** (2013) 1964–1967.
- [2] MD. Slater, D. Kim, E. Lee, C.S. Johnson, Sodium-Ion Batteries, *Advanced Functional Materials*. **23** (2013) 947–958. <https://doi.org/10.1002/adfm.201200691>.
- [3] C.-J. Yang, R.B. Jackson, Opportunities and barriers to pumped-hydro energy storage in the United States, *Renewable and Sustainable Energy Reviews*. **15** (2011) 839–844. <https://doi.org/10.1016/j.rser.2010.09.020>.
- [4] US Department of Energy (2017), Global energy storage database: Projects, www.energystorageexchange.org. (2017).
- [5] H. Chen, T.N. Cong, W. Yang, C. Tan, Y. Li, Y. Ding, Progress in electrical energy storage system: A critical review, *Progress in Natural Science*. **19** (2009) 291–312. <https://doi.org/10.1016/j.pnsc.2008.07.014>.
- [6] J. Kondoh, I. Ishii, H. Yamaguchi, A. Murata, K. Otani, K. Sakuta, N. Higuchi, S. Sekine, M. Kamimoto, Electrical energy storage systems for energy networks, *Energy Conversion and Management*. **41** (2000) 1863–1874. [https://doi.org/10.1016/S0196-8904\(00\)00028-5](https://doi.org/10.1016/S0196-8904(00)00028-5).
- [7] T. Oshima, M. Kajita, A. Okuno, Development of Sodium-Sulfur Batteries, *International Journal of Applied Ceramic Technology*. **1** (2004) 269–276. <https://doi.org/10.1111/j.1744-7402.2004.tb00179.x>.
- [8] R.J. Bones, D.A. Teagle, S.D. Brooker, F.L. Cullen, Development of a Ni, NiCl₂ Positive Electrode for a Liquid Sodium (ZEBRA) Battery Cell, *J. Electrochem. Soc.* **136** (1989) 1274–1277. <https://doi.org/10.1149/1.2096905>.
- [9] C.-H. Dustmann, Advances in ZEBRA batteries, *Journal of Power Sources*. **127** (2004) 85–92. <https://doi.org/10.1016/j.jpowsour.2003.09.039>.
- [10] D. Kundu, E. Talaie, V. Duffort, L.F. Nazar, The Emerging Chemistry of Sodium Ion Batteries for Electrochemical Energy Storage, *Angew. Chem. Int. Ed.* **54** (2015) 3431–3448. <https://doi.org/10.1002/anie.201410376>.
- [11] L. Marcoux, E. Seo, Sodium-Sulfur Batteries, in: *New Uses of Sulfur*, American Chemical Society, **140** (1975) 216–227. <https://doi.org/10.1021/ba-1975-0140.ch014>.
- [12] B.L. Ellis, L.F. Nazar, Sodium and sodium-ion energy storage batteries, *Current Opinion in Solid State and Materials Science*. **16** (2012) 168–177. <https://doi.org/10.1016/j.cossms.2012.04.002>.
- [13] R.S. Carmichael, *Physical properties of rocks and minerals*, CRC press Boca Raton, (1989).
- [14] A. Bauer, J. Song, S. Vail, W. Pan, J. Barker, Y. Lu, The Scale-up and Commercialization of Nonaqueous Na-Ion Battery Technologies, *Advanced Energy Materials*. **8** (2018) 1702869. <https://doi.org/10.1002/aenm.201702869>.
- [15] K. Smith, J. Treacher, D. Ledwoch, P. Adamson, E. Kendrick, Novel High Energy Density Sodium Layered Oxide Cathode Materials: from Material to Cells, *ECS Trans.* **75** (2017) 13–24. <https://doi.org/10.1149/07522.0013ecst>.
- [16] Y.-S. Hu, Development of Sodium-Ion Batteries for Grid-Scale Energy Storage, *Meet. Abstr. MA2016-03* (2016) 71. <https://doi.org/10.1149/MA2016-03/1/71>.
- [17] J. Barker, Towards the Commercialization of High Energy Density Na-Ion Batteries, [Http://www.faradion.co.uk](http://www.faradion.co.uk).

- [18] S. Kuze, J. Kageura, S. Matsumoto, T. Nakayama, M. Makidera, M. Saka, T. Yamaguchi, T. Yamamoto, K. Nakane, Development of a sodium ion secondary battery, Sumitomo Kagaku. **2013** (2013) 1–13.
- [19] J. Newman, W. Tiedemann, Porous-electrode theory with battery applications, AIChE Journal. **21** (1975) 25–41. <https://doi.org/10.1002/aic.690210103>.

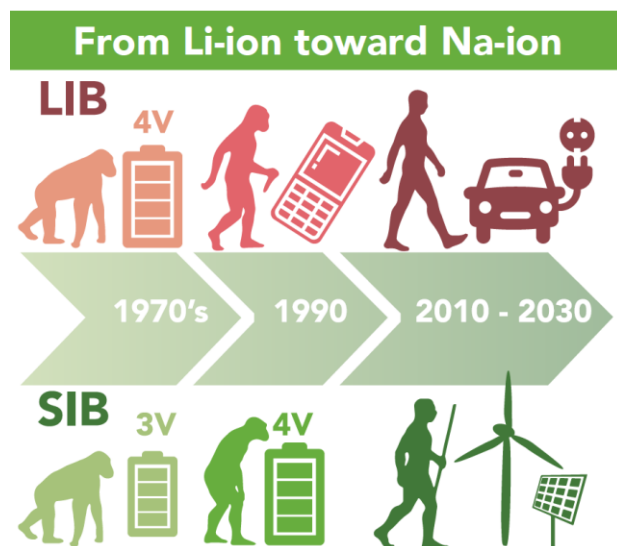
CHAPTER 2

FROM LI-ION BATTERIES TOWARD NA-ION CHEMISTRIES

The race of the Alkali Metals

Abstract

Among the existing energy storage technologies, LIBs have unmatched energy density and versatility. From the time of their first commercialization in 1991, the growth in LIBs has been phenomenal, driven by portable devices. In recent years, however, large-scale electric vehicles and stationary applications have emerged. Because LIB raw material deposits are unevenly distributed and prone to price fluctuations, these large-scale applications have exerted unprecedented pressure on the LIB value chain, resulting in the need for alternative energy storage chemistries. One of the most promising "beyond-lithium" energy storage technologies is the SIB chemistry. In this Chapter, the technological evolutions of both LIBs and SIBs are discussed with a key focus on material properties, technological drivers, and possible applications.



Parts of this Chapter have been published as:

K. Chayambuka, G. Mulder, D. L. Danilov, P.H.L. Notten, Sodium-Ion Battery Materials and Electrochemical Properties Reviewed, *Advanced Energy Materials*. **8** (2018) 1800079. <https://doi.org/10.1002/aenm.201800079>.

K. Chayambuka, G. Mulder, D.L. Danilov, P.H.L. Notten, From Li-Ion Batteries toward Na-Ion Chemistries: Challenges and Opportunities, *Advanced Energy Materials*. **10** (2020) 2001310. <https://doi.org/10.1002/aenm.202001310>.

2.1 Introduction

The year 2019 will be remembered by many in the battery community as the year of the crowning achievement. The Nobel prize in chemistry was finally awarded to John Goodenough, M. Stanley Whittingham, and Akira Yoshino [1], the inventors of the lithium-ion battery (LIB). Granted, the limitation to only 3 recipients is a restriction of the Nobel committee, other scientists should be acknowledged, some of whom will be mentioned in this Chapter, whose key contributions led to the development of a versatile energy storage device which, nowadays, powers anything from micro-sensors to electric vehicles.

Based on the discoveries of the aforementioned Nobel laureates, LIBs were commercialized in 1991 by SONY and immediately experienced double-digit growth in sales [2]. It only took 6 years for the LIB market share to surpass that of incumbent battery technologies, the likes of Nickel Cadmium (NiCd) and Nickel Metal Hydride (NiMH) batteries [3]. Such phenomenal growth was made possible by the rise in portable consumer electronic devices, such as cassette recorders, Discmans, personal care appliances, and mobile phones. The initial problem was powering these devices off-grid for long periods of time [4]. The lightweight and high energy density characteristics of LIBs thus made them ideal for this application. This property also meant that there was no direct competition between LIBs and the other battery technologies; for example, the sales in NiCd and NiMH in Japan did not decline due to the exponential growth in LIB sales [3]. Therefore, a new market segment had emerged, and the LIB was the ideal technology for this market.

Since the first commercial LIB, portable consumer electronics have evolved, both in form and function. Often, Moore's law is cited, an observation that the number of transistors on an integrated circuit doubles biennially [5,6]. This law means computing speed has roughly doubled every two years, giving rise to "smart" devices. The battery energy density to run these complex devices has also increased, albeit at a slower rate. This is because of fundamental chemical limitations. Increasing the useful energy density of batteries has proved to be an enormous challenge [7]. Nevertheless, there remains room to improve other battery properties, such as cost, cycling stability, safety, environmental toxicity, and cell design [8–11].

An outstanding feature of LIBs is their versatility in EES applications. Of late, battery electric vehicles pioneered by Tesla Inc., BYD and Nissan have been successfully commercialized, all

powered by LIBs [12]. A Tesla Model S with an onboard battery pack of 100 kWh has a driving range of 600 km, certified by the U.S. Environmental Protection Agency [13]. The global fleet of electric cars and busses currently stands at 4 million and is expected to reach 50 – 200 million by 2028 [14]. This transition toward electric mobility (e-mobility) is driven by clean energy policies to become climate-neutral [15]. Bigger LIB installations of the megawatt-hour scale are also anticipated in the stationary storage sector [16]. While in these applications, the battery weight and footprint are not primary considerations, LIBs are nevertheless expected to play a leading role. This is because other LIB performance metrics, such as cycling efficiency, high power and deep discharge capability, are important requirements for profitable grid ancillary services [17].

Although no apparent performance limit has been identified for the LIB technology, it has become difficult to source raw materials such as lithium carbonate and cobaltite [18–21]. As the size of battery packs and the number of installations increase, mining companies find it increasingly difficult to match the demand. As a case in point, in 2015, the price of lithium carbonate nearly tripled within a period of 10 months due to demand from the e-mobility sector [22]. The problem is that lithium carbonate is scarce and unevenly distributed [23]. Nearly half of the 2015 global production came from South America, which raises concerns of global supply shortage risk and overexploitation at the source. Moreover, cobalt and graphite, the other vital constituents of LIBs are classified as critical raw materials by the EU [24]. The recent large-scale deployments of LIBs have therefore put greater pressure on an already congested value chain, resulting in price fluctuations. It is, therefore, necessary and urgent to invest in research efforts on alternatives beyond lithium technologies to overcome this overreliance.

Concerns regarding the scalability of LIBs and the global transition toward clean and sustainable energy have thus motivated the research in alternative battery chemistries such as the SIB. Chapter 1 discussed the motivations to replace lithium with sodium. For SIBs to significantly contribute to the clean energy transition, it is imperative to evolve into an economic success. In this Chapter, the technological driving forces which have propelled different development paths of room temperature rechargeable batteries based on lithium and sodium are discussed. Particular attention is on the properties of candidate room temperature SIB cells. Remarkable progress in SIBs is attributed to the vast scientific knowledge in solid-state materials gained in developing LIBs, which has been useful in developing SIBs. In addition, similarities in electrode architecture have allowed the same industrial processing techniques for both SIBs and LIBs [25,26]. This

combination of positive factors has put wind in the sails of SIBs, a wind that is expected to carry SIBs to commercial success.

2.2 Physical properties of sodium and lithium

Sodium and lithium are two members of the group 1 elements of the periodic table. They are trivially named alkali metals, and they possess one loosely held electron in their valence shell. Alkali metals are therefore very reactive, and their melting point, hardness, conductivity, and first ionization energy decrease down the group. The revival of SIBs, operating at room temperature, is mainly inspired by contemporary concerns regarding lithium's cost and resource availability to meet the ever-increasing demands of electrical energy storage. Revival because up until the late 1980^s, SIBs were fervently investigated alongside LIBs [27,28]. The reason why these two charge carriers for energy storage were at one point equally regarded can be revealed from an analysis of their physical and chemical properties. **Table 2.1** lists the physical and chemical properties of Na and Li that are of interest in rechargeable battery applications

One of the most important figures of merit for comparison is the redox potentials of Na and Li. The standard reduction potential of Na^+/Na of -2.71 V vs. the standard hydrogen electrode (SHE) is about 330 mV above that of Li^+/Li of -3.04 V vs. SHE. This fact means, in most cases, that the anodic electrode potentials for SIBs will always be higher than those of LIBs. Since this potential forms the thermodynamic minimum limit for the anode, this 330 mV difference is an energy penalty in SIB cells compared with analogous LIB cells. Another important physical property to compare is the melting point of both metals. Na is a soft metal with a low melting point of 97.7 °C, while Li has a higher melting point of 180.5 °C. The low melting point of Na may present challenges for developing solid-state SIBs, considering the relatively high temperature often necessary for solid-state electrolyte conductivity.

Table 2.1. Physical properties of lithium and sodium.

Property ^(a)	Li	Na
Atomic mass (g mol ⁻¹)	6.94	22.99
Electron configuration ^(b)	[He] 2s ¹	[Ne] s ¹
Cationic radius (Å)	0.76	1.02
Standard electrode potential (V)	-3.04	-2.71
Melting point (°C)	180.5	97.7
Density (g cm ⁻³)	0.534	0.971
First ionization energy (kJ mol ⁻¹)	520.2	495.8
Theoretical gravimetric capacity (mAh g ⁻¹)	3861	1165
Theoretical volumetric capacity (mAh cm ⁻³)	2062	1131

(a) Data derived from refs. [29,30]. (b) The abbreviated notation is used for the electron configuration.

2.3 The shared history of sodium- and lithium-ion batteries

Pioneering discoveries of the reversible electrochemical intercalation reaction of Na and Li in layered TiS₂ first became public in the late 1970^s. In 1976, a Li//TiS₂ cell was first reported by Whittingham [31] and later in 1982, Johnson *et al.* [32] found Na and Li to be equally capable of intercalating in TiS₂, as well as in other transition-metal dichalcogenides. Due to the low open-circuit voltage of a TiS₂ cathode, of approximately 2.2 V *vs.* Li⁺/Li, and the instability of metallic anodes, the TiS₂-based cell could not be commercialized.

To improve the cathodic voltage, Goodenough *et al.* [33,34] proposed the layered metal-oxide family of compounds in the early 1980^s. Their chemical composition is NaMeO₂ and LiMeO₂ (Me = Co, Ni, Cr, Mn, Fe), in the case of Na- and Li-based compounds, respectively. Complementary works by Delmas, Hagenmuller, and co-workers during the same period led to discoveries of NaMeO₂ compounds [35–37]. However, in terms of cell voltage, Goodenough's discoveries were

groundbreaking. For example, LiCoO_2 (LCO) has an open-circuit voltage of 4.0 V, nearly double that of TiS_2 . In addition, the electrochemical properties of Li-based cells were found to be superior to the Na-based equivalents.

The anode of choice nevertheless remained either metallic lithium or sodium [38]. This choice is evident because Na and Li anodes result in cells with the highest energy density. **Table 2.1** gives an overview of the theoretical gravimetric and volumetric capacities of Na and Li anodes. Unfortunately, these highly electropositive alkali metals also react with the electrolyte, which means the cells are unstable. Furthermore, during plating and stripping cycles, dendrites grow uncontrollably, resulting in internal short-circuits and battery-related explosions. The challenge of making a rechargeable, room temperature battery using Na or Li anodes has remained unresolved for over 50 years, illustrating the complexity involved. In the case of Na, this challenge is aggravated by the higher reactivity and lower melting point of metallic Na (note that the reactivity of alkali-metal elements increases with the atomic number).

To circumvent this challenge, an idea initially proposed by Armand in 1980 to use two intercalation electrodes as anode and cathode started to gain traction [39–41]. In this way, no metals would be deposited on the anode since the intercalation anode will have a potential above the plating potential of the metal. This concept was named the "rocking-chair" battery [42], in reference to the reversible shuttling of ions between two interaction electrodes. In 1982, Scrosati *et al.* [41–44] demonstrated the feasibility of the rocking-chair battery concept by pairing high voltage cathodes with low voltage anodes such as LiWO_2 and $\text{Li}_6\text{Fe}_2\text{O}_3$. Although the resulting cells were stable, they involved a complex fabrication procedure and expensive active materials and thus remained elusive for commercial applications. After almost a decade of subdued interest, the rocking-chair battery was decisively revived by the discovery of cheap carbonaceous materials as anode materials. Yazami and Touzain demonstrated that graphite intercalates lithium at a desirably low voltage and high gravimetric capacity [45]. This groundbreaking discovery allowed Yoshino to then make the first LIB using a graphite anode and LCO cathode [46], a device which was successfully commercialized by SONY in 1991 [2]. It was SONY who also renamed the rocking-chair battery as "lithium ion rechargeable battery" [41,44], a name which has stuck to this day. Unfortunately, in the case of sodium, intercalation in graphite resulted in approximately 10 times lower storage capacity [47]. This drawback became a bottleneck and a second major setback for the commercial prospects of SIBs.

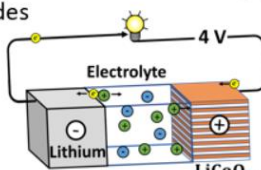
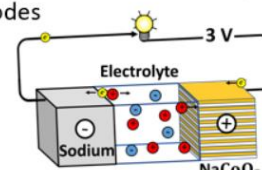
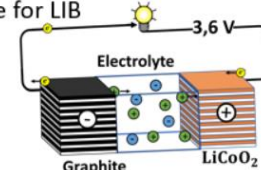




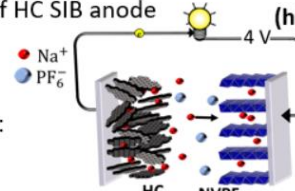


Period	Li-ion Batteries	Na-ion Batteries
1970 - 1980	<ul style="list-style-type: none"> - Goodenough's battery - LiMeO_2 cathodes <p>Applications: Research</p> 	<ul style="list-style-type: none"> - Na/S batteries - NaMeO_2 cathodes <p>Applications: Research</p> 
1980-1990	<ul style="list-style-type: none"> - The "rocking chair" battery - Graphite anode for LIB <p>Applications: Research</p> 	<ul style="list-style-type: none"> - High temperature Na batteries - Lack of a suitable SIB anode <p>Applications: e-Mobility, Grid</p> 
1990-2000	<ul style="list-style-type: none"> - First commercial LIB by SONY - Mixed metal oxides (research) <p>Applications: Portable electronic devices</p> 	<ul style="list-style-type: none"> - SIB research decline - Development of ZEBRA cells <p>Applications: Grid</p> 
2000-2010	<ul style="list-style-type: none"> - Si anodes - High energy density LIB <p>Applications: e-Mobility</p> 	<ul style="list-style-type: none"> - Discovery of HC SIB anode <p>Applications: Research</p> 
2010-2020	<ul style="list-style-type: none"> - Large scale LIB factories - Li supply concerns <p>Applications: e-Mobility, Grid</p> 	<ul style="list-style-type: none"> - Revival of SIB research - SIB start-ups <p>Applications: e-Mobility, Grid</p> 

Fig. 2.1. A shared history of LIB and SIB illustrating the technological evolutions and drivers in different decades. (a) Illustration of a Li//LiCoO₂ and (b) a Na//NaCoO₂ cell. (c) Schematic representation of a graphite//LiCoO₂ battery. (d) Ford Ecostar car, which was designed to use NaS batteries. (e) A Nokia 3310 portable device powered by LIB. (f) Commercial ZEBRA battery for grid energy storage applications. g,h) HC//Na₃V₂(PO₄)₂F₃ cell. (i) Illustration of a grid-scale LIB installation and (j) HiNa SIB installation in Liyang, China. (d) Reproduced with permission. Copyright 2020, Ford Motor Company. (f) Reproduced with permission [116]. Copyright 2003, Elsevier B.V. (j) Reproduced with permission [68]. Copyright 2019, Wiley-VCH.

In the wake of LIB commercialization, the period between the years 1990 and 2000 witnessed a sharp decline in SIB research [48]. During the same period, the market share and value of LIBs skyrocketed. The price of cobalt, a key ingredient in LCO cathodes, rose sharply due to the U.S. Government stockpile [49]. Scarcity, geopolitical and ethical concerns around cobalt extraction motivated the search for cheaper alternatives [44]. This resulted in the synthesis of a new type of metal oxide structures such as the spinel-type in LiMn_2O_4 (LMO) [50], and the olivine type in LiFePO_4 (LFP) [51]. Co substitution in nickel oxides was found to increase structural stability while simultaneously reducing Co content. This feature resulted in a trend of mixed metal oxides, such as $\text{LiNi}_{1-x-y}\text{Co}_x\text{Al}_y\text{O}_2$ (NCA) and $\text{LiNi}_{1-x-y}\text{Mn}_x\text{Co}_y\text{O}_2$ (NMC) toward the end of 2000 [52–54].

In spite of the decline in SIB research in the 1990^s, there were intensive developments in high-temperature sodium batteries [55]. The sodium-sulfur (NaS) systems operating between 300 and 350 °C were developed by the Ford Motor Company and then through a joint Japanese consortium of TEPCO and NGK [56]. A slightly lower temperature variant of NaS, the sodium nickel chloride battery, commonly known as ZEBRA cells, first appeared in 1994 [57,58]. ZEBRA cells operate between 250-300 °C and were first developed by Zeolite Battery Research Africa, from where the name ZEBRA is derived. A common feature of these battery systems is the molten sodium anode and ceramic separators. Application areas include stationary grid energy storage [59], electric mobility [60] and space missions [61]. They serve as proof of the feasibility of large-scale, sodium-based energy storage. Nevertheless, the high operating temperature brings other problems, such as corrosion issues and low energy efficiency.

The revived interest in room temperature SIBs can be traced back to the discovery of Na intercalation in hard carbon (HC) by Dahn and co-workers in 2000 [62,63]. HC in SIBs has a low voltage and high gravimetric capacity of 300 mAh g⁻¹ (which is close to that of graphite in LIBs of 372 mAh g⁻¹). Although this discovery is attributed to be the turning point in the renewed interest in SIBs, it did not spark an immediate rush toward the commercialization of SIBs. This apparent inertia can be attributed to a lack of technological drivers and incentives to replace lithium at the time. Furthermore, SIBs did not promise an increase in the energy density of rechargeable batteries. A patent-based analysis shows that SIB patent filings only began to rise 12 years later, in the year 2012. Therefore, it can be deduced that the driving force to replace LIBs with SIBs is the supply shortage risk due to large-scale LIB applications.

Since 2010, there has been unprecedented progress in SIB cathode materials. For example, the total number of cathode materials reported in the 3 years between 2010 and 2013 nearly equals the total number that existed prior [64]. The three leading families of SIB cathode materials are the layered metal oxides, the polyanion compounds, and the Prussian blue analogs (PBAs) [65]. The guiding mindset was to make cheap SIB electrode materials with similar performance characteristics as LIBs. This mindset explains the preferential choice of earth-abundant elements such as iron, manganese, and magnesium in the composition of these cathode materials. As for the anode, HC remained the prominent choice, with a research focus on finding cheap and abundant precursors.

From 2015, giant leaps toward SIB commercialization were undertaken, spearheaded by startup companies. The most prominent of these are Faradion Limited (UK), Tiamat (France), and HiNa (China). To date, a total of over 10 such companies have since emerged [66]. In November 2015, Tiamat became famous for the first "18650" (18 mm diameter, 65 mm height) cylindrical SIB cells which were developed through the French network for electrochemical energy storage (RS2E) [67], a collaboration of the French National Center for Scientific Research (CNRS), the French Alternative Energies and Atomic Energy Commission (CEA) and the Collège de France [25]. More recently, HiNa, a spinoff from the Institute of Physics Chinese Academy of Sciences (IoP-CAS), also made the news in April of 2019 by installing a 100 kWh (30 kW) container-size battery in China [66]. According to widely accepted press reports, several prototype and near-commercialization SIB cells include: HC//Na₃V₂(PO₄)₂F (NVPF) [68], HC//Na₃V₂(PO₄)₃ (NVP) [69], HC//Na_{0.44}MnO₂ (NMO) [69], HC//NaNi_{1-x-y-z}M_x¹M_y²M_z³O₂ (NMMMO) [70], where Mⁱ is any transition element or Ca, Sb, Bi, Te, Se, *etc.*, and HC//NaFe_{0.4}Mn_{0.3}Ni_{0.3}O₂ (NNFM) [71,72] are near commercialization, all based on HC anodes. **Fig. 2.1** illustrates the shared history in relation to the technological evolutions of both LIBs and SIBs.

2.4 Comparison between sodium- and lithium-ion batteries

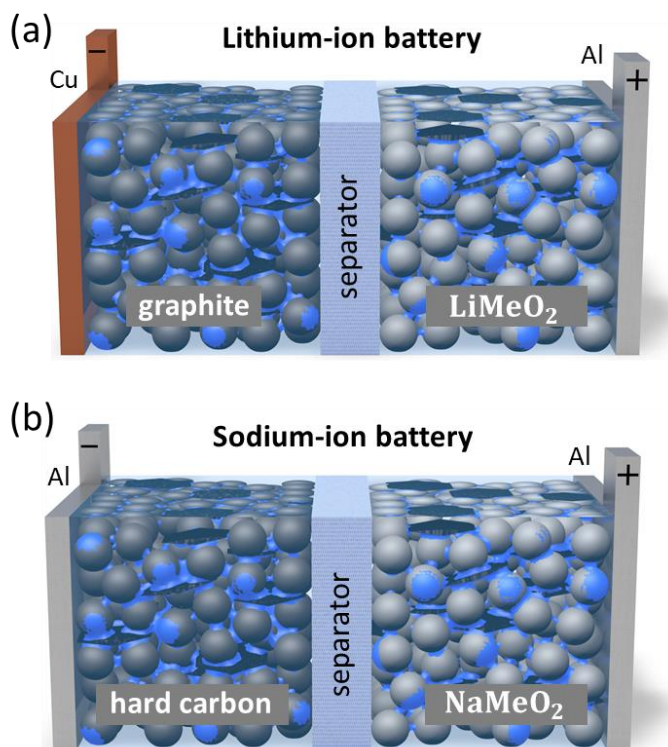


Fig. 2.2. Schematic representation of the components of (a) a LIB and (b) a SIB, showing spherical active electrode particles in gray, carbon conductive fillers in black hexagons, and binder in blue.

As outlined above, the electrochemical properties of SIBs and LIBs are similar. This similarity has allowed the vast knowledge and know-how accumulated in the formative years of LIBs to be directly transferred to the SIB, resulting in rapid progress. For example, the same manufacturing processes and assembly lines used to produce LIBs can produce SIBs. This fact means battery manufacturers would incur no additional capital expenses if they decide to produce SIBs. As such, SIB manufacturing has often been described as "drop-in" replacement, which partly explains the remarkable rate at which the technology has evolved [73]. The next frontier for SIBs is to "drop-in replace" LIBs in large-scale and emerging applications. For this, they need to either match or exceed the performance metrics of LIBs, which include power, energy density (volumetric and gravimetric), cyclability, safety and cost. **Fig. 2.2** illustrates the main components of LIBs (a) and SIBs (b).

2.4.1 Physical features

Judging by physical appearance, there is not much of a difference between a LIB and a SIB. The most common LIB cells are of the 18650 format, and Tiamat currently produces similar SIB cells. Other SIB manufactures have nevertheless opted for pouch cell formats with variable footprints [25,71,74]. Inside the cells, apart from chemical compositions, the composite electrode coatings also look similar because the same conductive carbon filler and binder materials are used in both cell chemistries. The only physical difference is the type of current collectors. In LIBs, copper and aluminum foils are used as anode and cathode current collectors, respectively. In SIBs, however, aluminum foils can be used as current collectors for both electrodes. This is because sodium does not alloy with the aluminum current at the anode [75]. Because aluminum is cheaper and less dense than copper, this property reduces the material costs and weight of SIBs. Using the same current collector has other advantages. Chief among them is the ability to discharge and store a SIB at zero volts, without any degradation. This highly safe characteristic has been demonstrated by Faradion, through their patent on the safe storage and/or transportation of sodium-ion cells at zero volts [76,77].

2.4.2 Energy density, Power and Cyclability

Since their inception, SIBs have demonstrated energy densities comparable to commercial LIBs. The energy density of the first generation 18650 cells was 90 Wh kg^{-1} which was already impressive. For comparison, the first SONY LIB had an energy density of 80 Wh kg^{-1} while state-of-the-art LIBs have approximately $150 - 200 \text{ Wh kg}^{-1}$ [78]. Pouch cell SIBs from Faradion and Novasis Energies have approximately 150 Wh kg^{-1} and 130 Wh kg^{-1} , respectively [25]. Although the energy densities are evidently in the lower range of LIBs, the power/rate capability of SIBs has been outstanding and, in some cases, superior to that of LIBs. **Fig. 2.3** (a) shows the rate performance of power-optimized 55 Wh kg^{-1} cylindrical SIB cells at room temperature. These cells reach 10 C-rate currents, *i.e.* 6 min discharge, with 84 % capacity retention [79]. SIB pouch cells have shown equally excellent rate capabilities, 10 C-rate with 84 % capacity retention [25].

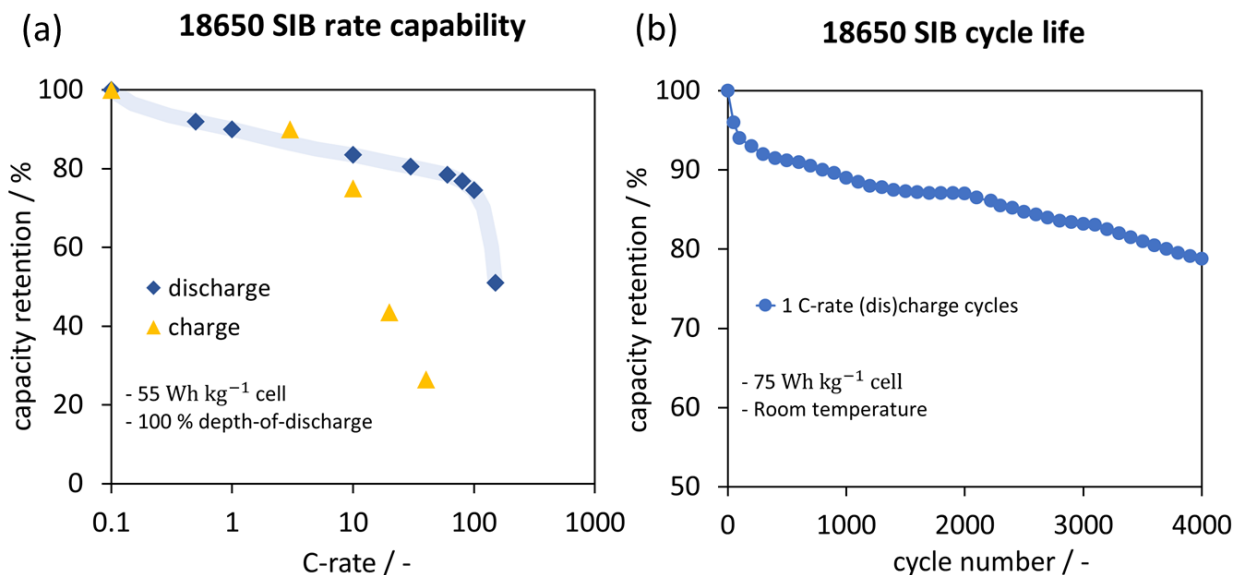


Fig. 2.3. SIB cycle life and rate capability tests. (a) The rate capability of a 55 Wh kg⁻¹ SIB showing outstanding (dis)charge rates. (b) Extended cycle life test of a SIB showing approximately 4000 cycles before end-of-life. SIB cells were cycled at room temperature and 100 % DoD in the voltage range 2–4.25 V. Data derived from [79].

Another performance metric is the cyclability of the cells. Electric vehicle battery test standards define the battery end-of-life as 80% initial/nominal capacity retention [80–83]. Different conditions of temperature, (dis)charge rate, and depth-of-discharge (DoD) are known to affect the cyclability of LIBs. Temperatures extremes (above and below 25 °C), high (dis)charge rates (above 1 C-rate) and high DoD (above 80 %) reduce the battery cycle life [84]. Recent studies have investigated the cyclability of SIBs under different conditions [25,79,85]. **Fig. 2.3** (b) shows the cycling performance of 75 Wh kg⁻¹ SIB cylindrical cells at 1 C-rate. The cylindrical SIBs reach close to 4000 cycles at room temperature, while SIB pouch cells cycled at 45 °C demonstrated 200 cycles with 95 % capacity retention [25]. Therefore, SIBs have shown the ability to operate in a wide range of ambient conditions, and their cyclability and rate capability rivals that of state-of-the-art LIBs.

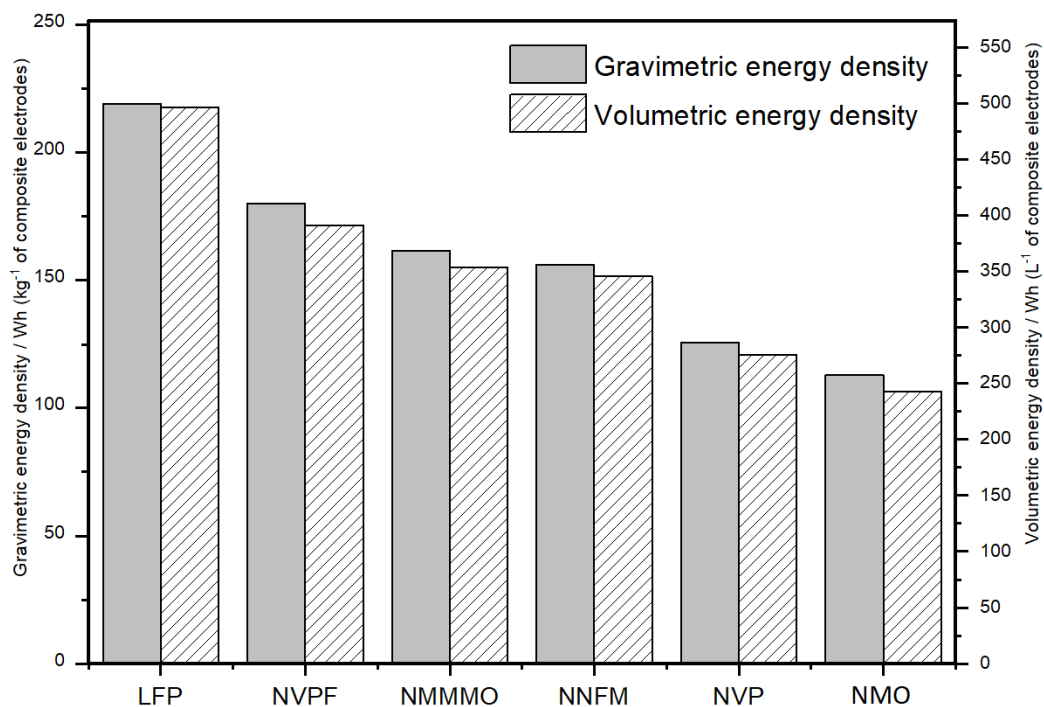


Fig. 2.4. Comparison of the gravimetric and volumetric energy density in SIB (NVPF, NMMMO, NNFM, NVP and NMO) and LIB (LFP) based on the mass of the composite anode and cathodes. Here the mass of the current collectors and other auxiliary battery components are not taken into consideration.

To anticipate the possible application areas of the different SIB chemistries, the energy density of SIB materials is compared to that of LFP, which is one of the most cost-effective LIBs. **Fig. 2.4** shows the volumetric and gravimetric energy densities of the SIBs: NVPF, NMMMO, NNFM, NVP, and NMO compared to the values of LFP-based LIB. Note, these energy densities are higher than those shown in **Fig. 2.3** because they are based on the mass and volume of the active materials and thus exclude non-active components such as separators and casing. **Table 2.2** shows the parameters used for the active materials in the calculations. HC and graphite were the assumed anodes for SIBs and LFP cells, respectively. The energy densities were finally determined using the model guidelines reported by Berg *et al.* [86] for cell balancing calculations.

Based on the results in **Fig. 2.4**, LFP has the highest gravimetric and volumetric energy density compared to all calculated SIBs. Another observation is that the gravimetric energy density scales linearly with volumetric energy density. Therefore, low gravimetric energy densities lead to lower volumetric energy densities among the SIBs. Comparatively close values in energy

density are, however, obtained in NVPF-, NMMMO- and NNFM-based SIBs. These encouraging results give a good indication of the ability of SIBs to match the LIB performance.

Meanwhile, NMO- and NVP-based SIBs suffer from low energy densities resulting from a combination of low cell voltage and low gravimetric capacity. In addition, the low active material loading in NMO and NVP due to nanosized active materials further aggravates their energy delivery. This property highlights the need to have micrometer-sized, high voltage, and high capacity cathode materials for SIB application. In conclusion, a combination of high cathodic potentials and gravimetric capacity is needed to match both the gravimetric and volumetric energy density of LIBs.

Table 2.2. Parameters used for the calculation of volumetric and gravimetric energy density

Cathode material	Cell voltage ^(a) [V]	Cathode capacity [mAh g ⁻¹]	Porosity ^(b) [-]	Density ^(d) [g cm ⁻³]
LFP	3.3	160	0.3	3.65 [86]
NVPF	3.5	120	0.3	3.01
NMMMO	3.7	145	0.3	3.20 ^(e)
NNFM	2.9	125	0.3	3.20 ^(e)
NVP	3	92	0.4 ^(c)	2.98
NMO	2.4	115	0.4 ^(c)	3.20 ^(e)

(a) Average cell voltage *vs.* graphite for LFP and *vs.* hard-carbon for SIB. (b) Porosity in composite electrodes, including a binder and conductive filler. (c) Higher porosity is assumed for electrodes with nanosized active particles. (d) Density values are taken from the Materials Project database unless a reference is given. (e) Estimated values due to unavailable data.

2.4.3 Safety

Because of the numerous cases of LIB fires, battery safety is of utmost importance to large battery shipping companies. Airlines, for example, are obliged to follow stringent regulations regarding onboard LIBs. These regulations followed two catastrophic LIB failures in 2013, which

forced the grounding of the Boeing 787 Dreamliner [87]. In the case of SIBs, blanket LIB regulations have been applied by extension.

Several abuse tolerance tests, such as crush, nail penetration, and accelerating rate calorimetry (ARC), have been performed on pouch and 18650 SIB cells [71,88]. **Fig. 2.5** (a) and (b) show cylindrical and pouch cells undergoing nail penetration tests, respectively. Remarkably, nail penetration tests on short-circuited (shorted) SIB cells show no temperature variation, proving the importance of storage and/or transport at zero volts. Such behavior indicates shorted SIBs have superior thermal stability and abuse tolerance and warrant relaxed transportation regulations, similar to shorted asymmetric capacitors, which can be transported as airfreight [88].

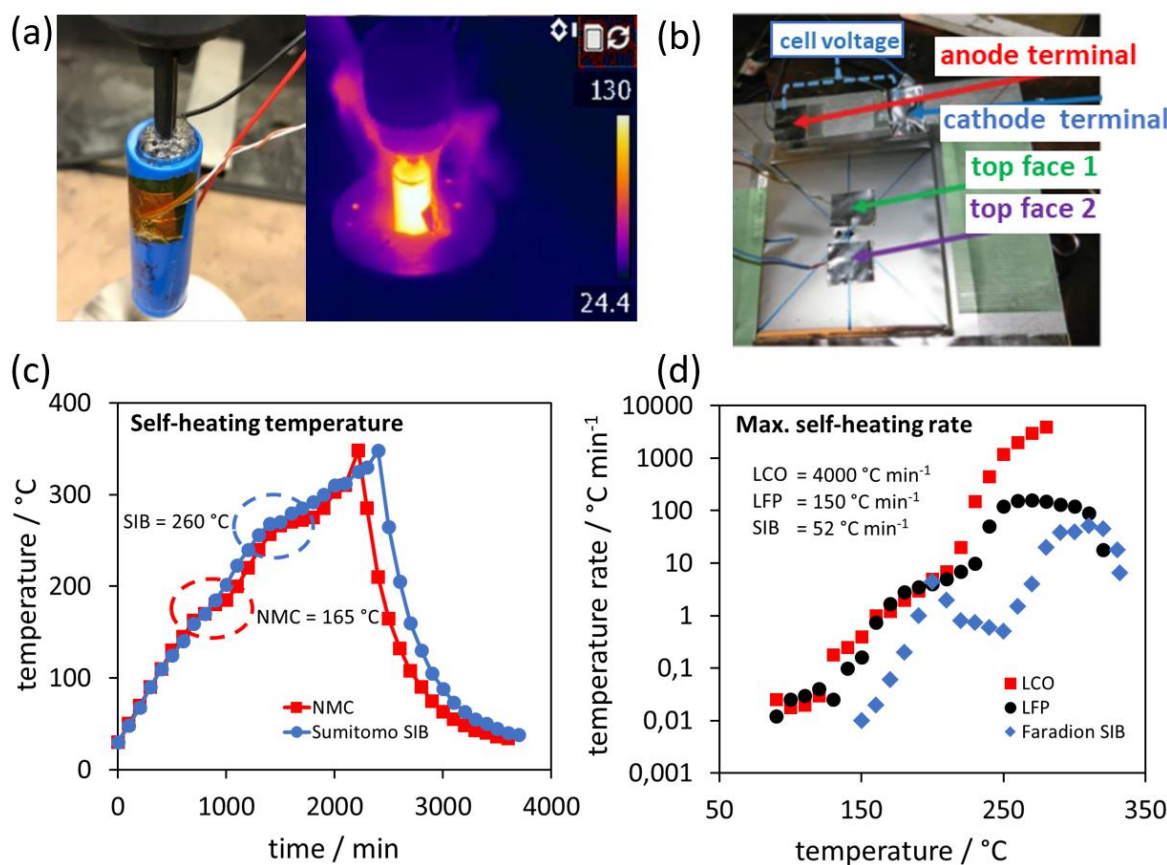


Fig. 2.5. Superior thermal stability and safety of SIBs compared to commercial LIBs. (a) Cylindrical SIBs undergoing nail penetration tests. (b) SIB pouch cell with four thermocouples after nail penetration test showing no flames. (c) ARC test of a SIB compared to NMC showing a high self-heating temperature for SIB. (d) ARC test of a SIB compared to LCO and LFP showing a low self-heating rate of the SIB. (a) Reproduced with permission [88]. Copyright 2019, the United Nations. (b) Reproduced with permission [25]. Copyright 2018, Wiley-VCH (c) Data derived from [71]. (d) Data derived from [89].

Fig. 2.5 (c) and (d) show results of ARC tests on SIBs, which are compared to NMC cells (c) and to LCO and LFP LIBs (d). During the ARC test, the cells are heated gradually to evaluate their self-heating temperature [90]. A temperature plateau indicates the self-heating temperature wherein the cell temperature is sustained by internal exothermic reactions. The results show that the self-heating temperature is higher in the case of the SIB (260 °C) than the LIB (165 °C). In addition, the SIBs show a delayed start of self-heating and have a lower maximum self-heating rate. This observation indicates superior thermal stability in the SIBs compared to the LIBs.

2.4.4 Cost

SIBs have ignited interest mainly because of their low cost potential for grid applications. Therefore, the cost factor has been a subject of investigation in recent studies [86,91,92]. However, the benchmarking task is made difficult by the differences in the maturity levels of the two energy storage technologies. Vaalma *et al.* [92] thus used a simplified approach wherein components of a LiMn_2O_2 //synthetic-graphite cell were swapped to construct a hypothetical NaMn_2O_2 //synthetic-graphite cell. This approach provides a rational comparison of battery material costs, although such a SIB cell is non-functional because sodium does not intercalate in graphite. The results show a 12.5 % cost reduction in the SIB compared to the analogous LIB.

A more holistic approach was provided by Novák *et al.* [86] using the energy-cost model. This approach accounts for the material costs, processing costs, and administrative overheads. The cost of an HC//NVPF SIB cell was 320 \$/kWh, while the graphite//LFP LIB cell was 280 \$/kWh. It reveals that, despite cheap material costs per-kWh, SIBs nevertheless emerged more expensive than LIBs per unit of stored energy. This observation highlights a second important dimension of battery cost analysis, the energy density of the active materials. High energy density materials have a twofold effect of reducing the material cost-per-kWh and the processing costs to reach a target cell energy. Therefore, the endeavor to make cost-competitive SIBs should be accompanied with an active outlook for high energy density active materials.

2.5 Sodium-ion battery materials and electrochemical properties

The mechanisms for sodium insertion into the matrix of the host active materials used in SIB electrodes can be classified as intercalation, alloying and conversion. **Fig. 2.6** outlines these three

charge insertion mechanisms and their concomitant structural changes [93]. Although this illustration is based on host materials for LIB, it also remains relevant for understanding insertion mechanisms in SIB materials.

The terms insertion and intercalation in electrode materials can be somewhat confusing. Armand *et al.* [94] defined an insertion material as an electrode that intrinsically possesses the three functions of electronic and ionic conductivity, *i.e.*, mixed conductivity, and a source of chemical potential. The IUPAC recommendations of 1994 define intercalation as a term strictly reserved for the case of topotactic insertion of a guest into a two-dimensional host [95]. Nevertheless, no strict differentiation exists in literature between insertion and intercalation, and in some cases, both terms are used synonymously [96].

In this thesis, the term intercalation is solely reserved to the restricting condition that the host matrix largely retains its structural integrity during the charge insertion/disinsertion process. This is primarily true for interlayer insertion of sodium guest ions in crystalline compounds and not, for example, sodium insertion into a metallic matrix during alloying since such processes are associated with major structural changes. Compared to other insertion mechanisms, volume changes associated with intercalation reactions are generally negligible. The larger size of Na^+ can, however, be expected to impose a greater strain on the volume and structure of the host compared to analogous, lithium-based intercalation.

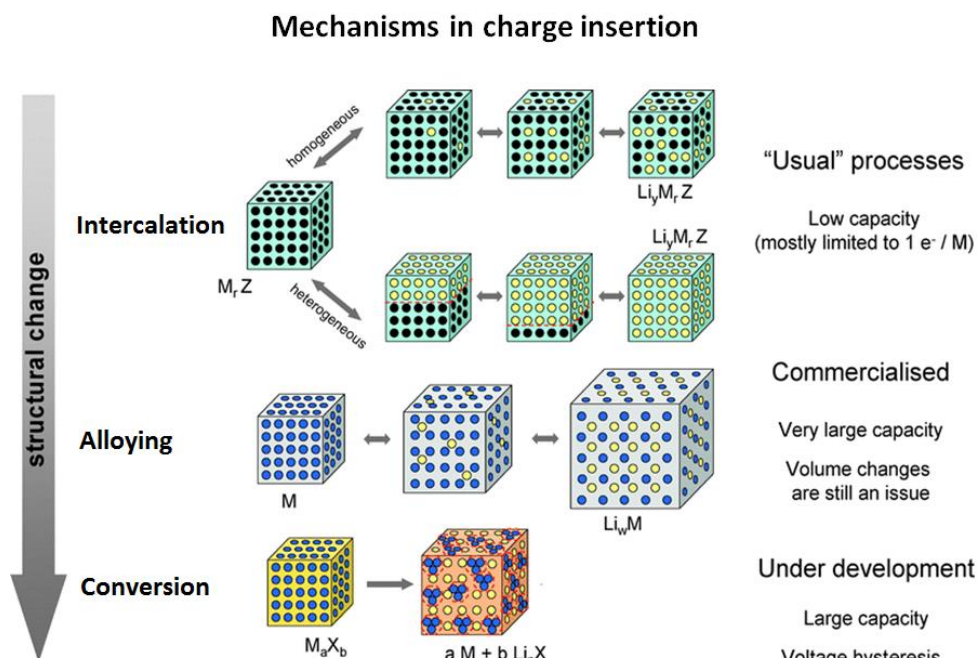


Fig. 2.6. A schematic representation of the different mechanisms in charge insertion observed in electrode materials for lithium-ion batteries. Black circles: voids in the crystal structure, blue circles: metal, yellow circles: lithium. Similar classifications are also used in sodium-ion batteries. Image adapted with permission [93].

2.5.1 Anode materials

The anode, which is also referred to as the negative electrode in primary and secondary batteries, constitutes the electrode with the lowest potential. In SIBs where solvated Na^+ ions are the principle charge carriers, the thermodynamic electrode potential limit at the anode is given by the reduction potential of sodium ($-2.71 V$ vs. SHE). To increase the cell's energy density, it is therefore desirable to have metallic sodium, which guarantees the lowest anode potential and the highest energy density.

Since its inception, HC has remained the prominent anode material for SIB application. Hard carbons are usually prepared by high-temperature carbonization of solid-phase organic and polymer precursors such as cellulose [97], glucose [62], sugar [98] and polypyrrole [99]. The complex microstructure of HC is composed of graphene-like parallel layers embedded in a microporous amorphous phase. This structure is frequently exemplified by the "house of cards" model. The voltage profile of HC is shown in **Fig. 2.7** (a) and (b). From these results, two

characteristic features are evident; (i) a sloping region from ca. 1 V, and (ii) a long plateau region commencing from about 0.1 V until reaching 0 V (vs. Na^+/Na).

Correlating the microstructural properties of HC to the observed voltage profile has been controversial and led to spirited systematic studies to elucidate the correct sodium storage mechanism [100,101]. **Fig. 2.7** illustrates three different mechanisms proposed so far. Early studies by Dahn and Stevens (2001) and subsequent works by Komaba *et al.* [102] (2011) hypothesized an intercalation mechanism between parallel graphene sheets for the sloping voltage region, while nanopore filling in a process analogous to adsorption was ascribed to the plateau voltage region [63]. This mechanism was termed "intercalation-adsorption" and is shown in **Fig. 2.7** (a).

Contradictory findings, however, emerged as Tsai *et al.* [103] (2015) sought to clarify the Na insertion mechanism in HC using DFT calculations. The effect of the graphene interlayer distance and the presence of copious point defects in HC was therein explored. It was concluded that a large initial graphene interlayer distance of 3.8 Å, as well as the presence of vacancy defects, could enhance sodium storage due to the strong ionic bonds between Na^+ ions and the defects. An "adsorption-intercalation" mechanism, here illustrated in **Fig. 2.7** (b), was thus premised. The sloping region was thus correlated to simultaneous adsorption on defect sites in graphene layers. In contrast, the plateau region was assigned an intercalation mechanism on sites around the defects. Experimental studies by Bommier *et al.* [104] (2015) on "defect-free" glassy carbon and samples of sucrose-derived HC, carbonized in the temperature range of 1100 – 1600 °C, further corroborated this mechanism.

Later, Zhang *et al.* [101] (2016) prepared carbon nanofibers with tailored graphitization degrees by varying the pyrolysis temperature to obtain different pore size distribution, active surface area, *d*-spacing, degree of graphitization, and amount of N and O heteroatoms. As the carbonization temperature increased, a rise in the degree of graphitization, a decrease in the active surface area, and a gradual disappearance of heteroatom surface groups is reported. The pore width migrates from an average of 1,2 nm for low-temperature synthesized carbon nanofibers to 3.2 nm (small mesopores) for carbon nanofibers synthesized at temperatures above 950 °C. Based on systematic experimental results, the Na storage mechanism in the sloping voltage region is described as two processes of Na^+ bonding on the defect sites induced by heteroatoms and Na adsorption onto the surfaces of randomly oriented graphene layers. The low voltage plateau was

therein correlated to "small mesopore" filling. This interpretation marked a partial return to Dahn and Stevens's initial nanopore filling model. **Fig. 2.7** (c) illustrates the three proposed stages in the "adsorption-filling" mechanism. Although *in situ* X-ray diffraction (XRD) experimental evidence could not conclusively exclude the possibility of intercalation in the sloping region, the consistency of the obtained *d*-spacing, however, discarded possibilities of either intercalation or Na plating in the low voltage plateau region.

While being supported by meticulous experimental evidence, these contradictory hypotheses could also be rooted in the different materials and methods in the original studies. Regardless of this apparent lack of a universally agreed mechanistic model, several significant steps toward optimizing HC anode materials in SIB have been realized recently [105–107].

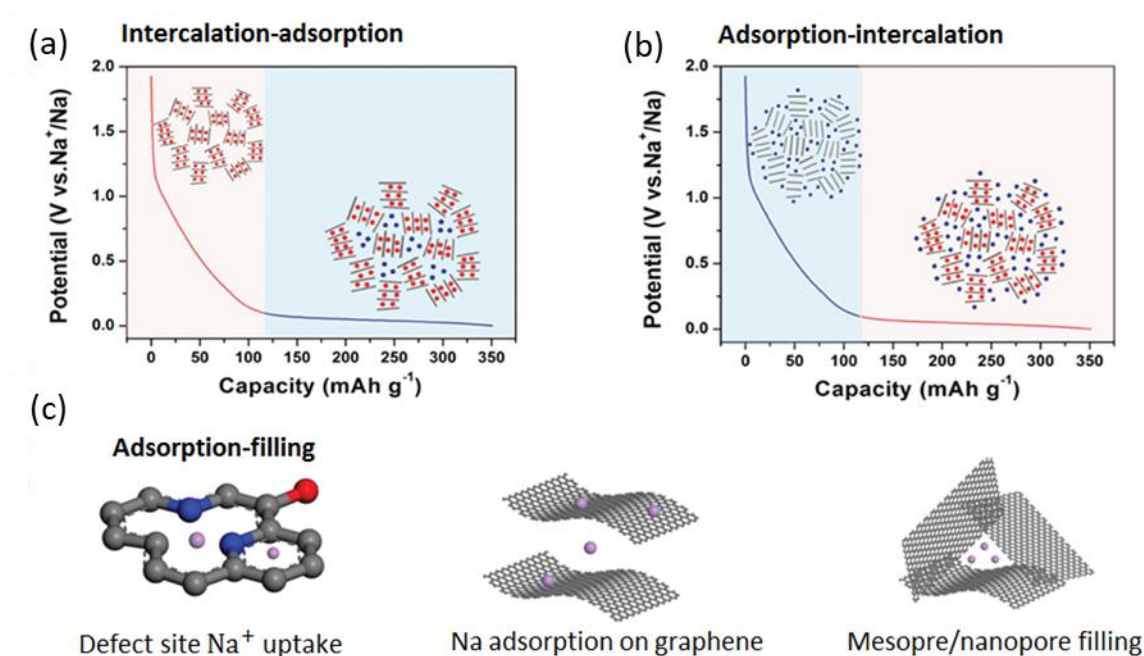


Fig. 2.7. Controversy in correlating the microstructural properties of HC. (a) The intercalation–adsorption mechanism. (b) The adsorption–intercalation mechanism. (c) The adsorption-filling mechanism in hard carbon based SIB anodes. (a), (b) Reproduced with permission [100]. Copyright 2017, Wiley-VCH. (g) Reproduced with permission [101]. Copyright 2015, Wiley-VCH.

Fig. 2.8 shows the voltage and gravimetric storage capacity of available SIB anode materials. The blue circles represent intercalation-based materials. The red squares represent conversion materials, while cyan diamonds represent alloy-based materials. For energy density reasons, the

generally agreed voltage limit for anodes is 2 V *vs.* Na⁺/Na. In this figure, contour lines of energy density at 100, 150, 200, 250, 300, and 350 Wh kg⁻¹ are shown. A hypothetical cathode material with a gravimetric capacity of 120 mAh g⁻¹ and average potential of 3.7 V *vs.* Na⁺/Na is herein assumed for these energy density calculations.

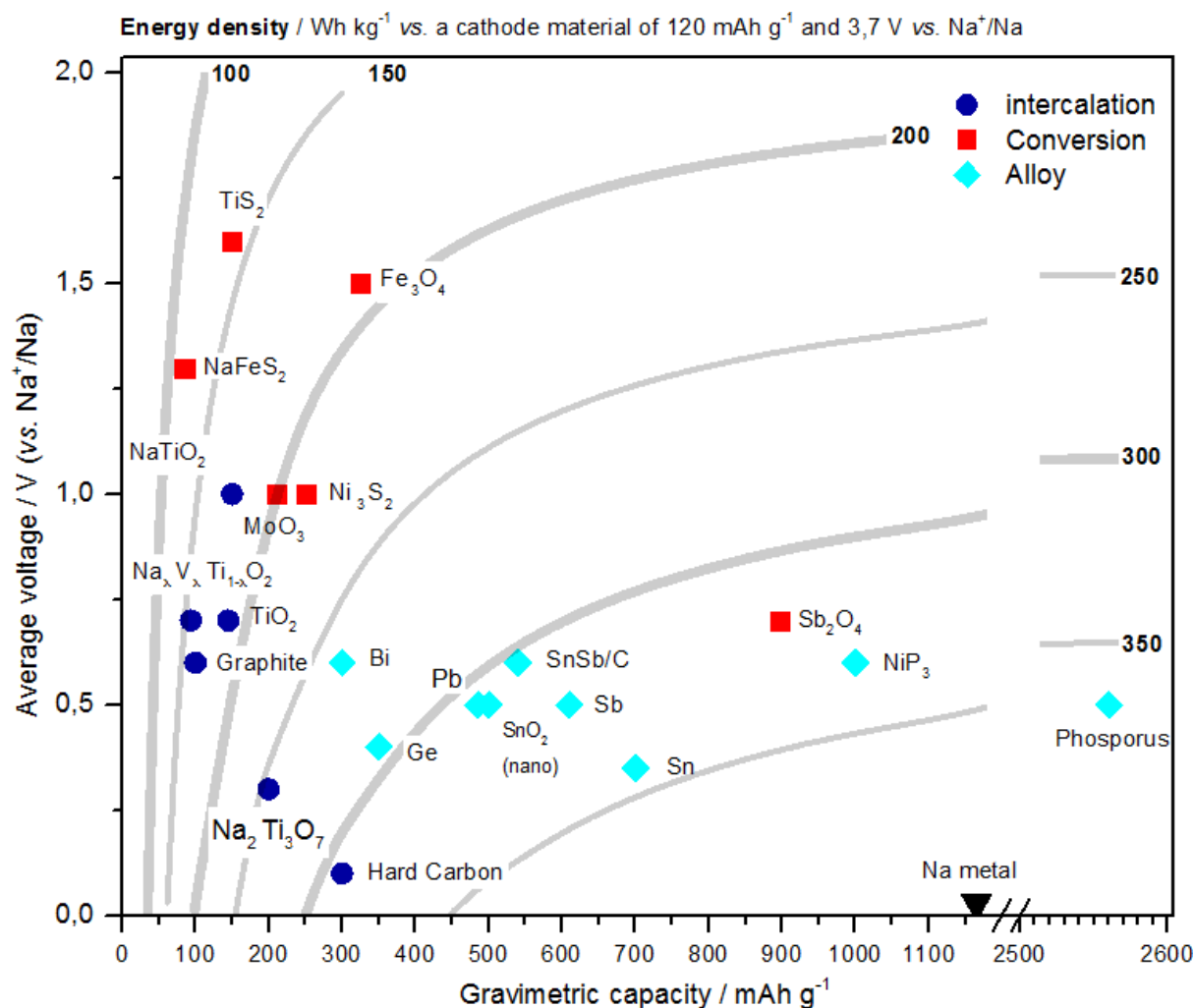


Fig. 2.8. Average voltage *vs.* the discharge capacity of various sodium-based anode materials. Intercalation materials (blue circles), conversion materials (red squares), and alloy materials (cyan diamonds). The energy density calculations are shown in the 6 contour lines (100, 150, 200, 250, 300, and 350 Wh kg⁻¹), are based on the weight of the active material, using a theoretical cathode material with 120 mAh g⁻¹ and 3.7 V *vs.* Na⁺/Na. Data derived from refs. [98,108–117,117–134].

While the intercalation-based anode materials have desirably low electrode potentials, they generally suffer from a low gravimetric capacity. In this category, HC is the outstanding performer given that it has the lowest electrode potential and highest gravimetric capacity of about 300 mAh g⁻¹. Alloy-based materials, on the other hand, attain even higher gravimetric capacities compared to intercalation materials, which aides their volumetric energy densities. The perils, however, of this phenomenally high capacity is a large volume expansion upon charge insertion, which brings about destructive structural deformations. Newcomer, conversion-based anode materials, in contrast, tend to have moderate to high voltages and are characterized by relatively low gravimetric capacities. Here, Sb₂O₄ is a standout performer, yet challenges regarding voltage hysteresis result in low energy efficiency in full cell batteries, which further explains the subdued interest in these materials.

2.5.2 Cathode materials

Positive electrode materials with potential above 2 V *vs.* Na⁺/Na are generally classified as cathode materials. In SIBs, the two main classes of compounds are the layered metal oxides and the polyanionic compounds. The layered metal oxides are the pioneering materials closely related to Li-based cathode materials. The layered metal oxides, however, remain popular in research. Since 2010, they are the most extensively studied materials in relation to cathode materials for SIBs [29]. On the other hand, the most widely studied polyanionic groups are those based on sulfate (SO₄)²⁻, phosphate (PO₄)³⁻ and pyrophosphate (P₂O₇)⁴⁻ ions [135]. Compared to the layered metal oxides, polyanionic compounds have remarkable structural stability and an adjustable electrode potential due to the inductive effect [136–138].

One of the most appealing family of electrode materials is the polyanion vanadium-based fluorophosphate, with the general formula: Na₃V₂O_{2x}(PO₄)₂F_{3-2x}, where 0 ≤ x ≤ 1. This family of electrode materials was first introduced by Barker and co-workers [139–141]. As x varies, the crystal structure, as well as the oxidation state of vanadium (between 3+ and 4+), changes [142]. The most prominent forms are the two end members: Na_{1.5}V^{IV}OPO₄F_{0.5}, where x = 1 and Na₃V₂^{III}(PO₄)₂F₃, where x = 0. Sauvage *et al.* [143] investigated the crystal structure and electrochemical properties of Na_{1.5}V^{IV}OPO₄F_{0.5}. The discharge voltage curve exhibited two exceptionally high voltage plateaus nested at about 3.6 and 4.0 V (*vs.* Na⁺/Na). However, the low

electronic conductivity at room temperature ($1.8 \times 10^{-7} \text{ S cm}^{-1}$) of the material was thought to be the reason for the poor transport properties. Therefore, carbon-coating was expected to enhance the electrode performance.

Fig. 2.9 illustrates the structure (a) and electrochemical features (b) of $\text{Na}_3\text{V}_2^{III}(\text{PO}_4)_2\text{F}_3$ as described above. For high energy density considerations, $\text{Na}_3\text{V}_2^{III}(\text{PO}_4)_2\text{F}_3$ is the most attractive phase [144]. More impressively, a higher electrode capacity close to the theoretical 128 mAh g^{-1} with exceptional capacity retention (98 % after 40 cycles) has been achieved, resulting in a high theoretical energy density of 507 Wh kg^{-1} ($128 \text{ mAh g}^{-1} \times 3.95 \text{ V}$) [144,145].

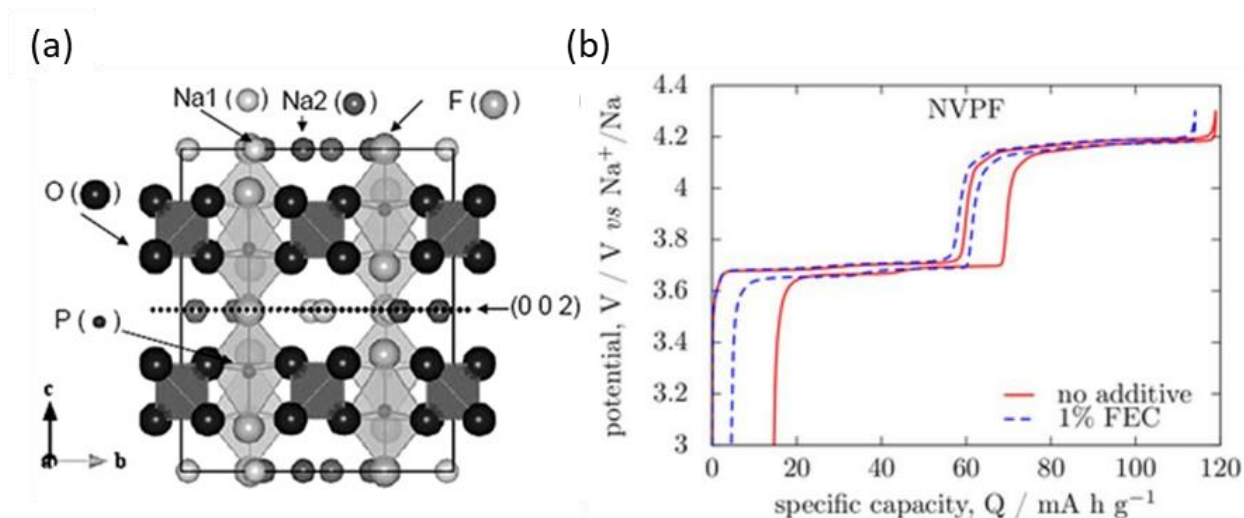


Fig. 2.9. Properties of $\text{Na}_3\text{V}_2(\text{PO}_4)_2\text{F}$ cathode material. (a) The 3D structure of $\beta - \text{Na}_3\text{V}_2(\text{PO}_4)_2\text{F}$, viewed along the *a*-axis. (b) The (dis)charge voltage profile in $\text{Na}/\text{Na}_3\text{V}_2(\text{PO}_4)_2\text{F}$ half-cell at C/10 rate. (a) Reproduced with permission [145]. Copyright 2012, Elsevier B.V. (b) Reproduced under the terms of the CC-BY Licence 4.0 [146]. Copyright 2016, The Authors.

Fig. 2.10 shows the average voltage and gravimetric capacity of layered metal oxides (red squares), polyanionic compounds (blue circles), and other insertion structures (yellow triangles), which include PBAs. Contour lines representing the theoretically calculated energy densities of SIBs fabricated with such cathode materials, calculated per kilogram of both the anode and cathode and assuming an HC anode. In this figure, 4 contour lines of energy density at 150, 200, 250, and 300 Wh kg^{-1} are shown. Compared to the anode materials, a larger repertoire of material choices exists in cathode materials.

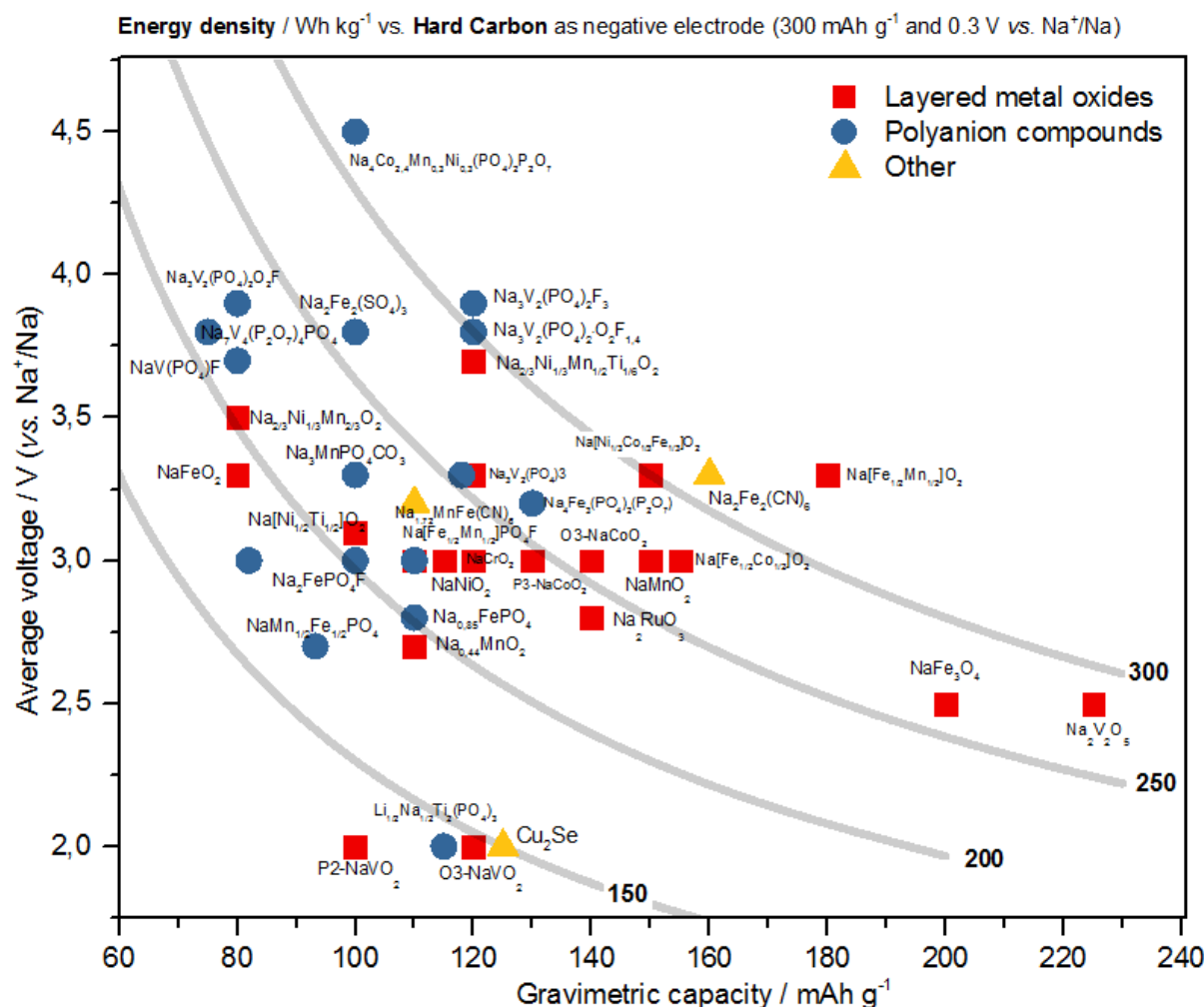


Fig. 2.10. Average cathode voltage during discharge vs. the storage capacity of various cathode materials. Layered metal oxides (red squares), polyanionic compounds (blue circles) as well as other insertion structures (yellow triangles) are shown. The 4 contour lines (150, 200, 250, 300 Wh kg⁻¹) represent the energy density calculations of SIB fabricated with such cathodes, calculated per kilogram of both the anode and cathode and assuming an HC anode. Calculations based on data presented in refs. [28,29,71,102,143,145,147–192].

It can be seen that the polyanionic compounds generally have a desirably high electrode potential. In contrast, the electrode potential of the layered metal oxides are mostly moderate, in the range of 2.5 and 3.5 V. However, layered metal oxides show higher gravimetric capacities compared to polyanionic compounds because of the heavy polyanionic species $(\text{XO}_4)^{3-}$. In general, the achievable energy densities among the different cathode materials is encouraging, using a LiMn_2O_4 -based LIB as a benchmark whose energy density is approximately 300 Wh kg⁻¹. Several cathode materials are found beyond the 300 Wh kg⁻¹ contour line range

and can thus compete with LIBs. Note that these energy density results are higher than what can be achieved in real cells because only the weight of active materials is accounted for in the calculations.

2.5.3 Electrolytes

Although usually perceived as a passive component, the electrolyte constitutes an integral part of any electrochemical device and, indeed, batteries. Besides the interest in bulk properties of electrolytes, such as conductivity and viscosity, interfaces formed between the electrolyte and the two electrodes are often decisive to the overall performance of batteries. Therefore, mastering the chemical nature of electrolytes as well as the structure and properties of the electrolyte/electrode interphases is a vital step in the development of SIB and LIB cells. This ability constitutes the bedrock of modern electrochemistry [193]. In general, an electrolyte solvent should, satisfy the following criteria [194]: (a) A large electrochemical stability window (ESW), ensuring that it does not react at the surfaces of either electrode within the operating voltage window; (b) A wide operating temperature, which allows the solvent to remain in the desired state, *i.e.*, solid or liquid in the operating temperature range; (c) A low viscosity which increases the ionic conductivity; (d) A high dielectric permittivity to dissociate the ionic species high solute concentrations; (e) Finally, the solvent should be non-toxic.

Because the cell voltage window of LIBs and SIBs is almost the same, there is little difference in the ESW and hence the choice of electrolyte solvents for both batteries [195]. Nevertheless, It is important to note that the solid electrolyte interface (SEI) formed in SIBs and LIBs is different, even when the same solvent is used [102]. Ponrouch *et al.* [98,196] carried out systematic studies to compare the performance of different electrolyte blends for SIB application. Solvent formulations that have been investigated in SIBs include binary and tertiary mixtures of ethylene carbonate (EC), propylene carbonate (PC), dimethyl carbonate (DMC), 1,2 dimethoxyethane (DME), and diethyl carbonate (DEC) [196,197]. It is therein shown that the EC_{0.5}:PC_{0.5} (w/w) and the EC_{0.4}:PC_{0.4}:DMC_{0.1} (w/w) are the optimum electrolyte blends for SIB applications due to their wide ESW and high reversible capacity.

Differences with LIB electrolytes arise in the salt. Whereas LiPF₆ is the most frequently used salt in LIBs, NaPF₆ is frequently used in SIBs. The typical salt concentration used is 1 M because

of optimal conductivity and viscosity at this concentration. There were some unsuccessful attempts to use NaClO_4 salts which were abandoned due to explosion hazards [198]. Early NaPF_6 salts had purity issues which resulted in turbid electrolytes. This issue negatively impacted the performances of the half-cells and sodium reference electrodes. These are some of the practical challenges in developing a new battery chemistry. Nevertheless, high purity, battery grade NaPF_6 is commercially available at a price 4 times cheaper than LiPF_6 . For comparison, the price of LiPF_6 is approximately 8.9 €/g while that of NaPF_6 is 2.2 €/g. This price disparity is due to the similarity in synthesis routes and precursor materials, except for the upstream alkali-metal carbonates (Li_2CO_3 and Na_2CO_3) [199].

2.6 SIB technology trend and outlook

Technological trends based on cumulative patent numbers, usually follow an S-shaped profile. This growth trajectory proceeds in the four successive stages of (i) predevelopment (emerging), (ii) take-off (growth), (iii) acceleration (maturity) and (iv) stabilization (saturation) [200,201]. The predevelopment stage is characterized by an exponential rise in annual patent numbers. In contrast, the growth stage is characterized by a drop in patent numbers as companies consolidate and commercialize the technology.

Fig. 2.11 (a) illustrates the technological trend for an emerging technology. Patent numbers remain the most convenient approach to benchmark technological trends because they give insight into the most recent technological activities. Furthermore, this information is directly accessible through dedicated patent search engines [356]. For our purpose, the open online services of Espacenet are employed as an international patent database and used to find intelligent search features to specify keywords and filling dates. **Fig. 2.11** (b) shows the trends in SIB technology. This analysis was first carried out in 2017 and concluded that the SIB technology was in the emerging stage due to a monotonous and sharp increase in annual patent fillings [65]. However, since 2019, there has been a drop in annual SIB patent numbers, which marks the beginning of the consolidation/growth stage. Such a drop in patent numbers is caused by the curtailment of research efforts, as companies focus on commercialization [201]. Combining these patent trends with the positive results seen in prototype SIB announcements, there is reason to expect commercial SIBs on the market soon.

In terms of technological outlook, it appears different roadmap strategies are being pursued. Some hope SIBs will eventually replace LIBs as a cheaper and resource-abundant alternative. Others find no reasons to justify the replacement strategy and instead believe SIBs should be identified as a separate class of batteries [203]. By taking lessons from the historical evolution of LIBs, it is evident that any battery technology needs a matching application. In the case of LIBs, the application was portable electronic devices, and now the technology driver is e-mobility. It is important to identify the target application for SIBs and aim for the most satisfying long-term outcome to avoid the pitfall of giving the right technological solutions to wrong/misplaced policies. Aiming to catch up to an established technology such as LIB is undoubtedly an enormous task, which is justified by the need to avert lithium supply risk shortage. Besides that, the SIB technology should find its unique path in the long-term, for example, in areas such as solid-state batteries and rechargeable metal-air batteries. Such a daring endeavor creates great opportunities in fundamental and applied research to exploit the subtle yet unique properties of SIBs for future applications.

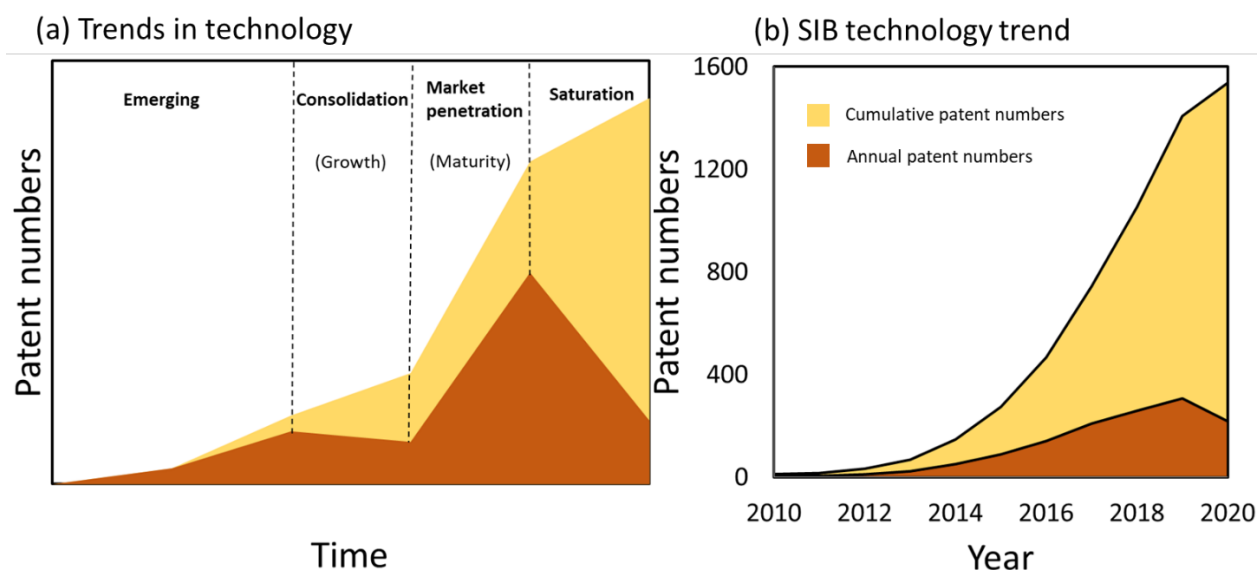


Fig. 2.11. Trends in SIB technology. (a) Illustration of the growth patterns based on annual patent applications and cumulative patents for an emerging technology. (b) Trends in SIB patents from 2010 to 2020. Data derived from Espacenet [202].

2.7 Conclusions

Progress toward the commercialization of room temperature sodium-ion batteries (SIBs) continues to gain traction since the discovery of hard carbon (HC) as a functional anode material. Among the limited number of anode material options available, HC remains the material of choice at the moment. On the cathode side, more attractive options have been unveiled, primarily inspired by similarities in material synthesis methods from lithium-ion batteries (LIBs). Polyanionic compounds, layered metal oxides, and the recently introduced Prussian blue analogs have emerged as the most stable structures, able to accommodate sodium in their crystal lattices reversibly. The choice of elemental compositions has emerged as a strategy to tune the redox potentials and avoid scarce elements. At the same time, nanosizing and carbon coating improve the material's rate capability and cyclability. It is important to consider the storage capacity, voltage characteristics, and cycling ability to identify the most appropriate electrode material. The roadmap toward developing superior cathode materials for SIB applications is thus guided by resource constraints and mastering crystallography and elemental compositions.

Electrolyte development through systematic studies has been able to identify mixed electrolytes based on ethylene carbonate, propylene carbonate, and dimethyl carbonate as the optimum choice in the voltage window of SIBs. In terms of gravimetric and volumetric energy density, SIBs can compete with some of the most prominent LIBs, such as LiFePO_4 and LiMn_2O_4 batteries. Given the achieved milestones above, the roadmap toward commercialization of SIBs now depends on large-scale industrial adoptions of this groundbreaking technology.

References

- [1] The Royal Swedish Academy of Sciences, The Nobel Prize in Chemistry (2019). <https://www.nobelprize.Org>. (accessed April 13, 2020).
- [2] K. Ozawa, Lithium-ion rechargeable batteries with LiCoO₂ and carbon electrodes: the LiCoO₂/C system, *Solid State Ionics* **69** (1994) 212–221. [https://doi.org/10.1016/0167-2738\(94\)90411-1](https://doi.org/10.1016/0167-2738(94)90411-1).
- [3] R. Brodd, Recent developments in batteries for portable consumer electronics applications, *The Electrochemical Society Interface* **8** (1999).
- [4] Sony, Keywords to understanding Sony Energy Devices (2016). <http://www.sonyenergy-devices.co.jp/en/keyword/> (accessed April 13, 2020).
- [5] G.E. Moore, Cramming More Components Onto Integrated Circuits, *Proceedings of the IEEE* **86** (1998) 82–85. <https://doi.org/10.1109/JPROC.1998.658762>.
- [6] D. Takahashi, Forty years of Moore's Law, *The Seattle Times* (2005). <https://www.seattletimes.com/business/forty-years-of-moores-law/> (accessed April 13, 2020).
- [7] M. M. Thackeray, C. Wolverton, E. D. Isaacs, Electrical energy storage for transportation—approaching the limits of, and going beyond, lithium-ion batteries, *Energy & Environmental Science* **5** (2012) 7854–7863. <https://doi.org/10.1039/C2EE21892E>.
- [8] H. Maruyama, H. Nakano, M. Ogawa, M. Nakamoto, T. Ohta, A. Sekiguchi, Improving battery safety by reducing the formation of Li dendrites with the use of amorphous silicon polymer anodes, *Scientific Reports* **5** (2015) 1–9. <https://doi.org/10.1038/srep13219>.
- [9] H. Wu, D. Zhuo, D. Kong, Y. Cui, Improving battery safety by early detection of internal shorting with a bifunctional separator, *Nature Communications* **5** (2014) 1–6. <https://doi.org/10.1038/ncomms6193>.
- [10] S. Nieto, S.B. Majumder, R.S. Katiyar, Improvement of the cycleability of nano-crystalline lithium manganate cathodes by cation co-doping, *Journal of Power Sources* **136** (2004) 88–98. <https://doi.org/10.1016/j.jpowsour.2004.05.020>.
- [11] European Commission, Ecodesign preparatory Study for Batteries, (2020). <https://ecodesignbatteries.eu/> (accessed April 13, 2020).
- [12] Statista, Worldwide BEV sales by brand 2019, Statista (2019). <https://www.statista.com/statistics/666130/global-sales-of-electric-vehicles-ytd-by-brand/> (accessed April 13, 2020).
- [13] US DOE, Fuel Economy, (2020). <https://www.fueleconomy.gov/> (accessed April 13, 2020).
- [14] I. Tsiropoulos, D. Tarvydas, N. Lebedeva, Li-ion batteries for mobility and stationary storage applications: scenarios for costs and market growth., (2018). <http://op.europa.eu/en/publication-detail/-/publication/e65c072a-f389-11e8-9982-01aa75ed71a1/language-en> (accessed April 13, 2020).
- [15] European Commission, A European Green Deal, European Commission - European Commission. (2020). https://ec.europa.eu/info/strategy/priorities-2019-2024/european-green-deal_en (accessed April 13, 2020).
- [16] InsideEVs, Total To Build France's Largest Li-Ion ESS Using Saft Batteries, InsideEVs. (2020). <https://insideevs.com/news/406987/total-france-largest-battery-ess-saft/> (accessed April 13, 2020).

- [17] D.M. Davies, M.G. Verde, O. Mnyshenko, Y.R. Chen, R. Rajeev, Y.S. Meng, G. Elliott, Combined economic and technological evaluation of battery energy storage for grid applications, *Nature Energy* **4** (2019) 42–50. <https://doi.org/10.1038/s41560-018-0290-1>.
- [18] C. Grosjean, P.H. Miranda, M. Perrin, P. Poggi, Assessment of world lithium resources and consequences of their geographic distribution on the expected development of the electric vehicle industry, *Renewable and Sustainable Energy Reviews* **16** (2012) 1735–1744. <https://doi.org/10.1016/j.rser.2011.11.023>.
- [19] J. Speirs, M. Contestabile, Y. Houari, R. Gross, The future of lithium availability for electric vehicle batteries, *Renewable and Sustainable Energy Reviews* **35** (2014) 183–193. <https://doi.org/10.1016/j.rser.2014.04.018>.
- [20] D. Kushnir, B.A. Sandén, The time dimension and lithium resource constraints for electric vehicles, *Resources Policy* **37** (2012) 93–103. <https://doi.org/10.1016/j.resourpol.2011.11.003>.
- [21] C. Wadia, P. Albertus, V. Srinivasan, Resource constraints on the battery energy storage potential for grid and transportation applications, *Journal of Power Sources* **196** (2011) 1593–1598. <https://doi.org/10.1016/j.jpowsour.2010.08.056>.
- [22] D.-W. Kim, J.R. Park, N.-K. Ahn, G.-M. Choi, Y.-H. Jin, J.-K. Yang, A review on the recovery of the lithium carbonate powders from lithium-containing substances, *Journal of the Korean Crystal Growth and Crystal Technology* **29** (2019) 91–106. <https://doi.org/10.6111/JKCGCT.2019.29.3.091>.
- [23] E.A. Olivetti, G. Ceder, G.G. Gaustad, X. Fu, Lithium-Ion Battery Supply Chain Considerations: Analysis of Potential Bottlenecks in Critical Metals, *Joule* **1** (2017) 229–243. <https://doi.org/10.1016/j.joule.2017.08.019>.
- [24] S. Bobba, P. Claudiu, D. Huygens, P. Alves-Dias, B. Gawlik, E. Tzimas, D. Wittmer, P. Nuss, M. Grohol, H. Saveyn, F. Buraoui, G. Orveillon, T. Hámor, S. Slavko, F. Mathieux, M. Gislev, C. Torres De Matos, G.A. Blengini, F. Ardente, D. Blagoeva, E. Garbarino, Report on critical raw materials and the circular economy., (2018). <http://op.europa.eu/en/publication-detail/-/publication/d1be1b43-e18f-11e8-b690-01aa75ed71a1/language-en/format-PDF> (accessed April 13, 2020).
- [25] A. Bauer, J. Song, S. Vail, W. Pan, J. Barker, Y. Lu, The Scale-up and Commercialization of Nonaqueous Na-Ion Battery Technologies, *Advanced Energy Materials* **8** (2018) 1702869. <https://doi.org/10.1002/aenm.201702869>.
- [26] S. Roberts, E. Kendrick, The re-emergence of sodium ion batteries: testing, processing, and manufacturability, *Nanotechnol Sci Appl.* **11** (2018) 23–33. <https://doi.org/10.2147/NSA.S146365>.
- [27] K. West, B. Zachau-Christiansen, T. Jacobsen, S. Skaarup, Sodium insertion in vanadium oxides, *Solid State Ionics* **28** (1988) 1128–1131. [https://doi.org/10.1016/0167-2738\(88\)90343-8](https://doi.org/10.1016/0167-2738(88)90343-8).
- [28] J.M. Tarascon, G.W. Hull, Sodium intercalation into the layer oxides $\text{Na}_x\text{Mo}_2\text{O}_4$, *Solid State Ionics* **22** (1986) 85–96. [https://doi.org/10.1016/0167-2738\(86\)90062-7](https://doi.org/10.1016/0167-2738(86)90062-7).
- [29] N. Yabuuchi, K. Kubota, M. Dahbi, S. Komaba, Research Development on Sodium-Ion Batteries, *Chem. Rev.* **114** (2014) 11636–11682. <https://doi.org/10.1021/cr500192f>.
- [30] H. Kang, Y. Liu, K. Cao, Y. Zhao, L. Jiao, Y. Wang, H. Yuan, Update on anode materials for Na-ion batteries, *J. Mater. Chem. A* **3** (2015) 17899–17913. <https://doi.org/10.1039/C5TA03181H>.

- [31] M.S. Whittingham, Electrical Energy Storage and Intercalation Chemistry, *Science* **192** (1976) 1126–1127. <https://doi.org/10.1126/science.192.4244.1126>.
- [32] W.B. Johnson, W.L. Worrell, Lithium and sodium intercalated dichalcogenides: Properties and electrode applications, *Synthetic Metals* **4** (1982) 225–248. [https://doi.org/10.1016/0379-6779\(82\)90015-7](https://doi.org/10.1016/0379-6779(82)90015-7).
- [33] K. Mizushima, P.C. Jones, P.J. Wiseman, J.B. Goodenough, Li_xCoO_2 (0, *Materials Research Bulletin* **15** (1980) 783–789. [https://doi.org/10.1016/0025-5408\(80\)90012-4](https://doi.org/10.1016/0025-5408(80)90012-4).
- [34] M.M. Thackeray, P.J. Johnson, L.A. de Picciotto, P.G. Bruce, J.B. Goodenough, Electrochemical extraction of lithium from LiMn_2O_4 , *Materials Research Bulletin* **19** (1984) 179–187. [https://doi.org/10.1016/0025-5408\(84\)90088-6](https://doi.org/10.1016/0025-5408(84)90088-6).
- [35] C. Delmas, J.-J. Braconnier, C. Fouassier, P. Hagenmuller, Electrochemical intercalation of sodium in Na_xCoO_2 bronzes, *Solid State Ionics* **3** (1981) 165–169. [https://doi.org/10.1016/0167-2738\(81\)90076-X](https://doi.org/10.1016/0167-2738(81)90076-X).
- [36] J.J. Braconnier, C. Delmas, P. Hagenmuller, Etude par desintercalation electrochimique des systemes Na_xCrO_2 et Na_xNiO_2 , *Materials Research Bulletin* **17** (1982) 993–1000. [https://doi.org/10.1016/0025-5408\(82\)90124-6](https://doi.org/10.1016/0025-5408(82)90124-6).
- [37] A. Mendiboure, C. Delmas, P. Hagenmuller, Electrochemical intercalation and deintercalation of Na_xMnO_2 bronzes, *Journal of Solid State Chemistry* **57** (1985) 323–331. [https://doi.org/10.1016/0022-4596\(85\)90194-X](https://doi.org/10.1016/0022-4596(85)90194-X).
- [38] C. Delmas, Sodium and Sodium-Ion Batteries: 50 Years of Research, *Advanced Energy Materials* **8** (2018) 1703137. <https://doi.org/10.1002/aenm.201703137>.
- [39] M.B. Armand, Intercalation electrodes in "Materials for advanced batteries", DW Murphy, J. Pl. Press, NY. (1980).
- [40] A. Mauger, C.M. Julien, J.B. Goodenough, K. Zaghib, Tribute to Michel Armand: from Rocking Chair – Li-ion to Solid-State Lithium Batteries, *J. Electrochem. Soc.* **167** (2019) 070507. <https://doi.org/10.1149/2.0072007JES>.
- [41] B. Scrosati, Lithium Rocking Chair Batteries: An Old Concept?, *J. Electrochem. Soc.* **139** (1992) 2776–2781. <https://doi.org/10.1149/1.2068978>.
- [42] M. Lazzari, B. Scrosati, A Cyclable Lithium Organic Electrolyte Cell Based on Two Intercalation Electrodes, *J. Electrochem. Soc.* **127** (1980) 773. <https://doi.org/10.1149/1.2129753>.
- [43] On the use of rocking chair configurations for cyclable lithium organic electrolyte batteries, *Journal of Power Sources* **8** (1982) 289–299. [https://doi.org/10.1016/0378-7753\(82\)80062-1](https://doi.org/10.1016/0378-7753(82)80062-1).
- [44] B. Scrosati, History of lithium batteries, *J Solid State Electrochem.* **15** (2011) 1623–1630. <https://doi.org/10.1007/s10008-011-1386-8>.
- [45] R. Yazami, P. Touzain, A reversible graphite-lithium negative electrode for electrochemical generators, *Journal of Power Sources* **9** (1983) 365–371. [https://doi.org/10.1016/0378-7753\(83\)87040-2](https://doi.org/10.1016/0378-7753(83)87040-2).
- [46] A. Yoshino, The Birth of the Lithium-Ion Battery, *Angewandte Chemie International Edition* **51** (2012) 5798–5800. <https://doi.org/10.1002/anie.201105006>.
- [47] P. Ge, M. Foulletier, Electrochemical intercalation of sodium in graphite, *Solid State Ionics* **28** (1988) 1172–1175. [https://doi.org/10.1016/0167-2738\(88\)90351-7](https://doi.org/10.1016/0167-2738(88)90351-7).
- [48] M.H. Han, E. Gonzalo, G. Singh, T. Rojo, A comprehensive review of sodium layered oxides: powerful cathodes for Na-ion batteries, *Energy Environ. Sci.* **8** (2014) 81–102. <https://doi.org/10.1039/C4EE03192J>.

- [49] A.D. Patricia, B. Darina, P. Claudiu, A. Nikolaos, Cobalt: demand-supply balances in the transition to electric mobility, in: Publications Office of the European Union, 2018. <https://doi.org/10.2760/97710>.
- [50] R.J. Gummow, A. De Kock, M.M. Thackeray, Improved capacity retention in rechargeable 4 V lithium/lithium manganese oxide (spinel) cells, *Solid State Ionics* **69** (1994) 59–69. <https://researchspace.csir.co.za/dspace/handle/10204/1662> (accessed April 14, 2020).
- [51] A.K. Padhi, K.S. Nanjundaswamy, C. Masquelier, S. Okada, J.B. Goodenough, Effect of Structure on the $\text{Fe}^{3+} / \text{Fe}^{2+}$ Redox Couple in Iron Phosphates, *J. Electrochem. Soc.* **144** (1997) 1609–1613. <https://doi.org/10.1149/1.1837649>.
- [52] Z. Liu, A. Yu, J.Y. Lee, Synthesis and characterization of $\text{LiNi}_{1-x-y}\text{Co}_x\text{Mn}_y\text{O}_2$ as the cathode materials of secondary lithium batteries, *Journal of Power Sources* **81–82** (1999) 416–419. [https://doi.org/10.1016/S0378-7753\(99\)00221-9](https://doi.org/10.1016/S0378-7753(99)00221-9).
- [53] M. Yoshio, H. Noguchi, J. Itoh, M. Okada, T. Mouri, Preparation and properties of $\text{LiCo}_y\text{Mn}_x\text{Ni}_{1-x-y}\text{O}_2$ as a cathode for lithium ion batteries, *Journal of Power Sources* **90** (2000) 176–181. [https://doi.org/10.1016/S0378-7753\(00\)00407-9](https://doi.org/10.1016/S0378-7753(00)00407-9).
- [54] M.S. Whittingham, Lithium Batteries and Cathode Materials, *Chem. Rev.* **104** (2004) 4271–4302. <https://doi.org/10.1021/cr020731c>.
- [55] K. B. Hueso, M. Armand, T. Rojo, High temperature sodium batteries: status, challenges and future trends, *Energy & Environmental Science* **6** (2013) 734–749. <https://doi.org/10.1039/C3EE24086J>.
- [56] T. Oshima, M. Kajita, A. Okuno, Development of Sodium-Sulfur Batteries, *International Journal of Applied Ceramic Technology* **1** (2004) 269–276. <https://doi.org/10.1111/j.1744-7402.2004.tb00179.x>.
- [57] J.L. Sudworth, Zebra batteries, *Journal of Power Sources* **51** (1994) 105–114. [https://doi.org/10.1016/0378-7753\(94\)01967-3](https://doi.org/10.1016/0378-7753(94)01967-3).
- [58] A. Hartenbach, M. Bayer, C.-H. Dustmann, 21 - The Sodium Metal Halide (ZEBRA) Battery: An Example of Inorganic Molten Salt Electrolyte Battery, in: F. Lantelme, H. Groult (Eds.), *Molten Salts Chemistry*, Elsevier, Oxford, 2013: pp. 439–450. <https://doi.org/10.1016/B978-0-12-398538-5.00021-4>.
- [59] R. Benato, N. Cosciani, G. Crugnola, S. Dambone Sessa, G. Lodi, C. Parmeggiani, M. Todeschini, Sodium nickel chloride battery technology for large-scale stationary storage in the high voltage network, *Journal of Power Sources* **293** (2015) 127–136. <https://doi.org/10.1016/j.jpowsour.2015.05.037>.
- [60] R. Stepler, Coming: Speedy electric delivery, *Popular Science* **242** (1993).
- [61] W. Auxer, The PB sodium sulfur cell for satellite battery applications (1986) 49–54.
- [62] D.A. Stevens, J.R. Dahn, High Capacity Anode Materials for Rechargeable Sodium-Ion Batteries, *J. Electrochem. Soc.* **147** (2000) 1271–1273. <https://doi.org/10.1149/1.1393348>.
- [63] D.A. Stevens, J.R. Dahn, The Mechanisms of Lithium and Sodium Insertion in Carbon Materials, *J. Electrochem. Soc.* **148** (2001) A803–A811. <https://doi.org/10.1149/1.1379565>.
- [64] D. Larcher, J.-M. Tarascon, Towards greener and more sustainable batteries for electrical energy storage, *Nature Chemistry* **7** (2015) 19–29. <https://doi.org/10.1038/nchem.2085>.
- [65] K. Chayambuka, G. Mulder, D.L. Danilov, P.H.L. Notten, Sodium-Ion Battery Materials and Electrochemical Properties Reviewed, *Advanced Energy Materials* **8** (2018) 1800079. <https://doi.org/10.1002/aenm.201800079>.
- [66] Y.-S. Hu, S. Komaba, M. Forsyth, C. Johnson, T. Rojo, A New Emerging Technology: Na-Ion Batteries, *Small Methods* **3** (2019) 1900184. <https://doi.org/10.1002/smtd.201900184>.

- [67] J. Ayre, 18650 Sodium-Ion Battery Developed At RS2E, CleanTechnica. (2015). <https://cleantechnica.com/2015/12/01/18650-sodium-ion-battery-developed-at-rs2e/> (accessed April 14, 2020).
- [68] A promising new prototype of battery, CNRS (2015). <http://www2.cnrs.fr/en/2659.htm> (accessed December 15, 2017).
- [69] X. Li, J. Liu, Y. Shao, H. Pan, P. Yan, C. Wang, W. Wang, V. Sprenkle, Room Temperature Na-ion Battery Development, DOE Office of Electricity Energy Storage Program (2014).
- [70] J. Barker, R. Heap, N. Roche, C. Tan, R. Sayers, Y. Liu, Low Cost Na-ion Battery Technology, Faradion Ltd, San Francisco, US (2014).
- [71] S. Kuze, J. Kageura, S. Matsumoto, T. Nakayama, M. Makidera, M. Saka, T. Yamaguchi, T. Yamamoto, K. Nakane, Development of a sodium ion secondary battery, Sumitomo Kagaku **2013** (2013) 1–13.
- [72] Sumitomo Electric to start supplying sodium-ion batteries, Nikkei Asian Review. (n.d.). <https://asia.nikkei.com/Business/Companies/Sumitomo-Electric-to-start-supplying-sodium-ion-batteries> (accessed October 5, 2017).
- [73] K. Smith, J. Treacher, D. Ledwoch, P. Adamson, E. Kendrick, Novel High Energy Density Sodium Layered Oxide Cathode Materials: from Material to Cells, ECS Trans. **75** (2017) 13–24. <https://doi.org/10.1149/07522.0013ecst>.
- [74] X. Rong, L. Yaxiang, Q. Xingguo, Z. Quan, K. Weihe, T. Kun, C. Liquan, H. Yongsheng, Sodium ion batteries: from basic research to engineering exploration, Energy Storage Science and Technology **9** (2020) 515–522. <https://doi.org/10.19799/j.cnki.2095-4239.2020.0054>.
- [75] J.L. Murray, The Al–Na (Aluminum–Sodium) system, Bulletin of Alloy Phase Diagrams **4** (1983) 407–410. <https://doi.org/10.1007/BF02868094>.
- [76] Sodium technology could make transporting more than three billion batteries cheaper and easier – Faradion (2015). <https://www.faradion.co.uk/sodium-technology-could-make-transporting-more-than-three-billion-batteries-cheaper-and-easier/> (accessed February 25, 2020).
- [77] J. Barker, C.J. Wright, Storage and/or transportation of sodium-ion cells, WO2016027082A1 (2016). <https://patents.google.com/patent/WO2016027082A1/en> (accessed April 14, 2020).
- [78] T. Placke, R. Kloepsch, S. Dühnen, M. Winter, Lithium ion, lithium metal, and alternative rechargeable battery technologies: the odyssey for high energy density, J. Solid State Electrochem. **21** (2017) 1939–1964. <https://doi.org/10.1007/s10008-017-3610-7>.
- [79] T. Broux, F. Fauth, N. Hall, Y. Chatillon, M. Bianchini, T. Bamine, J.-B. Leriche, E. Suard, D. Carlier, Y. Reynier, L. Simonin, C. Masquelier, L. Croguennec, High Rate Performance for Carbon-Coated Na₃V₂(PO₄)₂F₃ in Na-Ion Batteries, Small Methods **3** (2019) 1800215. <https://doi.org/10.1002/smt.201800215>.
- [80] ISO 12405-4, Electrically propelled road vehicles —Test specification for lithium-ion traction battery packs and systems — Part 4: Performance testing, ISO (2018). <https://www.iso.org/cms/render/live/en/sites/isoorg/contents/data/standard/07/14/71407.html> (accessed April 3, 2020).
- [81] IEC 61982, Secondary batteries (except lithium) for the propulsion of electric road vehicles - Performance and endurance tests, IEC (2012).
- [82] IEC 62660-1, Rechargeable Cells Standards Publication Secondary lithium-ion cells for the propulsion of electric road vehicles. Part 1: Performance testing, IEC (2010).

- [83] SAE J2288, Life Cycle Testing of Electric Vehicle Battery Modules, SAE (2008).
- [84] N. Omar, M.A. Monem, Y. Firouz, J. Salminen, J. Smekens, O. Hegazy, H. Gaulous, G. Mulder, P. Van den Bossche, T. Coosemans, J. Van Mierlo, Lithium iron phosphate based battery – Assessment of the aging parameters and development of cycle life model, *Applied Energy* **113** (2014) 1575–1585. <https://doi.org/10.1016/j.apenergy.2013.09.003>.
- [85] L. Mu, S. Xu, Y. Li, Y.-S. Hu, H. Li, L. Chen, X. Huang, Prototype Sodium-Ion Batteries Using an Air-Stable and Co/Ni-Free O₃-Layered Metal Oxide Cathode, *Adv. Mater.* **27** (2015) 6928–6933. <https://doi.org/10.1002/adma.201502449>.
- [86] E. Berg, C. Villevieille, D. Streich, S. Trabesinger, P. Novak, Rechargeable Batteries: Grasping for the Limits of Chemistry, *J. Electrochem. Soc.* **162** (2015) A2468–A2475.
- [87] N. Williard, W. He, C. Hendricks, M. Pecht, Lessons Learned from the 787 Dreamliner Issue on Lithium-Ion Battery Reliability, *Energies* **6** (2013) 4682–4695. <https://doi.org/10.3390/en6094682>.
- [88] Sub-Committee of Experts on the Transport of Dangerous Goods, Sodium-ion batteries - comments on document ST/SG/AC.10/C.3/2019/35 (2019). <https://www.unece.org/trans/main/dgdb/dgsubc3/c3inf55.html> (accessed April 15, 2020).
- [89] J. Barker, Commercialization of Faradion's High Energy Density Na-ion Battery Technology (2016).
- [90] O.S. Mendoza-Hernandez, S. Taniguchi, H. Ishikawa, K. Tanaka, S. Fukuda, Y. Sone, M. Umeda, Accelerating Rate Calorimetry Tests of Lithium-Ion Cells Before and After Storage Degradation at High Temperature, *E3S Web Conf.* **16** (2017) 07001. <https://doi.org/10.1051/e3sconf/20171607001>.
- [91] Y. Kim, K.-H. Ha, S.M. Oh, K.T. Lee, High-Capacity Anode Materials for Sodium-Ion Batteries, *Chemistry – A European Journal* **20** (2014) 11980–11992. <https://doi.org/10.1002/chem.201402511>.
- [92] C. Vaalma, D. Buchholz, M. Weil, S. Passerini, A cost and resource analysis of sodium-ion batteries, *Nature Reviews Materials* **3** (2018) 1–11. <https://doi.org/10.1038/natrevmats.2018.13>.
- [93] M. Rosa Palacín, Recent advances in rechargeable battery materials: a chemist's perspective, *Chemical Society Reviews* **38** (2009) 2565–2575. <https://doi.org/10.1039/B820555H>.
- [94] C. Poinignon, M. Armand, Insertion Materials for Batteries-Principles and Development, *Europhys. News* **24** (1993).
- [95] J.B. Clarke, J.W. Hastie, L.H.E. Kihlberg, R. Metselaar, M.M. Thackeray, Definitions of terms relating to phase transitions of the solid state (IUPAC Recommendations 1994), *Pure and Applied Chemistry* **66** (2009) 577–594. <https://doi.org/10.1351/pac199466030577>.
- [96] M. Winter, J.O. Besenhard, M.E. Spahr, P. Novák, Insertion Electrode Materials for Rechargeable Lithium Batteries, *Adv. Mater.* **10** (1998) 725–763. [https://doi.org/10.1002/\(SICI\)1521-4095\(199807\)10:10<725::AID-ADMA725>3.0.CO;2-Z](https://doi.org/10.1002/(SICI)1521-4095(199807)10:10<725::AID-ADMA725>3.0.CO;2-Z).
- [97] V. Simone, A. Boulineau, A. de Geyer, D. Rouchon, L. Simonin, S. Martinet, Hard carbon derived from cellulose as anode for sodium ion batteries: Dependence of electrochemical properties on structure, *Journal of Energy Chemistry* **25** (2016) 761–768. <https://doi.org/10.1016/j.jechem.2016.04.016>.

- [98] A. Ponrouch, A.R. Goñi, M.R. Palacín, High capacity hard carbon anodes for sodium ion batteries in additive free electrolyte, *Electrochemistry Communications* **27** (2013) 85–88. <https://doi.org/10.1016/j.elecom.2012.10.038>.
- [99] B. Jin, F. Gao, Y.-F. Zhu, X.-Y. Lang, G.-F. Han, W. Gao, Z. Wen, M. Zhao, J.-C. Li, Q. Jiang, Facile Synthesis of Non-Graphitizable Polypyrrole-Derived Carbon/Carbon Nanotubes for Lithium-ion Batteries, *Scientific Reports* **6** (2016) 19317. <https://doi.org/10.1038/srep19317>.
- [100] S. Qiu, L. Xiao, M.L. Sushko, K.S. Han, Y. Shao, M. Yan, X. Liang, L. Mai, J. Feng, Y. Cao, X. Ai, H. Yang, J. Liu, Manipulating Adsorption–Insertion Mechanisms in Nanostructured Carbon Materials for High-Efficiency Sodium Ion Storage, *Adv. Energy Mater.* **7** (2017). <https://doi.org/10.1002/aenm.201700403>.
- [101] B. Zhang, C.M. Ghimbeu, C. Laberty, C. Vix-Guterl, J.-M. Tarascon, Correlation Between Microstructure and Na Storage Behavior in Hard Carbon, *Adv. Energy Mater.* **6** (2016). <https://doi.org/10.1002/aenm.201501588>.
- [102] S. Komaba, W. Murata, T. Ishikawa, N. Yabuuchi, T. Ozeki, T. Nakayama, A. Ogata, K. Gotoh, K. Fujiwara, Electrochemical Na Insertion and Solid Electrolyte Interphase for Hard-Carbon Electrodes and Application to Na-Ion Batteries, *Adv. Funct. Mater.* **21** (2011) 3859–3867. <https://doi.org/10.1002/adfm.201100854>.
- [103] P. Tsai, S.-C. Chung, S. Lin, A. Yamada, Ab initio study of sodium intercalation into disordered carbon, *Journal of Materials Chemistry A* **3** (2015) 9763–9768. <https://doi.org/10.1039/C5TA01443C>.
- [104] C. Bommier, T.W. Surta, M. Dolgos, X. Ji, New Mechanistic Insights on Na-Ion Storage in Nongraphitizable Carbon, *Nano Lett.* **15** (2015) 5888–5892. <https://doi.org/10.1021/acs.nanolett.5b01969>.
- [105] Y. Chen, L. Shi, S. Guo, Q. Yuan, X. Chen, J. Zhou, H. Song, A general strategy towards carbon nanosheets from triblock polymers as high-rate anode materials for lithium and sodium ion batteries, *Journal of Materials Chemistry A* **5** (2017) 19866–19874. <https://doi.org/10.1039/C7TA06453E>.
- [106] X. Dou, C. Geng, D. Buchholz, S. Passerini, Research Update: Hard carbon with closed pores from pectin-free apple pomace waste for Na-ion batteries, *APL Materials* **6** (2018) 047501. <https://doi.org/10.1063/1.5013132>.
- [107] S. Huang, Z. Li, B. Wang, J. Zhang, Z. Peng, R. Qi, J. Wang, Y. Zhao, N-Doping and Defective Nanographitic Domain Coupled Hard Carbon Nanoshells for High Performance Lithium/Sodium Storage, *Adv. Funct. Mater.* **28** (2018) 1706294. <https://doi.org/10.1002/adfm.201706294>.
- [108] B. Jache, P. Adelhelm, Use of Graphite as a Highly Reversible Electrode with Superior Cycle Life for Sodium-Ion Batteries by Making Use of Co-Intercalation Phenomena, *Angew. Chem. Int. Ed.* **53** (2014) 10169–10173. <https://doi.org/10.1002/anie.201403734>.
- [109] A.P. Cohn, K. Share, R. Carter, L. Oakes, C.L. Pint, Ultrafast Solvent-Assisted Sodium Ion Intercalation into Highly Crystalline Few-Layered Graphene, *Nano Lett.* **16** (2016) 543–548. <https://doi.org/10.1021/acs.nanolett.5b04187>.
- [110] L. Wu, D. Buchholz, D. Bresser, L. Gomes Chagas, S. Passerini, Anatase TiO₂ nanoparticles for high power sodium-ion anodes, *Journal of Power Sources* **251** (2014) 379–385. <https://doi.org/10.1016/j.jpowsour.2013.11.083>.

- [111] Y. Xu, E.M. Lotfabad, H. Wang, B. Farbod, Z. Xu, A. Kohandehghan, D. Mitlin, Nanocrystalline anatase TiO_2 : a new anode material for rechargeable sodium ion batteries, *Chemical Communications* **49** (2013) 8973–8975. <https://doi.org/10.1039/C3CC45254A>.
- [112] M. Keller, C. Vaalma, D. Buchholz, S. Passerini, Development and Characterization of High-Performance Sodium-Ion Cells based on Layered Oxide and Hard Carbon, *ChemElectroChem* **3** (2016) 1124–1132. <https://doi.org/10.1002/celec.201600152>.
- [113] Y. Liu, N. Zhang, L. Jiao, Z. Tao, J. Chen, Ultrasmall Sn Nanoparticles Embedded in Carbon as High-Performance Anode for Sodium-Ion Batteries, *Adv. Funct. Mater.* **25** (2015) 214–220. <https://doi.org/10.1002/adfm.201402943>.
- [114] J. Qian, Y. Chen, L. Wu, Y. Cao, X. Ai, H. Yang, High capacity Na-storage and superior cyclability of nanocomposite Sb/C anode for Na-ion batteries, *Chemical Communications* **48** (2012) 7070–7072. <https://doi.org/10.1039/C2CC32730A>.
- [115] P. Senguttuvan, G. Rousse, M.E. Arroyo y de Dompablo, H. Vezin, J.-M. Tarascon, M.R. Palacín, Low-Potential Sodium Insertion in a NASICON-Type Structure through the Ti(III)/Ti(II) Redox Couple, *J. Am. Chem. Soc.* **135** (2013) 3897–3903. <https://doi.org/10.1021/ja311044t>.
- [116] G.H. Newman, L.P. Klemann, Ambient Temperature Cycling of an Na - TiS_2 Cell, *J. Electrochem. Soc.* **127** (1980) 2097–2099. <https://doi.org/10.1149/1.2129353>.
- [117] L.D. Ellis, B.N. Wilkes, T.D. Hatchard, M.N. Obrovac, In Situ XRD Study of Silicon, Lead and Bismuth Negative Electrodes in Nonaqueous Sodium Cells, *J. Electrochem. Soc.* **161** (2014) A416–A421. <https://doi.org/10.1149/2.080403jes>.
- [118] A. Rudola, K. Saravanan, C. W. Mason, P. Balaya, $\text{Na}_2\text{Ti}_3\text{O}_7$: an intercalation based anode for sodium-ion battery applications, *Journal of Materials Chemistry A* **1** (2013) 2653–2662. <https://doi.org/10.1039/C2TA01057G>.
- [119] H. Pan, X. Lu, X. Yu, Y.-S. Hu, H. Li, X.-Q. Yang, L. Chen, Sodium Storage and Transport Properties in Layered $\text{Na}_2\text{Ti}_3\text{O}_7$ for Room-Temperature Sodium-Ion Batteries, *Adv. Energy Mater.* **3** (2013) 1186–1194. <https://doi.org/10.1002/aenm.201300139>.
- [120] A. Rudola, K. Saravanan, S. Devaraj, H. Gong, P. Balaya, $\text{Na}_2\text{Ti}_6\text{O}_{13}$: a potential anode for grid-storage sodium-ion batteries, *Chemical Communications* **49** (2013) 7451–7453. <https://doi.org/10.1039/C3CC44381G>.
- [121] Y. Wang, X. Yu, S. Xu, J. Bai, R. Xiao, Y.-S. Hu, H. Li, X.-Q. Yang, L. Chen, X. Huang, A zero-strain layered metal oxide as the negative electrode for long-life sodium-ion batteries, *Nature Communications* **4** (2013) 2365. <https://doi.org/10.1038/ncomms3365>.
- [122] N. Yabuuchi, Y. Matsuura, T. Ishikawa, S. Kuze, J.-Y. Son, Y.-T. Cui, H. Oji, S. Komaba, Phosphorus Electrodes in Sodium Cells: Small Volume Expansion by Sodiation and the Surface-Stabilization Mechanism in Aprotic Solvent, *ChemElectroChem* **1** (2014) 580–589. <https://doi.org/10.1002/celec.201300149>.
- [123] L. Xiao, Y. Cao, J. Xiao, W. Wang, L. Kovarik, Z. Nie, J. Liu, High capacity, reversible alloying reactions in SnSb/C nanocomposites for Na-ion battery applications, *Chemical Communications* **48** (2012) 3321–3323. <https://doi.org/10.1039/C2CC17129E>.
- [124] J. Fullenwarth, A. Darwiche, A. Soares, B. Donnadieu, L. Monconduit, NiP_3 : a promising negative electrode for Li- and Na-ion batteries, *Journal of Materials Chemistry A* **2** (2014) 2050–2059. <https://doi.org/10.1039/C3TA13976J>.
- [125] J. Park, J.-S. Kim, J.-W. Park, T.-H. Nam, K.-W. Kim, J.-H. Ahn, G. Wang, H.-J. Ahn, Discharge mechanism of MoS_2 for sodium ion battery: Electrochemical measurements and

- characterization, *Electrochimica Acta* **92** (2013) 427–432. <https://doi.org/10.1016/j.electacta.2013.01.057>.
- [126] T.B. Kim, J.W. Choi, H.S. Ryu, G.B. Cho, K.W. Kim, J.H. Ahn, K.K. Cho, H.J. Ahn, Electrochemical properties of sodium/pyrite battery at room temperature, *Journal of Power Sources* **174** (2007) 1275–1278. <https://doi.org/10.1016/j.jpowsour.2007.06.093>.
- [127] Y. Wang, J. Liu, B. Lee, R. Qiao, Z. Yang, S. Xu, X. Yu, L. Gu, Y.-S. Hu, W. Yang, K. Kang, H. Li, X.-Q. Yang, L. Chen, X. Huang, Ti-substituted tunnel-type $\text{Na}_{0.44}\text{MnO}_2$ oxide as a negative electrode for aqueous sodium-ion batteries, *Nat Commun.* **6** (2015) 6401. <https://doi.org/10.1038/ncomms7401>.
- [128] L. Baggetto, J.K. Keum, J.F. Browning, G.M. Veith, Germanium as negative electrode material for sodium-ion batteries, *Electrochemistry Communications* **34** (2013) 41–44. <https://doi.org/10.1016/j.elecom.2013.05.025>.
- [129] D. Su, C. Wang, H. Ahn, G. Wang, Octahedral tin dioxide nanocrystals as high capacity anode materials for Na-ion batteries, *Physical Chemistry Chemical Physics* **15** (2013) 12543–12550. <https://doi.org/10.1039/C3CP52037D>.
- [130] Q. Sun, Q.-Q. Ren, H. Li, Z.-W. Fu, High capacity Sb_2O_4 thin film electrodes for rechargeable sodium battery, *Electrochemistry Communications* **13** (2011) 1462–1464. <https://doi.org/10.1016/j.elecom.2011.09.020>.
- [131] H.-S. Ryu, J.-S. Kim, J. Park, J.-Y. Park, G.-B. Cho, X. Liu, I.-S. Ahn, K.-W. Kim, J.-H. Ahn, J.-P. Ahn, S.W. Martin, G. Wang, H.-J. Ahn, Degradation mechanism of room temperature Na/Ni $_3$ S $_2$ cells using Ni $_3$ S $_2$ electrodes prepared by mechanical alloying, *Journal of Power Sources* **244** (2013) 764–770. <https://doi.org/10.1016/j.jpowsour.2013.02.001>.
- [132] S. Hariharan, K. Saravanan, P. Balaya, α -MoO $_3$: A high performance anode material for sodium-ion batteries, *Electrochemistry Communications* **31** (2013) 5–9. <https://doi.org/10.1016/j.elecom.2013.02.020>.
- [133] R. Fielden, L. Cole, M.N. Obrovac, Low Voltage Sodium Intercalation in $\text{Na}_x\text{V}_x\text{Ti}_{1-x}\text{O}_2$ ($2/3 \leq x \leq 1$), *J. Electrochem. Soc.* **164** (2017) A490–A497. <https://doi.org/10.1149/2.1361702jes>.
- [134] Y. Wen, K. He, Y. Zhu, F. Han, Y. Xu, I. Matsuda, Y. Ishii, J. Cumings, W. Chunsheng, Expanded graphite as superior anode for sodium-ion batteries, *Nature Communications* **4033** (2014) 1–10.
- [135] P. Barpanda, J.-M. Tarascon, Fluorine-Based Polyanionic Compounds for High-Voltage Electrode Materials, in: B. Scrosati, K.M. Abraham, W.V. Schalkwijk, J. Hassoun (Eds.), *Lithium Batteries*, John Wiley & Sons, Inc., 2013: pp. 127–160. <https://doi.org/10.1002/9781118615515.ch7>.
- [136] A. Manthiram, J.B. Goodenough, Lithium insertion into $\text{Fe}_2(\text{MO}_4)_3$ frameworks: Comparison of $\text{M} = \text{W}$ with $\text{M} = \text{Mo}$, *Journal of Solid State Chemistry* **71** (1987) 349–360. [https://doi.org/10.1016/0022-4596\(87\)90242-8](https://doi.org/10.1016/0022-4596(87)90242-8).
- [137] A. Manthiram, J.B. Goodenough, Lithium insertion into $\text{Fe}_2(\text{SO}_4)_3$ frameworks, *Journal of Power Sources* **26** (1989) 403–408. [https://doi.org/10.1016/0378-7753\(89\)80153-3](https://doi.org/10.1016/0378-7753(89)80153-3).
- [138] C. Masquelier, L. Croguennec, Polyanionic (Phosphates, Silicates, Sulfates) Frameworks as Electrode Materials for Rechargeable Li (or Na) Batteries, *Chem. Rev.* **113** (2013) 6552–6591. <https://doi.org/10.1021/cr3001862>.

- [139] J. Barker, M.Y. Saidi, J.L. Swoyer, Alkali/transition metal halo—and hydroxy-phosphates and related electrode active materials, US6777132 B2 (2004). <http://www.google.be/patents/US6777132>.
- [140] J. Barker, M.Y. Saidi, J.L. Swoyer, A Comparative Investigation of the Li Insertion Properties of the Novel Fluorophosphate Phases, NaVPO₄F and LiVPO₄F, *J. Electrochem. Soc.* **151** (2004) A1670–A1677. <https://doi.org/10.1149/1.1785796>.
- [141] J. Barker, M.Y. Saidi, J.L. Swoyer, Sodium ion batteries, US6872492 B2 (2005). <http://www.google.be/patents/US6872492>.
- [142] M. Bianchini, N. Brisset, F. Fauth, F. Weill, E. Elkaim, E. Suard, C. Masquelier, L. Croguennec, Na₃V₂(PO₄)₂F₃ Revisited: A High-Resolution Diffraction Study, *Chem. Mater.* **26** (2014) 4238–4247. <https://doi.org/10.1021/cm501644g>.
- [143] F. Sauvage, E. Quarez, J.-M. Tarascon, E. Baudrin, Crystal structure and electrochemical properties vs. Na⁺ of the sodium fluorophosphate Na_{1.5}VOPO₄F_{0.5}, *Solid State Sciences* **8** (2006) 1215–1221. <https://doi.org/10.1016/j.solidstatesciences.2006.05.009>.
- [144] M. Bianchini, F. Fauth, N. Brisset, F. Weill, E. Suard, C. Masquelier, L. Croguennec, Comprehensive Investigation of the Na₃V₂(PO₄)₂F₃–NaV₂(PO₄)₂F₃ System by Operando High Resolution Synchrotron X-ray Diffraction, *Chem. Mater.* **27** (2015) 3009–3020. <https://doi.org/10.1021/acs.chemmater.5b00361>.
- [145] K. Chihara, A. Kitajou, I.D. Gocheva, S. Okada, J. Yamaki, Cathode properties of Na₃M₂(PO₄)₂F₃ [M = Ti, Fe, V] for sodium-ion batteries, *Journal of Power Sources* **227** (2013) 80–85. <https://doi.org/10.1016/j.jpowsour.2012.10.034>.
- [146] R. Dugas, B. Zhang, P. Rozier, J.M. Tarascon, Optimization of Na-Ion Battery Systems Based on Polyanionic or Layered Positive Electrodes and Carbon Anodes, *J. Electrochem. Soc.* **163** (2016) A867–A874. <https://doi.org/10.1149/2.0051605jes>.
- [147] M.J. Aragón, C. Vidal-Abarca, P. Lavela, J.L. Tirado, Improving the electrochemical performance of titanium phosphate-based electrodes in sodium batteries by lithium substitution, *Journal of Materials Chemistry A* **1** (2013) 13963–13969.
- [148] J.-L. Yue, Q. Sun, Z.-W. Fu, Cu₂Se with facile synthesis as a cathode material for rechargeable sodium batteries, *Chemical Communications* **49** (2013) 5868–5870.
- [149] Y. Takeda, J. Akagi, A. Edagawa, M. Inagaki, S. Naka, A preparation and polymorphic relations of sodium iron oxide (NaFeO₂), *Materials Research Bulletin* **15** (1980) 1167–1172. [https://doi.org/10.1016/0025-5408\(80\)90081-1](https://doi.org/10.1016/0025-5408(80)90081-1).
- [150] N. Yabuuchi, H. Yoshida, S. Komaba, Crystal Structures and Electrode Performance of Alpha-NaFeO₂ for Rechargeable Sodium Batteries, *Electrochemistry* **80** (2012) 716–719. <https://doi.org/10.5796/electrochemistry.80.716>.
- [151] R. Berthelot, D. Carlier, C. Delmas, Electrochemical investigation of the P₂–Na_xCoO₂ phase diagram, *Nature Materials* **10** (2011) 74–80.
- [152] C.-Y. Chen, K. Matsumoto, T. Nohira, R. Hagiwara, A. Fukunaga, S. Sakai, K. Nitta, S. Inazawa, Electrochemical and structural investigation of NaCrO₂ as a positive electrode for sodium secondary battery using inorganic ionic liquid NaFSA–KFSA, *Journal of Power Sources* **237** (2013) 52–57. <https://doi.org/10.1016/j.jpowsour.2013.03.006>.
- [153] S. Komaba, C. Takei, T. Nakayama, A. Ogata, N. Yabuuchi, Electrochemical intercalation activity of layered NaCrO₂ vs. LiCrO₂, *Electrochemistry Communications* **12** (2010) 355–358. <https://doi.org/10.1016/j.elecom.2009.12.033>.
- [154] P. Vassilaras, X. Ma, X. Li, G. Ceder, Electrochemical Properties of Monoclinic NaNiO₂, *J. Electrochem. Soc.* **160** (2013) A207–A211. <https://doi.org/10.1149/2.023302jes>.

- [155] C. Didier, M. Guignard, C. Denage, O. Szajwaj, S. Ito, I. Saadoune, J. Darriet, C. Delmas, Electrochemical Na-Deintercalation from NaVO_2 , *Electrochem. Solid-State Lett.* **14** (2011) A75–A78. <https://doi.org/10.1149/1.3555102>.
- [156] D. Hamani, M. Ati, J.-M. Tarascon, P. Rozier, Na_xVO_2 as possible electrode for Na-ion batteries, *Electrochemistry Communications* **13** (2011) 938–941. <https://doi.org/10.1016/j.elecom.2011.06.005>.
- [157] H. Yoshida, N. Yabuuchi, S. Komaba, $\text{NaFe}_0.5\text{Co}_0.5\text{O}_2$ as high energy and power positive electrode for Na-ion batteries, *Electrochemistry Communications* **34** (2013) 60–63. <https://doi.org/10.1016/j.elecom.2013.05.012>.
- [158] P. Vassilaras, A.J. Toumar, G. Ceder, Electrochemical properties of $\text{NaNi}_{1/3}\text{Co}_{1/3}\text{Fe}_{1/3}\text{O}_2$ as a cathode material for Na-ion batteries, *Electrochemistry Communications* **38** (2014) 79–81. <https://doi.org/10.1016/j.elecom.2013.11.015>.
- [159] N. Yabuuchi, M. Yano, H. Yoshida, S. Kuze, S. Komaba, Synthesis and Electrode Performance of O3-Type $\text{NaFeO}_2\text{-NaNi}_{1/2}\text{Mn}_{1/2}\text{O}_2$ Solid Solution for Rechargeable Sodium Batteries, *J. Electrochem. Soc.* **160** (2013) A3131–A3137. <https://doi.org/10.1149/2.018305jes>.
- [160] S. Komaba, N. Yabuuchi, T. Nakayama, A. Ogata, T. Ishikawa, I. Nakai, Study on the Reversible Electrode Reaction of $\text{Na}_{1-x}\text{Ni}_{0.5}\text{Mn}_{0.5}\text{O}_2$ for a Rechargeable Sodium-Ion Battery, *Inorg. Chem.* **51** (2012) 6211–6220. <https://doi.org/10.1021/ic300357d>.
- [161] K. Kubota, H. Yoshida, N. Yabuuchi, I. Ikeuchi, A. Garsuch, M. Schulz-Dobrick, S. Komaba, P2-Type $\text{Na}_{2/3}\text{Ni}_{1/3}\text{Mn}_{2/3-x}\text{Ti}_x\text{O}_2$ as a 3.7 V Class Positive Electrode for Na-Ion Batteries, *Meet. Abstr. MA2014-04* (2014) 232–232.
- [162] H. Yu, S. Guo, Y. Zhu, M. Ishida, H. Zhou, Novel titanium-based O3-type $\text{NaTi}_{0.5}\text{Ni}_{0.5}\text{O}_2$ as a cathode material for sodium ion batteries, *Chemical Communications* **50** (2014) 457–459.
- [163] B. Koo, S. Chattopadhyay, T. Shibata, V.B. Prakapenka, C.S. Johnson, T. Rajh, E.V. Shevchenko, Intercalation of sodium ions into hollow iron oxide nanoparticles, *Chemistry of Materials* **25** (2013) 245–252.
- [164] Y. Cao, L. Xiao, W. Wang, D. Choi, Z. Nie, J. Yu, L.V. Saraf, Z. Yang, J. Liu, Reversible Sodium Ion Insertion in Single Crystalline Manganese Oxide Nanowires with Long Cycle Life, *Adv. Mater.* **23** (2011) 3155–3160. <https://doi.org/10.1002/adma.201100904>.
- [165] S. Tepavcevic, H. Xiong, V.R. Stamenkovic, X. Zuo, M. Balasubramanian, V.B. Prakapenka, C.S. Johnson, T. Rajh, Nanostructured Bilayered Vanadium Oxide Electrodes for Rechargeable Sodium-Ion Batteries, *ACS Nano*. **6** (2012) 530–538. <https://doi.org/10.1021/nn203869a>.
- [166] M. Tamaru, X. Wang, M. Okubo, A. Yamada, Layered Na_2RuO_3 as a cathode material for Na-ion batteries, *Electrochemistry Communications* **33** (2013) 23–26.
- [167] P. Moreau, D. Guyomard, J. Gaubicher, F. Boucher, Structure and Stability of Sodium Intercalated Phases in Olivine FePO_4 , *Chem. Mater.* **22** (2010) 4126–4128. <https://doi.org/10.1021/cm101377h>.
- [168] K. Zaghib, J. Trottier, P. Hovington, F. Brochu, A. Guerfi, A. Mauger, C.M. Julien, Characterization of Na-based phosphate as electrode materials for electrochemical cells, *Journal of Power Sources* **196** (2011) 9612–9617. <https://doi.org/10.1016/j.jpowsour.2011.06.061>.
- [169] Y. Fang, Q. Liu, L. Xiao, X. Ai, H. Yang, Y. Cao, High-Performance Olivine NaFePO_4 Microsphere Cathode Synthesized by Aqueous Electrochemical Displacement Method for

- Sodium Ion Batteries, *ACS Appl. Mater. Interfaces* **7** (2015) 17977–17984. <https://doi.org/10.1021/acsami.5b04691>.
- [170] P. Barpanda, T. Ye, S. Nishimura, S.-C. Chung, Y. Yamada, M. Okubo, H. Zhou, A. Yamada, Sodium iron pyrophosphate: A novel 3.0 V iron-based cathode for sodium-ion batteries, *Electrochemistry Communications* **24** (2012) 116–119. <https://doi.org/10.1016/j.elecom.2012.08.028>.
- [171] H. Kim, R.A. Shakoor, C. Park, S.Y. Lim, J.-S. Kim, Y.N. Jo, W. Cho, K. Miyasaka, R. Kahraman, Y. Jung, J.W. Choi, Na₂FeP₂O₇ as a Promising Iron-Based Pyrophosphate Cathode for Sodium Rechargeable Batteries: A Combined Experimental and Theoretical Study, *Adv. Funct. Mater.* **23** (2013) 1147–1155. <https://doi.org/10.1002/adfm.201201589>.
- [172] C.-Y. Chen, K. Matsumoto, T. Nohira, C. Ding, T. Yamamoto, R. Hagiwara, Charge–discharge behavior of a Na₂FeP₂O₇ positive electrode in an ionic liquid electrolyte between 253 and 363K, *Electrochimica Acta* **133** (2014) 583–588. <https://doi.org/10.1016/j.electacta.2014.04.038>.
- [173] H. Kim, I. Park, D.-H. Seo, S. Lee, S.-W. Kim, W.J. Kwon, Y.-U. Park, C.S. Kim, S. Jeon, K. Kang, New Iron-Based Mixed-Polyanion Cathodes for Lithium and Sodium Rechargeable Batteries: Combined First Principles Calculations and Experimental Study, *J. Am. Chem. Soc.* **134** (2012) 10369–10372. <https://doi.org/10.1021/ja3038646>.
- [174] J.Y. Jang, H. Kim, Y. Lee, K.T. Lee, K. Kang, N.-S. Choi, Cyclic carbonate based-electrolytes enhancing the electrochemical performance of Na₄Fe₃(PO₄)₂(P₂O₇) cathodes for sodium-ion batteries, *Electrochemistry Communications* **44** (2014) 74–77. <https://doi.org/10.1016/j.elecom.2014.05.003>.
- [175] B.L. Ellis, W.R.M. Makahnouk, Y. Makimura, K. Toghill, L.F. Nazar, A multifunctional 3.5 V iron-based phosphate cathode for rechargeable batteries, *Nat Mater.* **6** (2007) 749–753. <https://doi.org/10.1038/nmat2007>.
- [176] N. Recham, J.-N. Chotard, L. Dupont, K. Djellab, M. Armand, J.-M. Tarascon, Ionothermal Synthesis of Sodium-Based Fluorophosphate Cathode Materials, *J. Electrochem. Soc.* **156** (2009) A993–A999. <https://doi.org/10.1149/1.3236480>.
- [177] Y. Kawabe, N. Yabuuchi, M. Kajiyama, N. Fukuhashi, T. Inamasu, R. Okuyama, I. Nakai, S. Komaba, A comparison of crystal structures and electrode performance between Na₂FePO₄F and Na₂Fe_{0.5}Mn_{0.5}PO₄F synthesized by solid-state method for rechargeable Na-ion batteries, *Electrochemistry* **80** (2012) 80–84.
- [178] H. Chen, Q. Hao, O. Zivkovic, G. Hautier, L.-S. Du, Y. Tang, Y.-Y. Hu, X. Ma, C.P. Grey, G. Ceder, Sidorenkite (Na₃MnPO₄CO₃): A New Intercalation Cathode Material for Na-Ion Batteries, *Chem. Mater.* **25** (2013) 2777–2786. <https://doi.org/10.1021/cm400805q>.
- [179] P. Barpanda, G. Oyama, S. Nishimura, S.-C. Chung, A. Yamada, A 3.8-V earth-abundant sodium battery electrode, *Nat Commun.* **5** (2014). <https://doi.org/10.1038/ncomms5358>.
- [180] J. Mao, C. Luo, T. Gao, X. Fan, C. Wang, Scalable synthesis of Na₃V₂(PO₄)₃/C porous hollow spheres as a cathode for Na-ion batteries, *Journal of Materials Chemistry A* **3** (2015) 10378–10385. <https://doi.org/10.1039/C5TA01007A>.
- [181] Y. Uebou, T. Kiyabu, S. Okada, J.-I. Yamaki, Electrochemical Sodium Insertion into the 3D-framework of Na₃M₂(PO₄)₃ (M= Fe, V), *Kyushu University Institutional Repository* **16** (2002) 1–5.
- [182] T. Liu, B. Wang, X. Gu, L. Wang, M. Ling, G. Liu, D. Wang, S. Zhang, All-climate sodium ion batteries based on the NASICON electrode materials, *Nano Energy* **30** (2016) 756–761.

- [183] Q. Liu, D. Wang, X. Yang, N. Chen, C. Wang, X. Bie, Y. Wei, G. Chen, F. Du, Carbon-coated $\text{Na}_3\text{V}_2(\text{PO}_4)_2\text{F}_3$ nanoparticles embedded in a mesoporous carbon matrix as a potential cathode material for sodium-ion batteries with superior rate capability and long-term cycle life, *Journal of Materials Chemistry A* **3** (2015) 21478–21485. <https://doi.org/10.1039/C5TA05939A>.
- [184] Z. LIU, X. WANG, W. Ying, A. TANG, S. YANG, L. HE, Preparation of $\text{NaV}_{1-x}\text{Al}_x\text{PO}_4\text{F}$ cathode materials for application of sodium-ion battery, *Transactions of Nonferrous Metals Society of China* **18** (2008) 346–350.
- [185] J. Barker, M.Y. Saidi, J.L. Swoyer, A sodium-ion cell based on the fluorophosphate compound NaVPO_4F , *Electrochemical and Solid-State Letters* **6** (2003) A1–A4.
- [186] Y. Jiang, Z. Yang, W. Li, L. Zeng, F. Pan, M. Wang, X. Wei, G. Hu, L. Gu, Y. Yu, Nanoconfined Carbon-Coated $\text{Na}_3\text{V}_2(\text{PO}_4)_3$ Particles in Mesoporous Carbon Enabling Ultralong Cycle Life for Sodium-Ion Batteries, *Adv. Energy Mater.* **5** (2015) n/a-n/a. <https://doi.org/10.1002/aenm.201402104>.
- [187] Y.-U. Park, D.-H. Seo, H.-S. Kwon, B. Kim, J. Kim, H. Kim, I. Kim, H.-I. Yoo, K. Kang, A new high-energy cathode for a Na-ion battery with ultrahigh stability, *Journal of the American Chemical Society* **135** (2013) 13870–13878.
- [188] S.Y. Lim, H. Kim, J. Chung, J.H. Lee, B.G. Kim, J.-J. Choi, K.Y. Chung, W. Cho, S.-J. Kim, W.A. Goddard, Y. Jung, J.W. Choi, Role of intermediate phase for stable cycling of $\text{Na}_7\text{V}_4(\text{P}_2\text{O}_7)_4\text{PO}_4$ in sodium ion battery, *PNAS* **111** (2014) 599–604. <https://doi.org/10.1073/pnas.1316557110>.
- [189] M. Nose, S. Shiotani, H. Nakayama, K. Nobuhara, S. Nakanishi, H. Iba, $\text{Na}_4\text{Co}_{2.4}\text{Mn}_{0.3}\text{Ni}_{0.3}(\text{PO}_4)_2\text{P}_2\text{O}_7$: High potential and high capacity electrode material for sodium-ion batteries, *Electrochemistry Communications* **34** (2013) 266–269.
- [190] L. Wang, Y. Lu, J. Liu, M. Xu, J. Cheng, D. Zhang, G. John, A Superior Low-Cost Cathode for a Na-Ion Battery, *Angew. Chem. Int. Ed.* **52** (2013) 1964–1967.
- [191] K.T. Lee, T.N. Ramesh, F. Nan, G. Botton, L.F. Nazar, Topochemical Synthesis of Sodium Metal Phosphate Olivines for Sodium-Ion Batteries, *Chem. Mater.* **23** (2011) 3593–3600. <https://doi.org/10.1021/cm200450y>.
- [192] G. Venkatesh, B. Kishore, R. Viswanatha, D. Aurbach, N. Munichandraiah, P2-Type $\text{Na}_{0.67}\text{Mn}_{0.65}\text{Fe}_{0.20}\text{Ni}_{0.15}\text{O}_2$ Microspheres as a Positive Electrode Material with a Promising Electrochemical Performance for Na-Ion Batteries, *J. Electrochem. Soc.* **164** (2017) A2176–A2182. <https://doi.org/10.1149/2.1661709jes>.
- [193] J. Böckris, A. Reddy, M. Gamboa-Aldeco, *Modern Electrochemistry, 2A: Fundamentals of Electrodics*, 2nd ed, Plenum Press, New York, 2000.
- [194] K. Xu, Nonaqueous liquid electrolytes for lithium-based rechargeable batteries, *Chemical Reviews* **104** (2004) 4303–4418.
- [195] A. Ponrouch, D. Monti, A. Boschini, B. Steen, P. Johansson, M. R. Palacín, Non-aqueous electrolytes for sodium-ion batteries, *Journal of Materials Chemistry A* **3** (2015) 22–42. <https://doi.org/10.1039/C4TA04428B>.
- [196] A. Ponrouch, E. Marchante, M. Courty, J.-M. Tarascon, M. Rosa Palacín, In search of an optimized electrolyte for Na-ion batteries, *Energy & Environmental Science* **5** (2012) 8572–8583. <https://doi.org/10.1039/C2EE22258B>.
- [197] A. Ponrouch, R. Dedryvère, D. Monti, A. E. Demet, J.M.A. Mba, L. Croguennec, C. Masquelier, P. Johansson, M. Rosa Palacín, Towards high energy density sodium ion

- batteries through electrolyte optimization, *Energy & Environmental Science* **6** (2013) 2361–2369. <https://doi.org/10.1039/C3EE41379A>.
- [198] K. Kubota, S. Komaba, Review—Practical Issues and Future Perspective for Na-Ion Batteries, *J. Electrochem. Soc.* **162** (2015) A2538–A2550.
- [199] J.F. Peters, A. Peña Cruz, M. Weil, Exploring the Economic Potential of Sodium-Ion Batteries, *Batteries* **5** (2019) 10. <https://doi.org/10.3390/batteries5010010>.
- [200] R. Wagner, N. Preschitschek, S. Passerini, J. Leker, M. Winter, Latest Research Trends and Prospects Among the Various Materials and Designs Used in Lithium-Based Batteries, *Meet. Abstr. MA2014-01* (2014) 78–78.
- [201] R. Wagner, N. Preschitschek, S. Passerini, J. Leker, M. Winter, Current research trends and prospects among the various materials and designs used in lithium-based batteries, *J Appl Electrochem.* **43** (2013) 481–496. <https://doi.org/10.1007/s10800-013-0533-6>.
- [202] European patent office, Espacenet. <http://www.epo.org/> (accessed March 5, 2018).
- [203] A. Eftekhari, D.-W. Kim, Sodium-ion batteries: New opportunities beyond energy storage by lithium, *Journal of Power Sources* **395** (2018) 336–348. <https://doi.org/10.1016/j.jpowsour.2018.05.089>.

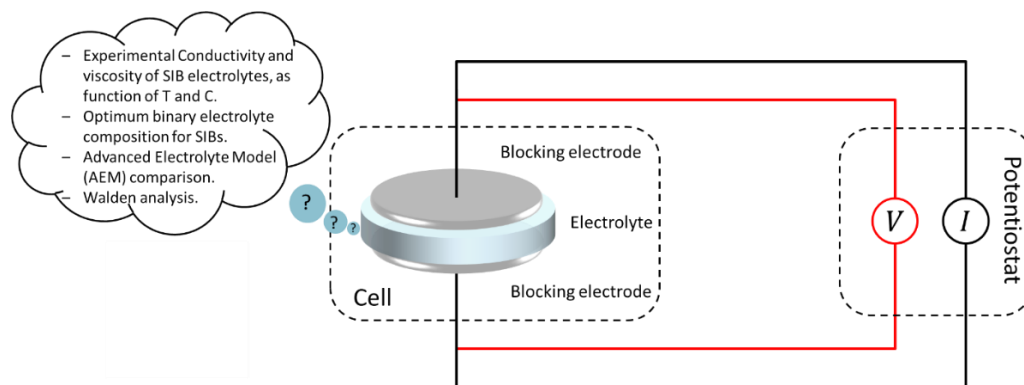
CHAPTER 3

AN EXPERIMENTAL AND MODELING STUDY OF SODIUM-ION BATTERY ELECTROLYTES

A model-enhanced study of electrolyte properties

Abstract

Because electrolytes play an integral role in the successful operation of any battery chemistry, the reemergence of SIBs has therefore necessitated the search for optimized salts and solvents. Based on systematic experimental studies, it has been found that 1 M NaPF₆ in EC and PC, EC_{0.5}:PC_{0.5} (w/w) is the best binary electrolyte for SIBs. However, mathematical models to elucidate these experimental findings have so far been lacking. In addition, there have been few attempts to understand the effect of the formulation of EC on the electrolyte conductivity and stability. In this Chapter, the viscosity and conductivity profiles of NaPF₆ in EC_{0.5}:PC_{0.5} electrolyte are unraveled by the combined use of experimental and modeling approaches at different temperatures and salt concentrations. The viscosity is measured in a double-wall Couette cell. For the first time, the ionic conductivity is determined using two Pt blocking electrodes in a PAT-Cell. The modeling of electrolyte properties is performed using the Advanced Electrolyte Model (AEM), a statistical mechanics software.



Parts of this Chapter have been published as:

K. Chayambuka, R. Cardinaels, K. L. Gering, G. Mulder, D. L. Danilov, P.H.L. Notten, An experimental and modeling study of Sodium-ion battery electrolytes, *Journal of Power Sources* **516** (2021) 230658 <https://doi.org/10.1016/j.jpowsour.2021.230658>

3.1 Introduction

In the wake of the technological developments in the SIB field as outlined in Chapter 2, SIBs have emerged as the most prominent "post lithium" energy storage technology, with the potential to complement and match the performances of LIBs in electric vehicles and grid energy storage applications [1–4].

In this battery chemistry transition endeavor, it is important to optimize SIB electrolytes and elucidate their properties at different concentrations and temperatures. This is because electrolytes play an essential role in several important performance metrics such as safety, rate capability, and electrode stability [5,6]. However, optimizing electrolyte properties is a nontrivial task given that binary, ternary and quaternary mixtures of solvents are necessary to obtain the optimal ESW, ionic conductivity, viscosity, and thermal stability [5,6]. Blends of SIB electrolytes include solvents such as EC, PC, DMC, DME, and DEC [7,8]. In addition, the commercial availability of battery-grade salts is often the crucial missing step in the development process of emerging battery chemistries [9]. As a result of the complexity involved, it is necessary to leverage modeling techniques as complementary tools to speed up the development and optimization of battery electrolytes.

One highly successful modeling strategy is the statistical mechanics approach using the Advanced Electrolyte Model (AEM) created at the Idaho National Laboratory [10–13]. The AEM was developed by Gering for application in battery electrolytes and other electrolyte working fluids [12,13]. The success of the AEM originates from the provided fundamental understanding of solvation thermodynamics based on molecular level interactions between the solvent and ionic species [14]. This method differs from the classical approach of solvation thermodynamics based on bulk macroscopic properties, such as viscosity and conductivity. The AEM has shown exceptional accuracy in predicting conductivity and viscosity properties of LIB electrolytes [10,11]. The AEM allows a wide selection and combination of the most common LIB and SIB salts and solvents, including water, aprotic solvents, and room temperature ionic liquids. The AEM can be further used as an optimization tool for electrolytes of different compositions. Such optimization can enhance the SIB technology. For example, increasing the ionic conductivity and ESW would allow thicker electrode coatings and high voltage cells [15,16]. These strategies can significantly increase the energy density and reduce the manufacturing costs of batteries [17].

Although the $\text{EC}_{0.5}:\text{PC}_{0.5}$ (w/w) solvent has been identified as the most attractive for SIB application because of its high thermally stability and wide ESW [7], it is equally important to elucidate its extensive parameters such as viscosity and conductivity as a function of temperature and salt concentration, for application in electrochemical battery models. Herein, the SIB electrolytes composed of NaPF_6 salt and $\text{EC}_{0.5}:\text{PC}_{0.5}$ (w/w) binary solvent is investigated by experimental and modeling techniques. Properties of conductivity and viscosity are measured experimentally over a concentration and temperature range of 0 to 2 mol kg^{-1} and -10 to 50 °C, respectively, and the results are compared to the AEM predictions. Based on the experimental and AEM results, it is herein shown that the conductivity and viscosity relationship for the $\text{EC}_{0.5}:\text{PC}_{0.5}$ electrolyte follows a simple Stokes' law. This result demonstrates that ion-pairing effects in the liquid organic electrolyte remain low over the concentration and temperature range studied.

In this Chapter, the experimental conductivity is determined using electrochemical impedance spectroscopy (EIS) on two Pt blocking electrodes in an EI-Cell, PAT-Cell electrochemical setup. The electrolyte viscosity is determined in a double-wall Couette cell, which allows for a low volume of electrolytes and constant temperature control. The agreement between the AEM model results and experimental results for the $\text{EC}_{0.5}:\text{PC}_{0.5}$ solvent validates the experimental techniques and allows further optimization of the conductivity of the $\text{EC}_x:\text{PC}_{1-x}$ solvent by tuning the EC composition. It is shown that the optimum EC composition varies with temperature and is governed by competing viscosity and ion-pairing effects. Finally, comparing Li- and Na-based electrolytes reveals that Na-based electrolytes have a higher conductivity at high salt concentrations. These results encourage the exploration of highly concentrated SIB electrolytes, which have improved safety and charge transfer kinetics [18,19].

3.2 Theoretical background for conductivity measurements

Electrolyte conductivity can be measured from the impedance response of two identical blocking electrodes separated by the electrolyte. The two blocking electrodes are electrochemically inert electrodes that behave like an ideal capacitor upon polarization. The impedance response of such a blocking circuit is given by [20]

$$Z(\omega) = j\omega L + R_e + \frac{1}{(j\omega)^\alpha Q} , \quad (3.1)$$

where Z is the total impedance [Ω], j the imaginary unit, ω the frequency of the applied alternating signal [rad s^{-1}], L the inductance due to, for example, the cable connections [H], and R_e is the ionic resistance in the (bulk) electrolyte [Ω]. The frequency independent parameters α and Q are associated with a constant phase element (CPE), which accounts for the non-ideal capacitive response of the system [21]. Three possible scenarios of the CPE are as follows: (i) $\alpha = 1$, the impedance response is akin to that of a pure capacitor and Q represents the double layer capacitance (Q_{dl}) [F m^{-2}]. (ii) $\alpha = 0$, the impedance response is similar to that of a pure resistor, and (iii) $0 < \alpha < 1$, the impedance response shows local capacity dispersion due to electrode surface heterogeneity [20–22].

Fig. 3.1 (a) illustrates an ionic conducting electrolyte in contact with two blocking electrodes and a corresponding series inductor-resistor-capacitor equivalent circuit. **Fig. 3.1** (b) shows the complex impedance plane (Nyquist plot) measured with the blocking electrode setup and modeled with Eq. 3.1. At low ω , the imaginary component of the impedance approaches $-\infty$, meaning direct current flow is blocked in the low-frequency limit. As ω increases, the imaginary component of the impedance approaches zero. In the equivalent circuit model, $L = 0$ because the experimental data does not intersect with the real axis at high ω (see the inset in **Fig. 3.1** (b)). R_e can thus be determined from the intercept with the real axis in the Nyquist plot. In an ideal system wherein $\alpha = 1$, a vertical line is observed in the Nyquist plot. Nevertheless, in real practical systems, $\alpha \neq 1$ and a sloping line is observed due to the CPE.

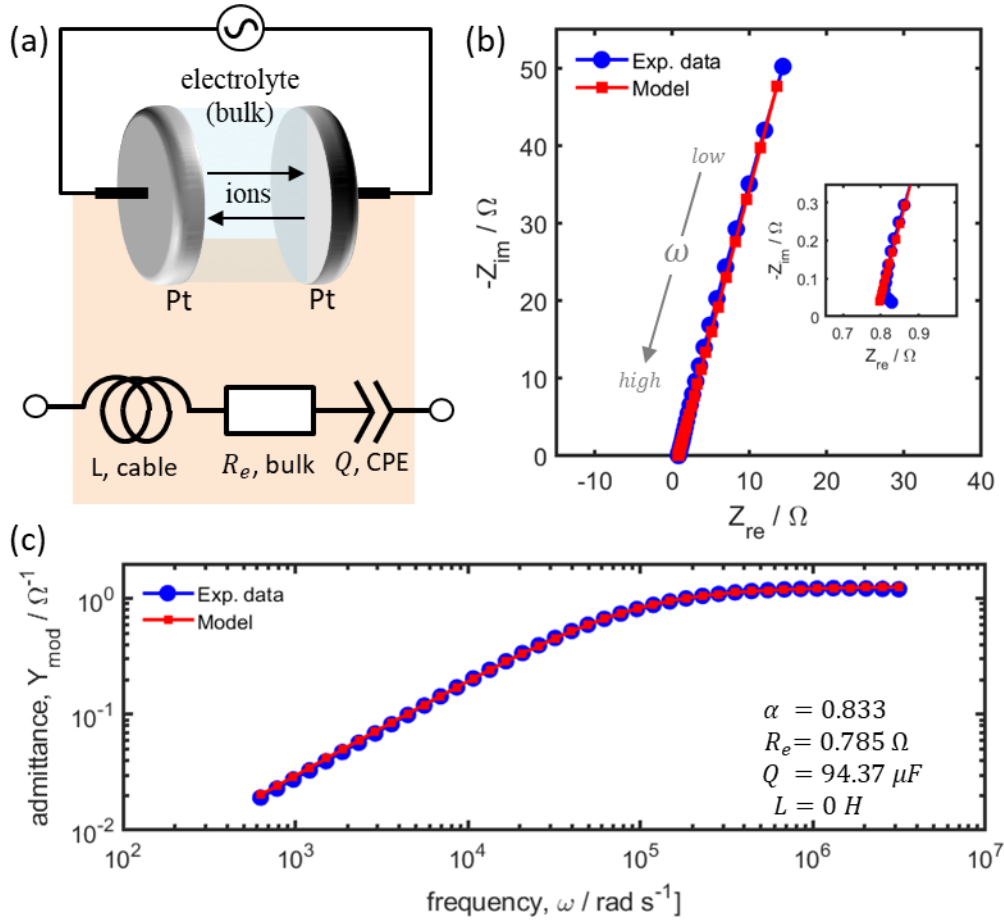


Fig. 3.1. Schematic representation of a blocking electrode measurement setup and corresponding equivalent circuit (a). Nyquist plot of the impedance response of two blocking disk electrodes separated by an electrolyte and inset showing data near the high-frequency intercept with the real axis (b). Bode plot of the modulus of admittance vs. frequency (c). Typical experimental (blue) and model optimization results (red) obtained in this work are shown in (b) and (c).

The Nyquist plot is, however, not an accurate sequential graphical method to determine R_e , because the data is not linear at high frequencies, and an intercept with the real axis can also be observed at high frequencies (due to cable inductance, for example). Instead, a Bode plot of the modulus of the admittance vs. ω can separate R_e from the inductive artifacts [23]. The admittance Y [S] is defined as the inverse of the impedance

$$Y(\omega) = \frac{1}{Z(\omega)} = \frac{Z'}{|Z|^2} - j \frac{Z''}{|Z|^2}, \quad (3.2)$$

where Z' and Z'' are the real and imaginary parts of the impedance, respectively [Ω]. The modulus of the admittance, Y_{mod} [S] is then calculated as

$$Y_{mod} = \frac{1}{\sqrt{Z'^2 + Z''^2}} \quad (3.3)$$

By fitting the impedance response of the model in Eq. 3.1 to the experimental EIS data in a Bode plot of Y_{mod} vs. ω , accurate values of R_e can thus be determined. **Fig. 3.1** (c) illustrates the fitting of the equivalent circuit model shown in Eq. 3.1 to the experimental data in the Bode plot of Y_{mod} vs. ω . The model parameters are therefore determined in **Fig. 3.1** (c) and further verified in the Nyquist plot (**Fig. 3.1** (b)).

The ionic conductivity σ [S m^{-1}] can finally be deduced from R_e by

$$\sigma = \frac{K_{cell}}{R_e} \quad (3.4)$$

where K_{cell} is the cell constant [m^{-1}]. K_{cell} is determined using solutions of known conductivity (standard conductivity solutions) and depends on the blocking electrode surface area, the distance between the electrodes, and the tortuosity of the separator between the electrodes, if present.

3.3 Experimental

3.3.1 Preparation of electrolytes

An aprotic binary solvent mixture consisting of 50 wt.% ethylene carbonate (EC, Aldrich, anhydrous, 99.0%) and 50 wt.% propylene carbonate (PC, Aldrich, anhydrous, 99.0%), was used for the conductivity and viscosity experiments. The $\text{EC}_{0.5}:\text{PC}_{0.5}$ (w/w) solvent was prepared at 60 °C, to melt and dissolve the EC. This procedure was carried out in an argon-filled glove box (Innovative Technology, Inc. Newburyport, MA), with controlled moisture and oxygen content. For the evaluation of viscosity and conductivity at different salt concentrations, NaPF_6 (Kishida, anhydrous, 99.0%) was dissolved in the $\text{EC}_{0.5}:\text{PC}_{0.5}$ solvent, to make concentrations of 0.15, 0.5, 1, 1.5 and 2 m (mol kg^{-1} of solvent). The molality scale is experimentally most convenient because the electrolyte volume varies with the amount of salt and temperature. In addition, salt concentrations are defined on the molality scale in the AEM software and corresponding molarity values are provided for comparison. All electrolytes and salts were used as-received.

3.3.2 Conductivity measurements

Electrolyte conductivities were measured in a hermetically-sealed PAT-Cell (EL-Cell GmbH, Hamburg, Germany) using EIS measurements on two Pt blocking electrodes, in the frequency range of 500—0.1 kHz using 40 logarithmically spaced frequencies. EIS measurements were performed in the potentiostatic mode using an amplitude of 10 mV (Autolab PGSTAT302N).

Fig. 3.2 shows the PAT-Core mounted in the PAT-Cell used for the conductivity measurements. The PAT-Cell consists of an inner core, the PAT-Core, wherein two Pt discs (EL-Cell GmbH, $\varnothing = 18$ mm, Pt > 99.0%) were used as blocking electrodes, and two stainless-steel upper and lower plungers (EL Cell GmbH, 316L) were used as current collectors. The electrodes were separated by a 25 μm thick separator (EL Cell GmbH, Freudenberg Viledon). A polypropylene insulation sleeve was used to keep the electrodes, separator, and current collectors in place and thus seal the PAT-Core. To evaluate the cell constant, 1 mM KCl conductance standard solution (Aldrich, 99.0%) was used as an electrolyte in the PAT-Cells. The EIS measurements were repeated 7 times on different cell assemblies at 25 °C. An average cell constant of 0.9882 m^{-1} was determined with an accuracy of $\pm 3 \%$ (based on standard error calculations).

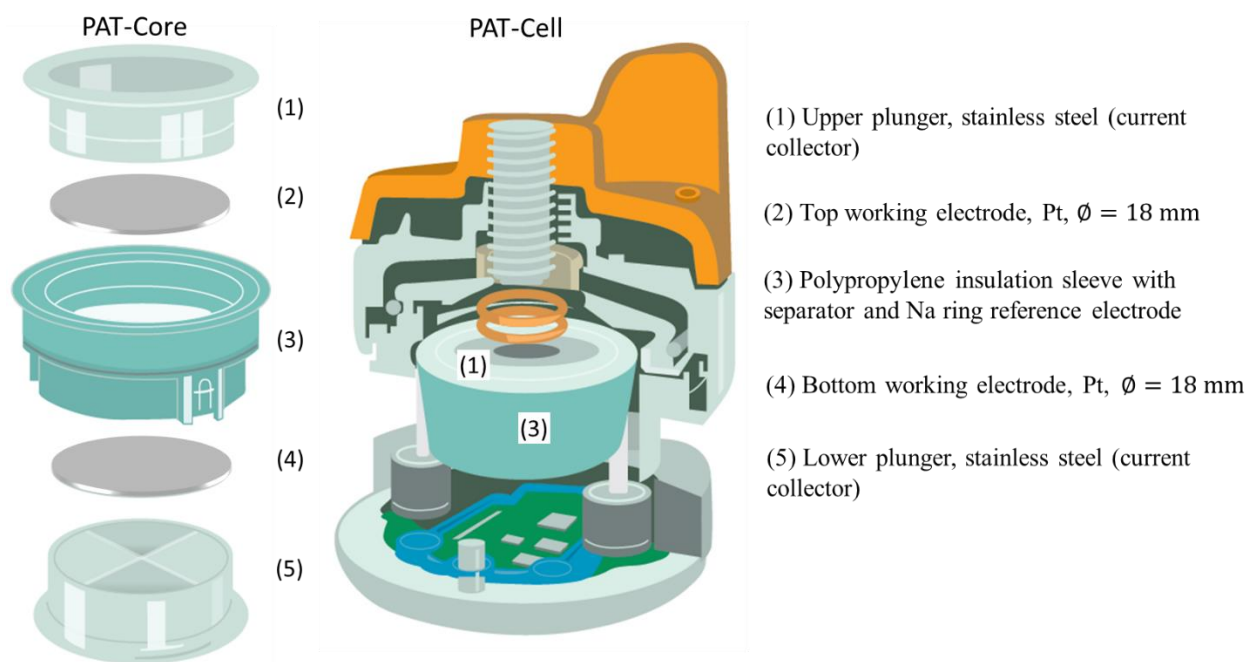


Fig. 3.2. Configuration of the PAT-Core and EL-Cell PAT-Cell used for the EIS electrolyte conductivity measurements.

Except for the KCl conductance standard test cells, all PAT-Cells were assembled and hermetically sealed in an argon-filled glove box. After sealing, the cells were taken out of the glove box and placed in a temperature chamber (Maccor, MTC-010). Inside the temperature chamber, the temperature was automatically set from -10 to 50°C (10°C steps). Each isothermal step was maintained for 5 hours, and the EIS measurements were repeated at hourly intervals. The sealing of the PAT-Cells thus ensured stable measurements of the volatile electrolyte over a wide temperature range.

3.3.3 Viscosity measurements

The dynamic viscosity characterization of the $\text{EC}_{0.5}:\text{PC}_{0.5}$ (w/w) electrolyte at NaPF_6 concentrations of 0, 0.15, 0.5, 1, 1.5, and 2 mol kg^{-1} was performed using a rotational rheometer with a Peltier temperature control unit. The rheometer (Anton Paar GmbH, MCR501) was configured and controlled via Rheoplus (software version 3.62). The temperature was set between -10 and 50°C (10°C steps). At each temperature step, a waiting time of 20 minutes was required for the electrolyte temperature to reach a steady state. Due to the electrolyte samples' low viscosity and low volume constraints, a double-wall Couette cell measuring system (Anton Paar, DIN 54453) was selected to maximize the torque resolution for low volume electrolytes. In addition, a solvent trap system consisting of a pure $\text{EC}_{0.5}:\text{PC}_{0.5}$ solvent was used to minimize electrolyte evaporation from the cell during the tests and to limit the electrolyte-air contact. The solvent trap system works by creating a saturated solvent atmosphere in the cell [25].

Viscosity *vs.* time curves were thus obtained at shear rates of 10, 100 and 1000 s^{-1} . Each shear rate was applied to the sample for a duration of 60 s with a sampling time of 1 s. All surfaces coming in contact with the electrolytes were thoroughly cleaned before measurements, first with deionized water and then with acetone, and left to dry in ambient air. An empty cell torque for the setup was determined, a parameter which is dominated by the solvent trap friction. An electrolyte volume of 3.8 mL was added to the cell, and the aforementioned shear rates were applied. Thixotropy was checked by the successive execution of two shear rate sweeps. The hysteresis between viscosity curves obtained with increasing *vs.* decreasing shear rate was negligible, thus proving the absence of thixotropy. Moreover, the viscosity values did not depend on the applied shear rate, thereby demonstrating the Newtonian flow behavior of the electrolyte samples. At the

shear rate of 1000 s^{-1} for example, a sample torque ranging between 0.2 and 30 mNm was obtained at the different temperatures and salt concentrations. By taking the average cell torque from the 3 shear rates, the electrolyte sample torque was finally calculated from the difference between the average cell torque and the empty cell torque.

3.3.4 AEM calculations

The AEM version 2.19.1 used in this work contains a graphic user interface and a library of 39 solvents and 28 salts. Specific details of the AEM methodology can be found in the following dedicated literature [12,13]. The user has an option to select a mixed electrolyte of up to 5 solvents and 2 salts. For the comparison between experimental and model results, in terms of viscosity and conductivity predictions at different temperature and concentration conditions, the $\text{EC}_{0.5}:\text{PC}_{0.5}$ (w/w) solvent and NaPF_6 salt were selected. The salt concentration range of 0 to 3 mol kg^{-1} was specified in combination with a temperature range of -10 to $50 \text{ }^\circ\text{C}$ (5°C steps). The software gives 5 or 10°C step options, and the former offers a finer grid and better fidelity in the Arrhenius calculations. In the input method for handling triple ion stability, the option $[\text{ABA}^+] = [\text{BAB}^-]$ was selected. Finally, the Surface-Charge Attenuated Electrolyte Permittivity (SCAEP) and electrochemical double-layer calculations were not included. For the above calculations, the AEM does not require sophisticated computational power. Results are available in a few seconds on a standard desktop computer.

To compare properties of Na-based and Li-based electrolytes, AEM calculations were performed by selecting $\text{EC}_{0.5}:\text{PC}_{0.5}$ (w/w) solvent and LiPF_6 salt in the concentration and temperature range of 0 to 3 mol kg^{-1} and -10 to $50 \text{ }^\circ\text{C}$ (5°C steps). The results of the Li-based electrolyte were thus compared with that of the Na-based electrolyte at the same temperature and concentration conditions.

The AEM calculations were also used for the optimization of a 1 M NaPF_6 in $\text{EC}_x:\text{PC}_{1-x}$ (w/w) electrolyte by analysis of the conductivity as a function of temperature and EC mass fraction (x). The choice of the salt concentration is based on the fact that most prototype SIBs are using this concentration. Therefore, the AEM conductivity results were analyzed at temperatures of -10 , 30 , and $50 \text{ }^\circ\text{C}$, and x was varied from 0.3 to 0.8 in steps of 0.05.

Using AEM data and experimental data from independent literature studies [7,8], the factors contributing to different EC-based binary and ternary electrolytes having poor reversible capacity on HC electrodes were further investigated. The binary solvents include: EC_{0.5}:PC_{0.5}, EC_{0.5}:DMC_{0.5}, EC_{0.5}:DME_{0.5} and EC_{0.5}:DEC_{0.5}, while the ternary solvents include: EC_{0.45}:PC_{0.45}:DMC_{0.1}, EC_{0.4}:PC_{0.4}:DMC_{0.2}, EC_{0.4}:PC_{0.4}:DME_{0.2} and EC_{0.4}:PC_{0.4}:DEC_{0.2}. In this investigation, 1M NaClO₄ salt was selected from the AEM library to match the conditions in the respective literature studies. The objective is to determine if the HC reversible capacity can be correlated to the amount of EC in the various electrolyte blends. Therefore, the reversible capacity of HC reported in the literature was correlated to the mass fraction, volume fraction, mole fraction, and the cationic preferential ion solvation (PIS) of EC in different electrolytes.

3.4 Results and discussion

3.4.1 Comparison between experimental data and AEM results

The conductivity and viscosity results are listed in **Table 3.1** and **Table 3.2**, respectively. **Fig. 3.3** (a) and (b) show the conductivity and viscosity results of the EC_{0.5}:PC_{0.5} (w/w) electrolyte as a function of concentration and temperature, respectively. The conductivity of the electrolyte increases with increasing NaPF₆ concentration in dilute electrolyte solutions (**Fig. 3.3** (a)). However, in concentrated electrolytes, the conductivity levels off and even decreases at high concentrations. This phenomenon is related to a concomitant increase in several counteracting effects, such as electrolyte viscosity, ion-ion associations, and the coordinated ion solvation shells [13]. Therefore, the conductivity attains a maximum at a molality of about 1 mol kg⁻¹. On the other hand, the electrolyte viscosity is shown to increase exponentially with increasing salt concentration (**Fig. 3.3** (b)). Sharp increases in viscosity are found at low temperatures.

The AEM results shown in **Fig. 3.3** are close to the experimental results over the full concentration, and temperature range studied. Errors in the experimental conductivity measurements, represented by the error bars, were calculated based on the following analytical approximation [26]

$$\kappa(c, T) = K_{1,T} c^3 + K_{2,T} c^{3/2} + K_{3,T} c, \quad (3.5)$$

where κ is the electrolyte conductivity [S m^{-1}], c the electrolyte concentration [mol kg^{-1}] and K is a temperature-dependent coefficient given by

$$K_{i,T} = K_{i,25^\circ\text{C}} \exp\left(\frac{E_{a,i}}{R} \left(\frac{1}{298.15} - \frac{1}{T}\right)\right), \quad i = \{1,2,3\} \quad (3.6)$$

where $E_{a,i}$ is the activation energy [J mol^{-1}] of the i^{th} temperature-dependent coefficient, R the universal gas constant [$8.314 \text{ J K}^{-1} \text{ mol}^{-1}$] and T is the temperature [K]. This model has been previously applied to experimental conductivity data of lithium-ion batteries [26]. Eqs. 3.5 and 3.6 result in an analytical expression for the conductivity at various concentrations and temperatures, which is useful in battery modeling applications. A maximum conductivity uncertainty of $\pm 4 \%$ was obtained at 50°C and 2 mol kg^{-1} in the experiments.

Uncertainties in viscosity measurements were similarly calculated based on deviations from the Arrhenius expression [27]

$$\mu = \mu_\infty \exp\left(\frac{E_a}{RT}\right), \quad (3.7)$$

where μ is the dynamic viscosity [Pa s], μ_∞ the limiting viscosity at infinite temperature [Pa s], and E_a is the activation energy [J mol^{-1}]. A maximum viscosity uncertainty of $\pm 7 \%$ was obtained at -10°C and 2 mol kg^{-1} in the experiments. The uncertainties in viscosity at higher temperatures were less than $\pm 2 \%$. Alternatively, the viscosity as a function of concentration can be modeled by the Jones-Dole equation [28–30], which can be similarly applied to determine uncertainties. The resulting uncertainties are represented by the error bars on the experimental data points in **Fig. 3.3**.

Table 3.1. Conductivity experimental results for the NaPF_6 in $\text{EC}_{0.5}:\text{PC}_{0.5}$ (w/w) electrolyte at various temperatures and NaPF_6 concentrations.

Concentration (mol kg ⁻¹)	Conductivity (mS cm ⁻¹) at the indicated temperature (°C)						
	-10	0	10	20	30	40	50
0.15	1.53	2.11	2.73	3.36	4.04	4.71	5.40
0.5	2.62	3.66	4.86	6.03	7.20	8.41	9.75
1	2.70	4.11	5.57	7.18	8.83	10.48	12.2
1.5	2.52	3.55	5.27	7.03	8.61	10.7	12.5
2	1.35	2.48	3.96	5.69	7.60	9.65	11.7

Table 3.2. Viscosity experimental results for the NaPF_6 in $\text{EC}_{0.5}:\text{PC}_{0.5}$ (w/w) electrolyte at various temperatures and NaPF_6 concentrations.

Concentration (mol kg ⁻¹)	Viscosity (cP) at the indicated temperature (°C)						
	-10	0	10	20	30	40	50
0	6.23	4.65	3.59	2.90	2.36	1.94	1.63
0.15	7.67	5.52	4.16	3.30	2.64	2.15	1.77
0.5	10.3	7.35	5.52	4.34	3.46	2.88	2.42
1	17.0	12.4	8.73	6.85	5.21	4.09	3.32
1.5	38.0	22.2	14.4	10.1	7.60	5.80	4.54
2	76.2	39.4	23.3	16.3	11.1	8.04	6.05

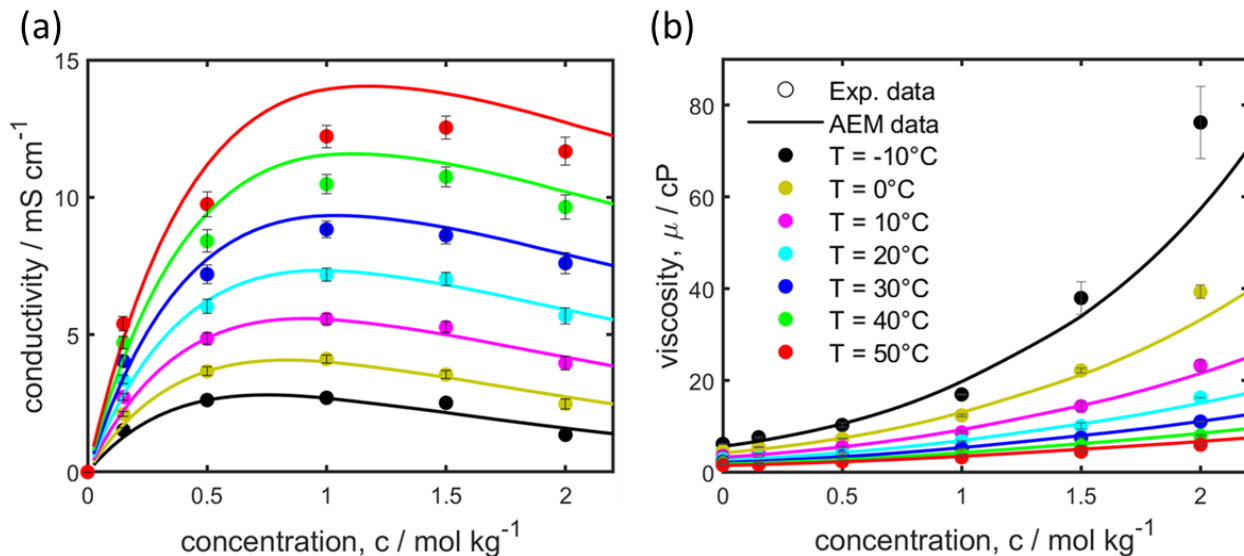


Fig. 3.3. Comparison of the conductivity (a) and viscosity (b) in the experiments (symbols) and AEM simulations (lines) of $EC_{0.5}:PC_{0.5}$ (w/w) electrolytes at various temperatures and $NaPF_6$ concentrations. The error bars are calculated from standard deviation from analytical equations.

Fig. 3.4 (a) and (b) show the analysis of the mean absolute error in conductivity and viscosity between the AEM and experimental data as a function of concentration and temperature, respectively. It can be concluded that the absolute error in conductivity is more or less constant within 1 mS cm^{-1} (**Fig. 3.4** (a)), and tends to increase somewhat with increasing temperature (**Fig. 3.4** (b)). In contrast, the absolute error in electrolyte viscosity increases substantially with increasing the $NaPF_6$ concentration (**Fig. 3.4** (a)) and decrease with increasing temperature (**Fig. 3.4** (b)). In general, deviations between the AEM simulations and viscosity experiments are the highest at the lowest temperature of -10°C and at the highest concentration of 2 mol kg^{-1} .

Fig. 3.4 (c) and (d) shows the mean relative error in conductivity and viscosity between the AEM and experimental data as a function of concentration and temperature, respectively. The relative error is highest at the concentration extremes (0.15 and 2 mol kg^{-1}) and temperature extremes (-10 and 50°C). The maximum relative error of 15% is recorded for the conductivity at the lowest concentration of 0.15 mol kg^{-1} . At all other intermediate temperature and concentration conditions, the mean relative error in viscosity and conductivity is less than 10%, which is quite accurate and shows improvement from previous versions of the AEM [31].

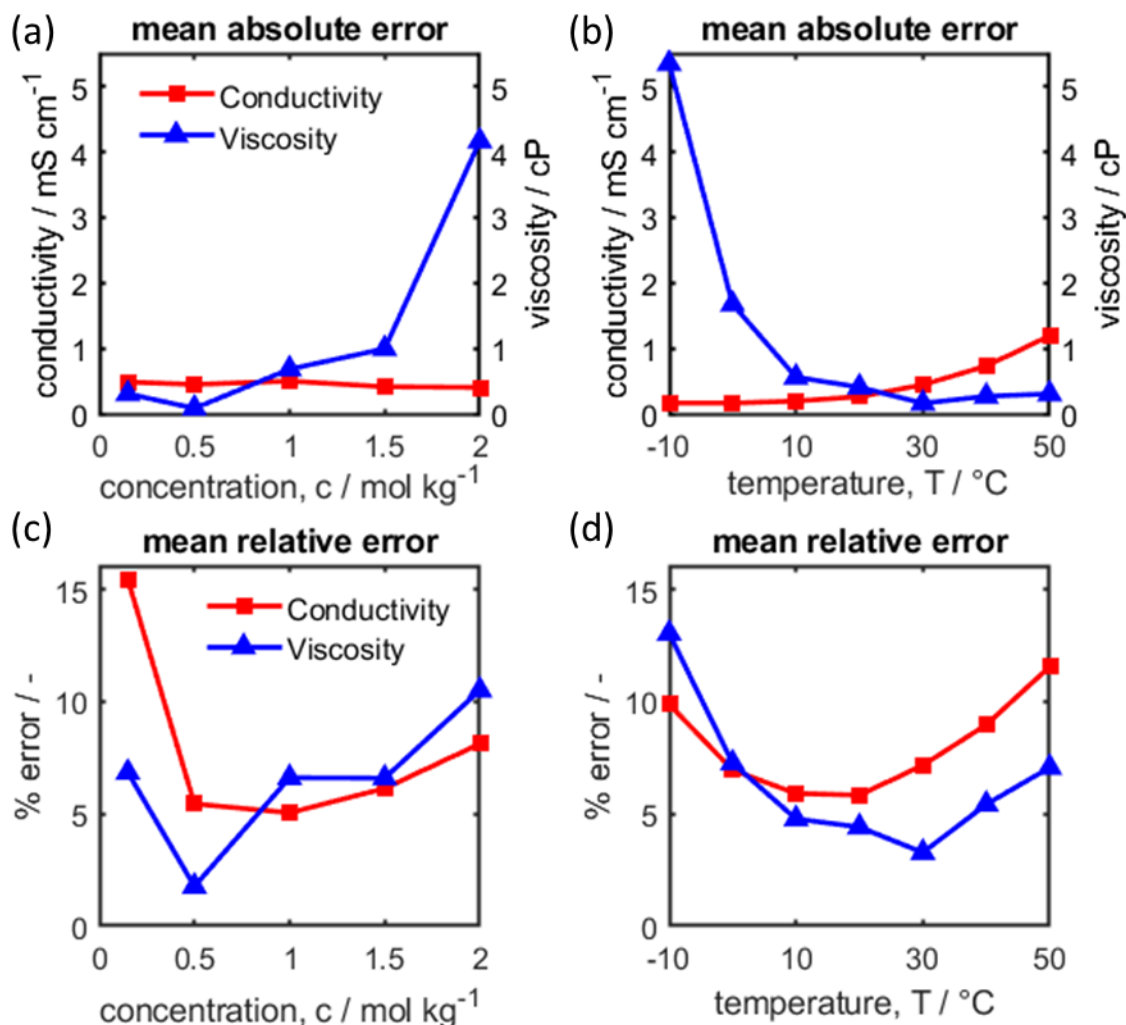


Fig. 3.4. Mean absolute error and relative error of the conductivity (red) and viscosity (green) between the experiments and AEM simulations at various concentrations and temperatures. Mean absolute error (a) and (b). Mean relative error (c) and (d). Mean calculated over all temperature points in (a) and (c). Mean calculated over all concentration points in (b) and (d)

3.4.2 Walden analysis

The relationship between the ionic conductivity and viscosity has been shown to follow a simple Stokes' law in previous investigations of ionic liquids [32] and aprotic LIB electrolytes [33]. Herein, we investigate if a similar relationship can be obtained based on experimental and AEM results of SIB electrolytes. Using Stokes' law, the ionic conductivity is expressed as a function of the electrolyte viscosity and ionic radius, as

$$\sigma = \sum_i \frac{z_i^2 F e c_i^*}{6\pi\mu r_i} , \quad (3.8)$$

where z_i is the charge, F is the Faraday constant $96485 \text{ [C mol}^{-1}\text{]}$, e is the elementary charge $1.602 \times 10^{-19} \text{ [C]}$, c_i^* is the molar concentration $[\text{mol l}^{-1}]$ and r_i is the Stokes' radius of the i^{th} ionic species $[\text{m}]$. r_i represents the effective solvated ion radius, including the solvation shell, for ionic conductivity [11]. Considering a monovalent salt such as NaPF_6 , Eq. 3.8 can be expressed as

$$\sigma = \frac{F e c_{\pm}^*}{6\pi\mu} \left(\frac{1}{r_+} + \frac{1}{r_-} \right) , \quad (3.9)$$

where r_+ and r_- are the Stokes' radii of the cations and anions, respectively, and c_{\pm}^* is the molar concentration of dissociated cations or anions in the electrolyte. The electroneutrality condition for a monovalent electrolyte stipulates the equality of ionic concentrations for oppositely charged ions. Note that, c_{\pm}^* is only equal to the salt concentration for a fully dissociated electrolyte.

Assuming the Stokes' radii to remain constant and the salt to be either fully dissociated or the degree of dissociation to be constant, Eq. 3.9 can be simplified to

$$\Lambda = \frac{\sigma}{c_{\pm}^*} = \frac{\beta}{\mu} , \quad (3.10)$$

where Λ is the molar conductivity $[\text{S cm}^2 \text{mol}^{-1}]$ and β is a constant which is inversely proportional to the Stokes' radii. According to Eq. 3.10, plots of Λ vs. $1/\mu$ are linear. This theoretical expression has been validated experimentally in ideal electrolyte solutions according to Walden rule [32,34]

$$\log(\Lambda) \propto \log\left(\frac{1}{\mu}\right) . \quad (3.11)$$

Eq. 3.11 has been experimentally validated using 1 M KCl solutions, which is assumed to represent a fully dissociated, ideal electrolyte solution [32]. The KCl data are therefore used as a reference in the present experiments to assess the ionicity or degree of dissociation of an electrolyte.

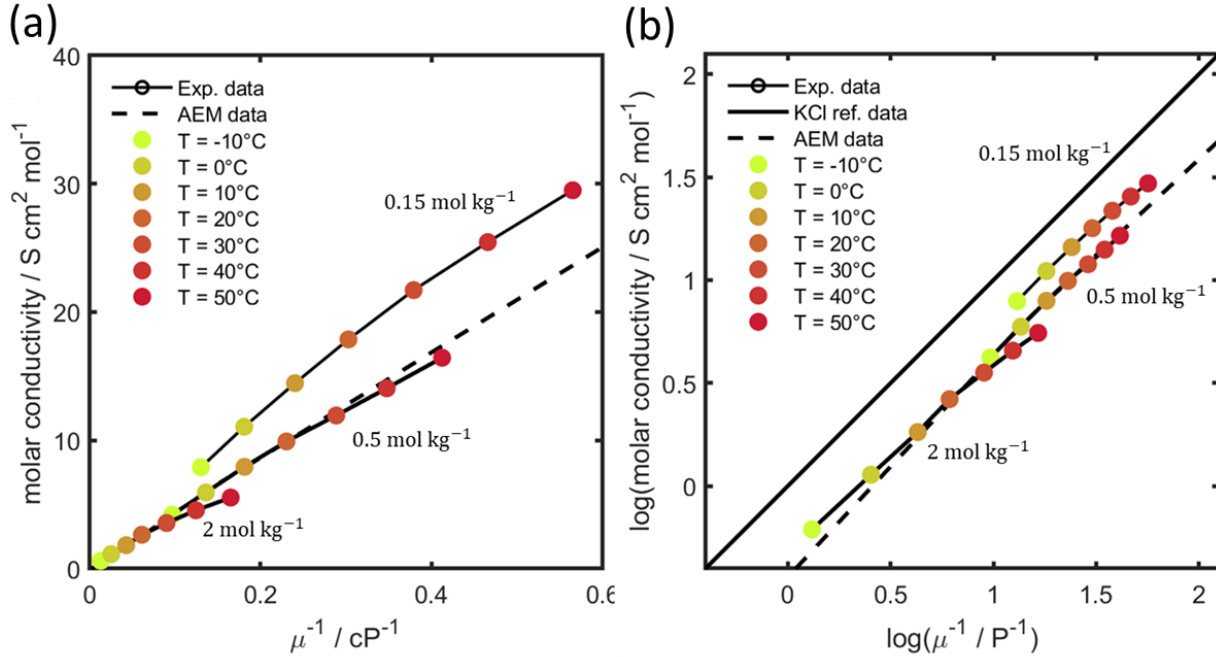


Fig. 3.5. Walden analysis for NaPF₆ in EC_{0.5}:PC_{0.5} (w/w) SIB electrolyte. (a) Molar conductivity vs. the inverse of the viscosity. (b) Walden plot showing the logarithmic of the molar conductivity vs. the inverse of the viscosity. The experimental data are shown as colored dots; lines are used to group electrolytes of the same molality. The dotted line represents AEM modeling. The KCl reference data line is shown in (b).

Fig. 3.5 (a) and (b) show the molar conductivity as a function of the inverse of the viscosity (Eq. 3.10) and the Walden plot (Eq. 3.11), respectively. The experimental data (symbols) are grouped by concentration (solid lines), while colored dots illustrate the various temperatures. In **Fig. 3.5** (a), the AEM predicted Walden dependency (dashed line) matches the experimental data very well in all cases. This observation is another illustration of the accuracy of the AEM approach in predicting experimental data. The AEM uses a revised Stokes' law, which accounts for additional effects omitted by the simple Stokes' law. That form includes solvent-ion effects, ion association effects, counter-ion diffusion, random motion of ions, ionic hopping, viscosity as a function of salt concentration, and solvated ion size as a function of salt concentration [12]. Therefore, comparing the AEM results and the simple Stokes' law reveals the extent to which these additional effects influence ionic conductivity.

Fig. 3.5 (b) shows a comparison of the experimental data (colored dots), the AEM data (dashed line), and the simple Stokes' law, which is represented by the KCl reference data (solid black line). The simple Stokes' law is also shown to be a reasonable approximation of the

experimental conductivity as a function of the viscosity for the electrolyte. Nevertheless, the experimental and AEM data lie below the KCl line. Points above the KCl line are characteristic of highly ionic solutions (superionic conductors), while points below the KCl line are typical for poor ionic conductors [35]. Therefore, the ionic conductivity of the EC_{0.5}:PC_{0.5} electrolyte is lower than ideally expected. It is worth mentioning that the Walden rule in a rigorous interpretation of electrolyte temperature or solvent-composition dependence has been questioned [36]. Nevertheless, the empirical rule provides a facile and qualitative assessment of the degree of dissociation in electrolytes in comparative studies [37].

Because the AEM and experimental results at concentrations 0.15, 0.5, and 2 mol kg⁻¹ are approximately linear and close to the KCl line, the additional effects of the revised Stokes' law do not have a large influence on the conductivity of the EC_{0.5}:PC_{0.5} electrolyte. This conclusion means that, viscosity has a greater influence on electrolyte conductivity than ion interaction effects in the concentration range studied. The characteristic drop in conductivity at concentrations above 1 mol kg⁻¹ NaPF₆ in **Fig. 3.3** (a) is therefore primarily caused by the increase in electrolyte viscosity.

Nevertheless, several trends of the experimental data compared to the KCl reference data can be observed from **Fig. 3.5** (b). The experimental data deviates slightly further from the KCl data as the concentration and temperature increase. This observation indicates that non-ideal ion solvation effects increase at high concentrations and temperatures. Increased deviations at 2 mol kg⁻¹ are indeed expected since electrolytes are only fully dissociated at infinite dilution. This is herein illustrated by the decrease in the mole fraction of single ions as the concentration increases (see **Fig. 3.6** (c)). The deviations at 50 °C can be explained by the gradual increase in the mole fraction of triple ions as the temperature increases due to reduced electrolyte relative permittivity at higher temperatures [38].

3.4.3 Comparison of Na-ion and Li-ion battery electrolytes

It is often reported that SIB electrolytes have a higher conductivity compared to analogous LIB electrolytes [39,40]. The AEM is herein used to investigate and compare properties of 1 M NaPF₆ and 1 M LiPF₆ in EC_{0.5}:PC_{0.5} (w/w). Using the same solvent removes the question of the

dielectric permittivity, and using salts of the same anion and concentration, allows any differences to be attributed to the charge density of the cation.

Table 3.3. Comparison of AEM-simulated electrolyte properties of 1 M NaPF₆ and 1M LiPF₆ in EC_{0.5}:PC_{0.5} (w/w) at 25 °C.

Property	LiPF ₆	NaPF ₆	Unit	% Difference ^(a)
Electrolyte conductivity	7.117	8.211	mS cm ⁻¹	15.4
Electrolyte Viscosity	6.12	5.34	cP	-12.7
Effective diffusivity	1.02×10^{-10}	1.16×10^{-10}	m ² s ⁻¹	13.7
Free energy of solvation	483.17	323.23	kJ mol ⁻¹	-33.1
Solvated cation diameter	7.52	7.38	Å	-1.9
Solvated anion diameter	6.41	6.35	Å	-0.9
Cation solvation number	4.244	4.065	-	-4.2
Anion solvation number	1.313	1.301	-	-0.9
Cation transference number	0.453	0.457	-	0.9

(a) based on the formula $([\text{NaPF}_6] - [\text{LiPF}_6])/[\text{LiPF}_6] \times 100$.

Table 3.3 shows a comparison of the main electrolyte properties at 25°C determined by the AEM. The main advantages of Na-based electrolytes over Li-based electrolytes are a higher conductivity (15%), lower viscosity (-13%), higher diffusivity (14%), and better solubility, as indicated by the lower free energy of solvation (-33%). For this reason, Na-based salts can dissolve in low dielectric solvents and therefore display better ion transport properties. Other effects such as the solvated ion diameter, ion solvation numbers, and cation transference numbers have only a marginal influence (< 4%). The solvated ion diameter here represents the effective transport diameter, which includes the bare-ion diameter and the hard-sphere or collision diameter [13]. Based on the ion solvation numbers, it is apparent that anions are poorly solvated. This corroborates the findings that the electrolyte conductivity is mainly influenced by solvated cations [41]. Finally, the transference numbers of the two electrolytes are almost identical due to the similarities in solvated ion size.

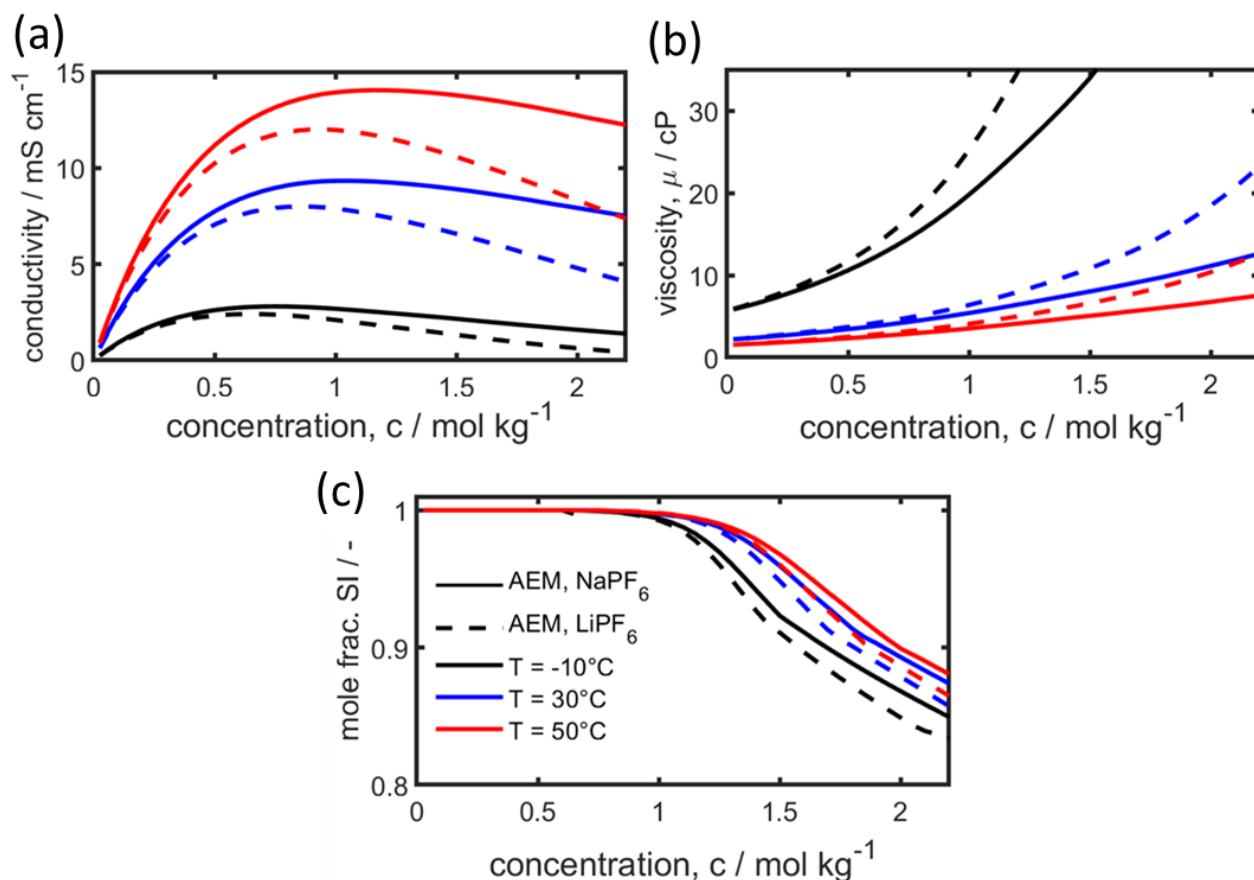


Fig. 3.6. Comparison of AEM simulated conductivity (a), viscosity (b) and mole fraction of single ions (SI) (c) for NaPF₆- (solid lines) and LiPF₆-based (dashed lines) electrolytes in EC_{0.5}:PC_{0.5} (w/w) at -10 (black lines), 30 (blue lines), and 50°C (red lines) as a function of concentration (molality).

Fig. 3.6 shows AEM results comparing properties of NaPF₆- and LiPF₆-based EC_{0.5}:PC_{0.5} (w/w) electrolytes as a function of the salt concentration and electrolyte temperature. **Fig. 3.6** (a), (b), and (c) show the conductivity, viscosity, and mole fraction of single ions (SI), as a function of electrolyte concentration and temperature, respectively. A series of thermodynamic mass action law (MAL) expressions within AEM predict the equilibrium proportions of single ions, ion pairs (IP), and triple ions (TI), as well as the onset of solid solvates. MAL calculations are sensitive to the relative permittivity of the electrolyte solution, which is allowed to vary over salt concentration due to the absolute concentrations and electrostatic fields of SI, IP, and TI species. While the conductivity, viscosity, and SI values are nearly indistinguishable in (dilute) concentrations below 0.5 mol kg⁻¹, the differences between the two salts become more pronounced at higher concentrations. At concentrations above 1 mol kg⁻¹, the conductivity and

the mole fraction of SI decrease more rapidly in LiPF_6 compared to NaPF_6 , while the viscosity of LiPF_6 increases more sharply compared to that of NaPF_6 . This drop in conductivity is due in part to the 2% larger solvated cation diameter of Li^+ , as shown in **Table 3.3**, which corresponds to a substantially larger solvated proportion of its diameter compared to Na^+ once their bare ions are subtracted from their solvated volumes. Nevertheless, ion dissociation remains high even as the concentration exceeds 2 mol kg^{-1} with the mole fraction of SI above 85%. This result indicates that the dilute solution theory can be adequately applied to model most LIB and SIB electrolytes whose equilibrium concentrations are typically around 1 M.

An interesting feature on the conductivity profile of the NaPF_6 electrolyte is that the conductivity remains high and close to the peak at high concentrations. Na-based electrolytes, therefore, outperform analogous Li-based electrolytes at high salt concentration and low-temperature conditions. These results should encourage the exploration of highly concentrated SIB electrolytes, which have improved thermal stability, a wider electrochemical stability window, and fast electrode kinetics [18,19]. Nevertheless, the high viscosity under these conditions might present wettability challenges when using common separators.

3.4.4 Preferential ion solvation (PIS) – why some electrolyte combinations fail

EC is an electrolyte solvent with high dielectric permittivity and forms a stable SEI on HC and graphite electrodes [42,43]. Due to these properties, EC is considered an indispensable component in mixed battery electrolytes [5]. Nevertheless, EC has a high viscosity and is a solid at room temperature, making its use as a pure solvent impossible. EC is, therefore, commonly found in mixed solvents containing low viscosity solvents such as PC, DMC, DME, or DEC, which improves electrolyte properties with respect to viscosity, conductivity, and liquidus temperature [5,6].

Several fundamental empirical studies have been performed to optimize binary and ternary mixtures of SIB electrolytes [7,8]. These studies concluded that $\text{EC}_{0.5}:\text{PC}_{0.5}$ (w/w) and $\text{EC}_{0.4}:\text{PC}_{0.4}:\text{DMC}_{0.1}$ (w/w) are the optimum electrolyte blends for SIB applications due to their wide ESW and the high reversible capacity of HC electrodes. The results of these studies are summarized in **Table 3.4**.

Table 3.4. Fractional composition of EC in 1 M NaClO₄ binary and ternary electrolytes at 25 °C.

Electrolyte	Composition of EC at 25 °C in different units				ESW (V vs. HC	Cap.
	Weight	Volume	Mole	Cation PIS ^(a)	Na ⁺ /Na ^(b)	(mAhg ⁻¹)
EC:PC	0.50	0.47	0.54	0.46	0.1 – 5.0	200 ^(b) /300 ^(c)
EC:DMC	0.50	0.44	0.51	0.36	0.1 – 4.8	180 ^(b)
EC:DME	0.50	0.39	0.51	0.34	0.4 – 4.5	70 ^(b)
EC:DEC	0.50	0.42	0.57	0.41	1.0 – 4.6	185 ^(b)
EC: PC: DMC _{0.2}	0.40	0.36	0.43	0.33	-	265 ^(c)
EC: PC: DME _{0.2}	0.40	0.35	0.43	0.32	-	100 ^(c)
EC: PC: DEC _{0.2}	0.40	0.36	0.45	0.35	-	270 ^(c)
EC: PC: DMC _{0.1}	0.45	0.42	0.48	0.39	-	310 ^(c)

(a) Data derived from AEM v. 2.19.1 Data derived from literature: Ponrouch *et al.* [7]. (b) Data derived from literature: Ponrouch *et al.* [8].

While the different electrolyte blends prepared based on equal EC solvent weight show different results on the reversible capacity of HC electrodes, it is interesting to investigate trends which arise when the EC solvent composition is expressed in other units such as volume and mole fraction. The objective is to understand if HC's reversible capacity reported in literature can be correlated to the amount of EC in the solvent blends (expressed in volumetric and mole fraction units) and whether the minimum composition of EC needed for stable electrolytes can be defined. Furthermore, the AEM provides values of the preferential ion solvation (PIS), a measure of the probability of finding a solvent molecule in the primary solvation shell of an ion. Due to the preferential association of different solvent molecules with a cation, the PIS number does not correlate with the bulk quantities of the mixed solvent (mass, volume, and mole fraction) mentioned above [5]. In this study, the PIS of EC on the Na⁺-cation is the most interesting quantity, which governs the amount of EC delivered by the cation onto the HC interface during ion intercalation and SEI formation. Therefore, high values of the EC PIS on the cation can be expected to improve the cycle stability on HC electrodes.

Fig. 3.7 shows the measured reversible capacity of HC (bar graphs) and calculated PIS (squares), EC volume fraction (diamonds), and EC mole fraction (triangles). **Fig. 3.7** (a) and (b) show results for the binary and ternary SIB electrolyte mixtures, respectively. There is a direct

correlation between the reversible storage capacity and the EC PIS in all solvent mixtures with correlation factors (R^2) of 0.92 and 0.95 for the binary and ternary solvents, respectively. In addition, it can be deduced that a PIS minimum value of 0.4 is necessary for the long-term cycle stability of HC.

The other quantitative measures are, however, inconsistent between binary and ternary mixtures. For example, in volumetric terms, the binary and ternary R^2 value are 0.63 and 0.98, respectively, while in molar terms, the R^2 values are 0.05 and 0.90, respectively. As a result, it is impossible to define a target EC fraction based on volumetric or molar properties. However, the volume fraction shows better correlation factors compared to the molar units. It, therefore, presents a better choice for comparing different solvent mixtures when the PIS is not available.

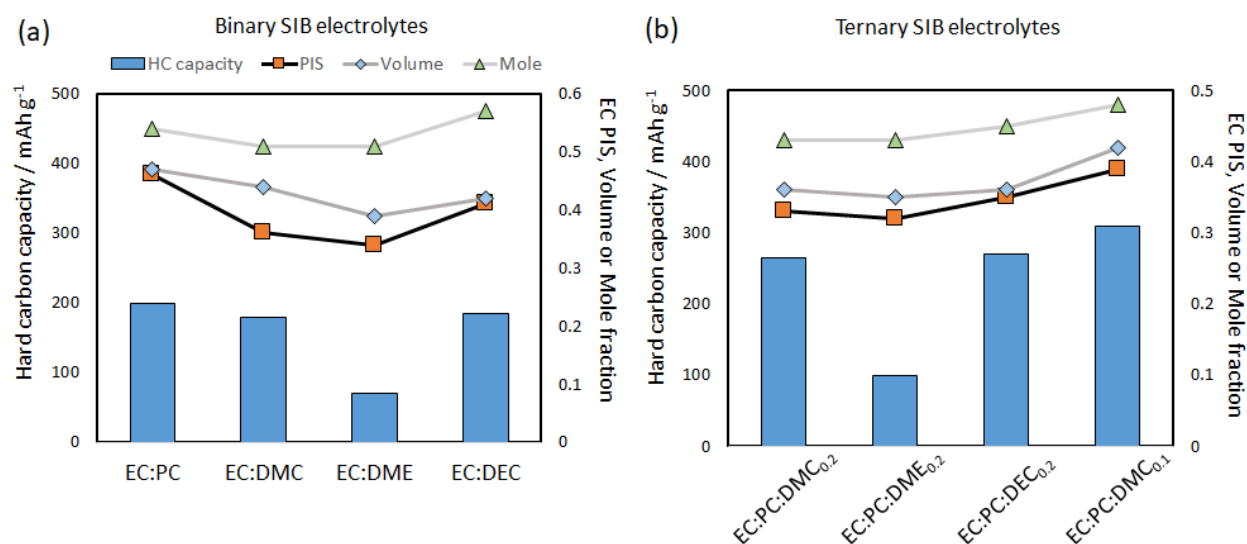


Fig. 3.7. Effect of EC preferential ion solvation (PIS) on the reversible capacity of hard carbon (HC) anodes for 1 M NaClO₄ binary (a) and ternary SIB electrolytes. HC data was derived from Ponrouch *et al.* [7,8].

3.4.5 Optimization of 1 M NaPF₆ EC_x: PC_{1-x} electrolytes

Having specified the EC PIS minimum value, it is now possible to optimize the conductivity of 1 M NaPF₆ as a function of the EC_x: PC_{1-x} (w/w) electrolyte composition. Note that for the 1 M NaPF₆ EC_x: PC_{1-x} electrolyte, the EC PIS on the cation was found to be equal to the EC weight fraction. **Fig. 3.8** shows the AEM calculated conductivity of 1 M NaPF₆ in EC_x: PC_{1-x} (w/w) as function of the EC content fraction x at 50 (a), 30 (b), and -10°C (c). Low amounts of EC are

undesirable because they result in poor SEI formation at HC electrodes. Furthermore, ion-pairing effects increase under these conditions due to a low dielectric permittivity, resulting in a low ionic conductivity. On the other hand, excessive amounts of EC are also unsuitable because the electrolyte conductivity is reduced by the increase in viscosity (see **Fig. 3.8** (a)) and results in wettability issues with separators. Therefore, the optimum composition is between these extremes, a situation best illustrated at -10°C in **Fig. 3.8** (c). This figure further illustrates the importance of mixed solvents and why pure EC and PC solvents have lower conductivities compared to their mixed solvents. Therefore, the optimum EC composition is 0.55, 0.70, and 0.75 (w/w) at -10 , 30 , and 50°C , respectively, which are all above the EC PIS minimum value of 0.4. Because the viscosity effects are more pronounced at low temperatures, the optimum EC composition locus is lower at low temperatures.

Nevertheless, the improvements in conductivity as a result of the EC composition are marginal. For example, a change in the EC weight fraction from 0.4 to 0.7 results in a 4% conductivity increase at 30°C . There are also cost factors to consider because EC is generally the most expensive solvent. Therefore, in practice, the PIS constraint may override conductivity optimization in the final formulation.

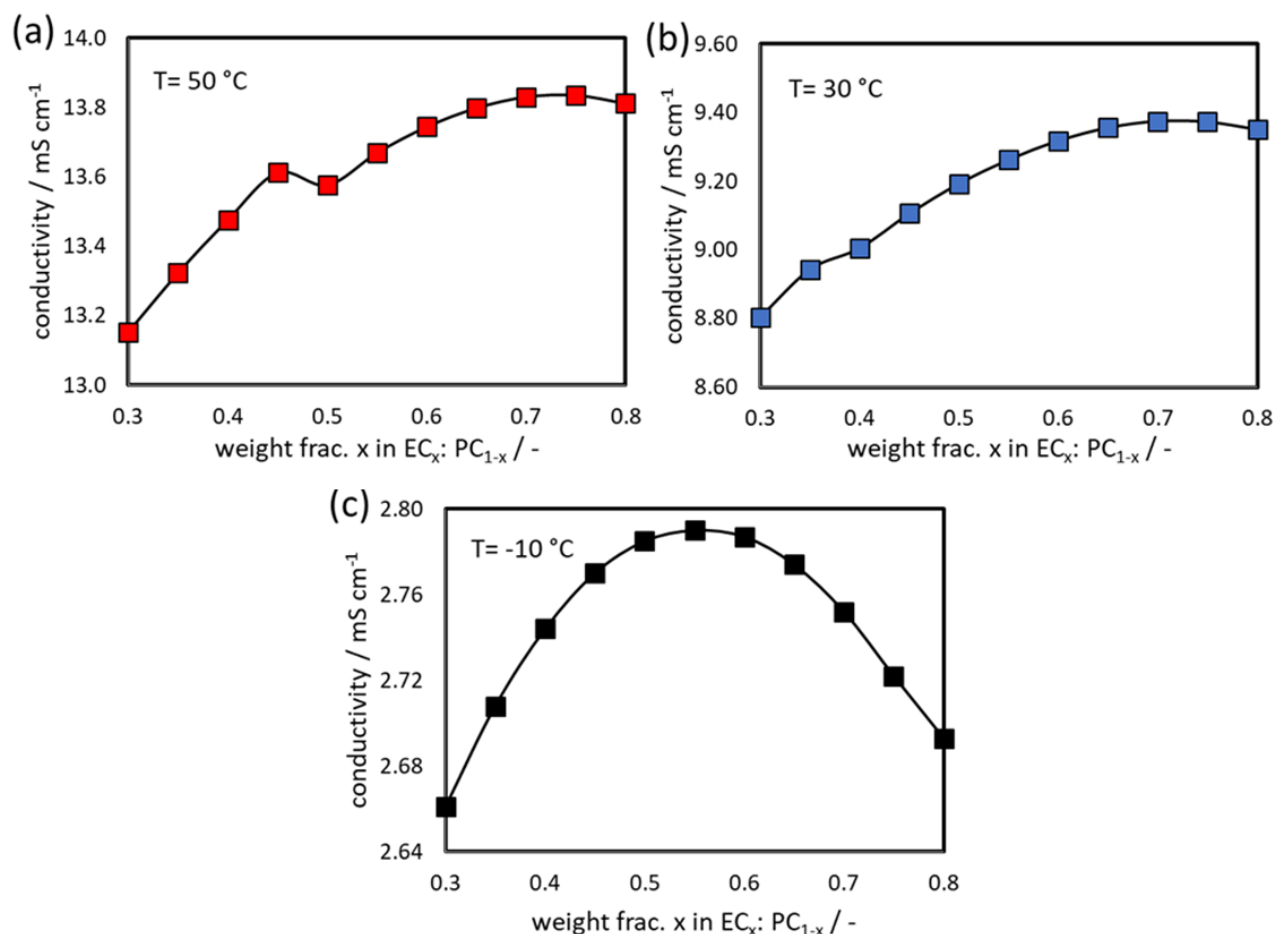


Fig. 3.8. Optimized AEM simulations of 1 M NaPF₆ EC _{x} :PC_{1- x} (w/w) electrolytes. Conductivity as function of EC composition x at 50 (a), 30 (b) and -10°C (c).

3.5 Conclusions

In this Chapter, experimental electrolyte conductivity and viscosity measurements were used in combination with the Advanced Electrolyte Model (AEM) to derive extensive properties of sodium-ion battery (SIB) electrolytes. Based on the agreement between the experimental and model data, the AEM is shown to be a reliable software to obtain extensive properties that are often difficult to measure experimentally. In addition, a method of conductivity measurement using two Pt blocking electrodes and electrochemical impedance spectroscopy (EIS) is validated and shown to be reliable for the first time in a PAT-Cell setup.

It is herein shown that the NaPF₆ EC_{0.5}:PC_{0.5} (w/w) SIB electrolyte in the concentration range 0 to 2 mol kg⁻¹ follows the simple Stokes' law, based on the Walden analysis. This result implies that the electrolyte conductivity is highly dependent on the viscosity and not on ion-pairing effects.

This justifies the search for low-viscosity, liquefied gas electrolytes for improved battery performance at low temperatures [44]. This validates the use of the dilute solution theory to model SIB electrolytes since the Simple Stokes' law neglects ion-ion interactions.

Comparing 1 M NaPF_6 and LiPF_6 electrolytes shows that the Na-based electrolyte has a higher conductivity (15%), lower viscosity (-13%), higher diffusivity (14%), and better solubility, as indicated by the lower free energy of solvation (-33%). As a result, Na-based salts dissolve in lower dielectric solvents and display better ion transport properties. An interesting feature on the concentration vs. conductivity profile of the NaPF_6 electrolyte is that the conductivity remains high and close to the peak at high salt concentrations. This feature therefore encourages the exploration of superconcentrated SIB electrolyte, which have improved electrochemical stability and safety. In general, Na-based electrolytes outperform analogous Li-based electrolytes at high salt concentration and low-temperature conditions.

Finally, the optimization of the 1M NaPF_6 $\text{EC}_x:\text{PC}_{1-x}$ (w/w) electrolyte was carried out using AEM data. It is revealed that the optimized mass fraction of EC is temperature-dependent and ranges between 0.55 and 0.75 at -10 and 50 °C. Using literature-derived cycling data of hard carbon (HC) electrodes, it is herein shown that the cycling stability correlates with the preferential ion solvation (PIS) of EC on the cation. Based on a study of 8 binary and ternary electrolyte mixtures, those with cationic EC PIS below 0.4, exhibit poor cycle stability. This phenomena can be attributed to poor SEI formation. Given the high cost of EC, electrolyte mixture optimization might best prioritize the minimum EC PIS for stable cycling while adding a second or third low-cost and low-viscosity solvent for higher ionic conductivity.

References

- [1] K. Chayambuka, G. Mulder, D.L. Danilov, P.H.L. Notten, From Li-Ion Batteries toward Na-Ion Chemistries: Challenges and Opportunities, *Advanced Energy Materials* **10** (2020) 2001310. <https://doi.org/10.1002/aenm.202001310>.
- [2] Tiamat, Powerful, fast charging, enduring cells thanks to sodium-ion (2020). <http://www.tiamat-energy.com/> (accessed April 14, 2020).
- [3] J. Barker, R. Heap, N. Roche, C. Tan, R. Sayers, Y. Liu, Low Cost Na-ion Battery Technology, Faradion Ltd, San Francisco, US. (2014).
- [4] Y.-S. Hu, S. Komaba, M. Forsyth, C. Johnson, T. Rojo, A New Emerging Technology: Na-Ion Batteries, *Small Methods*. **3** (2019) 1900184. <https://doi.org/10.1002/smt.201900184>.
- [5] K. Xu, Electrolytes and Interphases in Li-Ion Batteries and Beyond, *Chem. Rev.* **114** (2014) 11503–11618. <https://doi.org/10.1021/cr500003w>.
- [6] K. Xu, Nonaqueous liquid electrolytes for lithium-based rechargeable batteries, *Chem. Rev.* **104** (2004) 4303–4418.
- [7] A. Ponrouch, E. Marchante, M. Courty, J.-M. Tarascon, M. Rosa Palacín, In search of an optimized electrolyte for Na-ion batteries, *Energy & Environmental Science* **5** (2012) 8572–8583. <https://doi.org/10.1039/C2EE22258B>.
- [8] A. Ponrouch, R. Dedryvère, D. Monti, A. E. Demet, J.M.A. Mba, L. Croguennec, C. Masquelier, P. Johansson, M. Rosa Palacín, Towards high energy density sodium ion batteries through electrolyte optimization, *Energy & Environmental Science* **6** (2013) 2361–2369. <https://doi.org/10.1039/C3EE41379A>.
- [9] K. Chayambuka, G. Mulder, D. L. Danilov, P. H. L. Notten, Sodium-Ion Battery Materials and Electrochemical Properties Reviewed, *Advanced Energy Materials* **8** (2018) 1800079. <https://doi.org/10.1002/aenm.201800079>.
- [10] E.R. Logan, E.M. Tonita, K.L. Gering, J. Li, X. Ma, L.Y. Beaulieu, J.R. Dahn, A Study of the Physical Properties of Li-Ion Battery Electrolytes Containing Esters, *J. Electrochem. Soc.* **165** (2018) A21. <https://doi.org/10.1149/2.0271802jes>.
- [11] E.R. Logan, E.M. Tonita, K.L. Gering, L. Ma, M.K.G. Bauer, J. Li, L.Y. Beaulieu, J.R. Dahn, A Study of the Transport Properties of Ethylene Carbonate-Free Li Electrolytes, *J. Electrochem. Soc.* **165** (2018) A705. <https://doi.org/10.1149/2.0981803jes>.

- [12] K.L. Gering, Prediction of Electrolyte Conductivity: Results from a Generalized Molecular Model Based on Ion Solvation and a Chemical Physics Framework, *Electrochimica Acta* **225** (2017) 175–189. <https://doi.org/10.1016/j.electacta.2016.12.083>.
- [13] K.L. Gering, Prediction of electrolyte viscosity for aqueous and non-aqueous systems: Results from a molecular model based on ion solvation and a chemical physics framework, *Electrochimica Acta* **51** (2006) 3125–3138. <https://doi.org/10.1016/j.electacta.2005.09.011>.
- [14] A.Y. Ben-Naim, *Solvation Thermodynamics*, Springer Science & Business Media (2013).
- [15] Y. Kuang, C. Chen, D. Kirsch, L. Hu, Thick Electrode Batteries: Principles, Opportunities, and Challenges, *Advanced Energy Materials* **9** (2019) 1901457. <https://doi.org/10.1002/aenm.201901457>.
- [16] J.-H. Kim, N.P.W. Pieczonka, L. Yang, Challenges and Approaches for High-Voltage Spinel Lithium-Ion Batteries, *ChemPhysChem* **15** (2014) 1940–1954. <https://doi.org/10.1002/cphc.201400052>.
- [17] E. Berg, C. Villevieille, D. Streich, S. Trabesinger, P. Novak, Rechargeable Batteries: Grasping for the Limits of Chemistry, *J. Electrochem. Soc.* **162** (2015) A2468–A2475.
- [18] B. Ravikumar, M. Mynam, B. Rai, Effect of Salt Concentration on Properties of Lithium Ion Battery Electrolytes: A Molecular Dynamics Study, *J. Phys. Chem. C* **122** (2018) 8173–8181. <https://doi.org/10.1021/acs.jpcc.8b02072>.
- [19] Y. Yamada, A. Yamada, Review—Superconcentrated Electrolytes for Lithium Batteries, *J. Electrochem. Soc.* **162** (2015) A2406. <https://doi.org/10.1149/2.0041514jes>.
- [20] V.M.-W. Huang, V. Vivier, M.E. Orazem, N. Pébère, B. Tribollet, The Apparent Constant-Phase-Element Behavior of an Ideally Polarized Blocking Electrode: A Global and Local Impedance Analysis, *J. Electrochem. Soc.* **154** (2006) C81. <https://doi.org/10.1149/1.2398882>.
- [21] M.E. Orazem, N. Pébère, B. Tribollet, Enhanced Graphical Representation of Electrochemical Impedance Data, *J. Electrochem. Soc.* **153** (2006) B129. <https://doi.org/10.1149/1.2168377>.
- [22] Z. Lukács, Evaluation of model and dispersion parameters and their effects on the formation of constant-phase elements in equivalent circuits, *Journal of Electroanalytical Chemistry* **464** (1999) 68–75. [https://doi.org/10.1016/S0022-0728\(98\)00471-9](https://doi.org/10.1016/S0022-0728(98)00471-9).

- [23] Gamry, Basics of EIS: Electrochemical Research-Impedance, <https://www.gamry.com/application-notes/EIS/basics-of-electrochemical-impedance-spectroscopy/> (accessed January 19, 2021).
- [24] EL-CELL - electrochemical test equipment, <https://el-cell.com/> (accessed March 6, 2021).
- [25] Anton Paar, Rheometry measuring systems, Anton Paar, <https://wiki.anton-paar.com/en/basics-of-rheology/rheometry-measuring-systems/> (accessed January 19, 2021).
- [26] H. Lundgren, M. Behm, G. Lindbergh, Electrochemical Characterization and Temperature Dependency of Mass-Transport Properties of LiPF₆ in EC:DEC, *J. Electrochem. Soc.* **162** (2015) A413–A420. <https://doi.org/10.1149/2.0641503jes>.
- [27] O.O. Okoturo, T.J. VanderNoot, Temperature dependence of viscosity for room temperature ionic liquids, *Journal of Electroanalytical Chemistry* **568** (2004) 167–181. <https://doi.org/10.1016/j.jelechem.2003.12.050>.
- [28] G. Jones, M. Dole, The viscosity of aqueous solutions of strong electrolytes with special reference to barium chloride, *J. Am. Chem. Soc.* **51** (1929) 2950–2964. <https://doi.org/10.1021/ja01385a012>.
- [29] C. L. Berhaut, D. Lemordant, P. Porion, L. Timperman, G. Schmidt, M. Anouti, Ionic association analysis of LiTDI, LiFSI and LiPF₆ in EC/DMC for better Li-ion battery performances, *RSC Advances* **9** (2019) 4599–4608. <https://doi.org/10.1039/C8RA08430K>.
- [30] C.L. Berhaut, P. Porion, L. Timperman, G. Schmidt, D. Lemordant, M. Anouti, LiTDI as electrolyte salt for Li-ion batteries: transport properties in EC/DMC, *Electrochimica Acta* **180** (2015) 778–787. <https://doi.org/10.1016/j.electacta.2015.08.165>.
- [31] E.R. Logan, E.M. Tonita, K.L. Gering, J.R. Dahn, A Critical Evaluation of the Advanced Electrolyte Model, *J. Electrochem. Soc.* **165** (2018) A3350. <https://doi.org/10.1149/2.0471814jes>.
- [32] C. Schreiner, S. Zugmann, R. Hartl, H.J. Gores, Fractional Walden Rule for Ionic Liquids: Examples from Recent Measurements and a Critique of the So-Called Ideal KCl Line for the Walden Plot, *J. Chem. Eng. Data* **55** (2010) 1784–1788. <https://doi.org/10.1021/je900878j>.
- [33] J.T. Dudley, D.P. Wilkinson, G. Thomas, R. LeVae, S. Woo, H. Blom, C. Horvath, M.W. Juzkow, B. Denis, P. Juric, P. Aghakian, J.R. Dahn, Conductivity of electrolytes for rechargeable lithium batteries, *Journal of Power Sources* **35** (1991) 59–82. [https://doi.org/10.1016/0378-7753\(91\)80004-H](https://doi.org/10.1016/0378-7753(91)80004-H).

- [34] P. Walden, Über organische Lösungs- und Ionisierungsmittel: III. Teil: Innere Reibung und deren Zusammenhang mit dem Leitvermögen, *Zeitschrift Für Physikalische Chemie*. **55** (1906) 207–249. <https://doi.org/10.1515/zpch-1906-5511>.
- [35] C.A. Angell, N. Byrne, J.-P. Belieres, Parallel Developments in Aprotic and Protic Ionic Liquids: Physical Chemistry and Applications, *Acc. Chem. Res.* **40** (2007) 1228–1236. <https://doi.org/10.1021/ar7001842>.
- [36] M. Nakahara, K. Ibuki, Is the Walden product useful?, *J. Phys. Chem.* **90** (1986) 3026–3030. <https://doi.org/10.1021/j100404a047>.
- [37] M. Dahbi, F. Ghamouss, F. Tran-Van, D. Lemordant, M. Anouti, Comparative study of EC/DMC LiTFSI and LiPF₆ electrolytes for electrochemical storage, *Journal of Power Sources* **196** (2011) 9743–9750. <https://doi.org/10.1016/j.jpowsour.2011.07.071>.
- [38] M. Valiskó, D. Boda, The effect of concentration- and temperature-dependent dielectric constant on the activity coefficient of NaCl electrolyte solutions, *J. Chem. Phys.* **140** (2014) 234508. <https://doi.org/10.1063/1.4883742>.
- [39] E. Jónsson, P. Johansson, Modern battery electrolytes: Ion–ion interactions in Li + /Na + conductors from DFT calculations, *Physical Chemistry Chemical Physics* **14** (2012) 10774–10779. <https://doi.org/10.1039/C2CP40612H>.
- [40] E. Flores, G. Åvall, S. Jeschke, P. Johansson, Solvation structure in dilute to highly concentrated electrolytes for lithium-ion and sodium-ion batteries, *Electrochimica Acta* **233** (2017) 134–141. <https://doi.org/10.1016/j.electacta.2017.03.031>.
- [41] Y. Aihara, T. Bando, H. Nakagawa, H. Yoshida, K. Hayamizu, E. Akiba, W.S. Price, Ion Transport Properties of Six Lithium Salts Dissolved in γ -Butyrolactone Studied by Self-Diffusion and Ionic Conductivity Measurements, *J. Electrochem. Soc.* **151** (2003) A119. <https://doi.org/10.1149/1.1630592>.
- [42] K. Xu, U. Lee, S. Zhang, J.L. Allen, T.R. Jow, Graphite/Electrolyte Interface Formed in LiBOB-Based Electrolytes : I. Differentiating the Roles of EC and LiBOB in SEI Formation, *Electrochem. Solid-State Lett.* **7** (2004) A273. <https://doi.org/10.1149/1.1774973>.
- [43] Y. Kim, K.-H. Ha, S.M. Oh, K.T. Lee, High-Capacity Anode Materials for Sodium-Ion Batteries, *Chemistry – A European Journal* **20** (2014) 11980–11992. <https://doi.org/10.1002/chem.201402511>.

- [44] Y. Yang, Y. Yin, D. M. Davies, M. Zhang, M. Mayer, Y. Zhang, E. S. Sablina, S. Wang, J. Z. Lee, O. Borodin, C. S. Rustomji, Y. Shirley Meng, Liquefied gas electrolytes for wide-temperature lithium metal batteries, *Energy & Environmental Science* **13** (2020) 2209–2219. <https://doi.org/10.1039/D0EE01446J>.

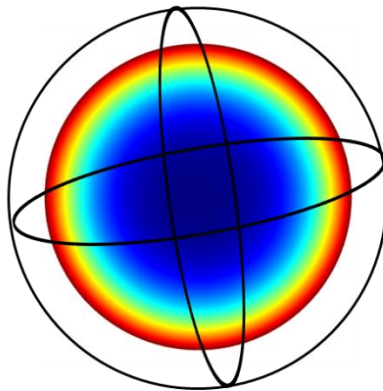
CHAPTER 4

MODELING THE DIFFUSION MECHANISM IN SPHERICAL ELECTRODE PARTICLES

Efficient analytical and numerical methods

Abstract

The solid-state spherical diffusion equation with flux boundary conditions is a common problem in SIB and LIB simulations. If numerical methods such as finite difference schemes are applied, many nodes across a discretized particle domain become necessary to obtain accurate solutions. However, for a constant diffusion coefficient problem, such a grid-based approach can be easily avoided by implementing analytical methods, which are computationally efficient. This Chapter discusses analytical and numerical solution methods to efficiently resolve the solid-state mass transport problem in spherical electrode particles commonly encountered in battery modeling.



- The spherical diffusion problem in P2D battery modeling
- Flux boundary conditions
- Cases of a constant and variable D_1
- Using analytical and numerical solution methods

Parts of this Chapter have been published as:

K Chayambuka, G Mulder, DL Danilov, PHL Notten, A modified pseudo-steady-state analytical expression for battery modeling, *Solid State Communications* **296** (2019), 49-53. <https://doi.org/10.1016/j.ssc.2019.04.011>

K Chayambuka, G Mulder, DL Danilov, PHL Notten, A Hybrid Backward Euler Control Volume Method to Solve the Concentration-Dependent Solid-State Diffusion Problem in Battery Modeling, *Journal of Applied Mathematics and Physics* **8** (2020), 1066-1080. <https://doi.org/10.4236/jamp.2020.86083>

4.1 Introduction

Historically, the coupling of two intercalation electrode materials is the fundamental basis of rechargeable batteries such as SIBs and LIBs. In the case of LIBs, the development of intercalation electrode materials won the 2019 Nobel prize in chemistry [1]. The mathematical modeling of this mechanism is equally critical to the success of physics-based battery models. Battery electrodes such as those found in SIBs and LIBs are typically porous. These electrodes are composed of a set of solid active particles and electron conductive filler materials. The morphology of a porous battery electrode is illustrated in **Fig. 4.1** (a) where a SIB porous electrode composed of carbon conductive filler (black circles) and active particles (blue circles) is shown. The voids created by the solid particles are occupied by a suitable electrolyte, and for the sake of simplicity, the polymer binder is not shown. Na metal is used as a counter electrode, and Al metal is used as the current collector.

Electrochemical models of the multi-scale and multi-physics phenomena inherent to a typical porous electrode combine thermodynamics, transport phenomena, and reaction kinetics at the surface of the active particles [2]. Following Newman's porous electrode theory, a 1D battery model considers the electrolyte and solid particles as two super-imposed continua [3,4]. Such a model description requires the introduction of a P2D domain, where the diffusion transport develops, occurring within the spherical active particles at a microscopic length scale [3,5,6]. Within such a macro-homogeneous P2D domain (representing discrete particles at different spatial positions across the porous electrode), time-dependent concentration profiles of intercalating species are simultaneously resolved. **Fig. 4.1** (b) illustrates the layout of a P2D battery model. In **Fig. 4.1**, the thickness of the separator and the porous electrode are represented by δ_s and δ_p , respectively.

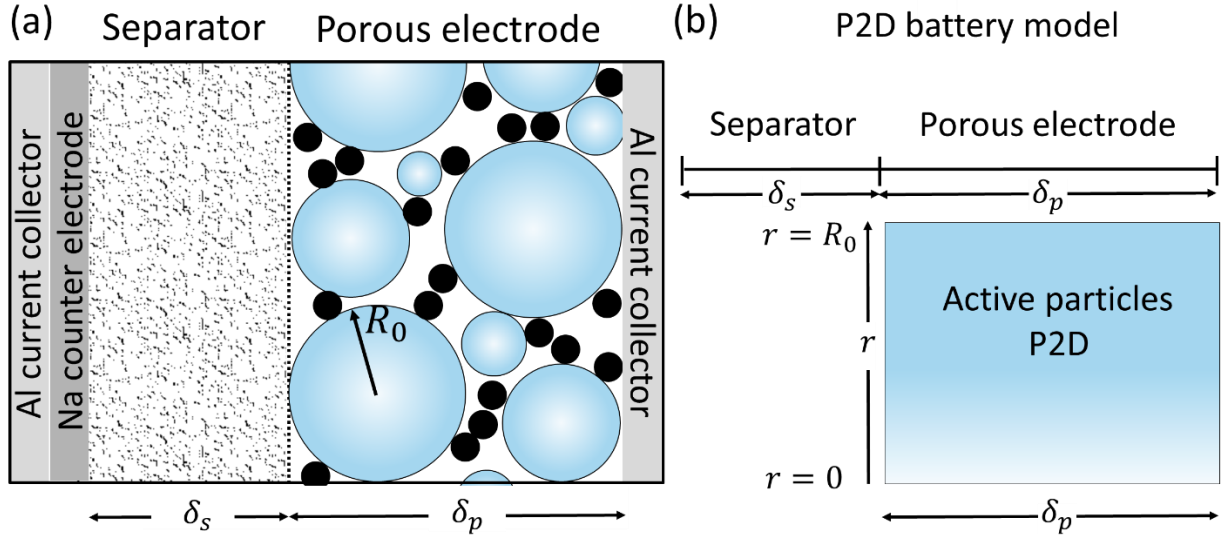


Fig. 4.1. (a) Schematic view of SIB showing the Al current collector, Na electrode, separator and SIB porous electrode. The blue circles represent the active electrode material, and the black circles represent the carbon-based conductive filler. (b) The layout of the P2D model of a porous electrode in a P2D simulation domain.

The solid-state spherical diffusion equation with flux boundary conditions is central in describing mass transport in SIB active particles. This equation is expressed as

$$\frac{\partial c_s}{\partial t} = \frac{1}{r^2} \frac{\partial}{\partial r} \left(D_1 r^2 \frac{\partial c_s}{\partial r} \right), \quad (4.1)$$

where $c_s = c_s(r, t)$ is the concentration of the intercalated species [mol m^{-3}], D_1 the solid-state diffusion coefficient [$\text{m}^2 \text{s}^{-1}$], r the radial distance from the center of the particle [m], and t is time [s]. The following Neumann boundary conditions are applied at the surface and center of the spherical particle, respectively:

$$-D_1 \frac{\partial c_s}{\partial r} = J(t), \quad \text{at } r = R_0, \quad t > 0, \quad (4.2)$$

$$\frac{\partial c_s}{\partial r} = 0, \quad \text{at } r = 0, \quad \text{for } \forall t, \quad (4.3)$$

where $J(t)$ is the flux of species at the surface of the particle [$\text{mol m}^{-2} \text{s}^{-1}$] and R_0 is the radius of the active particles [m]. The initial value for the problem of Eq. (4.1) is a known concentration profile at time $t = 0$, *i.e.*, $c_s(r, 0) = c_{s,0}$, where $c_{s,0}$ is a positive real number.

Note that the flux $J(t)$ is defined as positive for species diffusing out of the particle. The magnitude of $J(t)$ is the same at all points of the particle surface, *i.e.*, it is uniform. This

assumption, in turn, implies spherical symmetry. Eq. (4.1) also does not assume a constant D_1 , which may vary as a function of the concentration. A variable D_1 has consequences on the complexity of the solution method, as shall later be explored in detail. For a physics-based battery model, it should be stressed that the ultimate goal is to derive the particle surface concentration for a given surface flux boundary condition (Neumann boundary condition) using a numerical solution method that is both robust and computationally inexpensive. Such a goal is set because the surface and average concentrations are the only important parameters governing reaction kinetics and the SOC.

This Chapter focuses on modeling the diffusive transport of intercalating species in spherical active particles using analytical and numerical methods. Traditionally, analytical methods are the most popular in battery models because they have the advantage of computational speed. For example, Newman's model famously applied Duhamel's superposition integral in the porous electrode theory [3,5,6]. The interested reader is here referred to the seminal works of Carslaw and Jaeger on the conduction of heat in solids [7]. Nevertheless, in the more general case of a concentration-dependent diffusion coefficient, no analytical methods exist. In this case, one has to rely on numerical methods such as finite difference method (FDM), finite element method (FEM), and finite volume method (FVM). The challenge, however, with all grid-based numerical methods, is that many nodes across the discretized particle domain become necessary to obtain accurate solutions [8,9]. This means that the number of states in a system of coupled partial differential equations (PDEs) increases dramatically when the number of spatially distributed grid points increases.

This Chapter is organized as follows: first, the analytical methods are described with particular focus on the pseudo-steady state (PSS) method. Several improvements to the PSS method are herein introduced to address the problem of numerical instability. These improvements result in the modified PSS (MPSS) method. Then a fast MPSS (FMPSS) method is introduced, which is computationally efficient and numerically stable. Second, the grid-based numerical methods are discussed. The control volume method (CVM) is presented to resolve the spherical diffusion problem with a concentration-dependent D_1 . It has been found that the implicit backward Euler control volume method (BECV) is the most accurate and efficient method for P2D simulations. However, obtaining a full-implicit solution is slow because it involves a series of iterative steps. A hybrid backward Euler control volume method (HBECV) is therefore introduced.

The HBECV method is based on the linearization of the functional form of the diffusion coefficient and obtains the implicit solution in a single iteration. Using the HBECV, computationally efficient, accurate, and unconditionally stable results for the surface concentration are obtained.

4.2 Modeling solid-state diffusion using analytical methods

To avoid computationally intensive numerical methods (*i.e.*, FDM, FEM and FVM), analytical methods are usually applied with the assumption of a constant D_1 . As already mentioned, in the P2D model equations, only the average and surface concentrations are needed in the P2D model, while the rest of the concentration profile is not important. This observation raises the question of whether it is essential to calculate the full concentration profile if a numerical way to derive these two variables is available. Therefore, the "extra" pseudo dimension would be discarded, thus effectively reducing the size and computational runtime of the models while maintaining fidelity.

Several analytical methods have been developed to solve the boundary value problem of Eq. (4.1) [10–12]. These can be subdivided as either exact solution methods or approximate solution methods. Exact solution methods involve a convergent summation of an infinite series of terms considering the concentration profile history. In contrast, approximate solution methods involve empirical approximations and frequently do not consider the history of the concentration profile. Based on a comprehensive review of the different analytical methods relevant to P2D models, it was revealed that the PSS method and the high-order polynomial method are the leading analytical methods based on computation speed and accuracy [10]. The former is an exact solution method, while the latter is an approximate solution method.

Although approximate solution methods generally have speed advantages over exact solution methods, they lack the requisite solution accuracy in transient battery simulations; since they do not track the profile history and do not converge to the exact solution [13]. Existing approximate solution methods include the low order polynomial method [14], the high order polynomial method [14], the diffusion length method [15,16], and the penetration depth method [17]. On the other hand, exact solution methods offer high accuracy yet invoke considerable computational effort at short times and whenever the concentration profile undergoes abrupt changes. Exact solution

methods have a long and established history. In recent times, Ölçer's PSS approach, based on the finite integral transform, has gained recognition [18,19].

The PSS method resolves the seemingly antagonistic requirements of speed and accuracy, as demonstrated by Liu on a conceptual spherical particle [20]. The PSS method was applied to a porous electrode model in a benchmarking review by Zhang *et al.* [10]. Therein, the computational runtime of the PSS emerged of the same order of magnitude as approximate solution methods. Nevertheless, it has been reported that the PSS method is unstable when the number of summation terms increases [8]. This instability introduces numerical difficulties for control-oriented battery programming [21,22], resulting in fewer adoptions of the PSS method.

The origins of the numerical problems associated with the PSS method are herein investigated, and a modified PSS method (MPSS) is presented. The MPSS is, therefore, a numerically efficient and stable method. Furthermore, a programmable and computationally efficient, fast MPSS (FMPSS) method is presented, enabling rapid and accurate P2D modeling.

4.2.1 Derivation of the modified-PSS method

Assuming a constant D_1 , the diffusion-controlled transport of intercalated species in a spherical electrode particle, the exact solution to Eqs. (4.1)-(4.3) can be found using the PSS analytical method. The PSS method is based on established solutions for second-order PDEs with flux boundary conditions [18–20]. The PSS analytical expression is given by

$$\begin{aligned}
 c_s(r, t) = c_{s,0} - \frac{3}{R_0} \int_0^t J(t) dt + \frac{R_0}{2D_1} J(t) \left[\frac{3}{5} - \left(\frac{r}{R_0} \right)^2 \right] \\
 + \frac{2R_0}{D_1} \sum_{m=1}^{\infty} \frac{\sqrt{1 + \lambda_m^2}}{\lambda_m^3} \frac{\sin\left(\frac{\lambda_m r}{R_0}\right)}{\frac{r}{R_0}} \\
 \times e^{-\frac{\lambda_m^2 D_1 t}{R_0^2}} \left[e^{\frac{\lambda_m^2 D_1 t}{R_0^2}} J(t) - \frac{\lambda_m^2 D_1}{R_0^2} \int_0^t e^{\frac{\lambda_m^2 D_1 t}{R_0^2}} J(t) dt \right],
 \end{aligned} \tag{4.4}$$

where λ_m are the non-zero positive real roots of equation $\tan(\lambda_m) = \lambda_m$ [20]. The infinite summation series in Eq. (4.4) is truncated when the desired accuracy is obtained. However, Eq. (4.4) is not stable at long times irrespective of the number of summation terms. This artifact has been pointed out by Ramadesigan *et al.* [8] as a blow-up of coefficients when summation terms

increase. The reason for this instability is the occurrence of an exponential time function outside the integral term, which results in oscillatory and non-convergent solutions. As t becomes large, these oscillations become severe, resulting in the aforementioned numerical difficulties. To address this problem, both terms inside the square brackets in Eq. (4.4) are multiplied by $e^{-\frac{\lambda_m^2 D t}{R_0^2}}$, resulting in the following MPSS expression

$$\begin{aligned}
 c_s(r, t) = c_{s,0} - \frac{3}{R_0} \int_0^t J(\tau) d\tau + \frac{R_0}{2D_1} J(t) \left[\frac{3}{5} - \left(\frac{r}{R_0} \right)^2 \right] \\
 + \frac{2R_0}{D_1} \sum_{m=1}^{\infty} \frac{\sqrt{1 + \lambda_m^2}}{\lambda_m^3} \frac{\sin\left(\frac{\lambda_m r}{R_0}\right)}{\frac{r}{R_0}} \\
 \times \left[J(t) - \frac{\lambda_m^2 D_1}{R_0^2} \int_0^t e^{-\frac{\lambda_m^2 D_1}{R_0^2} (t-\tau)} J(\tau) d\tau \right].
 \end{aligned} \tag{4.5}$$

Note that separate time symbols t and τ are here introduced. The time at which the solution is calculated is denoted as t , while τ denotes the integration time variable. Thus, in $J(\tau)$ in Eq. (4.5), variable τ runs across a whole time-span of modeling, *i.e.*, from 0 to t .

When Eq. (4.5) instead of Eq. (4.4) is used to determine the surface concentration, MPSS delivers stable and uniformly convergent solutions. A corresponding test case comparing the PSS and the MPSS is shown in Section 4.4.1 where a constant surface flux of $J(t) = -10^{-3} \text{ mol m}^{-2} \text{ s}^{-1}$ is applied. Here, the negative sign indicates that the flux is directed towards the center of the particles. Whereas the PSS has a blow-up of solutions when the number of summation terms goes to infinity, the MPSS method uniformly converges with greater accuracy at all times. It can therefore be concluded that MPSS represents a stable and accurate implementation of the PSS method.

The MPSS method is, however, computationally demanding for the long times encountered in P2D simulations. As t increases, a longer time interval has to be integrated. For an efficient programming implementation of Eq. (4.5) it is possible to decompose t to

$$t = t' + \Delta t, \tag{4.6}$$

where t' is the previous moment of time and Δt is the time step. This decomposition relieves the redundancy of integration over previous time steps, whose results are known. Eq. (4.5) thus becomes

$$\begin{aligned}
 c_s(r, t) = c_{s,0} - \frac{3}{R_0} \int_0^{t'+\Delta t} J(\tau) d\tau + \frac{R_0}{2D_1} J(t) \left[\frac{3}{5} - \left(\frac{r}{R_0} \right)^2 \right] \\
 + \frac{2R_0}{D_1} \sum_{m=1}^{\infty} \frac{\sqrt{1+\lambda_m^2}}{\lambda_m^3} \frac{\sin\left(\frac{\lambda_m r}{R_0}\right)}{\frac{r}{R_0}} \\
 \times \left[J(t) - \frac{\lambda_m^2 D_1}{R_0^2} \int_0^{t'+\Delta t} e^{-\frac{\lambda_m^2 D_1}{R_0^2}(t'+\Delta t-\tau)} J(\tau) d\tau \right].
 \end{aligned} \tag{4.7}$$

Now, it is necessary to simplify the two integral terms in Eq. (4.7) and further avoid integration over the whole time interval to obtain faster solutions. Denote the convolution integral as a function of roots λ_m and time t as $\chi(\lambda_m, t)$, this leads to

$$\begin{aligned}
 \chi(\lambda_m, t) = \int_0^t e^{-\frac{\lambda_m^2 D_1}{R_0^2}(t-\tau)} J(\tau) d\tau = \int_0^{t'+\Delta t} e^{-\frac{\lambda_m^2 D_1}{R_0^2}(t'+\Delta t-\tau)} J(\tau) d\tau = \\
 \int_0^{t'} e^{-\frac{\lambda_m^2 D_1}{R_0^2}(t'+\Delta t-\tau)} J(\tau) d\tau + \int_{t'}^{t'+\Delta t} e^{-\frac{\lambda_m^2 D_1}{R_0^2}(t'+\Delta t-\tau)} J(\tau) d\tau = \\
 \chi(\lambda_m, t') + \int_{t'}^{t'+\Delta t} e^{-\frac{\lambda_m^2 D_1}{R_0^2}(t'+\Delta t-\tau)} J(\tau) d\tau.
 \end{aligned} \tag{4.8}$$

The remaining integral on the interval from t' to t can then be evaluated numerically. Applying trapezoidal integration yields

$$\int_{t'}^{t'+\Delta t} e^{-\frac{\lambda_m^2 D_1}{R_0^2}(t'+\Delta t-\tau)} J(\tau) d\tau \approx \frac{\Delta t}{2} \left(e^{-\frac{\lambda_m^2 D_1}{R_0^2} \Delta t} J(t') + J(t) \right), \tag{4.9}$$

where integration error tends to zero when time step Δt reduces. Substituting Eq. (4.9) into Eq. (4.8) leads to

$$\chi(\lambda_m, t) = \chi(\lambda_m, t') + \frac{\Delta t}{2} \left(e^{-\frac{\lambda_m^2 D_1}{R_0^2} \Delta t} J(t') + J(t) \right). \tag{4.10}$$

Indeed, $\chi(\lambda_m, t')$ represents known values from the previous time step while the second term corresponds to the integrand evaluated over time step Δt .

Now, note that

$$\chi(0, t) = \int_0^t J(\tau) d\tau, \quad (4.11)$$

i.e., $\chi(0, t)$ is the time-integrated cumulative flux. Therefore, as a particular case of Eq. (4.10), one obtains

$$\chi(0, t) = \chi(0, t') + \frac{\Delta t}{2} (J(t') + J(t)). \quad (4.12)$$

This equation represents an efficient way to calculate the cumulative flux, enabling a rapid determination of the average concentration. From the previous derivations, an expression for the FMPSS method is finally obtained

$$\begin{aligned} c_s(r, t) = c_{s,0} + \frac{R_0}{2D_1} J(t) \left[\frac{3}{5} - \left(\frac{r}{R_0} \right)^2 \right] - \frac{3}{R_0} \chi(0, t) \\ + \frac{2R_0}{D_1} \sum_{m=1}^{\infty} \frac{\sqrt{1 + \lambda_m^2}}{\lambda_m^3} \frac{\sin\left(\frac{\lambda_m r}{R_0}\right)}{\frac{r}{R_0}} \left[J(t) - \frac{\lambda_m^2 D_1}{R_0^2} \chi(\lambda_m, t) \right]. \end{aligned} \quad (4.13)$$

Eq. (4.13), together with the iterative Eq. (4.10) represent the FMPSS time-stepping algorithm.

4.3 Modeling solid-state diffusion using numerical methods

The FMPSS and other analytical methods which have been described in this Chapter are only valid when solving Eq. (4.1) if D_1 is constant. The assumption of a constant D_1 is one of the foremost simplifications in battery models, which reduces complexity and allows the analytical solution methods described in the previous section. A challenging problem, however, which has relatively remained unscrutinized for many years, is how to model the general case of a concentration-dependent diffusion coefficient $D_1(c_s)$ efficiently [23–25]. This challenge deserves renewed attention because of the need to address stress effects in particles [26], phase separation in two-phase materials, and temperature effects occurring at high discharge rates. Experimental evidence indeed suggests that a constant D_1 is a rare case in intercalation materials. For example, in nickel hydroxide particles, D_1 varies by 3 orders of magnitude [27,28], while in NVPF particles

D_1 varies by 2 orders of magnitude as a function of SOC [29,30]. Therefore, incorporating a concentration-dependent D_1 in electrochemical models leads to more accurate simulation results.

Because of the lack of analytical exact solution methods, one must rely on numerical methods to solve Eq. (4.1) [31]. Usually, this is accomplished using explicit and implicit FDMs [8,32]. Although the explicit FDMs have the advantage of finding the numerical solution in a single step, they are conditionally stable based on the time step size. For a grid spacing in particles Δr , the von Neumann stability condition for the explicit scheme is

$$\Delta t \leq \frac{\Delta r^2}{2D_1}. \quad (4.14)$$

This condition imposes a very small-time step size restriction for battery particles, whose sizes in R_0 is generally of the order of $0.5 - 5 \mu\text{m}$. In general, FDMs do not conserve a perfect mass balance. In a long time, the inaccuracy accumulates and propagated to the overall P2D simulation [33]. Other grid-based methods with perfect mass conservation include the FEM and the FVM. While both methods are renowned for their robustness, they have the inherent disadvantage of not calculating concentrations at specific node points, in particular, at the surface boundary [9,33]. Instead, one obtains volume-averaged concentrations within discrete volume elements. Additional computations are therefore needed to approximate the surface concentration in FEM and FVM. Nevertheless, all the above numerical methods have been successfully applied to battery simulations with variable D_1 .

To address the shortcomings of the FEM and FVM, Zeng *et al.* [9] proposed the CVM. The CVM is a class of finite volume discretization, which directly computes concentrations at node points. This feature means surface concentrations in the CVM are obtained without approximation. Compared to the FVM, the CVM has a higher accuracy for a given number of mesh points and is thus more suited for P2D modeling [9]. Herein a BECV is used to resolve the spherical diffusion problem with a variable D_1 . The BECV incorporates all the advantages of the CVM, with the added benefit of being stable and easier to implement.

Because a fully implicit BECV solution involves a series of iterative steps, a hybrid backward Euler control volume method (HBECV) is finally introduced. The HBECV method is based on the linearization of the functional form of $D_1(c_s)$ and obtains the implicit solution in a single iteration. Using the HBECV, computationally efficient, accurate, and unconditionally stable results are obtained for surface concentration calculations.

4.3.1 Derivation of the hybrid BECV method

Because the diffusion problem of Eqs, (4.1)-(4.3) is spherically symmetric, the concentration profile depends only on r . Now consider a set of N discretization points on r , such that

$$\{r_i\}_i^N, \quad \text{for } 1 \leq i \leq N \quad (4.15)$$

where the index i defines node positions of CVM, and N is a non-zero natural number of grid points. Accordingly, $r_1 = 0$ and $r_N = R_0$ are the particle center and surface, respectively.

Each i^{th} node point in Eq. (4.15) can be assigned a control volume element to it. For a spherical geometry, and for $2 \leq i \leq N - 1$, such a control volume element is a shell whose external faces (boundaries) are located halfway between adjacent nodes.

Let IB_i and OB_i define the i^{th} inner control volume boundary and outer control volume boundary, respectively, according to

$$IB_i = r_{i-1} + \frac{\Delta r_{i-1}}{2}, \quad \text{for } 2 \leq i \leq N - 1 \quad (4.16)$$

$$OB_i = r_i + \frac{\Delta r_i}{2}, \quad \text{for } 2 \leq i \leq N - 1 \quad (4.17)$$

where $\Delta r_i = r_{i+1} - r_i$ is the spacing between two adjacent node points. In this way, the i^{th} inner control volume element is a shell embedding node point i .

At the boundaries, exceptions arise. Both IB_1 and OB_N are not located between node points but right at node points r_1 and r_N , respectively. This situation implies, $IB_1 = 0$ and $OB_N = R$. On the other hand, OB_1 and IB_N are located between adjacent node points and can be expressed as

$$OB_1 = \frac{\Delta r_1}{2}, \quad (4.18)$$

$$IB_N = r_{N-1} + \frac{\Delta r_{N-1}}{2}. \quad (4.19)$$

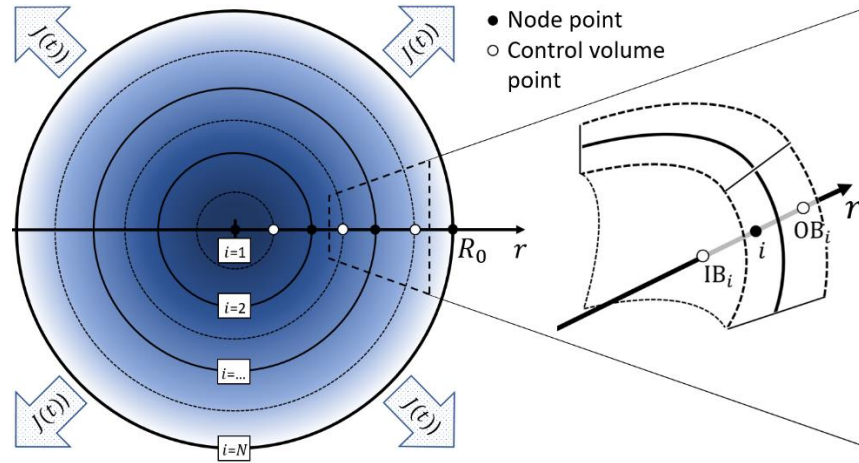


Fig. 4.2. Diffusion in a spherical particle illustrating the control volume discretization along the particle radius. The solid black lines and solid black dots represent grid point i , while the dotted black line and white dots represent control volume boundaries. In the magnified view, i is surrounded by an imaginary control volume between the outer boundary OB_i and inner boundary IB_i . The flux is defined as positive for species diffusing out of the particle.

Fig. 4.2 illustrates the CVM discretization. Black dots and solid black lines represent node points, while white dots and dotted black lines represent control volume boundaries. A magnified view of the discretized particle illustrates the 3D nature of spherical shells arising from inner control volume discretization. Several important features of the control volume discretization should be noted:

- i. Concentrations are calculated at the node points only. No concentrations are calculated at the boundaries between control volume elements.
- ii. The concentration profile between nodes is assumed to be linear.
- iii. Concentration gradients are calculated at spherical shell boundaries using concentration values from adjacent nodes.
- iv. The interior boundaries of the control volume shells are located halfway between adjacent nodes.

Let v_i denote the control volume element at node point i . Assume $m_i(t)$, the amount of electrochemically active species [mol] inside v_i at arbitrary time t , can be expressed as a product of the concentration at node point i and the volume of a corresponding spherical shell. Then

$$m_i(t) = \int_{v_i} c_s(r) dV(r) \approx c_s(r_i) \int_{v_i} dV(r) = c_s(r_i) U_i, \quad (4.20)$$

where U_i is the total volume of v_i [m^3]. Mass conservation law in the absence of source term(s) dictates that any change in m_i corresponds to the net-flux via the inner and outer control volume boundaries, *i.e.*

$$\Delta_t m_i(t) = \Delta_t c_{s,i} U_i = (J_i A_i - J_{i-1} A_{i-1}) \Delta t, \quad \text{for } 1 \leq i \leq N \quad (4.21)$$

where J_i represents mass flux through control volume boundaries [$mol\ m^{-2}\ s^{-1}$], Δt is the time step [s] and the symbol Δ_t denotes a change of a variable in time. A_i is the surface area of the i^{th} control volume boundary [m^2] which is defined as

$$A_i = 4\pi \left(r_i + \frac{\Delta r_i}{2} \right)^2, \quad \text{for } 1 \leq i \leq N-1, \quad (4.22)$$

at the surface boundary OB_N as

$$A_N = 4\pi R_0^2, \quad (4.23)$$

and at the center boundary IB_1 as

$$A_0 = 0. \quad (4.24)$$

Note that the absence of source term(s) in Eq. (4.21) is due to the lack of internal species production or consumption *within* the active particles. Now, according to remarks ii and iii, the fluxes at the control volume boundaries can be derived as follows

$$-D_1(c_s) \frac{\partial c_s}{\partial r} \Big|_{r=r_i+\frac{\Delta r_i}{2}} \approx -D_{1,i+1/2} \frac{c_{s,i+1} - c_{s,i}}{r_{i+1} - r_i} = -D_{1,i+1/2} \frac{c_{s,i+1} - c_{s,i}}{\Delta r_i}, \quad (4.25)$$

where $D_{1,i+1/2} = D_1(\frac{c_{s,i+1}+c_{s,i}}{2})$ is the concentration-dependent diffusion coefficient at the control volume boundary [$m^2\ s^{-1}$]. A half-sum is applied because of remarks ii and iv. Substituting Eqs. (4.22) and (4.25) into Eq. (4.21), gives

$$\begin{aligned} & -D_{1,i-\frac{1}{2}} \frac{c_{s,i} - c_{s,i-1}}{\Delta r_{i-1}} \left(r_{i-1} + \frac{\Delta r_{i-1}}{2} \right)^2 \Delta t + D_{1,i+\frac{1}{2}} \frac{c_{s,i+1} - c_{s,i}}{\Delta r_i} \left(r_i + \frac{\Delta r_i}{2} \right)^2 \Delta t \\ & = \frac{U_i}{4\pi} \Delta_t c_{s,i}, \quad \text{for } 2 \leq i \leq N-1. \end{aligned} \quad (4.26)$$

To eliminate the factor 4π from subsequent derivations, let a normalized volume V_i be defined as

$$V_i = \frac{1}{3} \left[\left(r_i + \frac{\Delta r_i}{2} \right)^3 - \left(r_{i-1} + \frac{\Delta r_{i-1}}{2} \right)^3 \right], \quad \text{for } 2 \leq i \leq N-1, \quad (4.27)$$

at the center ($i = 1$) and at the surface boundary ($i = N$), V_1 and V_N are defined as

$$V_1 = \frac{1}{24} \Delta r_1^3, \quad (4.28)$$

$$V_N = \frac{1}{3} \left[R_0^3 - \left(R_0 - \frac{\Delta r_{N-1}}{2} \right)^3 \right]. \quad (4.29)$$

To further economize notations, let variable K_i [m^3] be introduced

$$K_i = D_{1,i+1/2} \frac{\Delta t}{\Delta r_i} \left(r_i + \frac{\Delta r_i}{2} \right)^2, \quad \text{for } 1 \leq i \leq N-1. \quad (4.30)$$

Therefore, taking Eqs. (4.27) and (4.30) into account, Eq. (4.26) can be expressed in terms of K_i and V_i as

$$-K_{i-1} (c_{s,i} - c_{s,i-1}) + K_i (c_{s,i+1} - c_{s,i}) = V_i \Delta_t c_{s,i}, \quad \text{for } 2 \leq i \leq N-1. \quad (4.31)$$

Rearranging Eq. (4.31) gives

$$K_{i-1} c_{s,i-1} - (K_{i-1} + K_i) c_{s,i} + K_i c_{s,i+1} = V_i \Delta_t c_{s,i}, \quad \text{for } 2 \leq i \leq N-1. \quad (4.32)$$

Eq. (4.32) is defined at interior node points. It is possible, starting with the general mass balance expression of Eq. (4.21) and following the steps shown in Eq. (4.25) to (4.32), to obtain expressions for the two remaining boundary cases, $i = 1$ and $i = N$.

At the center (at $i = 1$), there is zero flux through IB_1 according to Eq. (4.3). Furthermore, the surface area at IB_1 is zero according to Eq. (4.24). Applying the general mass balance on v_1 gives

$$D_{1,1+1/2} \frac{c_{s,2} - c_{s,1}}{\Delta r_1} \left(r_1 + \frac{\Delta r_1}{2} \right)^2 \Delta t = V_1 \Delta_t c_{s,1}. \quad (4.33)$$

Finally, Eq. (4.33) expressed in terms of the variable K_i , becomes

$$K_1 (c_{s,2} - c_{s,1}) = V_1 \Delta_t c_{s,1}. \quad (4.34)$$

At the surface (at $i = N$), there is a uniform interfacial flux J . Applying the boundary condition of Eq. (4.2) and the general mass balance on v_N , results in

$$-D_{1,N-1/2} \frac{c_{s,N} - c_{s,N-1}}{\Delta r_{N-1}} \left(r_{N-1} + \frac{\Delta r_{N-1}}{2} \right)^2 \Delta t - J R_0^2 \Delta t = V_N \Delta_t c_{s,N}, \quad (4.35)$$

Finally, introducing the variable K_i into Eq. (4.35) gives

$$-K_{N-1} (c_{s,N} - c_{s,N-1}) - J R_0^2 \Delta t = V_N \Delta_t c_{s,N}. \quad (4.36)$$

Up to this point, the temporal discretization is intentionally omitted because the system of equations, Eqs. (4.32), (4.34), and (4.36) can be solved either by the forward Euler or the backward Euler method.

Now let the superscript j represent the current time step, and $j - 1$ represent the previous time step. Therefore, $\Delta_t c_{s,i} = c_{s,i}(t) - c_{s,i}(t - \Delta t) = c_{s,i}^j - c_{s,i}^{j-1}$. The system of equations, Eqs. (4.32), (4.34), and (4.36) is thus expressed in the backward Euler scheme as

$$-K_{i-1}^j c_{s,i-1}^j + (K_{i-1}^j + K_i^j + V_i) c_{s,i}^j - K_i^j c_{s,i+1}^j = V_i c_{s,i}^{j-1}, \quad (4.37)$$

for $2 \leq i \leq N - 1$

at the center

$$(K_1^j + V_1) c_{s,1}^j - K_1^j c_{s,2}^j = V_1 c_{s,1}^{j-1}, \quad (4.38)$$

and at the surface

$$-K_{N-1}^j c_{s,N-1}^j + (K_{N-1}^j + V_N) c_{s,N}^j = V_N c_{s,N}^{j-1} - J R^2 \Delta t. \quad (4.39)$$

Eqs. (4.37) to (4.39) represent a coupled system of equations since all values at time step j are unknown while values at time step $j - 1$ are known.

4.3.2 Solving the coupled system of equations

As a first step to finding the solution, the coupled system of equations, Eqs. (4.37) to (4.39) is expressed in matrix form, as

$$\mathbf{M} c_s^j = \mathbf{V} c_s^{j-1} - J R_0^2 \Delta t, \quad (4.40)$$

where c^j is a column vector containing concentrations at all node points at time index j , i.e. $c_s^j = (c_{s,1}^j, c_{s,2}^j, \dots, c_{s,N}^j)$, \mathbf{M} is an N -by- N matrix

$$\begin{pmatrix} (K_1^j + V_1) & -K_1^j & 0 & 0 & \cdots & 0 & 0 & 0 \\ -K_1^j & (K_1^j + K_2^j + V_2) & -K_2^j & & & 0 & 0 & 0 \\ 0 & -K_2^j & (K_2^j + K_3^j + V_3) & -K_3^j & \cdots & 0 & 0 & 0 \\ \vdots & \vdots & \vdots & \vdots & \ddots & \vdots & \vdots & \vdots \\ 0 & 0 & 0 & 0 & \cdots & -K_{N-2}^j & (K_{N-2}^j + K_{N-1}^j + V_{N-1}) & -K_{N-1}^j \\ 0 & 0 & 0 & 0 & \cdots & 0 & -K_{N-1}^j & (K_{N-1}^j + V_N) \end{pmatrix},$$

\mathbf{V} is expressed as

$$\mathbf{V} = \begin{pmatrix} V_1 & 0 & \cdots & 0 \\ 0 & V_2 & & \\ \vdots & & \ddots & \\ 0 & 0 & \cdots & V_N \end{pmatrix},$$

and \mathbf{J} is a (column) vector, $(0, 0, \dots, 0, J)^T$, whose only non-zero entry is at the N^{th} point, corresponding to the surface.

\mathbf{M} is a tridiagonal matrix. If $V_i > 0$, a condition that is trivially satisfied by the construction of sequence r as shown in Eq. (4.15) \mathbf{M} is strictly (row) diagonally dominant. By the Levy–Desplanques theorem, \mathbf{M} is non-singular and therefore invertible [34]. The tridiagonal matrix algorithm (TDMA) can thus be applied to solve Eq. (4.40) as a stable and fast solution method [35]. The TDMA, also known as the Thomas algorithm, is a variant of Gaussian elimination, which applies to a diagonally dominant tridiagonal system of N unknowns. Compared to the standard Gaussian elimination or matrix inversion, which require $O(N^3)$ operations to solve, the TDMA only requires $O(N)$ operations [36].

For a constant diffusion coefficient, Eq. (4.40) is linear. The solution c^j is rapidly obtained in a single run of the TDMA. However, for the problem posed above, the diffusion coefficient at time step j is not known *a priori* since D is an implicit function of c^j . Eq. (4.40), therefore, takes the form

$$\mathbf{M}(c_s^j) c_s^j = \mathbf{V} c_s^{j-1} - JR_0^2 \Delta t, \quad (4.41)$$

and represents a nonlinear system of equations. Eq. (4.41) can be iteratively solved by various fixed-point methods such as Newton's method, Jacobi, line-by-line, and Gauss-Seidel. These iterative methods can be used in combination with the TDMA to obtain convergent solutions

[35,37]. Newton's method, in particular, attains quadratic convergence if the initial guess is sufficiently close to the solution [9,37]. Nevertheless, great care must be taken to construct and solve the equation correctly. A poor initial guess may even result in a lack of convergence [37]. Herein, the following iterative scheme (Jacobi) is used

$$\mathbf{M}(c_{s,k-1}^j)c_{s,k}^j = \mathbf{V} c_s^{j-1} - JR_0^2 \Delta t, \quad \text{for } 1 \leq k \leq k_{tot} \quad (4.42)$$

where subscript k denotes the iteration number in a total of k_{tot} iterations. c_k^j is, therefore, the implicit solution obtained after k iterations. The initial value needed for the first iteration is defined as

$$c_{s,0}^j = c_s^{j-1}. \quad (4.43)$$

For $k_{tot} \approx 20$, the fully implicit BECV solution is obtained. It shall be demonstrated that due to the initial condition Eq. (4.43), the first iteration of Eq. (4.42) achieves a stable and approximately accurate solution, which is acceptable in many cases. This solution is referred to as the HBECV. The HBECV is, therefore, a linearization of the concentration-dependent \mathbf{M} , to obtain implicit solutions in a single iteration.

4.3.3 Grid spacing

To accurately determine concentration profiles, many grid points are required. However, more grid points come at considerable computational costs. The accuracy of the CVM for an economical number of grid points depends on the spatial distribution of these points. The choice of grid spacing, however, depends on the nature of the problem and boundary conditions. More points are required at the regions where the concentration profile has steep gradients, which holds at the particle surface boundary.

While the scheme of equations presented in this work allows for variable spacing of grid points, the literature around grid/mesh optimization is very sparse, making it challenging to comprehend the principal factors affecting the optimum grid spacing. To evaluate the different grid-point locations, the following geometric spacing equation is applied

$$r_i = R_0 * \left(1 - \frac{Y^{\frac{N-i}{N-1}} - 1}{Y - 1} \right), \quad 1 \leq i \leq N, \quad (4.44)$$

where Y is the common factor of the geometric series varying between 2 and 20. If $Y = 10$, the logarithmic spacing is obtained, which is the choice in a preceding publication [9]. To evaluate the error in each value of Y , as a function of D_1 and R_0 , a solution obtained from a linear spaced grid of 501 points and $dt = 5$ s is used as a reference solution.

4.4 Results and discussion

The results obtained from the analytical solution method and the numerical solution method are now discussed, starting with the analytical method.

4.4.1 Results of the analytical solution method

A test case of diffusion in a spherical particle is herein used to compare the PSS and MPSS behavior. **Fig. 4.3** shows a test particle undergoing intercalation at a flux j . To compare our results with literature, the parameters used by Liu [20] were adopted for this calculation. **Table 4.1** lists the parameters used.

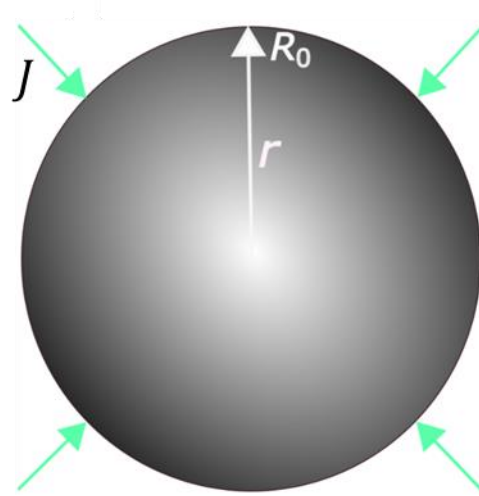


Fig. 4.3. Spherical particle of radius R_0 is used to determine the surface concentration. j is the boundary value flux, and a color gradient is used to illustrate the concentration profile.

Table 4.1. Parameters used in comparing the various analytical expressions.

Parameter	Unit	Description	Value
R_0	m	The radius of the particle	$3.5 \cdot 10^{-6}$
D_1	$m^2 s^{-1}$	Diffusion coefficient	$2.6 \cdot 10^{-10}$
Δt	s	Time step	$5 \cdot 10^{-6}$
J	$mol\ m^{-2}\ s^{-1}$	Interfacial boundary flux	$-1 \cdot 10^{-3}$
$c_{s,0}$	$mol\ m^{-3}$	Initial intercalated concentration	0

Fig. 4.4 shows the behavior of the PSS (solid lines) and MPSS (symbols) at four different simulation times ($t = 5, 50, 250$, and $500\ \mu s$) as a function of M , the number of summation terms. Although the PSS (Eq. (4.4)) and the MPSS (Eq. (4.5)) are both expected to produce identical results, it is evident that the PSS method does not converge to a constant value as time (t) increases. In contrast, the MPSS expression, uniformly convergent at all times and requires fewer terms to reach the steady-state solution. Therefore, the modifications introduced in Eq. (4.5) allow a stable implementation of the PSS method.

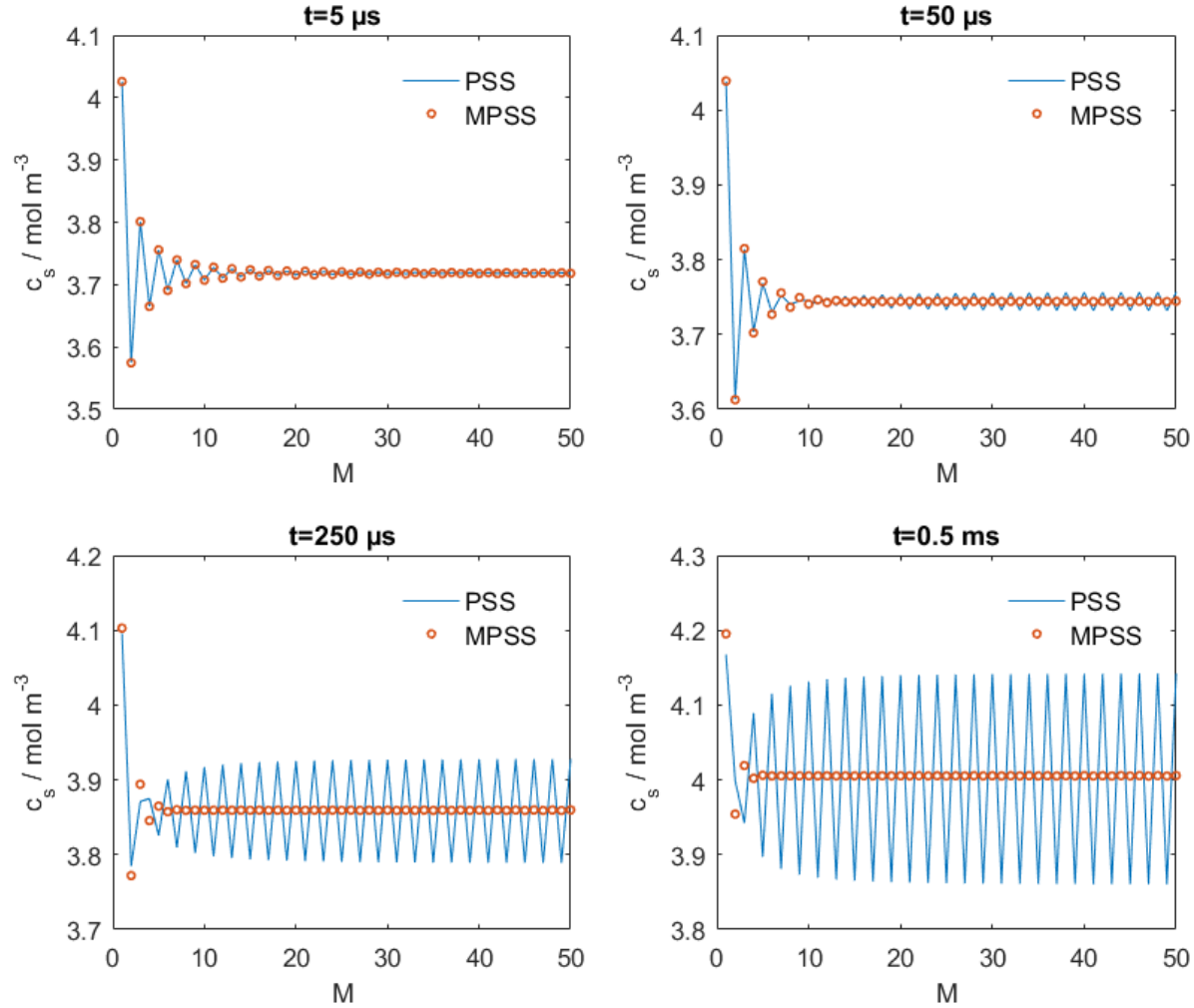


Fig. 4.4. Convergence of the MPSS and PSS methods as a function of M , the number of λ_m terms used in summation. PSS solutions become oscillatory as time increases, while the MPSS method gives uniform convergent solutions at all times.

Nevertheless, the MPSS method is not the most efficient way to calculate the surface concentration. At long simulation time intervals, stored data becomes large, and integrals from $t = 0$ become cumbersome. For this reason, the FMPSS in Eqs. (4.10) and (4.13) is programmed.

Fig. 4.5 shows the comparative speed performance between the two methods as a function of the simulation time. While similar analytical solutions are obtained using either the MPSS or the FMPSS, significant speed gains are achieved in the latter method. The results in **Fig. 4.5** show that the computational runtime per time step using the FMPSS remains constant. At the same time, it evolves linearly for the MPSS method. This behavior implies that the per-step complexity of MPSS is linear with respect to time, *i.e.*, $O(t)$, while that of the FMPSS method is constant, *i.e.*, $O(1)$.

After a simulation period of 0.05 s, the FMPSS method is shown to be approximately three orders of magnitude faster than MPSS. It is, therefore, a fast and uniformly convergent semi-analytical method.

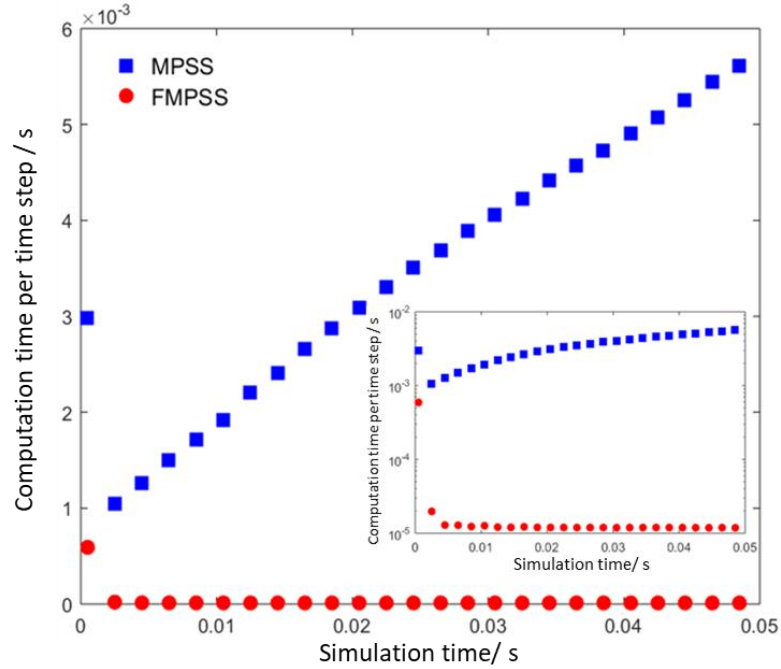


Fig. 4.5. Comparison of computation time using MPSS and FMPSS using parameters listed in **Table 4.1**. The results correspond to $M = 40$. Inset showing the semi-logarithmic plot of computation time. Approximately three orders of magnitude speed improvement is achieved by the FMPSS method.

4.4.2 Results of the numerical solution method

Table 4.2. Parameters used in comparing the various numerical methods.

Parameter	Unit	Description	Value
R_0	m	The radius of the particle	$5 \cdot 10^{-6}$
Δt	s	Time step	5
J	$mol\ m^{-2}\ s^{-1}$	Interfacial boundary flux	$-5.35 \cdot 10^{-5}$
$c_{s,0}$	$mol\ m^{-3}$	Initial intercalated concentration	$2 \cdot 10^4$
$c_{s,max}$	$mol\ m^{-3}$	Maximum concentration	$4.665 \cdot 10^4$

To investigate the accuracy of HBECV, the set of parameters used by Zeng *et al.* [9] is adopted for comparison. **Table 4.2** shows the parameters for $\text{Li}(\text{Ni}_{1/3}\text{Mn}_{1/3}\text{Co}_{1/3})\text{O}_2$ particles used in the referenced work and also here. In addition, the concentration-dependent diffusion coefficient for $\text{Li}(\text{Ni}_{1/3}\text{Mn}_{1/3}\text{Co}_{1/3})\text{O}_2$ used by Wu *et al.* [38] is

$$D_1(c_s) = D_1^{ref} \left[1 + 100 \left(\frac{\hat{C}_{theo}(c_{s,max} - c_s)}{\hat{C}_{prac} \times c_{s,max}} \right)^{\frac{3}{2}} \right], \quad (4.45)$$

where D_1^{ref} is defined as the reference diffusion coefficient of $2 \cdot 10^{-16} \text{ m}^2 \text{ s}^{-1}$, \hat{C}_{theo} is the theoretical capacity of the electrode material ($277.84 \text{ mAh g}^{-1}$) and \hat{C}_{prac} is the practical capacity of the electrode material of 160 mAh g^{-1} .

Fig. 4.6 illustrates the agreement between our results and the literature. After a discharge time $t=400 \text{ s}$, the surface concentration nearly reaches $c_{s,max}$ and thus the end of discharge. For the parameters in **Table 4.2**, a dense mesh of 501 grid points is used to eliminate errors due to spatial discretization. These results validate the BECV, whose solutions are obtained after $k_{tot} = 20$ iterations of the Jacobi method.

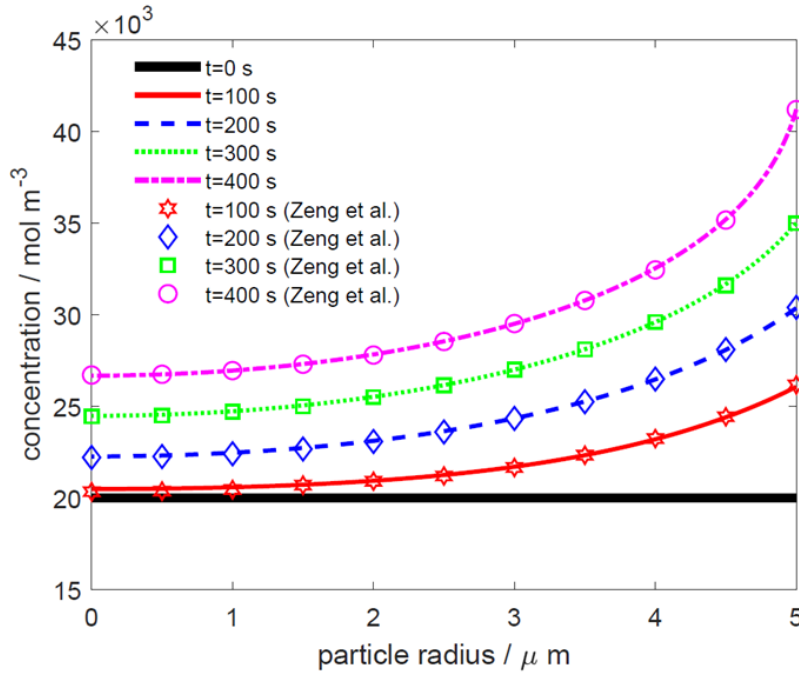


Fig. 4.6. Comparison of the results of the simulated concentration gradients obtained in this work, using the BECV method and results from Zeng *et al.* [21]. Results are obtained using 501 uniformly spaced grid points, using the parameters in **Table 4.2** and Eq. (4.45)

It is interesting to evaluate the effect of reducing k_{tot} because the computation speed increases with fewer iterations. **Fig. 4.7** shows that the relative error in surface concentration progressively increases when k_{tot} decreases. Furthermore, approximately 10 iterations of the Jacobi method are necessary to obtain a fully implicit BECV solution. With regards to fast simulations, the HBECV solution received when $k_{tot} = 1$ is interesting. From these results, the relative error on the surface concentration of the HBECV method is approximately 0.1 %, which is good enough for practical purposes, and moreover, the results are stable. This conclusion validates the HBECV and justifies its use as a fast, stable, and practically accurate method.

A uniform grid of 501 points is nevertheless impractical for use in P2D simulations where the number of grid points is limited. The first step in reducing the number of grid points is to optimize grid spacing. This goal is achieved by changing the grid spacing geometric factor Y in a model with 301 grid points while the solution from the model with a uniform grid of 501 points is used as a reference. The cost function is then determined from the normalized root of squared deviations between these solutions.

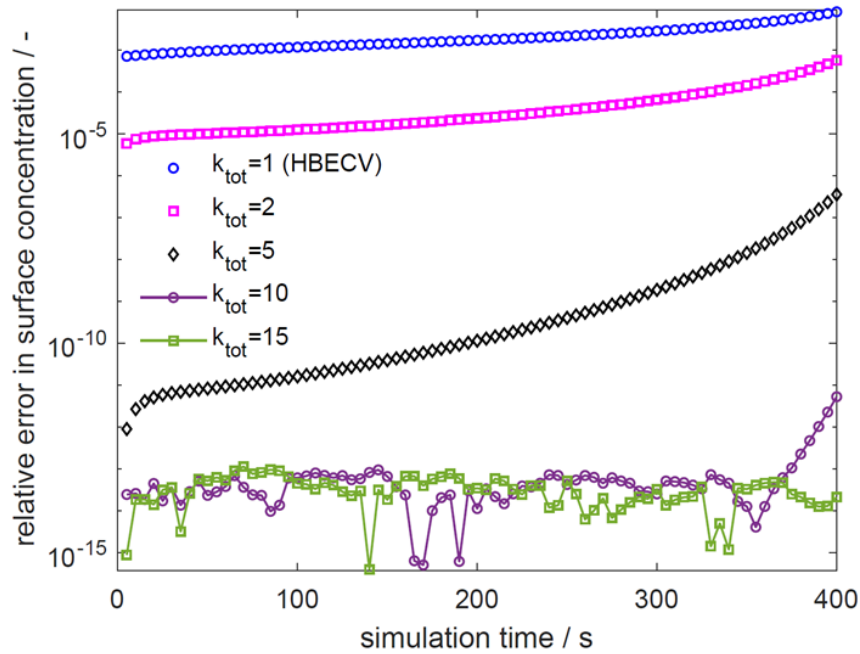


Fig. 4.7. Relative error in surface concentration over 400 s simulation as a function of the number of iterations. The relative error of the HBECV method is compared to the iterative implicit BECV method. 501 uniformly spaced grid points and parameters in **Table 4.2** are used to calculate the surface concentration. As the total number of iterations per time step, k_{tot} increases, the solution converges to the reference solution of 20 iterations.

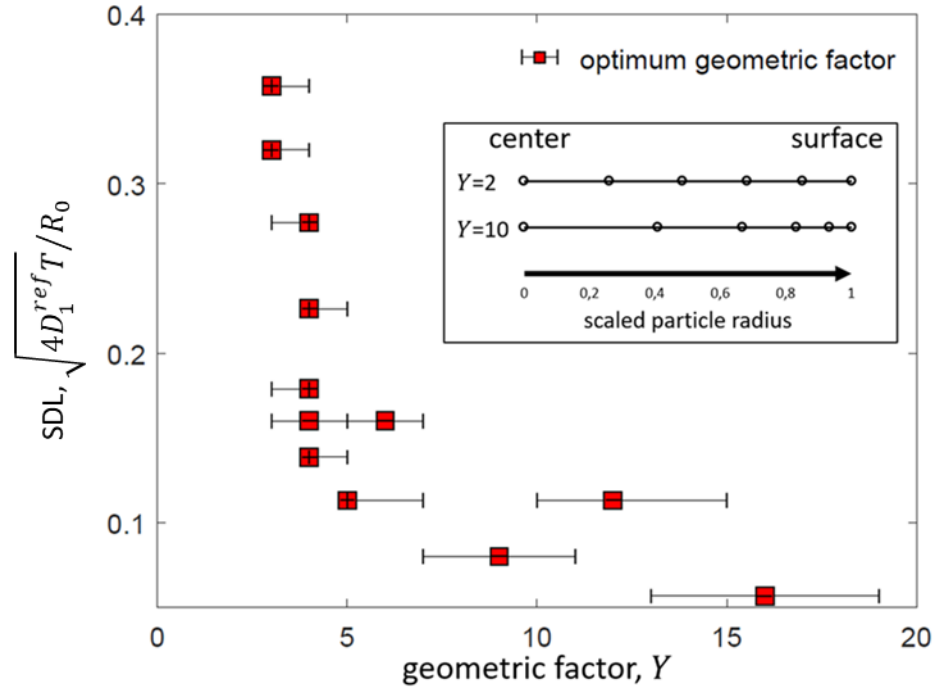


Fig. 4.8. Grid optimization, the effect of the geometric factor (Y) and the scaled diffusion length (SDL). The red squares show the optimum Y (Y_{opt}) for a given SDL. The bars represent variance within 1 % of Y_{opt} . Inset illustrating the grid spacing for $Y = 2$ and $Y = 10$.

However, the optimum grid spacing depends on the value of the diffusion coefficient and the size of the particles. A scaled diffusion length (SDL) is defined as

$$SDL = \sqrt{4D_1^{ref}T/R_0}, \quad (4.46)$$

to group these effects together. **Fig. 4.8** show the effect of the SDL on the optimum grid spacing Y (Y_{opt}). Two regions can be easily identified

- high diffusion length regions where $SDL > 0.1$ and $3 \leq Y_{opt} \leq 6$, and
- low diffusion length regions where $SDL \leq 0.1$ and $Y_{opt} > 6$.

Such a distinction means that for a high diffusion length problem, in which the diffusion length is more than 10% of R_0 , an evenly spaced grid defined by low Y values should be used. On the other hand, for a low diffusion length, which is less than 10% of R_0 , a logarithmic grid spacing, defined by high Y values, is more appropriate. The immediate conclusion is that more points are needed close to the surface only when the diffusion length is low. This conclusion highlights the importance of carefully selecting the grid spacing for a given D_1^{ref} and R_0 values and not rely on

an intuitive feeling of the grid spacing. For the parameters listed in **Table 4.2**, $Y_{opt} = 12$ and the number of grid points distributed by Y_{opt} is defined as N_{opt} .

It is also essential to further reduce N_{opt} to a practical number relevant to P2D modeling. **Fig. 4.9** shows the relative error on surface concentration at $t = 400$ s and $dt = 0.1$ s, as a function of N_{opt} . As expected, the error relative to the fine grid mesh increases as N_{opt} decreases. However, the BECV and the HBECV remarkably converge to the same error when N_{opt} is small. This behavior implies that the spatial discretization error exceeds the linearization error of the HBECV when the number of optimally spaced grid points is below 21. Therefore, based on the results shown in **Fig. 4.9**, the HBECV should be used in battery simulations instead of the more computationally expensive BECV.

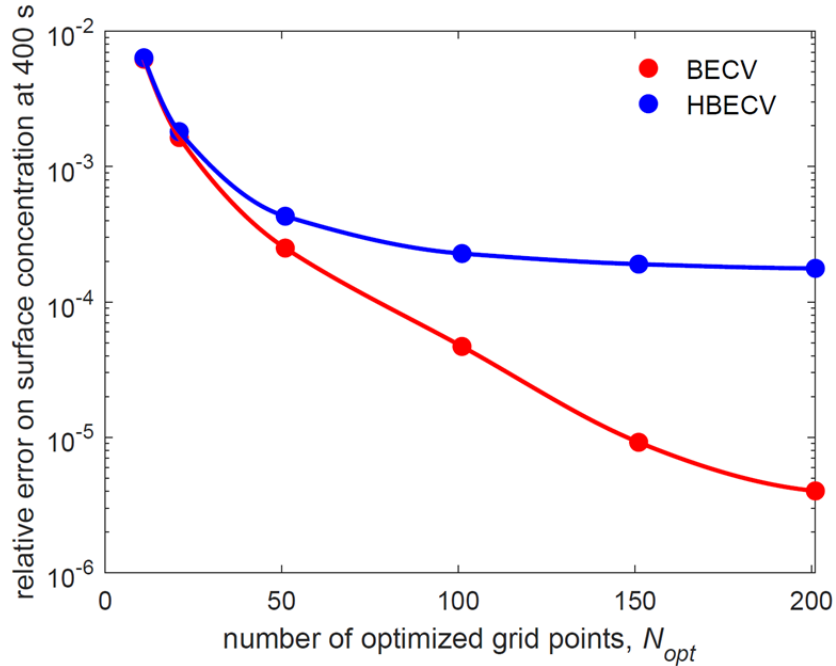


Fig. 4.9. Relative error on surface concentration at 400 s of the BECV and the HBECV as a function of N_{opt} , the number of optimized grid points. The optimum geometric factor, $Y_{opt} = 12$ and time step, $dt = 0.1$ s are used. The reference solution is obtained from 501 uniform grid points and $dt = 0.1$ s.

4.5 Conclusions

Expedient modifications of existing analytical and numerical solution methods for solving the time-dependent diffusion problem in spherical active particles were presented. In the case of a constant diffusion coefficient, fast numerical methods can be applied. However, a solution convergence problem in the pseudo-steady state (PSS) method is encountered in the existing form of the expression. A modified PSS (MPSS) expression, shown herein, produces stable results at all times. However, the MPSS has a linear time complexity, meaning the computation runtime per time step increases linearly as the simulation proceeds. Therefore, a fast MPSS (FMPSS) method is introduced, with constant computation time complexity.

In the case of a variable diffusion coefficient problem, the backward Euler control volume (BECV) and the hybrid backward Euler control volume (HBECV) methods are presented. The implicit scheme of nonlinear equations is herein shown to be strictly diagonally dominant. It can be efficiently solved by the tridiagonal matrix algorithm (TDMA). The fully implicit BECV is shown to require more computations, approximately 10 iterations of the TDMA, to reach a convergency. However, by linearization of the implicit scheme of equations, the HBECV only requires one iteration. Although, in comparison to the BECV method, the error in surface concentration in the HBECV method is around 0.1 %, for a fine grid of 501 points, the error difference decreases when the number of grid points decreases to practical values. It is shown that for a coarse grid of 21 optimally spaced grid points, the error in surface concentrations converges to the same order of magnitude. Such behavior demonstrates that the error due to spatial discretization outweighs the error due to the linearization introduced by the HBECV method. Therefore, the FMPSS and the HBECV are recommended techniques for fast, stable, and accurate battery modeling applications.

References

- [1] The Royal Swedish Academy of Sciences, The Nobel Prize in Chemistry 2019, NobelPrize.Org. (accessed April 14, 2020).
- [2] J. Newman, K.E. Thomas-Alyea, *Electrochemical systems* 3rd Ed., John Wiley & Sons, (2012).
- [3] T.F. Fuller, M. Doyle, J. Newman, Simulation and Optimization of the Dual Lithium Ion Insertion Cell, *J. Electrochem. Soc.* **141** (1994) 1–10. <https://doi.org/10.1149/1.2054684>.
- [4] R. Zhao, J. Liu, J. Gu, The effects of electrode thickness on the electrochemical and thermal characteristics of lithium ion battery, *Applied Energy*. **139** (2015) 220–229. <https://doi.org/10.1016/j.apenergy.2014.11.051>.
- [5] C.M. Doyle, *Design and Simulation of Lithium Rechargeable Batteries*, PhD. Thesis, University of California at Berkeley (1995)
- [6] B. Paxton, J. Newman, Modeling of Nickel/Metal Hydride Batteries, *J. Electrochem. Soc.* **144** (1997) 3818–3831. <https://doi.org/10.1149/1.1838098>.
- [7] H.S. Carslaw, J.C. Jaeger, *Conduction of heat in solids*: Oxford Science Publications, Oxford, England (1959).
- [8] V. Ramadesigan, V. Boovaragavan, J.C. Pirkle, V.R. Subramanian, Efficient Reformulation of Solid-Phase Diffusion in Physics-Based Lithium-Ion Battery Models, *J. Electrochem. Soc.* **157** (2010) A854–A860. <https://doi.org/10.1149/1.3425622>.
- [9] Y. Zeng, P. Albertus, R. Klein, N. Chaturvedi, A. Kojic, M.Z. Bazant, J. Christensen, Efficient Conservative Numerical Schemes for 1D Nonlinear Spherical Diffusion Equations with Applications in Battery Modeling, *J. Electrochem. Soc.* **160** (2013) A1565–A1571. <https://doi.org/10.1149/2.102309jes>.
- [10] Q. Zhang, R.E. White, Comparison of approximate solution methods for the solid phase diffusion equation in a porous electrode model, *Journal of Power Sources* **165** (2007) 880–886.
- [11] M. Guo, R.E. White, An approximate solution for solid-phase diffusion in a spherical particle in physics-based Li-ion cell models, *Journal of Power Sources* **198** (2012) 322–328. <https://doi.org/10.1016/j.jpowsour.2011.08.096>.
- [12] V.R. Subramanian, V.D. Diwakar, D. Tapriyal, Efficient Macro-Micro Scale Coupled Modeling of Batteries, *J. Electrochem. Soc.* **152** (2005) A2002–A2008. <https://doi.org/10.1149/1.2032427>.
- [13] Z. Deng, L. Yang, H. Deng, Y. Cai, D. Li, Polynomial approximation pseudo-two-dimensional battery model for online application in embedded battery management system, *Energy* **142** (2018) 838–850. <https://doi.org/10.1016/j.energy.2017.10.097>.
- [14] V.R. Subramanian, J.A. Ritter, R.E. White, Approximate Solutions for Galvanostatic Discharge of Spherical Particles I. Constant Diffusion Coefficient, *J. Electrochem. Soc.* **148** (2001) E444–E449. <https://doi.org/10.1149/1.1409397>.
- [15] C.Y. Wang, W.B. Gu, B.Y. Liaw, Micro-Macroscopic Coupled Modeling of Batteries and Fuel Cells I. Model Development, *J. Electrochem. Soc.* **145** (1998) 3407–3417. <https://doi.org/10.1149/1.1838820>.
- [16] C.Y. Wang, V. Srinivasan, Computational battery dynamics (CBD)—electrochemical/thermal coupled modeling and multi-scale modeling, *Journal of Power Sources* **110** (2002) 364–376. [https://doi.org/10.1016/S0378-7753\(02\)00199-4](https://doi.org/10.1016/S0378-7753(02)00199-4).

- [17] K. Smith, C.-Y. Wang, Solid-state diffusion limitations on pulse operation of a lithium ion cell for hybrid electric vehicles, *Journal of Power Sources* **161** (2006) 628–639. <https://doi.org/10.1016/j.jpowsour.2006.03.050>.
- [18] N.Y. Ölçer, On the theory of conductive heat transfer in finite regions, *International Journal of Heat and Mass Transfer* **7** (1964) 307–314. [https://doi.org/10.1016/0017-9310\(64\)90106-1](https://doi.org/10.1016/0017-9310(64)90106-1).
- [19] N.Y. Ölçer, On the theory of conductive heat transfer in finite regions with boundary conditions of the second kind, *International Journal of Heat and Mass Transfer* **8** (1965) 529–556. [https://doi.org/10.1016/0017-9310\(65\)90043-8](https://doi.org/10.1016/0017-9310(65)90043-8).
- [20] S. Liu, An analytical solution to Li/Li⁺ insertion into a porous electrode, *Solid State Ionics* **177** (2006) 53–58. <https://doi.org/10.1016/j.ssi.2005.09.053>.
- [21] Z. Chu, X. Feng, L. Lu, J. Li, X. Han, M. Ouyang, Non-destructive fast charging algorithm of lithium-ion batteries based on the control-oriented electrochemical model, *Applied Energy* **204** (2017) 1240–1250. <https://doi.org/10.1016/j.apenergy.2017.03.111>.
- [22] Y. Zhao, S.-Y. Choe, A highly efficient reduced order electrochemical model for a large format LiMn₂O₄/Carbon polymer battery for real time applications, *Electrochimica Acta* **164** (2015) 97–107. <https://doi.org/10.1016/j.electacta.2015.02.182>.
- [23] J. Mao, W. Tiedemann, J. Newman, Simulation of temperature rise in Li-ion cells at very high currents, *Journal of Power Sources* **271** (2014) 444–454. <https://doi.org/10.1016/j.jpowsour.2014.08.033>.
- [24] N. Kazemi, D.L. Danilov, L. Haverkate, N.J. Dudney, S. Unnikrishnan, P.H.L. Notten, Modeling of all-solid-state thin-film Li-ion batteries: Accuracy improvement, *Solid State Ionics* **334** (2019) 111–116. <https://doi.org/10.1016/j.ssi.2019.02.003>.
- [25] L.H.J. Raijmakers, D.L. Danilov, R.-A. Eichel, P.H.L. Notten, An advanced all-solid-state Li-ion battery model, *Electrochimica Acta* **330** (2020) 135147. <https://doi.org/10.1016/j.electacta.2019.135147>.
- [26] J. Christensen, J. Newman, Stress generation and fracture in lithium insertion materials, *J Solid State Electrochem.* **10** (2006) 293–319. <https://doi.org/10.1007/s10008-006-0095-1>.
- [27] S. Motupally, C.C. Streinz, J.W. Weidner, Proton Diffusion in Nickel Hydroxide Films Measurement of the Diffusion Coefficient as a Function of State of Charge, *J. Electrochem. Soc.* **142** (1995) 1401–1408. <https://doi.org/10.1149/1.2048589>.
- [28] S. Motupally, C.C. Streinz, J.W. Weidner, Proton Diffusion in Nickel Hydroxide Prediction of Active Material Utilization, *J. Electrochem. Soc.* **145** (1998) 29–34. <https://doi.org/10.1149/1.1838205>.
- [29] R. A. Shakoor, D.-H. Seo, H. Kim, Y.-U. Park, J. Kim, S.-W. Kim, H. Gwon, S. Lee, K. Kang, A combined first principles and experimental study on Na₃V₂(PO₄)₂F₃ for rechargeable Na batteries, *Journal of Materials Chemistry* **22** (2012) 20535–20541. <https://doi.org/10.1039/C2JM33862A>.
- [30] Z. Liu, Y.-Y. Hu, M.T. Dunstan, H. Huo, X. Hao, H. Zou, G. Zhong, Y. Yang, C.P. Grey, Local Structure and Dynamics in the Na Ion Battery Positive Electrode Material Na₃V₂(PO₄)₂F₃, *Chem. Mater.* **26** (2014) 2513–2521. <https://doi.org/10.1021/cm403728w>.
- [31] A.N. Ford Versypt, R.D. Braatz, Analysis of finite difference discretization schemes for diffusion in spheres with variable diffusivity, *Computers & Chemical Engineering* **71** (2014) 241–252. <https://doi.org/10.1016/j.compchemeng.2014.05.022>.

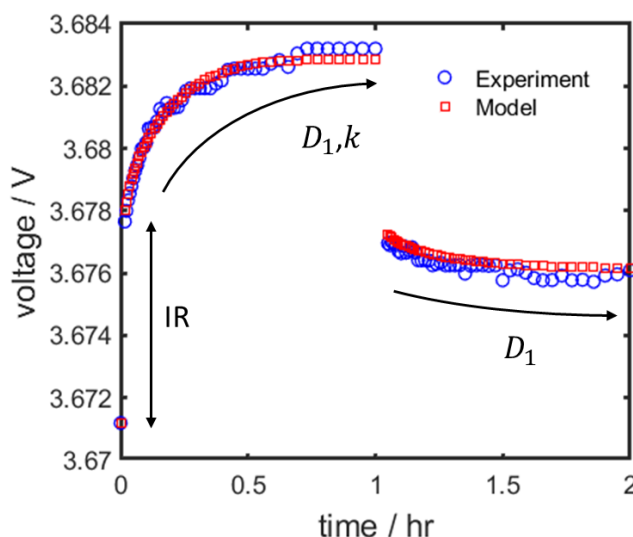
- [32] H.P. Langtangen, Finite difference methods for diffusion processes, University of Oslo. (2013).
- [33] P.C. Urisanga, D. Rife, S. De, V.R. Subramanian, Efficient Conservative Reformulation Schemes for Lithium Intercalation, *J. Electrochem. Soc.* **162** (2015) A852–A857. <https://doi.org/10.1149/2.0061506jes>.
- [34] O. Taussky, A Recurring Theorem on Determinants, *The American Mathematical Monthly* **56** (1949) 672–676. <https://doi.org/10.1080/00029890.1949.11990209>.
- [35] S. Patankar, Numerical heat transfer and fluid flow, CRC press, 2018.
- [36] N.J. Higham, Efficient Algorithms for Computing the Condition Number of a Tridiagonal Matrix, *SIAM J. Sci. and Stat. Comput.* **7** (1986) 150–165. <https://doi.org/10.1137/0907011>.
- [37] S.D. Conte, C. De Boor, Elementary numerical analysis: an algorithmic approach, SIAM, 2017.
- [38] S.-L. Wu, W. Zhang, X. Song, A.K. Shukla, G. Liu, V. Battaglia, V. Srinivasan, High Rate Capability of $\text{Li}(\text{Ni}_{1/3}\text{Mn}_{1/3}\text{Co}_{1/3})\text{O}_2$ Electrode for Li-Ion Batteries, *J. Electrochem. Soc.* **159** (2012) A438–A444. <https://doi.org/10.1149/2.062204jes>.

CHAPTER 5

DETERMINATION OF DIFFUSION COEFFICIENTS AND CHARGE TRANSFER RATE CONSTANTS BY GITT

Abstract

Chapter 4 introduced efficient methods to solve the solid-state diffusion problem in spherical particles. In this Chapter, these methods are used to simulate SIB electrode active particles in a P2D model setup. By comparing half-cell experimental and simulation results of galvanostatic intermittent titration technique (GITT) data, a method to optimize and determine electrode parameters such as the solid-state diffusion coefficient (D_1) and the charge transfer rate constant (k) is herein shown. This method is a significant departure from classical analytical approaches, which up till now were only based on simplified expressions. It is shown that these classical methods are inherently unsuitable for porous battery electrodes and generally lead to inaccurate results. In contrast, D_1 and k obtained using the P2D GITT model are accurately validated by agreement with experimental data.



Parts of this Chapter have been published as:

K Chayambuka, G Mulder, DL Danilov, PHL Notten, Determination of state-of-charge dependent diffusion coefficients and kinetic rate constants of phase changing electrode materials using physics-based models, *Journal of Power Sources Advances* **9** (2021), 100056. <https://doi.org/10.1016/j.powera.2021.100056>

5.1 Introduction

Understanding internal battery dynamics, in particular, the charge transport mechanisms in porous electrodes, is fundamental for building better batteries. Within LIB and SIB electrodes, solid-state diffusion is usually the slowest and thus rate-determining process. Knowledge of the solid-state diffusion coefficients (D_1) and charge transfer constants (k) is therefore fundamental in designing battery electrodes for optimized power and energy efficiency. As a result, it is important to develop experimentally accurate and validated characterization methods to determine these parameters.

State-of-the-art electroanalytical techniques to determine D_1 and k in battery electrode materials include, slow scan rate cyclic voltammetry (SSCV) [1], EIS [2], potentiostatic intermittent titration technique (PITT) [3–7], and galvanostatic intermittent titration technique (GITT) [8,9]. These techniques generally consist of displacing the electrochemical system from a state of equilibrium by imposing a current step, in either constant voltage (CV) or constant current (CC), while simultaneously measuring the voltage as a function of time. Each technique has characteristic input and output parameters, from which the electrode capacity and diffusion time constants (τ_d) are determined [10].

D_1 and k determined by each of the aforementioned electroanalytical techniques are known to vary by orders of magnitude [2,6,11]. This spread is primarily because of the different time scales at which the techniques are most accurate and the implicit assumptions in the analytical models used to derive the parameters. For example, EIS is most accurate in the frequency range of $5 \times 10^{-3} - 1 \times 10^5$ Hz, whereas the frequency range for $D_1 \approx 1 \times 10^{-14}$ [$\text{m}^2 \text{s}^{-1}$] is generally < 1 mHz [2,12]. Such measurements take several minutes and even hours, which results in high noise to EIS scan ratio. Most parameter discrepancies are not, however, inherent to the different experimental techniques themselves, since in most cases, the experiments are repeatable. However, the simplified analytical methods which are often used to derive the relevant parameters are a frequent source of error. In most cases, the analytical techniques are applied without careful thought, disregarding the underlying phenomena and experimental conditions.

The most common electroanalytical technique to determine D_1 and k is the GITT, which was first proposed by Weppner and Huggins in 1977 [8]. GITT starts with a cell in which electrodes have an equilibrium potential. A galvanostatic/CC pulse is then applied for a short period of time,

while the system voltage response is followed in real time. After the CC period is terminated, the cell is set in the open-circuit voltage (OCV) mode, and the voltage relaxation is recorded. The OCV of the cell approaches the equilibrium voltage in steady-state. Ideally, the GITT procedure is performed in a three-electrode half-cell configuration, in which the working electrode (WE) is composed of the electrode material under investigation, a metallic counter electrode (CE) and a reference electrode (RE) of the first kind. **Fig. 5.1** illustrates a three-electrode SIB half-cell configuration for GITT measurements. The Na reference electrode (Na-RE) is positioned in the vicinity of the NVPF WE to obviate the overpotential contributions from either the electrolyte or Na CE and thus obtain accurate measurements of the NVPF potential.

In developing a simplified analytical model for GITT measurements, Weppener *et al.* introduced several assumptions regarding electrochemical charge transport pathways and system dimensions. These include [7,13]:

- (i) Diffusion occurs across a 1-dimensional plane of a dense electrode geometry.
- (ii) Diffusion in the electrode is governed by Fick's laws and occurs within a very thin film close to the electrode/electrolyte interface (this assumes a semi-infinite medium).
- (iii) Concentration profiles in the electrolyte are considered negligible.
- (iv) The diffusion coefficient remains constant during a single pulse and subsequent relaxation period.
- (v) There are no phase transformations influencing the electrode diffusion and charge transfer kinetics.
- (vi) Volume and porosity changes are negligible.
- (vii) Overpotentials in the electrolyte and at the electrode/electrolyte interface are negligible.
- (viii) Electrochemical double-layer capacitances are ignored.

Based on these assumptions, the analytical expression for the diffusion coefficient following a GITT perturbation has been expressed as [14]

$$D_1 = \frac{4}{\pi\tau} \left(\frac{I V_m}{FA} \right)^2 \left(\frac{dU/dy}{dV/d\sqrt{\tau_{cc}}} \right)^2, \quad \forall \tau \ll L_m^2/D_1 \quad (5.1)$$

where D_1 is the diffusion coefficient inside the electrode material [$\text{m}^2 \text{s}^{-1}$], I the current during the GITT pulse [A], V_m the molar volume of the active material [$\text{m}^3 \text{mol}^{-1}$], F the Faraday's constant 95485 [C mol^{-1}], A the porous electrode active surface area [m^2], U and V are the electrode equilibrium potential and electrode potential during the CC pulse, respectively [V], τ_{cc}

the CC pulse duration [s], y the electrode state-of-charge (SOC) based on stoichiometry [-] and L_m is the thickness of the active material [m]. The limiting condition for τ , i.e. $\tau \ll L_m^2/D$, is necessary to satisfy the boundary conditions and assumptions for (i) and (ii) above.

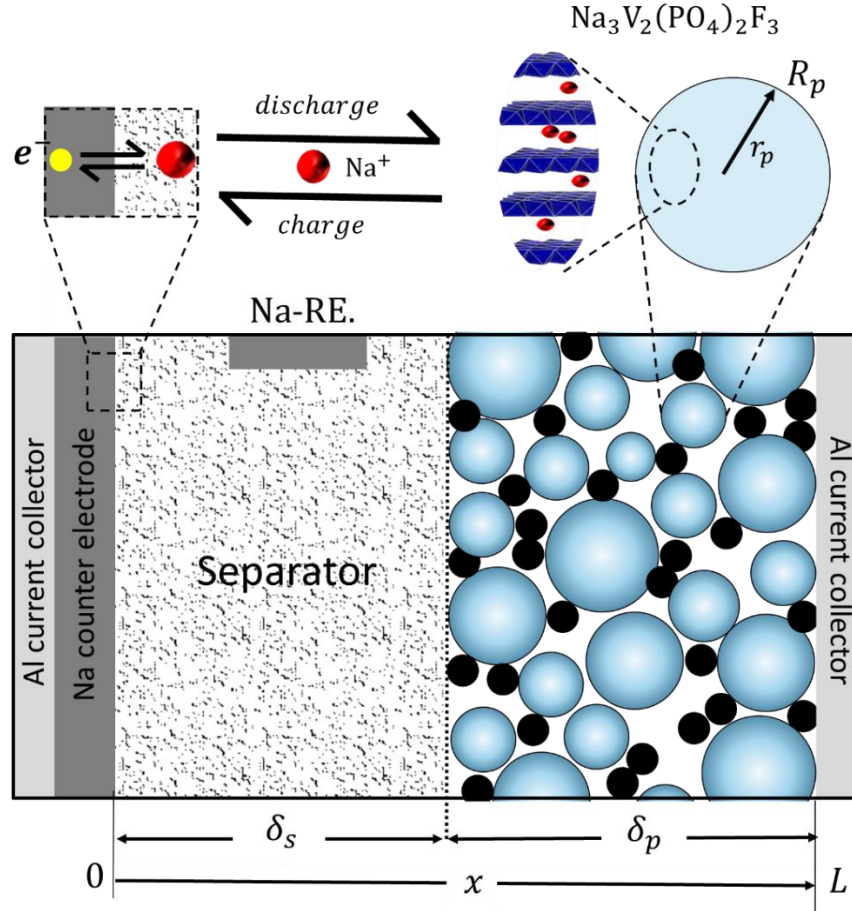


Fig. 5.1. Three electrode half-cell setup used in GITT experiments. The blue circles represent the NVPF active electrode material, and the black circles represent the carbon-based conductive filler. At the particle scale, the charge insertion mechanisms are shown in more detail at the electrode interface. The red and yellow spheres represent sodium cations and electrons, respectively.

Based on the aforementioned model assumptions, Eq. (5.1) is evidently not ideal for modern-day porous battery electrodes. This is because porous battery electrodes are composed of a macro-homogeneous mixture of spherical, micron-size active particles and electrolyte phase. This fundamentally differs from the description of a monolithic phase or "single-slab" active material used to derive Eq. (5.1). In addition, the diffusion time constant in spherical particles with radius (R_p) where $\tau'_d = R_p^2/4D_1$ is, in fact, four times less than $\tau_d = L_m^2/D_1$, the diffusion time constant

in a one-dimensional plane with thickness (L_m). As a result, mass transport in spherical, micron-sized active particles cannot be assumed to occur exclusively within a thin interfacial layer. Finally, concentration profiles and current distributions across the entire electrode thickness and electrolyte cannot be ignored.

Using porous battery electrodes, it is therefore practically impossible to create experimental conditions to satisfy the fundamental assumptions for Eq. (5.1). The best approximation for such a single-slab electrode would be a thin-film active material with a solid-state electrolyte. Moreover, it has proved problematic to confidently determine the A and V_m parameters for different electrode materials [15,16]. While there have been notable efforts to derive analytical GITT solutions for porous battery electrodes [17], it is scientifically prudent to forego the unnecessary simplifying assumptions and determine D_1 and k parameters using numerical models.

The application of numerical P2D models to analyze GITT can be traced back to 2009 [13,18–20]. P2D models use coupled, non-linear PDEs to describe mass transport and kinetics in porous battery electrodes. Dees *et al.* [13] developed a P2D model to analyze GITT experimental data for a Li//LiNi_{0.8}Co_{0.15}Al_{0.05}O₂ battery. Bernardi *et al.* [20] similarly applied a P2D model built in COMSOL Multiphysics® to analyze GITT data. In general, the GITT model predictions during (dis)charge pulses and subsequent relaxations show reasonable agreement with experimental data. These pioneering reports demonstrate the usefulness of physics-based models as GITT analytical tools. Nevertheless, the P2D GITT models lacked a clear parameter optimization strategy and they were only applied on a few selected points across the full SOC range. In addition, the experimental setups lacked a RE in the full cell battery configurations.

Surprisingly, however, the increased adoption of P2D GITT models in more recent studies has been underwhelming. To realize P2D GITT models' full potential, they must be available in openly accessible environments to allow experimentalist to analyze their results quickly. The recent development of PyBaMM, an open-access Python-based P2D model, is, in this regard, commendable [21]. In addition, the models should determine the unknown parameters at different SOC. Finally, the P2D GITT models should be equipped with optimization strategies to determine the D_1 and k parameters at different SOC, which is crucial for understanding phase transformations.

In this Chapter, a MATLAB® based P2D GITT model coupled with grid search optimization is used as a strategy to derive the D_1 and k parameters as a function of the transferred charge,

which is equivalent to the electrode/battery SOC. A three-electrode SIB half-cell based on an NVPF cathode/positive electrode, a Na CE, and a Na-RE is used to determine the GITT experimental data. Because of the high accuracy, experimental validation, and ease of parameter optimization, the P2D GITT model is a recommended analytical GITT method.

5.2 Experimental

PAT-Cells (EL-Cell GmbH, Hamburg, Germany) were used as electrochemical test cells. A PAT-Cell is composed of an 18 mm diameter PAT-core, in which battery electrodes can be assembled. Components of the PAT-core include a factory-built separator (FS-5P, Freudenberg Viledon FS 2226E + Lydall Solupor 5P09B) and a preassembled Na-RE

Na and NVPF electrodes in an electrolyte composed of 1 M NaPF₆ dissolved in ethylene carbonate (EC) and propylene carbonate (PC), EC_{0.5}:PC_{0.5} (w/w) were thus assembled into a half-cell configuration in an argon-filled glove box. The NVPF electrodes used had single-side mass loadings of 12 mg cm⁻². These were produced during the EU-funded NAIADES project and were supplied by the manufacturer (SAFT/CEA) [22,23]. The average electrode thickness was measured by a digital-micrometer screw gauge (Helios Preisser, Digi-Met). The particle size distributions were determined from scanning electron microscopy (SEM) micrographs obtained on Quanta FEG 650 (FEI, USA) (See **Fig. 6.3**)

After assembly in the glove box, the PAT-Cells were hermetically sealed and placed in a climate chamber at 25 °C. GITT was performed on the half-cells at 25 °C. Cell voltage measurements were recorded using a Maccor® automated cycling equipment (Model 4200), and cycling programs were configured in Maccor® standard test system software (MacTest 32). The cells initially underwent five formation cycles at a CC of 0.1 mA (0.039 mA cm⁻², C/30) and a reversible electrode capacity of 3.1 mAh was obtained in the voltage range of 3.0 to 4.3 V. The formation stage allows the growth of a protective layer at the electrode surface and results in stable cycles [24]. After the formation stage, the cells were discharged to 3.0 V in the CV mode for 3 hours to ensure a fully discharged starting point for all GITT cycles.

30 GITT steps, comprised of a CC charge of 0.1 mA until the cell capacity reached 0.1 mAh followed by an OCV relaxation for 1 hour, were applied. Because Coulomb counting was used to define the pulse breaks (and not time), the total pulse duration was approximately 1 hour. A low

charging current was applied to avoid high overpotentials and multiple parameter sensitivity. Besides, a long current pulse duration of 1 hour is necessary to eliminate the double-layer capacitance effects, which are not included in the present P2D model. Therefore, based on these experimental conditions, only the equilibrium potential, the charge transfer rate constant, and the solid-state diffusion coefficient are the sensitive parameters to the model voltage response.

5.3 Model

A P2D GITT model consisting of a set of coupled partial differential equations is coded in MATLAB. The model considered a CC pulse of $i_{tot} = 0.039 \text{ mA cm}^{-2}$ (C/30) applied for 1 hour, followed by an OCV relaxation for 1 hour.

Table 5.1 summarizes the set of equations used in the half-cell model. The equations and boundary conditions were discretized using backward and forward difference schemes. Variables c , φ , and i describe the concentration, electric potential, and current, respectively. Subscripts 1 and 2 in the variable symbols represent the phase in which the variable is defined, where 1 and 2 represent the solid and liquid electrolyte phase, respectively. Subscripts p and s represent the domain/region in which the variable is defined, where p and s represent the positive electrode and separator regions, respectively. In the P2D model, a distinction is thus made between the electronic current density in the positive electrode ($i_{1,p}$) and ionic current density ($i_{2,p}$). Both $i_{1,p}$ and $i_{2,p}$ add up to the total applied current density (i_{tot}) by charge conservation. Similarly, $\varphi_{1,p}$ and $\varphi_{2,p}$ represent the potential in the solid and electrolyte phase, respectively.

In the NVPF active particles, mass transport is described by Fick's second law, which determines the concentration $c_{1,p}$ and the average concentration $\bar{c}_{1,p}$ in time. Analytical and numerical methods can be applied to solve the solid-state diffusion problem with Neumann flux boundary conditions [25]. In this model, the hybrid backward Euler control volume method is used, which was introduced in Chapter 4 [26]. The NVPF electrode equilibrium potential (EMF), U_p is further determined by linear interpolation between two successive GITT relaxation endpoints.

Table 5.1. Summary of equations used in the P2D GITT model.

Model	Expression	Eq.	Boundary conditions
NVPF (positive) electrode $\delta_s \leq x \leq L$			
Mass balance in electrolyte	$\frac{\partial c_2}{\partial t} = \frac{\partial}{\partial x} \left(D_{2,p}^{eff} \frac{\partial c_2}{\partial x} \right) + (1 - t_+) a_p j_p$	(5.2)	$\frac{\partial c_2}{\partial x} \Big _{x=L} = 0$
Potential in electrolyte	$i_{2,p} = -\kappa_p^{eff} \frac{\partial \varphi_{2,p}}{\partial x} + \frac{\kappa_p^{eff} RT}{F} (1 - 2t_+) \cdot \nabla \ln c_2$	(5.3)	
Potential in solid	$i_{1,p} = -\sigma_p^{eff} \frac{\partial \varphi_{1,p}}{\partial x}$	(5.4)	
Charge conservation	$i_{tot} = i_{1,p} + i_{2,p}$	(5.5)	
Surface flux	$a_p j_p F = \frac{\partial i_{2,p}}{\partial x}$	(5.6)	$i_{2,p} \Big _{x=\delta_s} = i_{tot}$ $i_{2,p} \Big _{x=L} = 0$
Electrode kinetics	$j_p = j_{0,p} \left[\frac{c_{1,p}^s}{\bar{c}_{1,p}} \exp \left(\frac{\alpha F}{RT} \eta_p^{ct} \right) - \frac{c_{1,p}^{max} - c_{1,p}^s}{c_{1,p}^{max} - \bar{c}_{1,p}} \frac{c_2}{\bar{c}_2} \exp \left(-\frac{(1-\alpha)F}{RT} \eta_p^{ct} \right) \right]$	(5.7)	
Exchange current	$j_{0,p} = F k_p (c_{1,p}^{max} - \bar{c}_{1,p})^{\alpha_a} (c_2)^{\alpha_a} (\bar{c}_{1,p})^{\alpha_c}$	(5.8)	
Overpotential	$\eta_m^{ct} = \varphi_{1,p} - \varphi_{2,p} - U_p(c_{1,p}^s, T)$	(5.9)	
Fick's second law	$\frac{\partial c_{1,p}}{\partial t} = \frac{1}{r_p^2} \frac{\partial}{\partial r_p} \left(D_{1,p} r_p^2 \frac{\partial c_{1,p}}{\partial r_p} \right)$	(5.10)	$\frac{\partial c_{1,p}}{\partial r_p} \Big _{r=0} = 0$ $-D_{1,p} \frac{\partial c_{1,p}}{\partial r_p} \Big _{r_p=R_p} = j_p$
Separator (dilute solution theory) $0 \leq x \leq \delta_s$			
Potential distribution	$i_{tot} = i_{2,s} = -\kappa_s^{eff} \frac{\partial \varphi_{2,s}}{\partial x} + \frac{\kappa_s^{eff} RT}{F} (1 - 2t_+) \cdot \nabla \ln c_2$	(5.11)	$\varphi_{2,s} \Big _{x=0} = 0$
Fick's second law	$\frac{\partial c_2}{\partial t} = \frac{\partial}{\partial x} \left(D_{2,s}^{eff} \frac{\partial c_2}{\partial x} \right)$	(5.12)	$\frac{\partial c_2}{\partial x} \Big _{x=0} = -\frac{i_{tot} (1 - t_+)}{F D_{2,s}^{eff}}$
Battery voltage			
RE Potential	$\varphi_{1,ref} = \frac{RT}{F} \ln \left(\frac{c_2 _{x=0}}{c_2^{eq}} \right)$	(5.13)	
Battery voltage	$V_{bat} = \varphi_{1,p} \Big _{x=L} - \varphi_{1,ref}$	(5.14)	

The porous electrode surface area per unit volume a_p [m^{-1}] is calculated as

$$a_p = \frac{3(1 - \epsilon_p^e - \epsilon_p^f)}{R_p} \quad (5.15)$$

where R_p is the mean radius of the NVPF active particles [m] and ϵ_p^e and ϵ_p^f are the electrolyte and additive filler volume fractions, respectively [-]. ϵ_p^f includes volume fractions the binder and carbon conductive filler, the non-active constituents of the NVPF electrode.

The GITT half-cell voltage (V_{cell}) is finally calculated from the difference between the NVPF electrode potential and the RE potential ($\phi_{1,ref}$) [V]. The advantage of the Na-RE is that it does not introduce additional unknown parameters of the kinetics of the Na^+/Na CE to the model. This property is convenient in limiting the number of unknowns. **Table 5.2** lists the parameters for the three-electrode half-cell used in the P2D GITT model. Electrode parameters were either measured, optimized, or taken from literature. Separator properties were obtained from the manufacturer (EL Cell). The electrolyte properties were model-derived using the AEM software version. 2.19.1 [27].

The initial particles' concentration for each GITT step is calculated based on the electrode average cumulative capacity updated after each step. The only unknown parameters are, therefore, $D_{1,p}$ the solid-state diffusion coefficient in NVPF particles [$m^2 s^{-1}$] and k_p the charge transfer rate constant in NVPF [$m^{2.5} mol^{-1.5} s^{-1}$]. First, a range of expected values is determined. This is achieved by 'trial and error' to determine the upper and lower parameter boundaries. Then a set of evenly spaced values is selected from this range. By taking all pair combinations of $D_{1,p}$ and k_p and calculating the least-squared difference between experimental and model cell voltage (V_{cell}), a 2-dimensional grid of the least-squared difference is obtained. The optimum $D_{1,p}$ and k_p combination is then determined from the global minimum on this grid. This procedure is repeated for each GITT step. The estimation error range is finally determined from the range of $D_{1,p}$ and k_p combinations which result in 10 % variation from the optimum combination. Because the model can run fast, approximately 2 seconds for each GITT charge and relaxation, optimized results can be obtained in a reasonable time.

Table 5.2. Physical and electrochemical properties of the Na//NVPF half-cell.

Parameter	Unit	Description	Value	Reference
Physical properties				
δ_s	μm	Separator thickness	220	El cell
δ_p	μm	NVPF positive electrode thickness	68	measured
R_p	μm	The radius of NVPF particles	0.69	measured
A	cm^2	Electrode geometric surface area	2.545	measured
ϵ_p^e	-	Electrode porosity	0.23	optimized
ϵ_p^f	-	Binder and conductive filler fraction	0.22	optimized
ϵ_s^e	-	Separator porosity	0.95	El cell
ρ_p	g cm^{-3}	Density of NVPF	3.2	[28]
NVPF porous electrode properties				
$c_{1,p}^{max}$	mol l^{-1}	Maximum concentration	12.00	measured
$c_{1,p}^{min}$	mol l^{-1}	Minimum concentration	3.319	measured
$C_{1,p}^{rev}$	mAh g^{-1}	Reversible electrode capacity	100.5	measured
σ_p^{eff}	S m^{-1}	Electrode electric conductivity	50	estimated
η_p^{ct}	-	Charge transfer coefficient	0.5	estimated
Electrolyte properties				
c_2^{eq}	mol kg^{-1}	Equilibrium electrolyte concentration	1.0	measured
D_2	m^2s^{-1}	Diffusion coefficient	$4.46 \cdot 10^{-12}$	AEM
κ	S m^{-1}	ionic conductivity	1.0	AEM
t_+	-	Transference number	0.45	AEM

5.4 Results and discussion

Fig. 5.2 (a) shows the 5 initial formation cycles recorded for a Na//NVPF half-cell as a function of the transferred charge. The first (dis)charge cycle is shown in black lines, while the next indicated cycles are shown in various color curves. After 5 cycles, a constant and reversible gravimetric capacity of 101 mAh g^{-1} is obtained. **Fig. 5.2** (b) shows an overview of the experimental 30 GITT steps obtained after formation. The NVPF electrode shows an increase in voltage relaxation time at the voltage slopes compared to the plateau regions. By applying the P2D GITT model and the grid search optimization $D_{1,p}$ and k_p parameters can be determined as a function of transferred charge.

Figs. 5.3 and **5.4** show the experimental (blue symbols) and optimized model results (red curves) for 24 of the 30 GITT steps. The P2D GITT model predicts well both the CC charging and OCV relaxation stages by optimizing the $D_{1,p}$ and k_p parameters. It is worth highlighting that in the CC stage, both $D_{1,p}$ and k_p are sensitive, while in the relaxation step, only $D_{1,p}$ is sensitive. Comparing the simulated voltage profiles at the voltage plateau and sloping regions, it can be concluded that the model accuracy is higher in the plateau regions than in the voltage sloping regions. This difference is because of two main reasons: first, U_p is accurately deduced in the plateau regions from linear interpolation of successive GITT relaxation endpoints. Second, phase changes in the material do not occur instantaneously throughout the whole particle. Therefore, the model assumption of intercalation with a constant $D_{1,p}$ (over each GITT step), remains valid. Each GITT step is however assumed to have unique $D_{1,p}$ and k_p parameters.

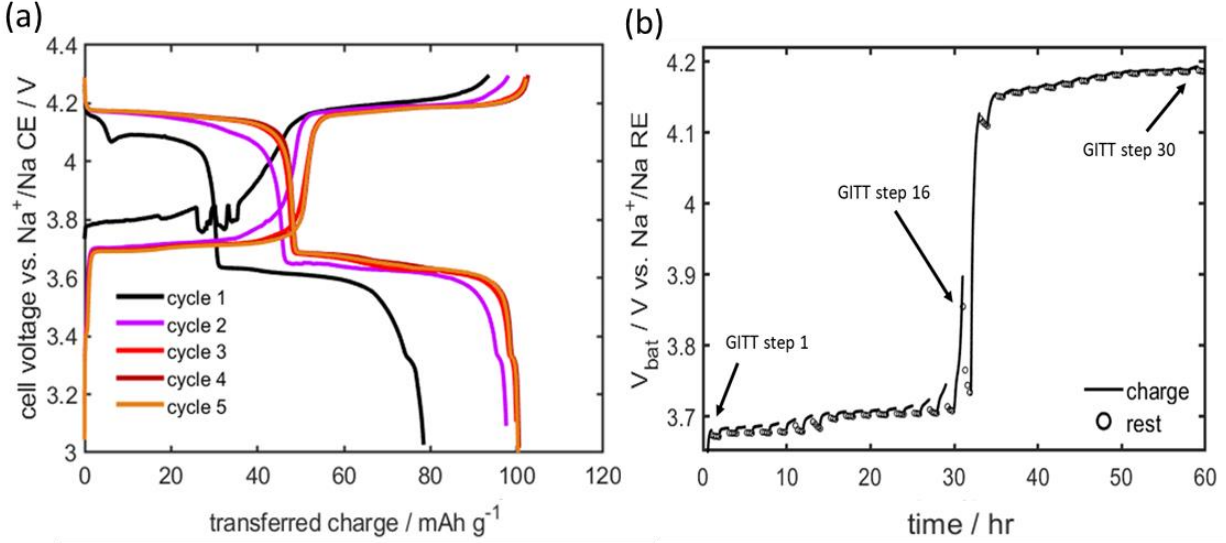


Fig. 5.2. First 5 formation cycles of a Na/NVPF cell (a). 30 GITT steps during charging, *i.e.* desodiation (solid lines), and resting (circles) (b).

Fig. 5.5 shows the EMF of NVPF obtained from GITT relaxations (a), the obtained $D_{1,p}$ (b) and k_p parameters (c) as a function of transferred charge. The EMF is shown to correlate the parameter variations with the different phases of the NVPF material. $D_{1,p}$ values show sharp increases at the NVPF steep voltage step points. In addition, moving from the low voltage GITT steps (step 1 to 16) to the high voltage GITT steps (step 17 to 30), $D_{1,p}$ values show a step increase in their order of magnitude. On the other hand, k_p values exponentially increase as the transferred charge increases. This means that the electrode kinetics increase as the Na⁺ concentration decreases in the NVPF electrode particles. These concentration-dependent $D_{1,p}$ and k_p parameters will therefore be used in the following chapters as input parameters in P2D modeling of SIBs.

Nevertheless, not all GITT steps could be accurately modeled by the P2D GITT model, particularly at the steep EMF voltage change regions around GITT steps 6, 7, and 16 (see **Fig. 5.2** (b)). This is because of the change from a 2-phase region (voltage plateau) to a single-phase solid-solution region (voltage slope) [30]. In addition, a clear EMF voltage hysteresis occurs in the single-phase region. These 'non-ideal' effects are not presently captured by the P2D GITT model. One can include in the model the intercalation dynamics of multiphase materials and moving boundary diffusion mechanisms to address this shortcoming [31]. These are possible areas of improvement.

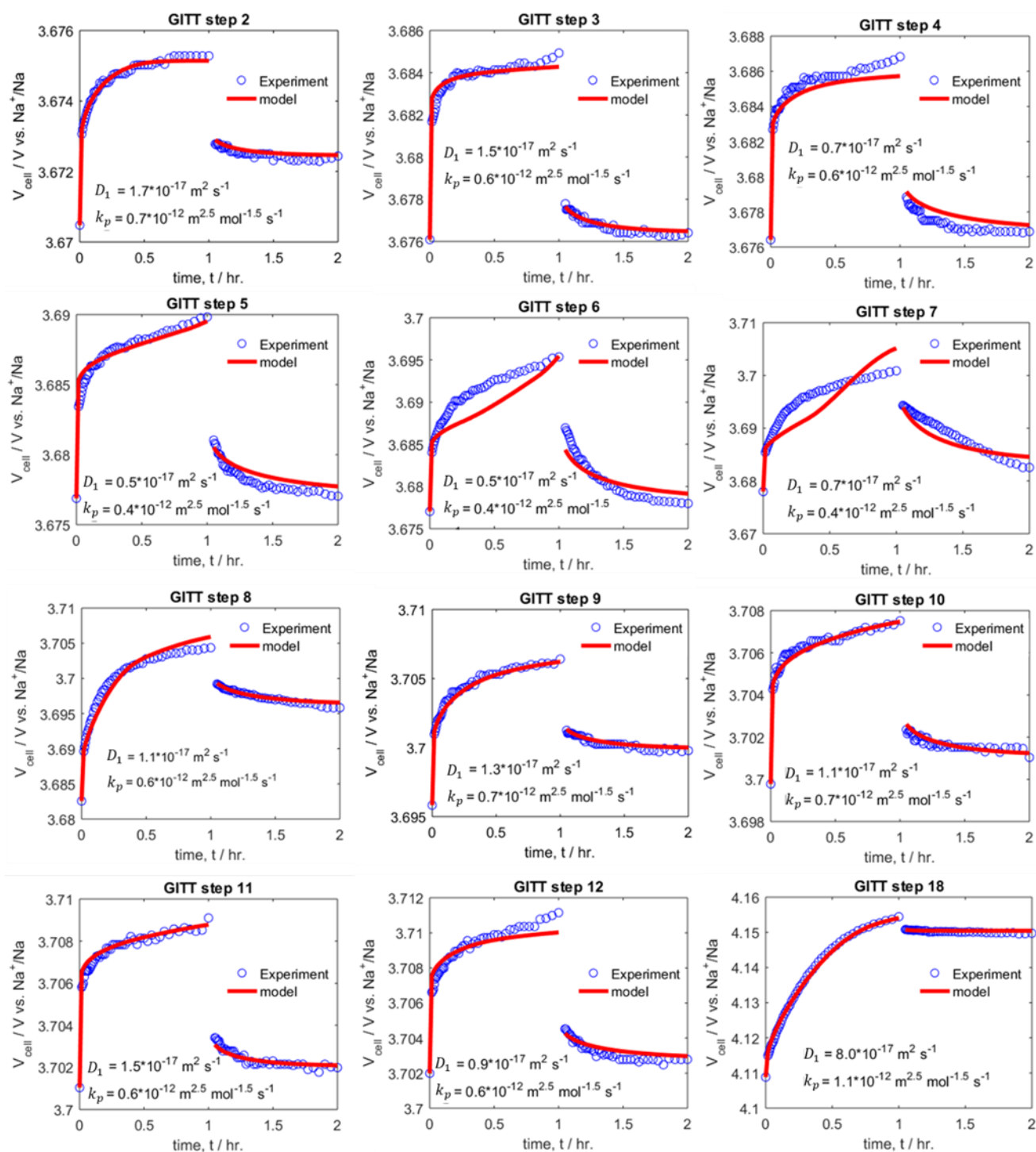


Fig. 5.3. Experimental (symbols) and modeled (lines) voltages and optimized diffusion coefficients and kinetic rate constants for GITT steps 2-18.

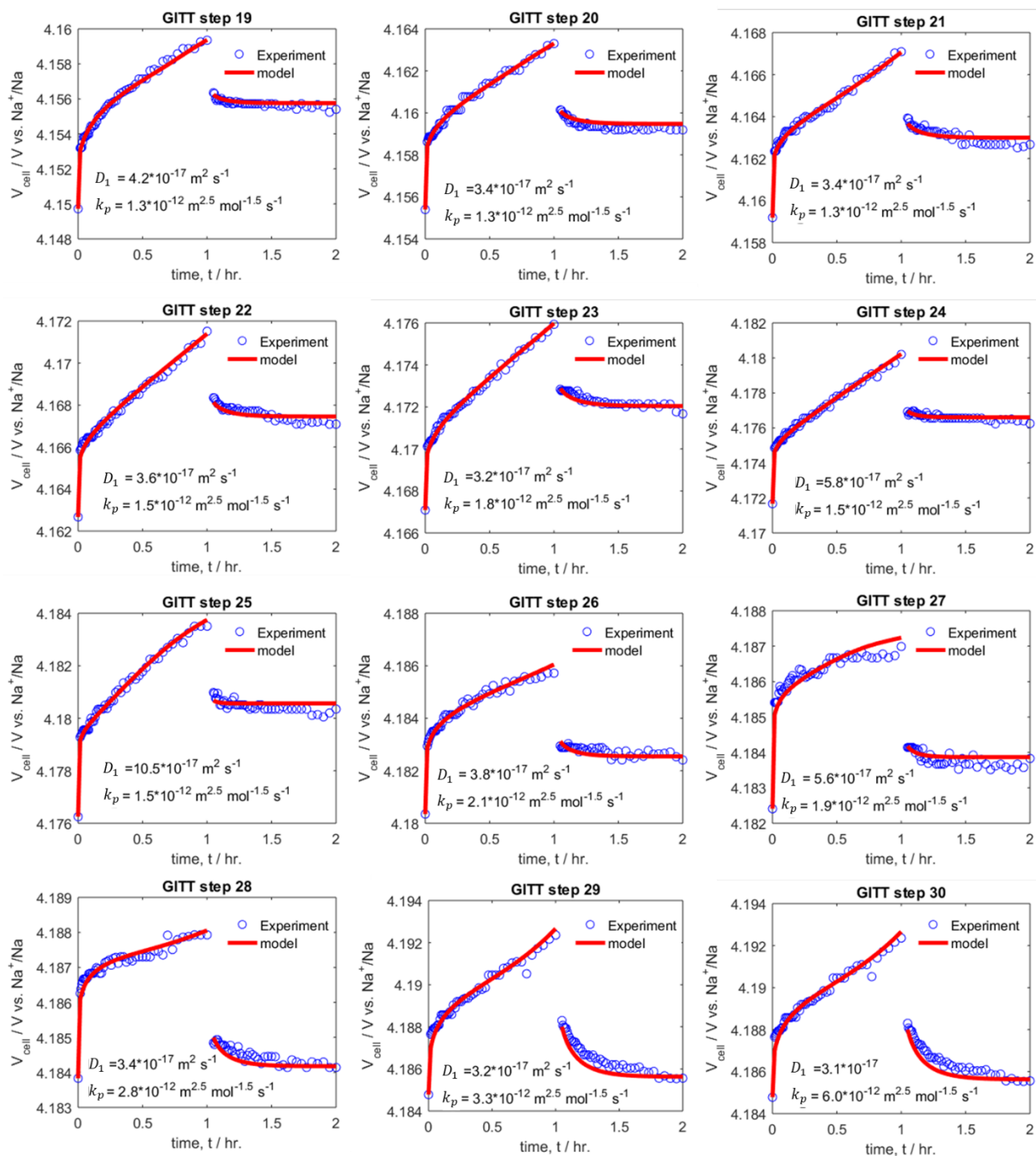


Fig. 5.4. Experimental (symbols) and modeled (lines) voltages, and optimized diffusion coefficients and kinetic rate constants for GITT steps 19-30.

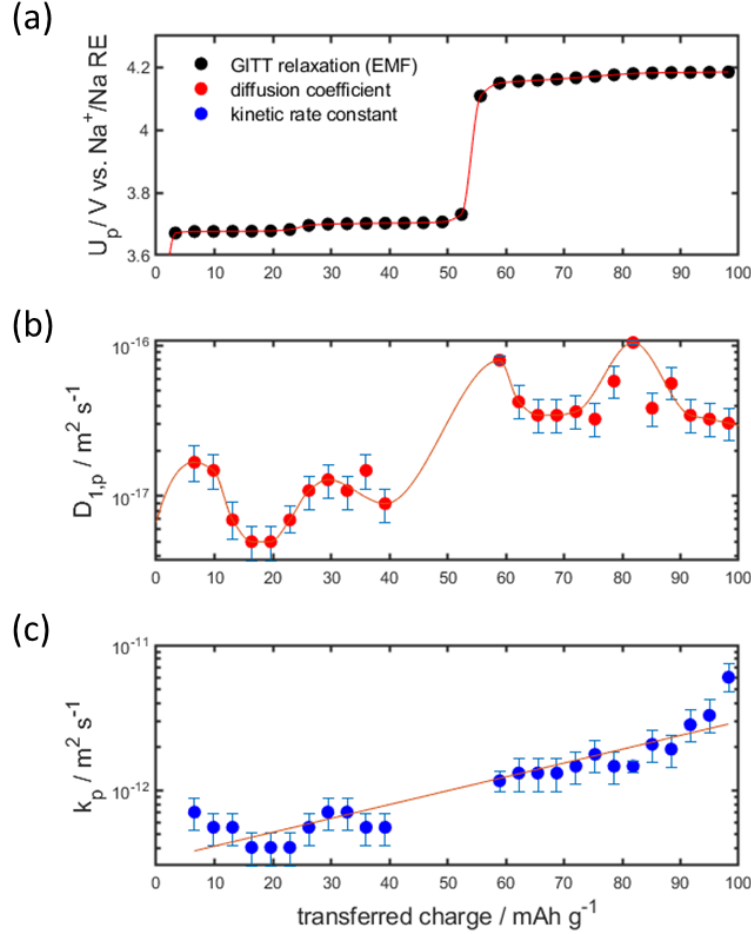


Fig. 5.5. Parameters of NVPF determined from GITT. EMF voltage profile of an NVPF electrode as determined by GITT relaxations (a). Calculated diffusion coefficients, D_1 (b) and charge transfer rate constants, k_p (c) as a function of transferred charge, which is equivalent to the electrode SOC. Error bars indicate $D_{1,p}$ and k_p combinations which result in 10 % error increase from the optimum.

Fig. 5.6 shows comparisons of $D_{1,p}$ results based on the P2D GITT model results and two other analytical model results. The black line shows results by Liu *et al.* [32]. The blue plot shows results based on the Weppner model [33] applied to the GITT data shown in **Fig. 5.2** (b). The red dots show the $D_{1,p}$ results obtained using the present P2D GITT model. Similar results are shown in **Fig. 5.5** (b). The analytical $D_{1,p}$ results shown in **Fig. 5.6** in blue are determined using the following analytical expression [33]

$$D_{1,p} = \left(\frac{4R_p^2}{\pi\tau} \right) \left(\frac{\Delta E_{ss}}{\Delta E_p} \right)^2, \quad \forall \tau \ll R_p^2/D_{1,p}, \quad (5.16)$$

where ΔE_{ss} is the difference between two successive GITT relaxation potentials and ΔE_p is the change in potential during the GITT periods. However, not all data points satisfy the condition $\tau \ll R_p^2/D_1$ of Eq. (5.16). This is because the CC pulse duration of 1 hour was too long for the diffusion coefficients obtained. These points are marked in blue circles and require shorter τ . However, some of the points satisfy the condition $\tau \leq 10 R_p^2/D_1$. These points are marked in blue and are used to compare with the results obtained with the analytical method and P2D GITT method.

Both the P2D GITT (red) and the Weppner model results (blue) are of the same order of magnitude. However, results taken from literature (black) are approximately 6 orders of magnitude higher, showing a sharp deviation. The reason for such a big difference is not fully clear yet. It could originate from the differences in the experimental conditions and the analytical methods used. Nevertheless, such high values for $D_{1,p}$ are unusual for electrode materials and approximates those observed in liquid electrolytes. In addition, none of the analytical methods show $D_{1,p}$ profiles which are consistent with the multiple phase changes occurring in the NVPF electrode.

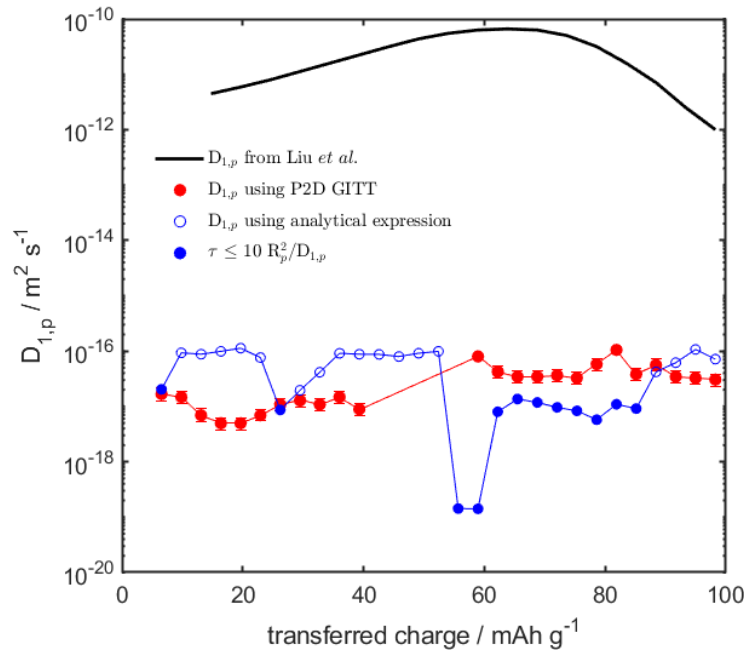


Fig. 5.6. Comparison of different methods to determine the diffusion coefficient. The P2D GITT results (red) are compared to the Weppner model applied to the GITT data (blue) and to the analytical model results from Liu *et al.* [32] (black).

5.5 Conclusions

A pseudo-two-dimensional (P2D) galvanostatic intermittent titration (GITT) model has been used as an analytical tool to simultaneously determine the solid-state diffusion coefficient (D_1) and kinetic rate constant (k) as a function of the transferred charge. The P2D GITT model is herein shown to accurately simulate the experimental voltage profiles of a $\text{Na}_3\text{V}_2(\text{PO}_4)_2\text{F}_3$ (NVPF) sodium-ion battery (SIB) half-cell. High model accuracy is obtained in the voltage plateau regions because the equilibrium potential could be accurately determined by the GITT relaxation, and the phase changes were not abrupt.

P2D models are often criticized for the large number of parameters used. However, in half-cell configurations and using a reference electrode, the number of parameters is drastically reduced. The low constant current pulses used in the GITT experiments ensure that other electrochemical parameters are not sensitive and therefore do not need to be conjointly optimized (as long as they fall within a reasonable range). As a result, the P2D GITT model can be optimized by two parameters only.

The advantages of the P2D GITT model over the classical analytical models originate from replacing unrealistic model assumptions with an accurate porous electrode description. Furthermore, GITT current pulses can be longer and are not restricted by the $\tau \ll L_m^2/D$ condition. This means experimental runtime can be shortened. Moreover, two key battery modeling parameters are obtained from one set of characterization data. Finally, parameter estimates are immediately validated by the quality of the simulations with respect to the experimental GITT profiles, which is not the case in any of the analytical models. For physics-based modeling, it is advantageous for D_1 and k parameters to be determined by the model, instead of relying on two different techniques with, as we have seen, different assumptions.

This Chapter shows that the P2D GITT model can offer reliable and physically meaningful D_1 and k parameters as a function of the transferred charge. This achievement is possible despite the NVPF electrode showing 'non-ideal' phase transitions and voltage hysteresis effects. The methods herein elaborated have been introduced for the NVPF cathode to illustrate the implementation of the P2D GITT modeling and parameter determination. This implementation also can be made for the HC electrode, as will be further outlined in the following Chapters, to model the performance of full cell SIBs.

References

- [1] D. Aurbach, M.D. Levi, E. Levi, H. Teller, B. Markovsky, G. Salitra, U. Heider, L. Heider, Common Electroanalytical Behavior of Li Intercalation Processes into Graphite and Transition Metal Oxides, *J. Electrochem. Soc.* **145** (1998) 3024. <https://doi.org/10.1149/1.1838758>.
- [2] D.R. Baker, C. Li, M.W. Verbrugge, Similarities and Differences between Potential-Step and Impedance Methods for Determining Diffusion Coefficients of Lithium in Active Electrode Materials, *J. Electrochem. Soc.* **160** (2013) A1794. <https://doi.org/10.1149/2.076310jes>.
- [3] M.D. Levi, D. Aurbach, Diffusion Coefficients of Lithium Ions during Intercalation into Graphite Derived from the Simultaneous Measurements and Modeling of Electrochemical Impedance and Potentiostatic Intermittent Titration Characteristics of Thin Graphite Electrodes, *J. Phys. Chem. B.* **101** (1997) 4641–4647. <https://doi.org/10.1021/jp9701911>.
- [4] S. Malifarge, B. Delobel, C. Delacourt, Guidelines for the Analysis of Data from the Potentiostatic Intermittent Titration Technique on Battery Electrodes, *J. Electrochem. Soc.* **164** (2017) A3925. <https://doi.org/10.1149/2.1591714jes>.
- [5] A.V. Churikov, A.V. Ivanishchev, I.A. Ivanishcheva, V.O. Sycheva, N.R. Khasanova, E.V. Antipov, Determination of lithium diffusion coefficient in LiFePO₄ electrode by galvanostatic and potentiostatic intermittent titration techniques, *Electrochimica Acta* **55** (2010) 2939–2950. <https://doi.org/10.1016/j.electacta.2009.12.079>.
- [6] E. Markevich, M.D. Levi, D. Aurbach, Comparison between potentiostatic and galvanostatic intermittent titration techniques for determination of chemical diffusion coefficients in ion-insertion electrodes, *Journal of Electroanalytical Chemistry* **580** (2005) 231–237. <https://doi.org/10.1016/j.jelechem.2005.03.030>.
- [7] J. Li, F. Yang, X. Xiao, M.W. Verbrugge, Y.-T. Cheng, Potentiostatic intermittent titration technique (PITT) for spherical particles with finite interfacial kinetics, *Electrochimica Acta* **75** (2012) 56–61. <https://doi.org/10.1016/j.electacta.2012.04.050>.
- [8] W. Weppner, R.A. Huggins, Electrochemical investigation of the chemical diffusion, partial ionic conductivities, and other kinetic parameters in Li₃Sb and Li₃Bi, *Journal of Solid State Chemistry* **22** (1977) 297–308. [https://doi.org/10.1016/0022-4596\(77\)90006-8](https://doi.org/10.1016/0022-4596(77)90006-8).
- [9] W. Weppner, R.A. Huggins, Electrochemical Methods for Determining Kinetic Properties of Solids, *Annual Review of Materials Science* **8** (1978) 269–311. <https://doi.org/10.1146/annurev.ms.08.080178.001413>.
- [10] M.D. Levi, D. Aurbach, The application of electroanalytical methods to the analysis of phase transitions during intercalation of ions into electrodes, *J Solid State Electrochem.* **11** (2007) 1031–1042. <https://doi.org/10.1007/s10008-007-0264-x>.
- [11] G. Hasegawa, N. Kuwata, Y. Tanaka, T. Miyazaki, N. Ishigaki, K. Takada, J. Kawamura, Tracer diffusion coefficients of Li⁺ ions in c-axis oriented Li_xCoO₂ thin films measured by secondary ion mass spectrometry, *Physical Chemistry Chemical Physics* **23** (2021) 2438–2448. <https://doi.org/10.1039/D0CP04598E>.
- [12] D.R. Baker, M.W. Verbrugge, Electroanalytical Methods Utilizing Small Signal Current or Potential Excitations for the Characterization of Porous Electrodes Comprising Insertion Materials, *J. Electrochem. Soc.* **160** (2013) A1319. <https://doi.org/10.1149/2.110308jes>.
- [13] D.W. Dees, S. Kawauchi, D.P. Abraham, J. Prakash, Analysis of the Galvanostatic Intermittent Titration Technique (GITT) as applied to a lithium-ion porous electrode,

- Journal of Power Sources. **189** (2009) 263–268. <https://doi.org/10.1016/j.jpowsour.2008.09.045>.
- [14] A. Verma, K. Smith, S. Santhanagopalan, D. Abraham, K.P. Yao, P.P. Mukherjee, Galvanostatic Intermittent Titration and Performance Based Analysis of $\text{LiNi}_0.5\text{Co}_0.2\text{Mn}_0.3\text{O}_2$ Cathode, *J. Electrochem. Soc.* **164** (2017) A3380. <https://doi.org/10.1149/2.1701713jes>.
- [15] H. Yang, H.J. Bang, J. Prakash, Evaluation of Electrochemical Interface Area and Lithium Diffusion Coefficient for a Composite Graphite Anode, *J. Electrochem. Soc.* **151** (2004) A1247. <https://doi.org/10.1149/1.1763139>.
- [16] A. Nickol, T. Schied, C. Heubner, M. Schneider, A. Michaelis, M. Bobeth, G. Cuniberti, GITT Analysis of Lithium Insertion Cathodes for Determining the Lithium Diffusion Coefficient at Low Temperature: Challenges and Pitfalls, *J. Electrochem. Soc.* **167** (2020) 090546. <https://doi.org/10.1149/1945-7111/ab9404>.
- [17] M.W. Verbrugge, B.J. Koch, Electrochemistry of Intercalation Materials Charge-Transfer Reaction and Intercalate Diffusion in Porous Electrodes, *J. Electrochem. Soc.* **146** (1999) 833. <https://doi.org/10.1149/1.1391689>.
- [18] K.E. Thomas, J. Newman, R.M. Darling, Mathematical Modeling of Lithium Batteries, in: W.A. van Schalkwijk, B. Scrosati (Eds.), *Advances in Lithium-Ion Batteries*, Springer US, Boston, MA, (2002) 345–392. https://doi.org/10.1007/0-306-47508-1_13.
- [19] Y. Ye, Y. Shi, N. Cai, J. Lee, X. He, Electro-thermal modeling and experimental validation for lithium ion battery, *Journal of Power Sources.* **199** (2012) 227–238. <https://doi.org/10.1016/j.jpowsour.2011.10.027>.
- [20] D.M. Bernardi, J.-Y. Go, Analysis of pulse and relaxation behavior in lithium-ion batteries, *Journal of Power Sources.* **196** (2011) 412–427. <https://doi.org/10.1016/j.jpowsour.2010.06.107>.
- [21] V. Sulzer, S.G. Marquis, R. Timms, M. Robinson, S.J. Chapman, Python Battery Mathematical Modelling (PyBaMM), ECSarXiv, (2020). <https://doi.org/10.1149/osf.io/67ckj>.
- [22] EU H2020 Program, Naiades, Sodium ion batteries, (2020). <http://www.naiades.eu/> (accessed August 29, 2017).
- [23] Naiades | Sodium ion batteries, (n.d.). <https://www.naiades.eu/> (accessed April 15, 2020).
- [24] D.L. Wood, J. Li, S.J. An, Formation Challenges of Lithium-Ion Battery Manufacturing, *Joule* **3** (2019) 2884–2888. <https://doi.org/10.1016/j.joule.2019.11.002>.
- [25] H.S. Carslaw, J.C. Jaeger, *Conduction of heat in solids*: Oxford Science Publications, Oxford, England (1959).
- [26] K. Chayambuka, G. Mulder, D.L. Danilov, P.H.L. Notten, A Hybrid Backward Euler Control Volume Method to Solve the Concentration-Dependent Solid-State Diffusion Problem in Battery Modeling, *Journal of Applied Mathematics and Physics* **8** (2020) 1066–1080. <https://doi.org/10.4236/jamp.2020.86083>.
- [27] K.L. Gering, Prediction of electrolyte viscosity for aqueous and non-aqueous systems: Results from a molecular model based on ion solvation and a chemical physics framework, *Electrochimica Acta* **51** (2006) 3125–3138. <https://doi.org/10.1016/j.electacta.2005.09.011>.
- [28] R. Dugas, B. Zhang, P. Rozier, J.M. Tarascon, Optimization of Na-Ion Battery Systems Based on Polyanionic or Layered Positive Electrodes and Carbon Anodes, *J. Electrochem. Soc.* **163** (2016) A867–A874. <https://doi.org/10.1149/2.0051605jes>.

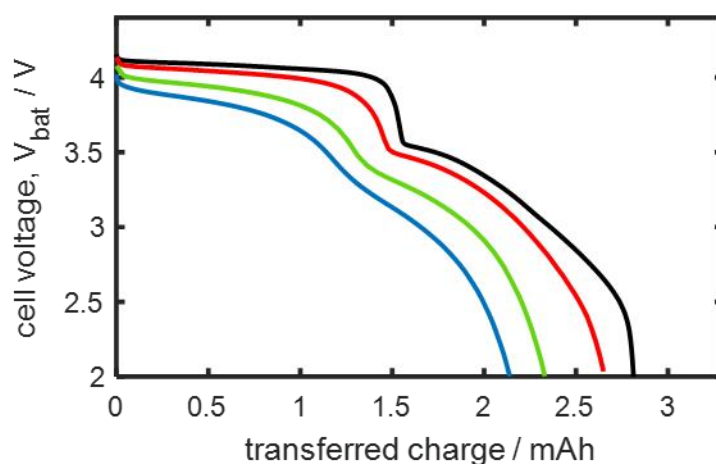
- [29] J. Lim, Y. Li, D.H. Alsem, H. So, S.C. Lee, P. Bai, D.A. Cogswell, X. Liu, N. Jin, Y. Yu, N.J. Salmon, D.A. Shapiro, M.Z. Bazant, T. Tyliczszak, W.C. Chueh, Origin and hysteresis of lithium compositional spatiodynamics within battery primary particles, *Science* **353** (2016) 566–571. <https://doi.org/10.1126/science.aaf4914>.
- [30] A. Ledovskikh, D. Danilov, P.H.L. Notten, Modeling of hydrogen storage in hydride-forming materials: Equilibrium gas-phase kinetics, *Phys. Rev. B* **76** (2007) 064106. <https://doi.org/10.1103/PhysRevB.76.064106>.
- [31] R.B. Smith, E. Khoo, M.Z. Bazant, Intercalation Kinetics in Multiphase-Layered Materials, *J. Phys. Chem. C* **121** (2017) 12505–12523. <https://doi.org/10.1021/acs.jpcc.7b00185>.
- [32] Z. Liu, Y.-Y. Hu, M.T. Dunstan, H. Huo, X. Hao, H. Zou, G. Zhong, Y. Yang, C.P. Grey, Local Structure and Dynamics in the Na Ion Battery Positive Electrode Material Na₃V₂(PO₄)₂F₃, *Chem. Mater.* **26** (2014) 2513–2521. <https://doi.org/10.1021/cm403728w>.
- [33] J. Kaspar, M. Graczyk-Zajac, R. Riedel, Determination of the chemical diffusion coefficient of Li-ions in carbon-rich silicon oxycarbide anodes by electroanalytical methods, *Electrochimica Acta* **115** (2014) 665–670. <https://doi.org/10.1016/j.electacta.2013.10.184>.

CHAPTER 6

EXPERIMENTAL DETERMINATION OF SIB MODELING PARAMETERS

Abstract

Before setting up the full-cell SIB model, several experimental characterizations are needed in order to elucidate the electrochemical parameters of the electrode materials. This experimental knowledge further dictates the most dominant physical phenomena and the level of complexity necessary to accurately model SIBs. This Chapter presents the experimental techniques applied to NVPF and HC electrodes, with the aim to deduce parameters to use in full cell SIB models. As a result, 18 model parameters are obtained from the two electrodes, which can be classified as geometric, thermodynamic, and kinetic parameters. Based on the analyses of Na//NVPF and Na//HC half-cells, diffusion mass transport limitations and Ohmic losses are identified in both electrodes. These overpotential losses are equally present in full cell SIB composed of NVPF and HC electrodes.



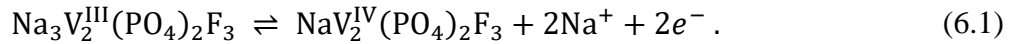
Parts of this Chapter have been submitted for publication as:

K Chayambuka, M. Jiang G Mulder, DL Danilov, PHL Notten, Physics-Based Modelling of Sodium-ion Batteries, Part I: Experimental parameter determination, *Electrochimica Acta* (2021)

6.1 Introduction

Among the several possible combinations of SIB active materials, the most promising is the one based on the $\text{Na}_3\text{V}_2(\text{PO}_4)_2\text{F}_3$ (NVPF) cathode and HC anode [1]. This battery was first developed via the collaboration of French institutions CNRS, CEA, and the Collège de France, under the umbrella of the French network for electrochemical energy storage (RS2E) [2]. Because of such an advanced technological readiness, it is judicious to further investigate this combination of electroactive compounds to deduce the most relevant electrochemical modeling parameters of the HC/NVPF SIB.

NVPF and HC are two electrode materials with different structures and charge storage mechanisms. NVPF belongs to the NASICON (Natrium Superionic Conductor) family of compounds [3–5]. Charge insertion in NVPF occurs via the reversible intercalation mechanism [6,7]. Because of the multiple oxidation states of vanadium, *i.e.* V^{3+} , V^{4+} , and V^{5+} and the inductive effects of the $(\text{PO}_4)^{3-}$ and F^- anions, NVPF exhibits a high cathodic voltage [8–10]. The charge transfer process in NVPF can be written as



Eq. (6.1) is a general electrochemical half-reaction showing the reversible exchange of 2 Na^+ per formula unit in NVPF. This results in a theoretical capacity of 128 mAh g^{-1} , which makes NVPF one of the most stable and high-energy-dense SIB cathode materials [11].

On the other hand, the HC anode is structurally composed of graphene-like parallel layers embedded in a microporous amorphous phase [12]. Charge insertion in HC occurs via mesopore/nanopore filling and adsorption on graphene layers [13–15]. It should be mentioned that correlating the microstructural properties of HC to the observed voltage profiles remains controversial and is therefore still an active area of research [11,16]. Nevertheless, HC achieves an impressively high specific capacity of about 300 mAh g^{-1} which approximates to that of graphite in LIBs.

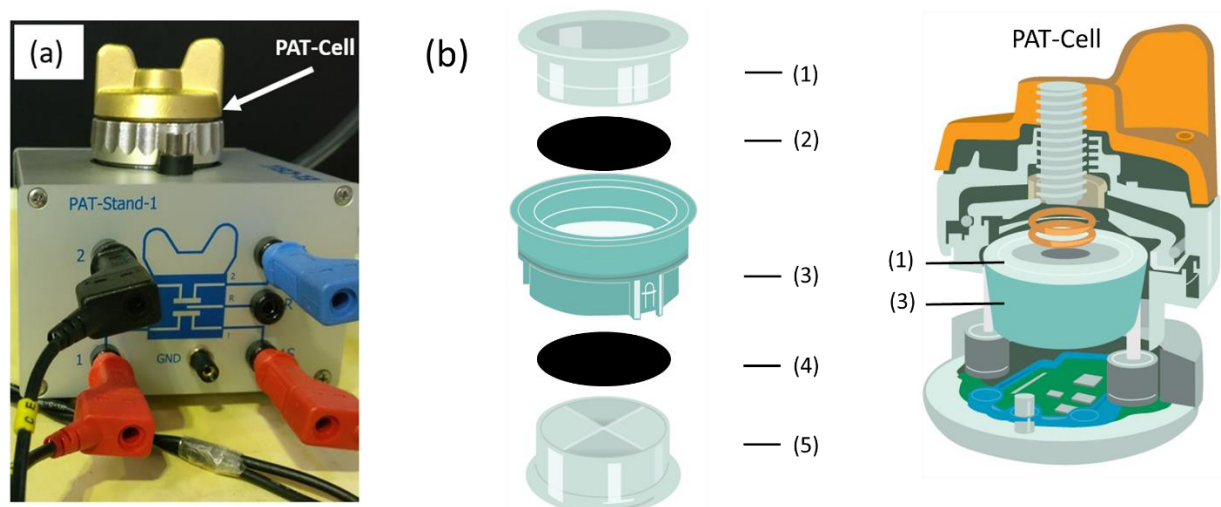
In this Chapter, the experimental methods applied to both NVPF and HC electrodes are described to derive parameters for physics-based P2D modeling. The model structure and P2D equations are described in the next Chapter. These models generally require many parameters classified as geometric, thermodynamic, transport, and kinetic properties [17,18]. As many as 35 model parameters were recently identified [19]. For a new battery chemistry, such as the SIB, the

need for reliable, experimentally determined parameters cannot be overstated. This problem is further complicated by the fact that most parameters are either unknown or not agreed upon. Yet, these model inputs within reasonable accuracy constitute the backbone for accurate, physics-based models. It is therefore imperative that the battery modeling parameters be derived from dedicated experiments designed for this purpose.

The physical and electrochemical parameters of room temperature SIBs based on NVPF and HC electrodes and 1 M NaPF₆ EC_{0.5}:PC_{0.5} (w/w) electrolyte are herein determined using half-cell and full cell experimental setups. Physical property tests based on SEM, electrochemical tests based on three-electrode half-cell GITT tests, and three-electrode full cell (dis)charge rate tests are used as a strategy to yield 15 model parameters in a few dedicated investigations. From the GITT analyses, concentration-dependent kinetic rate parameters and diffusion coefficients can be further derived, as illustrated in Chapter 5 [20]. Because battery manufacturers do not typically provide the requisite extensive parameter set, these experimental characterizations are necessary complementary tools to enable accurate P2D modeling.

6.2 Experimental

A PAT-Cell (EL-Cell GmbH, Hamburg, Germany) was used as the electrochemical test cell. The PAT-Cell is composed of an 18 mm diameter PAT-core in which battery electrodes can be assembled. The PAT-core components include a factory-assembled separator surrounded by a prefabricated Na-metal ring, which acts as the Na-RE. This configuration allows the Na-RE to be close enough to the battery electrodes for accurate measurements. In addition, two stainless steel upper and lower plungers complete the PAT-core configuration, allowing external electrical contact and uniform pressure distribution on the electrodes. In configuring the PAT-core, selecting the correct lower plunger size is also important, which ensures good electrode contact with the separator and avoids electrolyte leakage. Detailed images of the EL-Cell PAT-cell are shown in **Fig. 6.1**.



(1) Upper plunger, current collector (3) Insulation sleeve with separator and Na RE (5) Lower plunger, current collector
 (2) Top working electrode, $\varnothing = 18$ mm (4) Bottom working electrode, $\varnothing = 18$ mm

Fig. 6.1. The PAT-Cell components and configuration. Image of the PAT-Cell inside a climate chamber showing the potentiostat cable connectors and PAT-Stand which enables the connection with the PAT-Cell to the potentiostat cables (a). Components of the PAT-Cell (b).

Half-cells and full cells were thus assembled in an argon-filled glove box (Innovative Technology, Inc. Newburyport, MA), where oxygen and moisture levels were controlled below 1 ppm. These conditions prevent surface oxidation of the highly reactive metallic sodium electrodes. After assembly, the PAT-Cells were hermetically sealed with a polyethylene sealing ring and placed in a climate chamber (Maccor, model MTC-010) at 25 °C. Cell voltage measurements were recorded using Maccor® automated cycling equipment (Model 4200), and cycling programs were configured in Maccor® standard test software (MacTest 32).

Reproducible results were obtained with the PAT cells. Furthermore, the Na-RE was stable at all test conditions. The half-cell configuration allows individual electrodes to be cycled to their full capacity. As metallic Na CEs were used, it is necessary to use thick separators, which can withstand dendrite growth. Na-RE in a three-electrode configuration was used to obtain accurate measurements of the working electrode potentials. Such a design eliminates additional overpotentials arising from the thick separator and metallic CE.

6.2.1 Electrodes

Dry, double-side coated NVPF and HC electrodes with single-side mass loadings of 12 and 6 mg cm^{-2} respectively, were used. These coated electrodes were supplied by the manufacturer (SAFT/CEA). The electrode balancing work was completed in the recently concluded in EU-funded NAIADES project [21,22]. Because sodium does not alloy with aluminum at the anode-side, aluminum was used as the current collector for both electrodes. The advantages of using aluminum instead of copper as the anodic current collector have been discussed recently [23]. The double-coated electrodes were first scrapped on one side to delaminate and expose the current collector using a surgical blade. It is advisable to delaminate only the small area intended to be cut out because single-side coated electrodes curl and become difficult to handle. 18 mm diameter electrodes were then cut to size using an 18 mm diameter electrode punching tool. Better cuts were obtained when the laminated side was cut facing up on a soft plastic base. This procedure was followed for both the NVPF and HC electrodes.

Unlike Li, which is commercially available as a foil, Na is sold in cubes immersed in mineral oil. To prepare thin Na electrodes, Na metal cubes (Aldrich, 99.9 %) were first washed with propylene carbonate to remove the mineral oil and then wiped dry with a soft tissue. The cube was then cut in half using a surgical blade to expose the pristine metal surface. The half-cube and aluminum foil were then sealed in a polypropylene plastic bag. This procedure was carried out inside the glove box.

To prepare flat sodium electrodes, the sealed bag was taken outside the glove box, and the cube was pressed against the aluminum foil using a hydraulic press until a flat electrode surface was obtained. The plastic protects the pristine metal surface from air contamination and sticking to the press. The aluminum foil, therefore, becomes the current collector. Sodium electrodes with a thickness of 400 μm were thus obtained. After pressing, the sealed sodium electrode was reintroduced in the glove box, and 18 mm diameter electrodes were cut to size using the electrode punching tool. **Fig. 6.2** (a) shows the hydraulic press equipment used. **Fig. 6.2** (b) and (c) show the Na electrodes obtained.

Other studies have established that the procedure for making sodium electrodes has a significant impact on the stability of electrochemical results [24–26]. This is consistent with our own findings. For example, the electrodes obtained with an uncut sodium cube exhibit more

surface oxidation compared to the electrode obtained with a half-cube (compare **Fig. 6.2** (b) and (c)).

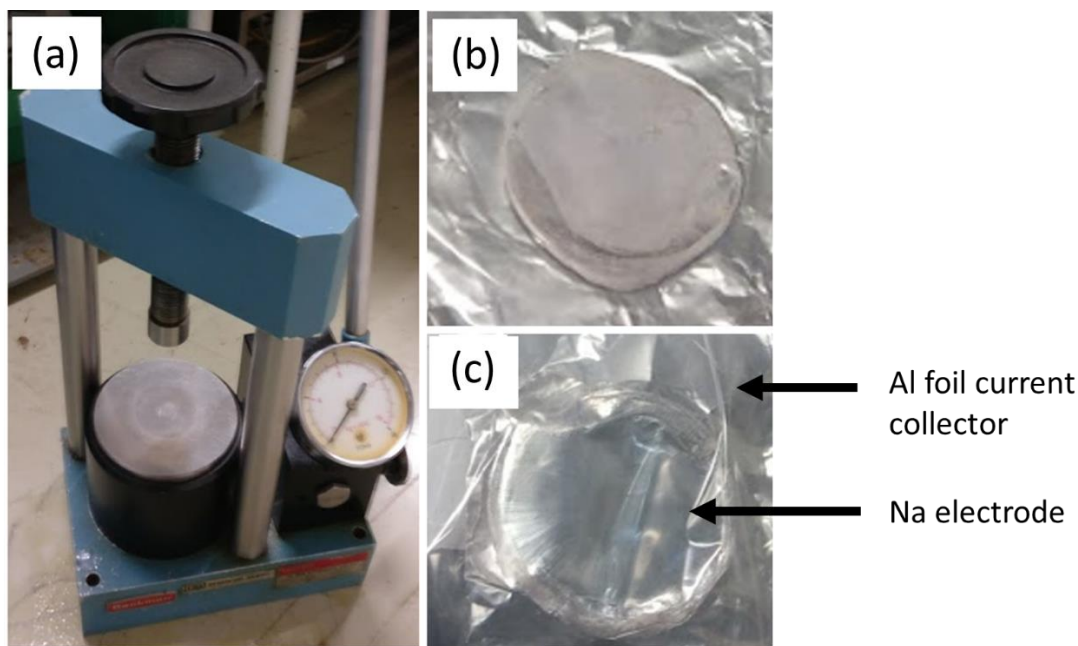


Fig. 6.2. Hydraulic press used in making flat Na electrodes (a). Surface oxidized Na electrode obtained when an uncut Na cube is used (b). Plastic-covered Na-electrode obtained after pressing a cut Na cube is used.

6.2.2 Electrolyte

1 M NaPF_6 $\text{EC}_{0.5}:\text{PC}_{0.5}$ (w/w) electrolyte was prepared starting with pure solvents and salt. Equal mass samples of EC and PC were mixed before being heated and stirred at 60 °C. The heating allows EC to melt and dissolve. The salt, NaPF_6 (Kishida, anhydrous, 99.0%) was finally dissolved in the $\text{EC}_{0.5}:\text{PC}_{0.5}$ (w/w) solvent to make an electrolyte of 1 M concentration, which was used in all investigations. This procedure was carried out in the glove box. No electrolyte additives were used, and all electrolytes and salts were used as received.

6.2.3 Physical property analyses

SEM micrographs obtained on Quanta FEG 650 (FEI, USA) environmental scanning electron microscope operated at a voltage of 20 kV were used to analyze the morphology of the NVPF and

HC electrodes as well as the 25 μm FS 3005-25 separator (Freudenberg Viledon). Gold sputtering was applied to the samples to enhance conductivity and reduce charge accumulation during measurements. The particle size distribution and the average particle radii of the positive and negative electrodes were determined from the scan images.

The thicknesses of the double-side coated NVPF and HC electrodes and the aluminum current collectors were measured by a digital-micrometer screw gauge (Helios Preisser, Digi-Met). Thickness measurements were taken at random points of the electrodes. The average single-side coating thickness was obtained by subtracting the current collector thickness from the average double-side coating thickness and dividing by 2. Electrode porosity was provided by the manufacturer (SAFT/CEA), while the thickness and porosity values of the separator were taken from the corresponding datasheets [27].

6.2.4 Electrochemical testing

The voltage profiles of the NVPF and HC electrodes were determined by three-electrode, half-cell measurements. These cells were composed of the aforementioned Na metal electrode as CE, a prefabricated Na-RE, and either an NVPF or HC porous electrode as working electrodes. In addition, 1 M NaPF_6 electrolyte and a 220 μm thick FS-5P (Freudenberg Viledon FS 2226E - Lydall Solupor 5P09B) separator were used. The FS-5P separator comprises two layers of nonwoven polypropylene fiber (FS: 180 μm thick, 67% porous) and a microporous polyethylene film (5P: 38 μm thick, 86% porous). Because of this composition and thickness, the FS-5P separator has a high porosity, good wettability, and high resistance to dendrite growth. These characteristics make it a good choice for half-cell tests.

After assembly in the argon-filled glove box, the PAT-Cell was hermetically sealed and placed in a climate chamber at 25 $^{\circ}\text{C}$. The Na//NVPF half-cells underwent 5 formation cycles at a constant current of 0.1 mA / 0.039 mA cm^{-2} (corresponding to approximately C/30, where C-rate is based on the storage capacity obtained at slow (dis)charge rate) in the cell voltage range of 3.0 to 4.3 V vs. Na^+/Na . The formation stage allows the growth of a protective surface layer on the active electrode particles and results in stable cycles [28]. After the formation stage, the cells were charged in 3 consecutive stages: (i) 0.1 mA CC charging until the upper cutoff cell voltage of 4.3 V, (ii) CV charging for 3 hours at 4.3 V, and (iii) OCV relaxation for 1 hour. The CV stage allows

the maximum cell capacity to be reached, while the OCV period allows the sodium concentration gradients to equilibrate. After charging, the cell underwent discharge rate testing at different currents of 0.1, 0.2, 0.3, and 0.4 mA, corresponding to C/30, C/15, C/10, and C/7.5, respectively. After each discharge rate test, the above-mentioned 3 stage charging protocol was repeated to maintain consistency in the initial discharging starting point.

The Na//HC half-cells similarly underwent an identical formation and cycling procedure in the voltage range of 30 mV to 2.0 V *vs.* Na⁺/Na. The formation stage consisted of 5 CC (dis)charge cycles at 0.2 mA / 0.078 mA cm⁻², corresponding to approximately C/15. After formation, a 3-stage discharge protocol was applied comprising of: (i) 0.1 mA CC until a cutoff voltage of 2 V has been reached (ii) 3 hours CV at 2 V followed by (iii) a 1-hour OCV relaxation period. Discharge herein refers to Na extraction from the HC electrodes, which increases the electrode potential. The half-cells were then sodiated upon charging at different rates of 0.1, 0.12, 0.14, and 0.16 mA (C/30, C/25, C/21, and C/19) until the cutoff voltage of 30 mV. Because of a long and flat voltage plateau close to 0 V *vs.* Na⁺/Na, finding the optimal lower cutoff voltage for the HC electrode is indeed challenging [24,29]. This is because, during charging, it is important to maintain HC electrode potentials above zero volts, to avoid Na plating and dendrite formation. However, the cutoff potentials are defined by the total cell voltage, a value that contains contributions of all overpotentials, including the activation and charge transfer overpotential of the CE electrode and the electrolyte Ohmic drop. For the HC electrode, a cell cutoff voltage of 30 mV, however, resulted in a high electrode capacity without Na plating. This cutoff voltage value can be different in other setups.

6.2.5 Determination of electrode parameters using GITT

GITT was performed with the assembled Na//NVPF and Na//HC half-cells. Starting with a fully discharged Na//NVPF half-cell, 30 GITT steps were applied, which comprised of a CC charging pulse of 0.1 mA (C/30) until the cell capacity reached 0.1 mAh followed by an OCV rest period of 1 hour. Because Coulomb counting was used to define the pulse duration (and not time), each GITT pulse was approximately 1 hour long. A low current of C/30 was applied during the CC period to minimize voltage overpotentials. The OCV stage was set for 1 hour, a time in which

voltage relaxation is expected to reach a steady state. After the 30 GITT steps, the cells were fully charged to 4.3 V in CV mode for 5 hours.

GITT with the assembled Na//NVPF half-cells was similarly performed using discharge current pulses. Starting with the fully charged cells, 30 GITT steps were applied, which comprised of a CC discharge pulse of 0.1 mA (C/30) until the discharge capacity reached 0.1 mAh, followed by an OCV relaxation period of 1 hour. After the 30 GITT steps, the cells were then finally discharged to 3 V in the CV mode for 5 hours.

The GITT procedure with the assembled Na//HC half-cells was performed using discharge current pulses. The cells were initially charged using a CC of 0.1 mA (C/30) until the cell voltage reached 30 mV. This cutoff voltage corresponds to fully charged HC electrodes. Afterwards, 29 GITT steps were applied to the cells, which comprised of CC discharge at 0.1 mA until the capacity reached 0.1 mAh followed by OCV relaxation for 1 hour. The Na//HC half-cells were then finally discharged at the CV of 2 V for a period of 5 hours. Because of the challenges at low anode potentials, namely the risk of Na plating and the flat low voltage profile of the HC electrodes, the GITT procedure has only been performed with discharge current pulses.

6.2.6 Full cell cycling

Galvanostatic discharge cycles of the HC//NVPF full cells were performed in a three-electrode setup, which included a Na-RE. The anode and cathode were comprised of 18 mm diameter, single-side coated NVPF and HC electrodes, respectively. In addition, a 25 μ m FS 3005-25 separator and 1 M NaPF₆ EC_{0.5}:PC_{0.5} (w/w) the electrolyte was used. Unlike in the half-cell configurations, wherein thick, 220 μ m separators had to be used, thin 25 μ m separators were used in the full cells. This choice is made because there is less risk of short circuits resulting from dendrite formation in full cells. Furthermore, a thin separator resembles the thickness used in practical SIBs. Therefore, the full cell setups closely mimic the performance of real SIBs.

After assembly in the argon-filled glove box, the PAT-Cell was hermetically sealed and placed in a climate chamber at 25 °C. 5 formation cycles at 0.2 mA were applied to the cells in the voltage range of 2.0 to 4.2 V. This allowed the SEI formation and stabilization of the cell capacity. After formation, the cells underwent multiple discharge cycles at different current densities of 0.5, 1, 2.5, 5, 7.5, 10, 12 and 24 A m⁻², corresponding to 0.05, 0.1, 0.3, 0.6, 0.9, 1.2, 1.4 and 3 C,

respectively, where $1 \text{ C-rate} = 8.3 \text{ A m}^{-2}$. To maintain consistency in the starting point of discharging, the charging cycle was performed in three stages: (i) galvanostatic CC charging at 0.2 mA, until the cell voltage of 4.2 V (ii) potentiostatic CV charging at 4.2 V for 3 hours and (iii) OCV relaxation for 1 hour. This 3-stage charging procedure is designed to maintain constant initial concentrations without concentration gradients in either the electrode particles or the electrolyte. This charging procedure results in initial conditions consistent with the initial value considerations in the P2D model.

6.3 Results and discussion

In the nomenclature of variables, a distinction is made between electrode and electrolyte parameters. In addition, an effort is herein made to distinguish between positive (NVPF) and negative (HC) electrode parameters. For instance, the concentration, diffusion coefficient, and kinetic rate parameters are written in the form: $c_{\theta,m}$, $D_{\theta,m}$ and k_m , respectively. The subscript θ symbolizes the phase of the variable, which can either be in the solid phase ($\theta = 1$) or in liquid/electrolyte phase ($\theta = 2$) and the subscript m symbolizes the cell domain, which can either be the positive NVPF electrode ($m = p$), the negative HC electrode ($m = n$) or the separator ($m = s$).

6.3.1 Physical analyses

Fig. 6.3 shows SEM micrographs of the NVPF and HC electrodes at different magnifications. The NVPF and HC active particles have a diameter of the order of $1 \mu\text{m}$ and $10 \mu\text{m}$, respectively. A mesoporous phase of conductive additives and binders can similarly be observed at a sub-micron scale. In general, the NVPF particles have smooth, spherical shapes, while the HC particles have irregular cubic shapes with sharp edges. The edges on the HC particles constitute highly reactive sites for electrochemical reactions [30]. The NVPF electrode exhibits a dual-scale porosity in its microstructure due to the agglomeration of active particles. Similar agglomerates have also been identified in $\text{LiNi}_{0.5}\text{Co}_{0.2}\text{Mn}_{0.3}$ electrodes [31]. Outside these agglomerates, macropores with a diameter of approximately $3 \mu\text{m}$ can be identified in the NVPF electrode at a magnification of 13,000. This dual-scale porosity is known to improve the overall rate performance of the electrodes [32]. This is because the macropores result in electrodes with low tortuosity and act as transport "highways" for Na^+ ions in the electrolyte.

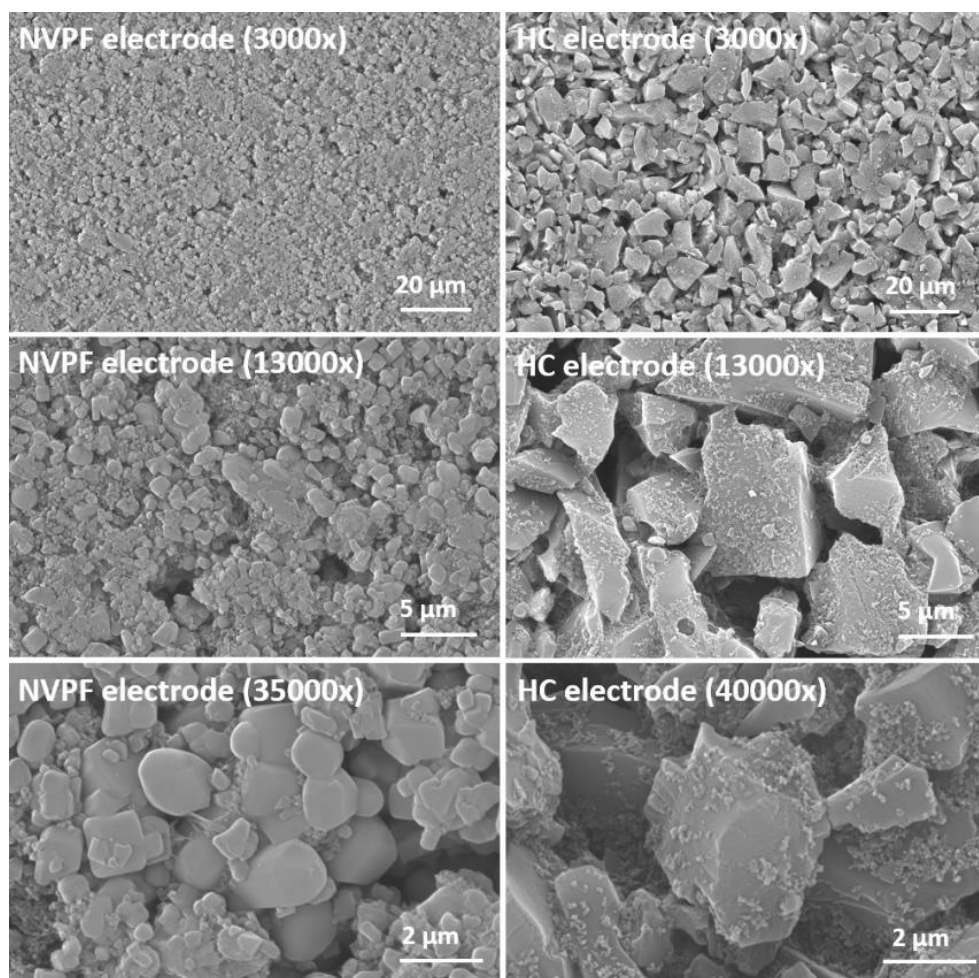


Fig. 6.3. Top view SEM micrographs of NVPF and HC electrodes at different magnifications.

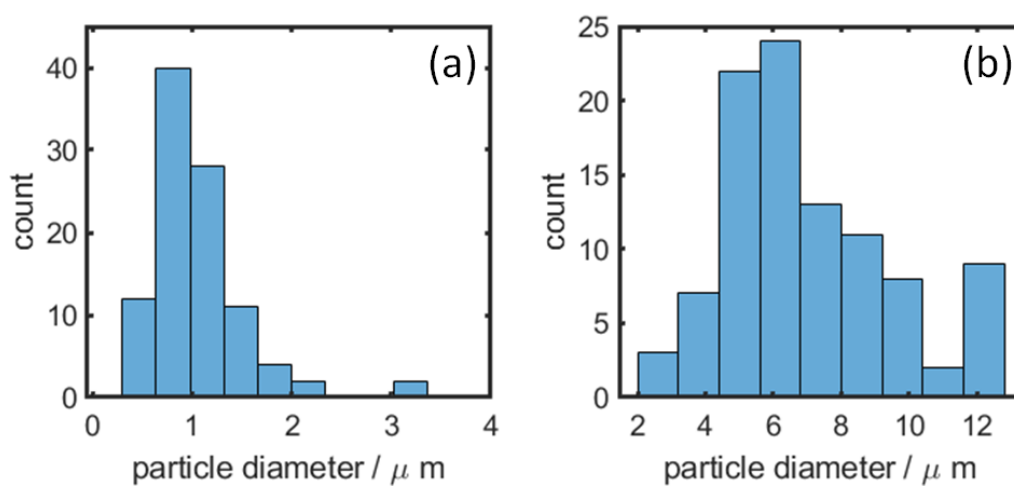


Fig. 6.4. Electrode particle size distribution of NVPF (a) and HC (b). Particle sizes determined from SEM micrographs.

Fig. 6.4 (a) and (b) show the particle size distribution of NVPF and HC electrodes. The average active particle radii of NVPF and HC are 0.59 and 3.48 μm , respectively. The two electrodes, however, exhibit a wide dispersion of particle sizes. The distribution of HC electrode particles, in particular, has a high standard deviation of 2.5 μm . In contrast, the NVPF electrode shows a standard deviation of 0.5 μm . The irregular shapes and the large particle size distribution in the HC electrode increase the slurry viscosity, which has been reported as one of the challenges encountered during HC electrode coating at an industrial scale [11,33–35].

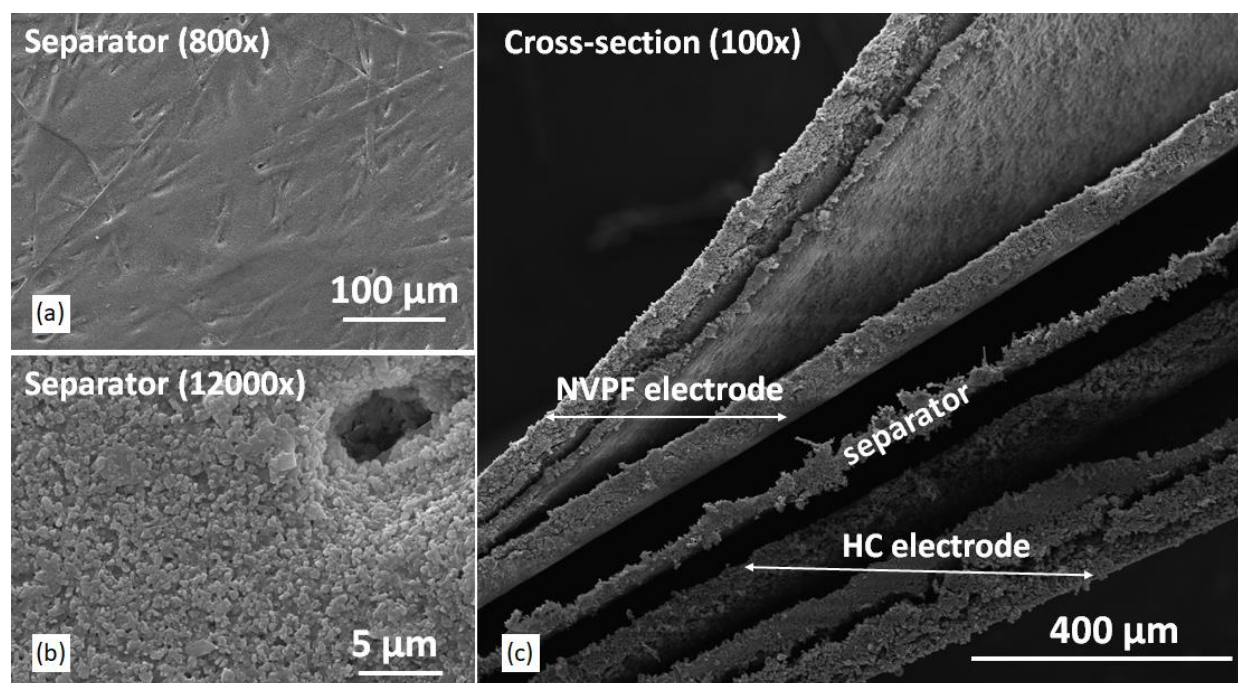


Fig. 6.5. SEM micrographs of a FS 3005-25 separator at a magnification of 800 (a) and 12.000 (b). Cross-sectional view of double-side coated NVPF electrode, HC electrode, and FS 3005-25 separator (c).

Fig. 6.5 (a) and (b) show SEM images of the FS 3005-25 separator used in the full cell SIBs. This separator is composed of a polypropylene fiber base impregnated by a mixture of binder and Al_2O_3 ceramic particles. The fibers and the particles can be observed at both magnifications. **Fig. 6.5** (c) shows the cross-section image of a double-side coated NVPF and HC electrode with a separator in between. On each electrode, 3 layers representing the Al current collector (in the middle) and two porous electrode coatings on either side of the Al current collector can be observed. It can also be observed that the NVPF electrode is more compact and hence has less

porosity than the HC electrode. The average thickness of the Al current collector is 22 μm . The average thickness of double-side coated NVPF and HC electrodes, including the current collector, are 158 and 149 μm , respectively.

Table 6.1. Summary of physical properties of the main SIB components.

Parameter	Unit	Description	NVPF	HC	Separator
L_{double}	μm	Double-side coating thickness (average)	153-163 (158)	137-155 (149)	-
L_{CC}	μm	Current collector thickness	22	22	-
δ_m	μm	Single-side thickness	68	64	25
R_m	μm	Mean particle radius	0.59	3.48	-
ρ_m	g cm^{-3}	Density	3.2 ^(a)	1.6-2.0 ^(b) (1.95)	1.4
A	cm^2	Area	2.545	2.545	2.545
ϵ_m^{el}	-	Electrolyte volume fraction	0.20-0.25	0.49-0.52	0.55

(a) Data derived from Dugas *et al.* [28] (b) Data derived from available literature sources [28,36–38]

Table 6.1 summarizes the physical electrode properties obtained. These electrode dimensions constitute important input in the P2D models because the optimization of the electrode thickness and particle size, starting with unknown parameters, requires remeshing and changes to the model time step, which can cause model instability. Moreover, the determination of extended parameters such as diffusion coefficients and kinetic rate constants is dependent on the accurate knowledge of the particle size and electrode thickness measurements. For these reasons, it is important to carry out extensive physical property characterizations of battery electrodes. Nevertheless, holistically incorporating the material properties in P2D models is not straightforward either. This is because P2D models conceptually consider spherical, monodisperse particles whereas, in reality, electrodes can have a broad particle size distribution, and the particles can have a variety of shapes (as shown in **Figs. 6.3** and **6.4**). In most cases, however, the particles can be assumed spherical, and the average particle size and electrode thickness can be used as the approximate and representative physical parameters.

6.3.2 Na//NVPF half-cell

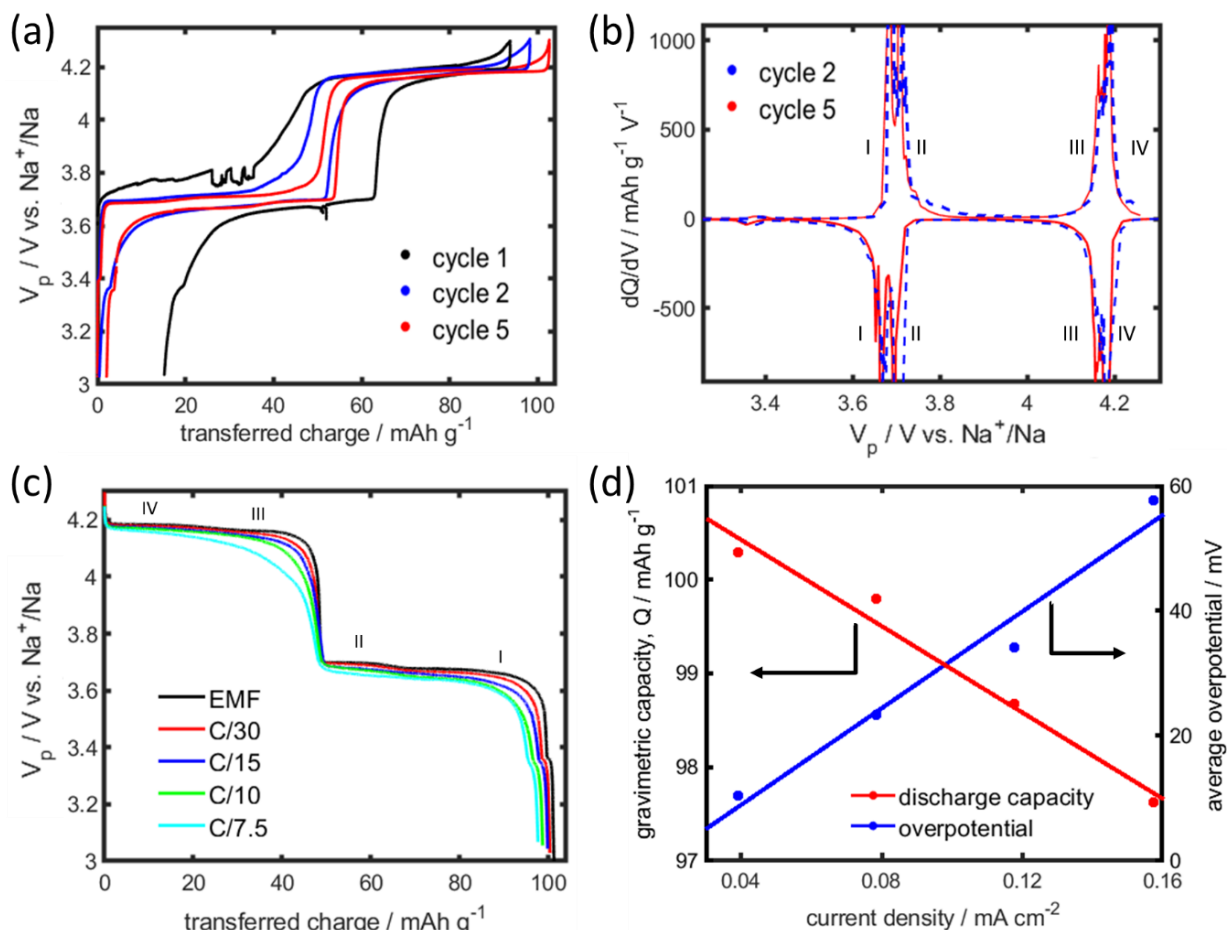


Fig. 6.6. Na//NVPF half-cell tests. Formation (dis)charge cycles, showing the electrode potential as a function of the transferred charge (a). dQ/dV curves of the 2nd and 5th cycle vs. the electrode potential (b). Low-current voltage discharge profiles of the NVPF electrode obtained at C/30, C/15, C/10, and C/7.5 (c). NVPF electrode rate-dependent discharge capacity (red line) and average overpotential (blue line) as a function of discharge current density (d).

Fig. 6.6 shows the results from 3-electrode electrochemical testing of a Na//NVPF half-cell in the voltage range of 3 to 4.3 V. The voltage profile of the NVPF electrode exhibits a characteristic steep voltage step around 3.7 to 4.1 V vs. Na^+/Na . **Fig. 6.6** (a) shows formation (dis)charge cycles performed at 0.1 mA (0.039 mA cm^{-2} , C/30). The electrode records a reversible capacity of 94, 98, and 103 mAh g^{-1} in the 1st, 2nd, and 5th cycle, respectively. In the 1st cycle, voltage artifacts around 3.8 V are observed. Note, these 1st cycle artifacts are only recorded in Na//NVPF half-cells and are related to secondary electrochemical reactions occurring at the Na

CE [25]. Subsequent cycles, however, demonstrate voltage stability and improved Coulombic efficiency. **Fig. 6.6** (b) shows dQ/dV curves for the 2nd and 5th cycles. Despite an increase in electrode capacity in the 5th cycle, the derivatives look similar. 4 voltage plateaus marked in Roman numerals I to IV can therefore be distinguished in the voltage range of 3.6 to 4.3 V vs. Na⁺/Na. Such a step-wise voltage profile is associated with crystallographic phase transitions in the NVPF electrode material [39,40].

Fig. 6.6 (c) shows the low current voltage discharge profiles of an NVPF electrode at 0.1, 0.2, 0.3, and 0.4 mA, corresponding to C/30, C/15, C/10, and C/7.5, respectively. The Roman numerals I to IV are again used to mark the respective voltage plateaus. Using the extrapolation-to-zero-current method, the electrode equilibrium potential (EMF) can be determined from the voltage profiles at low rates. The as-obtained EMF is shown in **Fig. 6.6** (c) by the black line. The extrapolation-to-zero-current method uses a set of low-current (dis)charge curves and applies polynomial extrapolation toward zero current to the experimental voltage and capacity to determine the EMF. More details of this method have been described by Danilov *et al.* [41–43]. Based on the NVPF EMF, a reversible electrode capacity of 101 mAh g⁻¹ is determined. **Fig. 6.6** (d) shows the NVPF electrode overpotential and rate-dependent discharge capacity as a function of discharge current. Considering more or less linear dependencies, the NVPF storage capacity decreases with increasing current density at a rate of 28 h cm² g⁻¹, while the average overpotential increases at a rate of 370 Ω cm². The average overpotential is calculated from the voltage difference between the EMF and the various voltage discharge curves. These numbers are highly relevant for comparison with those found for the HC electrode to be presented below.

6.3.3 Na//HC half-cell

Fig. 6.7 (a) shows the (dis)charge formation cycles obtained with an HC electrode at 0.2 mA (C/15 rate). Using a cutoff cell voltage of 30 mV, the electrode has a first cycle capacity and irreversible capacity loss of 125 and 9 mAh g⁻¹, respectively. The first cycle irreversible capacity loss is defined as the difference between the charging and discharging capacities. This difference is caused by entrapped Na in the micropores [44]. The HC irreversible capacity loss of only 9 mAh g⁻¹ is impressively low. By comparison, larger irreversible capacity losses of approximately 62 mAh g⁻¹ have been reported before [28]. Because in a full cell configuration, the cathode is

the only source of intercalated Na^+ and the standard practice is to oversize the anode to avoid Na plating. Any irreversible capacity related to the anode is therefore highly detrimental to the storage capacity [44]. The relatively low irreversible capacities of HC found herein are therefore very favorable for assembling high-capacity SIBs.

The subsequent HC cycles in **Fig. 6.7** (a) show improved Coulombic efficiencies. For example, the irreversible capacity loss found in the 5th cycle reduces to only 1 mAh g⁻¹. However, the HC electrode shows a significant voltage difference between (dis)charge cycles. Because this has the effect of reducing the energy efficiency of full cells, this phenomenon will be discussed in relation to full cell SIB voltage profiles.

Fig. 6.7 (b) shows the dV/dQ curves of the HC electrode in the 1st and 5th cycles. Identical dV/dQ profiles for the two cycles demonstrate a highly stable cycling behavior. The charge and discharge plateaus are located at 0.06 and 0.12 V vs. Na^+/Na , respectively. An SEI peak located at 0.9 V, as previously reported by Dugas *et al.* [28], is, however, not so pronounced in the present study because no electrolyte additives were used.

Fig. 6.7 (c) shows the voltage curves of an HC electrode during charging at 0.1, 0.12, 0.14, and 0.16 mA (C/30, C/25, C/21, C/19). Again, using the extrapolation-to-zero-current method [41–43], the EMF of the HC electrode was determined. This resulted in the black curve in **Fig. 6.7** (c), which has a reversible electrode capacity of 222 mAh g⁻¹. At the low charging current of 0.1 mA (C/30), the HC electrode has a capacity of 187 mAh g⁻¹. Increasing the charging rate from 0.1 mA to 0.16 mA results in a 23 % decline in electrode capacity, *i.e.*, from 187 to 144 mAh g⁻¹. Such a rapid decline demonstrates the difficulty of accessing the full capacity of the HC electrode because of the flat, low-voltage plateau toward full charge. It also points to a potential challenge for fast charging HC-based SIBs; because of the very low rates required to reach the full capacity while avoiding Na plating on the anode.

Fig. 6.7 (d) shows the variation of the electrode capacity and average overpotential as a function of current density. The average overpotentials at different charge rates are calculated as the average voltage difference between the HC EMF and the HC voltage profile at a given charge rate. As the current density increases, the rate-dependent electrode capacity linearly decreases at a rate of 1780 h cm² g⁻¹, while the overpotential increases linearly at a rate of 1600 Ω cm². Both numbers are significantly higher than those of the NVPF electrode (**Fig. 6.6** (d)), indicating that

the HC electrode can be considered the rate-limiting and capacity-limiting electrode in charging SIBs.

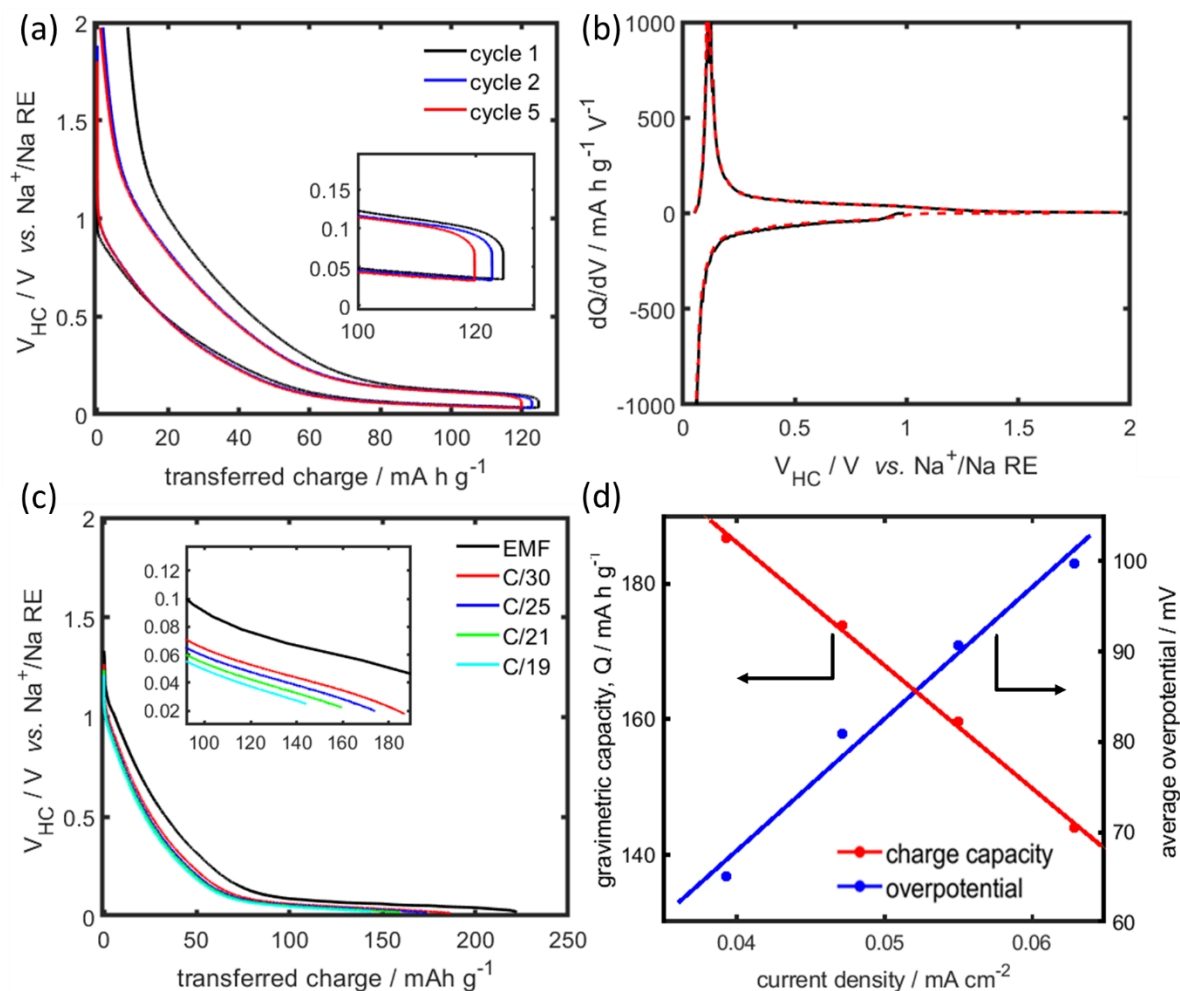


Fig. 6.7. Formation (dis)charge cycles of a Na/HC half-cell, showing the electrode potential vs. transferred charge (a). dQ/dV curves of the 1st and 5th cycles vs. electrode potential (b). Low current voltage charge curves at C/30, C/25, C/21, and C/19 (c). HC charge capacity (red line) and overpotentials (blue line) at the different discharge rates (d).

6.3.4 GITT measurements

Fig. 6.8 shows an overview of the 30 GITT steps obtained for the NVPF electrode in the voltage range of 3.0 to 4.3 V during charging (a) and discharging (b). The CC pulses are shown in red symbols, while the OCV rest periods are shown in blue. **Fig. 6.8** also shows the cathode voltage profiles in more detail, in the voltage range of 3.6 to 3.7 V vs. Na^+ / Na during charging (c) and

discharging (d). At this higher magnification, 2 voltage plateaus separated by about 20 mV can be identified, which were hardly visible in **Fig. 6.8** (a) and (b). The voltage plateaus correspond to phase transition regions, while the voltage slopes correspond to solid solution regions [45]. **Fig. 6.8** further shows in more detail the GITT profiles in the upper-voltage plateau region, in the voltage range of 4.1 to 4.2 V vs. Na^+/Na during charging (e) and discharging (f). Voltage plateaus can also be identified in this voltage region. However, the separation of the plateaus is not as distinct as in the low voltage region. In **Fig. 6.8** (c) to (f), variations in the GITT relaxation periods can be discerned at voltage slopes and voltage plateaus. These changes can be attributed to changes in the diffusion coefficient and phase transition in the material [46].

Fig. 6.9 (a) shows the 29 GITT steps obtained for the HC electrode during discharging in the voltage range of 30 mV to 2.0 V. The CC pulse and OCV relaxation are shown in red and blue dots, respectively. **Fig. 6.9** also shows in more detail the GITT profiles in the voltage sloping region (b) and in the low voltage plateau region (c). Compared to the NVPF GITT profiles in **Fig. 6.8**, the OCV voltage relaxation towards steady-state occurs faster for the HC electrode. This observation indicates a higher solid-state diffusivity of Na in the HC compared to the NVPF electrode.

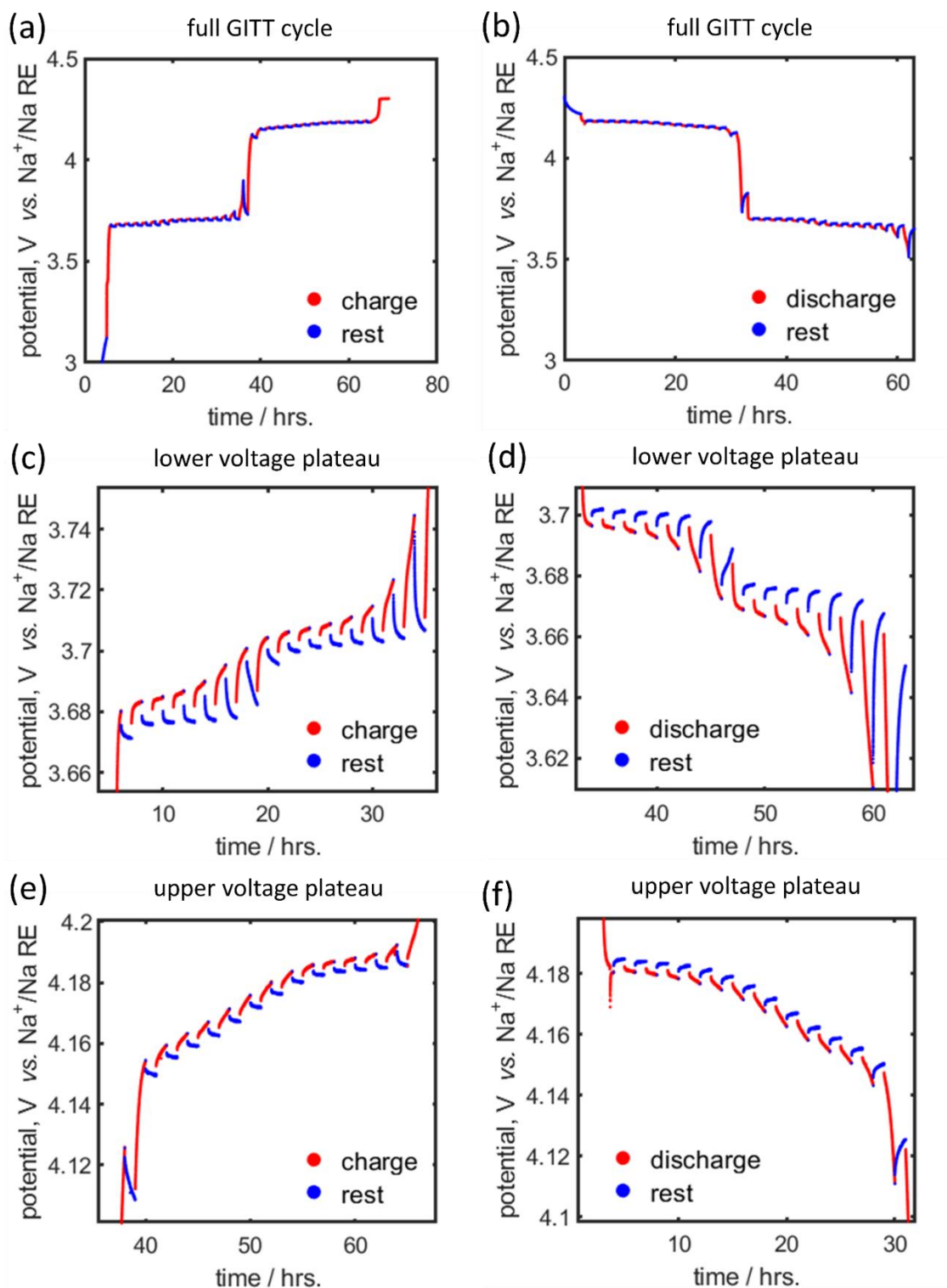


Fig. 6.8. GITT measurements of a Na/NVPF half-cell. Voltage profiles of 30 GITT steps obtained during charging (a) and discharging (b) in the voltage range of 3.0 to 4.3 V. Magnified view of profiles in the lower voltage plateau during charging (c) and discharging (d). Magnified view of profiles at the upper voltage plateau region during charging (e) and discharging (f).

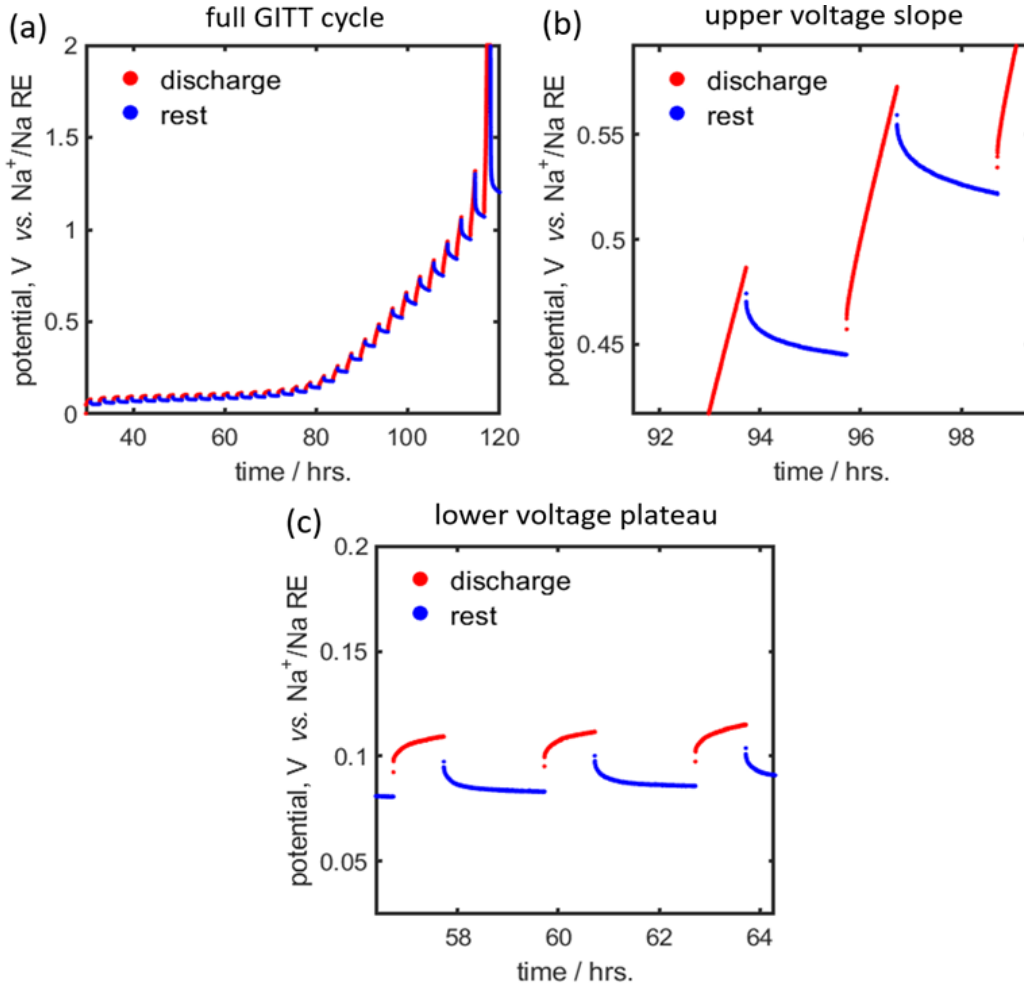


Fig. 6.9. GITT measurements of a Na/HC half-cell configuration. 29 discharge GITT steps are obtained in the cell voltage range 30 mV to 2.0 V (a). Magnified view of discharge GITT profiles obtained in the upper (b) and lower voltage region of HC (c).

GITT data in combination with a half-cell P2D model and optimization is used to simultaneously determine solid-state diffusion coefficient ($D_{1,m}$) and the kinetic rate constant (k_m) as a function of the transferred charge [20,47,48]. **Fig. 6.10** shows the calculated diffusion coefficient ($D_{1,p}$) and rate constant for the charge transfer reaction (k_p) of the NVPF electrode. The EMF of the NVPF cathode is, for comparative reasons, is shown in (a). This alignment allows a correlation between the EMF with the relevant parameters and various phase changes occurring in the NVPF electrode. **Fig. 6.10** (b) and (c) show $D_{1,p}$ and k_p as a function of transferred charge, respectively. There is a clear shift in the diffusion coefficient moving from the lower voltage

plateau region (average $D_{1,p} = 1.1 \cdot 10^{-17} \text{ m}^2 \text{ s}^{-1}$) to the upper voltage plateau region (average $D_{1,p} = 5.8 \cdot 10^{-17} \text{ m}^2 \text{ s}^{-1}$). On the other hand, the k_p values (c) show an exponential increase as a function of the transferred charge at the end of the charging process. An average value of $k_p = 1.3 \cdot 10^{-12} \text{ m}^{2.5} \text{ mol}^{-1.5} \text{ s}^{-1}$ is obtained for all measurements. However, not all $D_{1,p}$ and k_p values could be accurately determined using the P2D GITT model, particularly at the steep voltage slope regions. This failure can be explained by the short size of the single-phase region. It is, therefore, difficult to accurately define the EMF at steep voltage slope regions [20].

Fig. 6.11 shows results of the calculated diffusion coefficient ($D_{1,n}$) and rate constants (k_n) for the HC electrode. The EMF of HC is shown in **Fig. 6.11** (a) in order to align the EMF and the calculated parameters. **Fig. 6.11** (b) and (c) show $D_{1,n}$ and k_n , as a function of transferred charge, respectively. Comparing NVPF and HC, two materials with different crystallographic structures and charge storage mechanisms, it is evident that the HC parameters do not exhibit a significant variation as a function of the transferred charge. Average values of $D_{1,n} = 3.6 \cdot 10^{-16} \text{ m}^2 \text{ s}^{-1}$ and $k_n = 5.5 \cdot 10^{-12} \text{ m}^{2.5} \text{ mol}^{-1.5} \text{ s}^{-1}$ are obtained. In addition, HC parameters $D_{1,n}$ and k_n (**Fig. 6.11** (b) and (c)) are higher than NVPF parameters $D_{1,p}$ and k_p (**Fig. 6.10** (b) and (c)), This observation indicates solid-state mass transport and kinetic rates are higher in HC compared to NVPF particles.

Using the following diffusion length expression, it is now possible to estimate the time it takes for the diffusion of Na^+ in NVPF and HC particles. The diffusion time is calculated as

$$\tau_m = \frac{R_m^2}{4D_{1,m}}, \quad m = \{n, p\}, \quad (6.2)$$

where τ_m is the diffusion time in electrode particle m [s] and R_m is the mean particle radius. Taking $D_{1,p} = 1.1 \cdot 10^{-17} \text{ m}^2 \text{ s}^{-1}$ and $D_{1,n} = 9 \cdot 10^{-16} \text{ m}^2 \text{ s}^{-1}$, the average diffusion coefficients toward the end of discharge, the diffusion times obtained for NVPF and HC particles are $\tau_p = 2$ hours and $\tau_n = 1$ hour, respectively. These values show that diffusion limitations are more severe in NVPF particles, where large concentration gradients can be expected at moderately high discharge rates above 0.5 C. That is despite the submicron mean size of the NVPF particles. The implication of these results in the P2D model setup is that the NVPF particles should have a fine mesh close to the particle surface and use concentration dependent $D_{1,p}$ and k_p parameters, to obtain accurate concentration profiles [49].

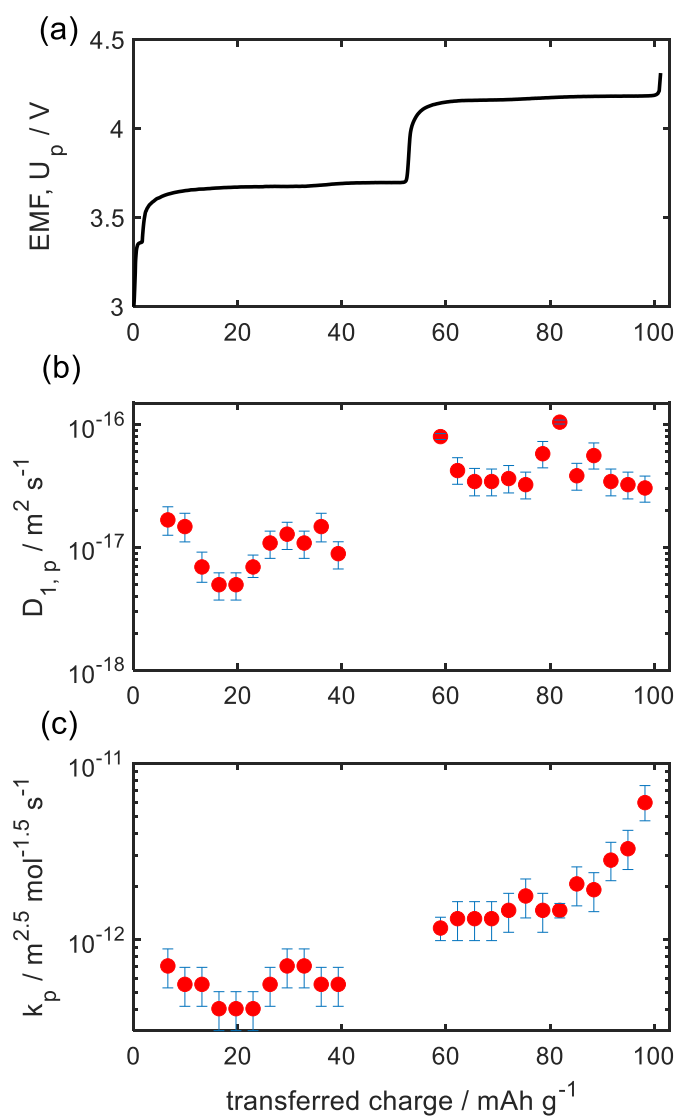


Fig. 6.10. NVPF parameters derived from GITT P2D simulations. EMF voltage curve of an NVPF electrode as determined by the extrapolation-to-zero-current method (a). Calculated diffusion coefficients, $D_{1,p}$ (b) and charge transfer rate constants, k_p (c) as a function of transferred charge in the electrode.

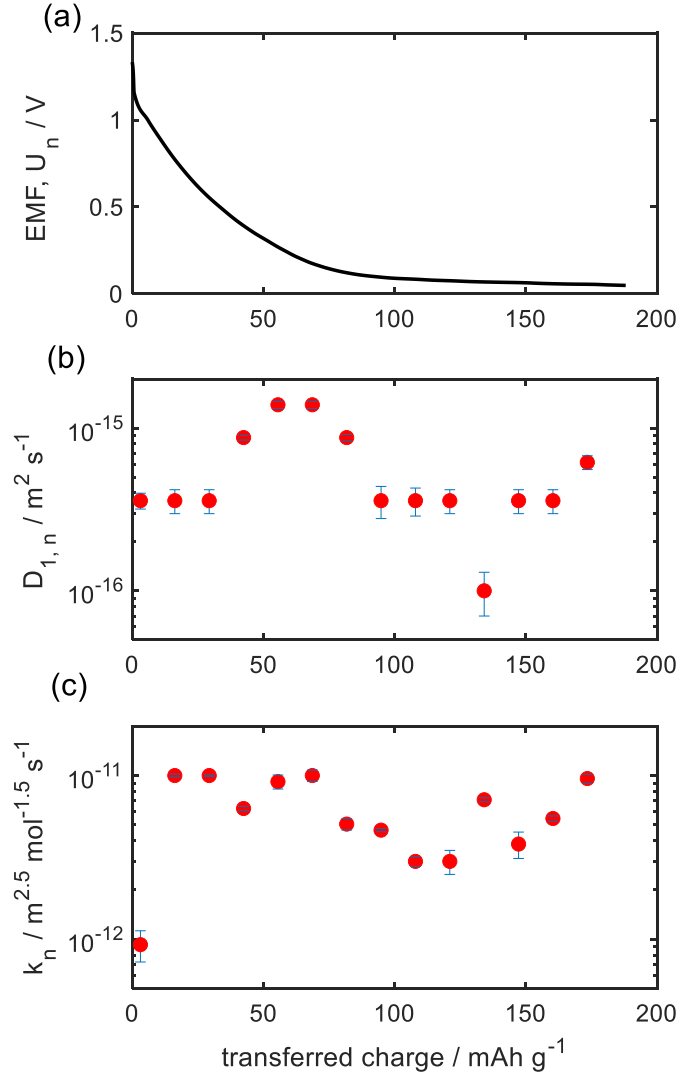


Fig. 6.11. HC parameters derived from GITT P2D modeling. The EMF profile of an HC electrode is determined by the extrapolation-to-zero-current method (a). Calculated diffusion coefficients, $D_{1,n}$ (b) and kinetic rate constants, k_n (c) as a function of transferred charge.

6.3.5 Complete batteries

In complete SIBs based on an NVPF cathode, an HC anode, and a Na-RE, the individual electrode potentials for the NVPF (V_p) and HC (V_n) are related to the full cell voltage (V_{bat}) as

$$V_{bat} = V_p - V_n. \quad (6.3)$$

Fig. 6.12 shows the voltage profiles obtained during the formation cycles for an HC//NVPF SIB. These profiles were obtained at a constant current of 0.2 mA (0.07C), and cutoff voltages 2 and

4.2 V. **Fig. 6.12** (a) shows profiles of V_{bat} while the individual voltage profiles V_p and V_n are shown in **Fig. 6.12** (b) and (c), respectively. During the first formation cycle (black curves), a high capacity of 3.3 mAh is recorded. Note, the first cycle voltage profile of NVPF shown in **Fig. 6.12** (b) does not exhibit the same voltage artifacts as was the case in the Na//NVPF half-cells (**Fig. 6.6** (a)), thus confirming the effect of the Na CE to the recorded voltage artifacts.

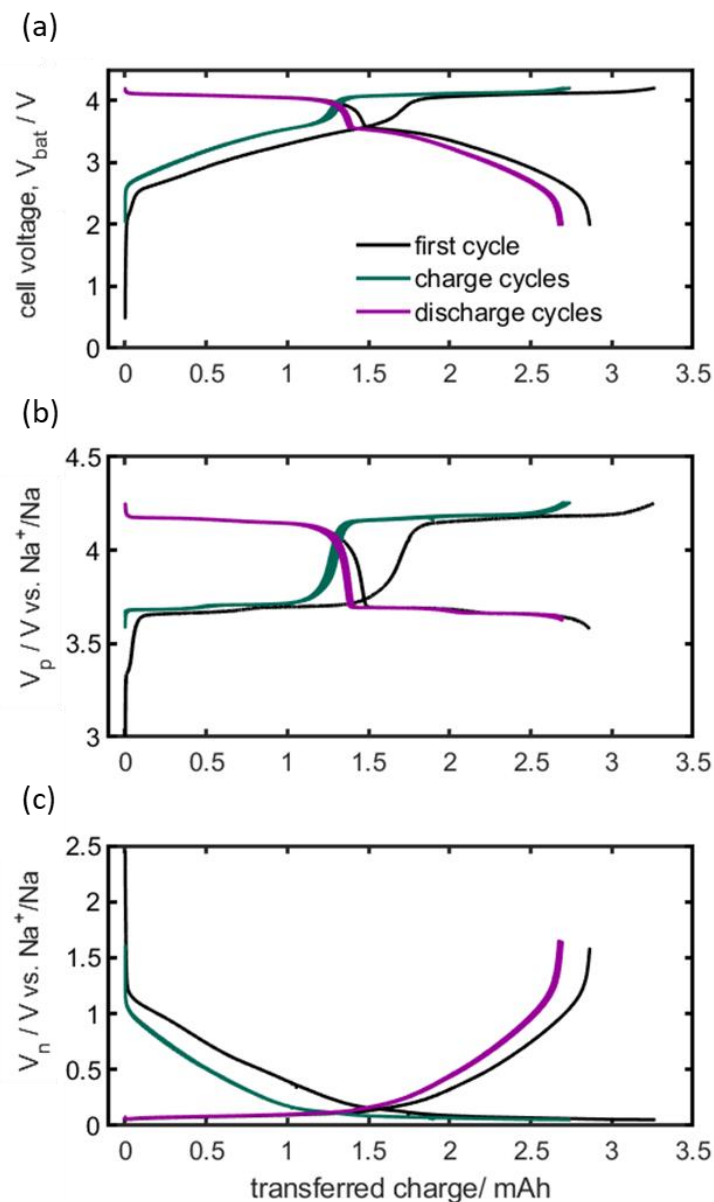


Fig. 6.12. Formation cycles of the HC//NVPF SIB cell showing the first cycle (black line), charge cycles (green line), and discharge cycles (purple line) obtained at 0.2 mA (0.07 C). Full cell voltage profiles (a). NVPF cathode voltage profiles (b). HC anode voltage profiles (c).

Fig. 6.13 shows the 5th (dis)charge cycle during formation. **Fig. 6.13** (a) shows profiles of V_{bat} while the individual voltage profiles V_p and V_n are shown in **Fig. 6.13** (b) and (c), respectively. It should be emphasized that the difference $V_p - V_n$ exactly matches V_{bat} . For example, at the lower cutoff voltage of 2 V, $V_p = 3.64$ V and $V_n = 1.64$ V vs. Na^+/Na , as expected. A characteristic feature of the HC//NVPF voltage profiles is the pronounced voltage difference between (dis)charge cycles. This phenomenon was also identified in the half-cell (dis)charge profiles (**Fig. 6.6** (a) and **Fig. 6.7** (a)). Integration of the area between the (dis)charge voltage curves for V_p and V_n and comparing these two areas to the area in V_{bat} reveals that V_n accounts for 60 % of the total voltage difference in full cell (dis)charge cycles. Therefore, the HC electrode has the largest contribution to the round-trip energy loss.

The SIB shown in **Fig. 6.13** is designed to maximize energy density in terms of electrode balancing. At full charge, the HC anode attains a high gravimetric capacity of 177 mAh g^{-1} at a low electrode potential at 0.05 V. During the same charging cycle, the NVPF cathode also attains a high reversible capacity of 89 mAh g^{-1} at 4.25 V. These gravimetric capacity calculations were based on the electrode loading of 6 mg cm^{-2} for HC and 12 mg cm^{-2} for NVPF. Nevertheless, safely charging such a high energy density SIB can be quite challenging because of the strong rate-dependent storage capacity of the HC electrode, especially in the low voltage plateau region (see **Fig. 6.7** (d)). This challenge implies very low charging rates must be applied to reach full charging capacities. In practice, this will inevitably prolong the charging period of energy-optimized SIBs using HC anodes.

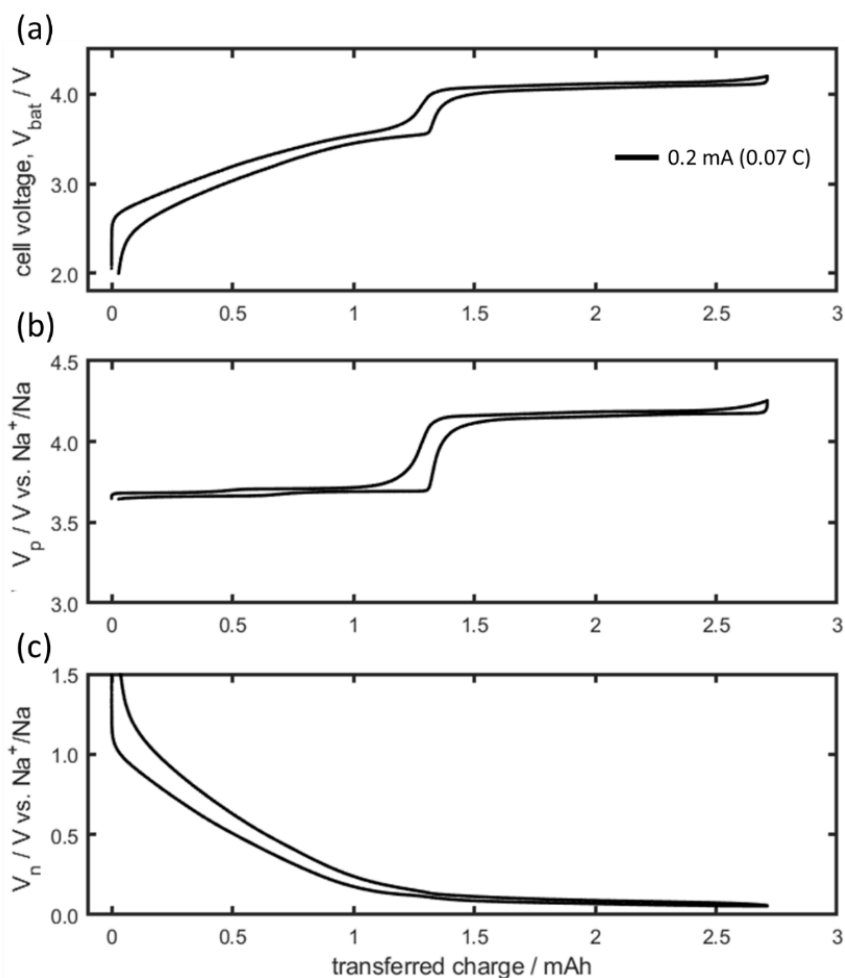


Fig. 6.13. 5th (dis)charge cycles during the formation of HC//NVPF full cell at 0.2 mA (0.07 C). Full cell voltage profile (a). NVPF cathode voltage profile (b). HC anode voltage profile (c). (b) and (c) measured with respect to the Na-RE.

Fig. 6.14 shows the voltage discharge curves of an HC//NVPF SIB at the various indicated discharge currents in the operation range of 2 to 4.2 V. **Fig. 6.14** (a) shows V_{bat} measured between the NVPF and HC electrodes. **Fig. 6.14** (b) and (c) show V_p and the V_n measured *vs.* Na-RE, respectively. The capacity of the HC//NVPF full cell at 0.5 A m^{-2} (0.05 C) is 2.81 mAh (**Fig. 6.14** (a)). At higher discharge rates, the discharge capacity decreases due to kinetic and mass transport limitations. Increasing the discharge rate from 0.5 to 24 A m^{-2} (0.05 to 3 C), decreases the cell capacity from 2.81 to 0.94 mAh. This difference corresponds to a 66 % decrease in storage capacity.

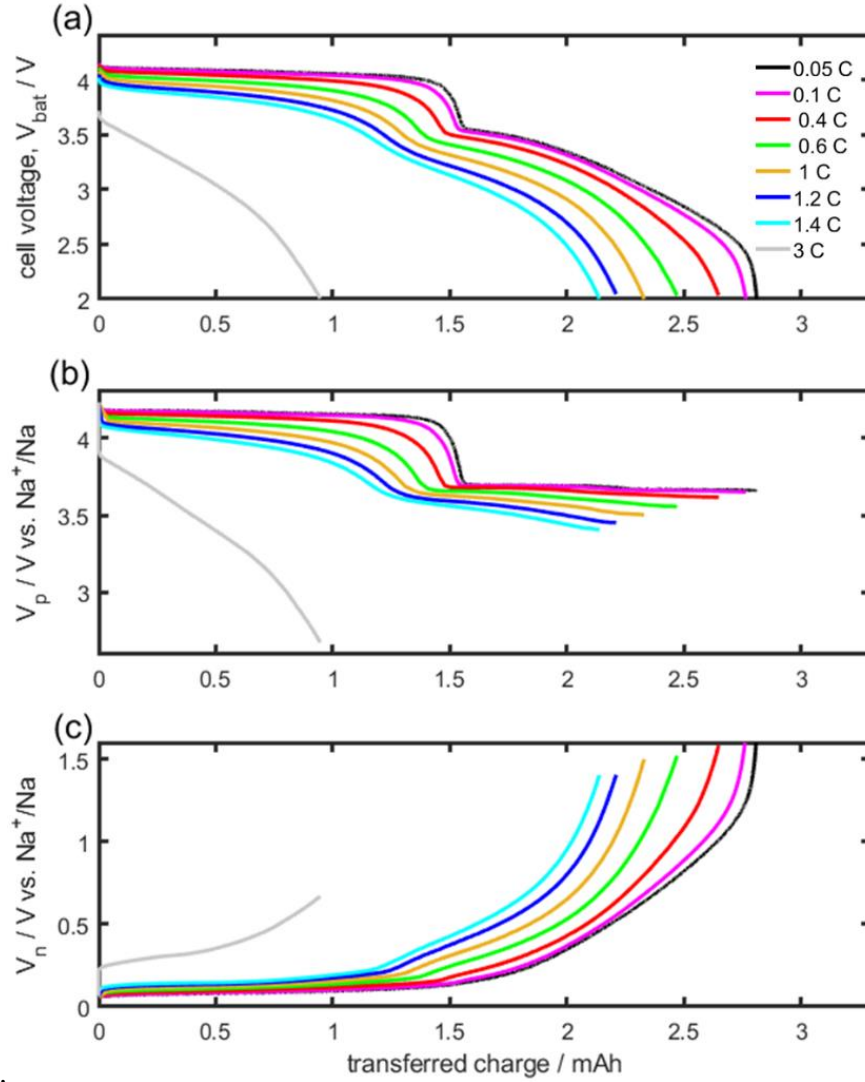


Fig. 6.14. HC/NVPF full cell voltage discharge profiles at different indicated C-rates (a). NVPF cathode potential during CC discharge (b). HC anode potential during CC discharge (c). (a) and (b) measured with respect to the Na-RE. Cycles obtained after 5 formation cycles

Another effect of increasing the discharge rate is the decrease in the cutoff electrode potentials of both V_p (b) and the V_n (c). The absolute potential change of an electrode (ΔV_m) can be calculated as

$$\Delta V_m = |V_m^{\text{ini}} - V_m^{\text{cut}}|, \quad m = \{n, p\} \quad (6.4)$$

where V_m^{ini} is the initial OCV of electrode m at full charge and V_m^{cut} is the cutoff electrode potential of electrode m at a given discharge rate. ΔV_m thus defines the contribution of electrode m to the full cell voltage drop. Therefore, the electrode with the largest ΔV_m can be viewed as the discharge

capacity-limiting electrode at a given C-rate. At the slow discharge rate of 0.1 C, the negative electrode is the discharge capacity-limiting electrode because $\Delta V_p = 0.7$ V is less than $\Delta V_n = 1.5$ V. However, at 3C discharge rate, the positive electrode becomes the discharge capacity-limiting electrode because $\Delta V_p = 1.6$ V is larger than $\Delta V_n = 0.6$ V. This means that the full cell V_{bat} profiles are dominated by the voltage change of the HC electrode at slow discharge rates. In contrast, at high discharge rates, they are dominated by the voltage change of the NVPF electrode. The high ΔV_p at high discharge rates corroborates the low diffusivity and rate constants found in the NVPF material (compare **Fig. 6.10** and **Fig. 6.11**).

Fig. 6.15 (a) shows the evaluation of individual electrode voltage drop as a function of the discharge current density. The initial voltage drop (iR) contributions from the anode and cathode are shown in **Fig. 6.15** (a). The initial voltage drop is calculated as the difference between V_m^{ini} and the electrode potential soon after the discharge current pulse is applied. Linear dependencies are obtained for both electrodes, consistent with Ohm's law. The slope of these lines determines the electrode Ohmic resistance, which includes that of the current collector, the porous electrode contact resistance, the porous matrix resistance, and electrolyte resistance. The NVPF and HC electrode specific resistances are calculated to be $99.4 \text{ } \Omega \text{ cm}^2$ and $43.2 \text{ } \Omega \text{ cm}^2$, respectively. Therefore, improvements to the SIB cells should further seek to reduce the NVPF electrode Ohmic resistance, which is very high and more than twice that of the HC electrode. This resistance results in Joule heating in the cells, which can hinder the scalability of the cells and modules in large battery pack installations. Previous modeling reports have identified contact resistance as the most dominant factor to the initial voltage drop [50,51]. Moreover, the NVPF material is a known poor electric conductor [52]. Therefore, there is a need to optimize the carbon conductive filler and NVPF electrode porosity. Such multiparameter optimization objectives can be guided by P2D model-based design [53].

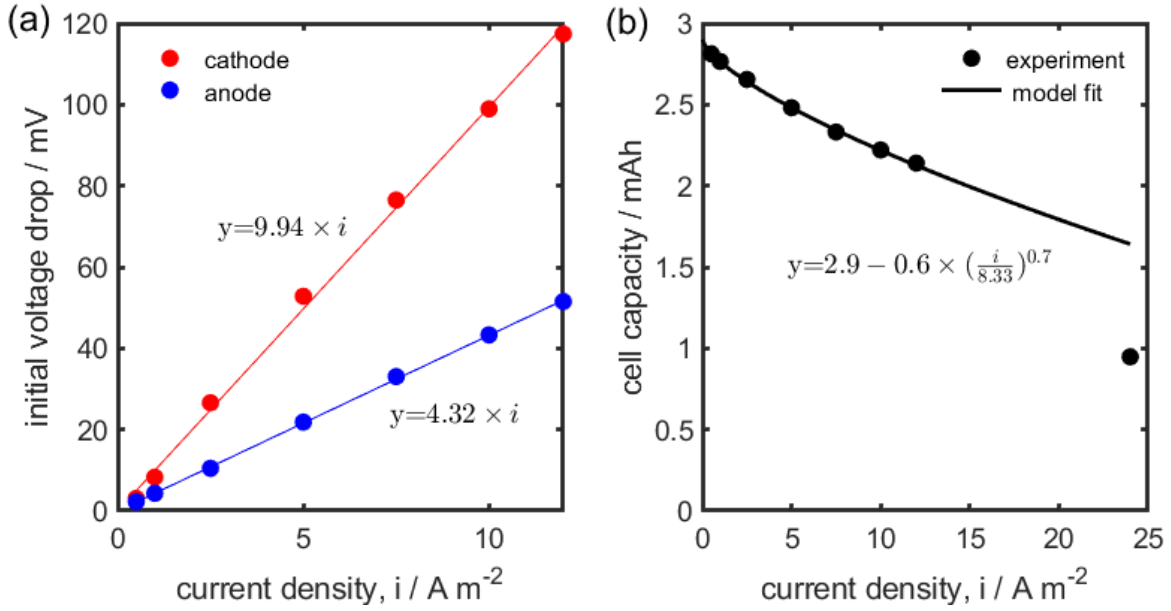


Fig. 6.15. Initial voltage drop contributions for the cathode (red) and anode (blue) at different discharge rates (a). Rate-dependent capacity as a function of current density (b).

The results in **Fig. 6.15** (a) may appear to contradict the low overpotentials in NVPF (shown in **Fig. 6.6** (d)) and the high overpotentials in HC (shown in **Fig. 6.7** (d)). This contradiction can be explained by the fact that Ohmic losses only consider electronic conductivity in the solid components of the electrode. In contrast, total overpotential also accounts for electrode kinetics and species mass transport in the electrodes and electrolytes [54].

Fig. 6.15 (b) shows the capacity decrease of the full cell SIB as a function of the discharge current density. The capacity decreases exponentially as a function of the discharge rate. Using this data, we can deduce an empirical model for the rate-dependent capacity of the SIB

$$\frac{C(i)}{C_0} = 1 - \left(1 - \frac{C(i_{1C})}{C_0}\right) \cdot \left(\frac{i}{i_{1C}}\right)^n, \quad (6.5)$$

where $C(i)$ is the cell capacity at discharge rate i [mAh], C_0 is the cell capacity extrapolated to zero current [mAh], i_{1C} is the 1-hour discharge current [A m^{-2}] and n is the dimensionless exponent. For this SIB, $C_0 = 2.9$ mAh, $C(i_{1C}) = 2.3$ mAh, $i_{1C} = 8.33 \text{ A m}^{-2}$ and $n = 0.7$. Eq. (6.5) is analogous to Peukert's law [55,56] and can be applied to deduce $C(i)$ for a constant discharge rate, and benchmark the rate performances of different SIBs. The only unknowns are C_0 and n which can be found by optimization. Alternatively, C_0 can be taken from the EMF. A further

simplification is that Eq. (6.5) is dimensionless and, therefore, can be applied to any SIB cell of a different dimension. Nevertheless, this relationship is not applicable at very high discharge rates.

Using the maximum cell capacity of 2.9 mAh and electrode loading of 12 and 6 mg cm⁻² for NVPF and HC, respectively, it is now possible to determine Q_m^{rev} the maximum reversible capacities of both electrodes. $Q_p^{rev} = 95 \text{ mAh g}^{-1}$ and $Q_n^{rev} = 190 \text{ mAh g}^{-1}$ for NVPF and HC electrodes, respectively. These values are close to the EMF capacities of 101 mAh g⁻¹ (**Fig. 6.6** (c)) and 222 (**Fig. 6.7** (c)) obtained in Na/NVPF and Na/HC half-cells, respectively. The half-cell and full cell values, therefore, only differ slightly.

For modeling purposes, it is also convenient to determine the maximum and minimum reversible concentrations in the particles. This definition can be given as

$$c_{1,m}^{max} = 3.6 \frac{\rho_m Q_m^{max}}{F}, \quad m = \{n, p\} \quad (6.6)$$

$$c_{1,m}^{min} = 3.6 \frac{\rho_m Q_m^{min}}{F}, \quad m = \{n, p\} \quad (6.7)$$

where $c_{1,m}^{max}$ and $c_{1,m}^{min}$ are the maximum and minimum concentrations in the electrode particles, respectively [mol m⁻³], ρ_m is the active material density [g m⁻³], Q_m^{max} the maximum gravimetric capacity in the electrode [mAh g⁻¹], Q_m^{min} the non-extractable charge [mAh g⁻¹], and F is the Faraday constant 96485 [C mol⁻¹]. Factor 3.6 originates from the conversion of charge units from coulomb to mAh. Based on Eq. (6.1), $Q_p^{max} = 128 \text{ mAh g}^{-1}$, while $Q_n^{max} = 222 \text{ mAh g}^{-1}$ is based on the EMF since there is no general equation for charge insertion in HC. **Table 6.2** summarizes the electrode parameters deduced from the above electrochemical tests.

Table 6.2. SIB parameters concluded from the electrochemical investigations.

Parameter	Unit	Description	NVPF electrode	HC electrode	Cell
C_{cell}	mAh	Cell capacity ^(a)	-	-	2.9
M_m	mg cm ⁻²	Active mass loading	12	6	-
Q_m^{rev}	mAh g ⁻¹	Reversible capacity ^(b)	95	190	-
Q_m^{max}	mAh g ⁻¹	Maximum capacity ^(c)	128	222	-
Q_m^{min}	mAh g ⁻¹	Non-extractable charge ^(d)	33	32	-
$c_{1,m}^{\text{max}}$	kmol m ⁻³	Max. concentration of Na ⁺	15.3	16.2	-
$c_{1,m}^{\text{min}}$	kmol m ⁻³	Min. concentration of Na ⁺	3.9	2.3	-
s_m^{max}	—	Maximum stoichiometric index	1	1	-
s_m^{min}	—	Minimum stoichiometric index	0.25	0.14	-
$R_{\text{contact},m}$	Ω cm ²	Contact resistance	99.4	43.2	142.6

(a) Based on extrapolation to zero current of the HC//NVPF SIB reversible capacity. (b) Reversible electrode capacity from full cell measurements, $Q_m^{\text{rev}} = C_{\text{cell}}/(M_m \cdot A)$. (c) Based on the theoretical capacity of NVPF and EMF capacity of HC. (d) $Q_m^{\text{min}} = Q_m^{\text{max}} - Q_m^{\text{rev}}$ is the non-extractable charge.

Another figure of merit to benchmark the performance of the HC//NVPF complete SIB is the Ragone plot, a logarithmic plot of energy density vs. power density and herein shown in **Fig. 6.16**. The energy density is calculated based on the total mass loading of the active materials (*i.e.*, 6 mg cm⁻² HC and 12 mg cm⁻² NVPF). Although high power operations such as discharge in less than 12 minutes are possible, there is a significant loss of energy density at these high rates. Considering the results in **Fig. 6.10** (b) and **Fig. 6.15** (a), the discharge power density of the HC//NVPF SIB is limited by the performance of NVPF at high rates due to the material's low solid-state diffusivity and high Ohmic drop. While low discharge rates, such as discharge in 5 hours (0.2 C), maximize the energy density and efficiency of the SIB, such operations, however, come at the inconvenience of low power density. The optimum compromise between energy and

power density is therefore found at the "knee" of the Ragone plot, corresponding to approximately the 1 C-rate (8.33 A m^{-2}) for the investigated electrode configuration.

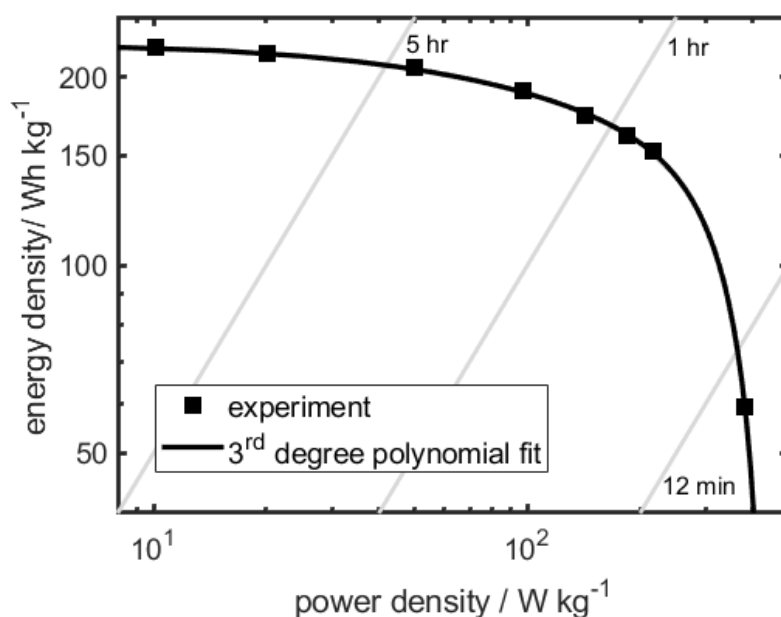


Fig. 6.16. Experimentally obtained Ragone plot for an HC//NVPF SIB.

6.4 Conclusions

This Chapter presented experimental results of sodium-ion battery (SIB) electrode materials based on hard carbon (HC) anode and $\text{Na}_3\text{V}_2(\text{PO}_4)_2\text{F}_3$ (NVPF) cathode. The experiments were conducted in half-cell, and full cell setups wherein a Na-reference electrode (Na-RE) was used as a third electrode.

Based on the analysis of physical properties, the electrode's particles generally exhibit irregular shapes and a wide particle size distribution. This observation is most evident in the HC particles. The knowledge of the particle sizes allowed the determination of the diffusion coefficients and the kinetic rate constants as a function of transferred charge. The results show that HC's diffusion coefficient is an order of magnitude higher than that of NVPF. As a result, improving the high-rate performance of the SIB is a question of overcoming diffusion mass transport limitations.

In the analysis of the full cell, the HC electrode shows impressively low Ohmic resistance and high discharge rate capability. However, the HC anode contributes 60 % of the total voltage

differences between (dis)charge cycles at low rates. Moreover, accessing the maximum capacity of the HC electrodes using constant current charging proved a challenge, even at very low currents. This drawback could hinder the fast-charging operations of HC-based SIBs. Battery management will undoubtedly require smart algorithms to attain the maximum capacity safely.

On the cathode side, the NVPF electrode exhibits outstanding performance in terms of low overpotentials and capacity retention at low rates. However, the NVPF electrode exhibits more than twice the Ohmic resistance of the HC electrode. Further, it becomes the limiting electrode at high discharge rates. The poor rate performance is related to the low diffusion coefficient in the material. The high Ohmic resistance is mainly attributed to the low NVPF conductivity. This Ohmic resistance can also result in Joule heating challenges in battery thermal management when the cells are scaled up. Therefore, NVPF electrode improvement should focus on optimizing the particle sizes and carbon conductive additive. Other strategies include carbon-coating on the NVPF particles as well as the Al current collectors.

Overall, the performances of the HC//NVPF SIBs are promising, and the results herein demonstrate chemistry and technology with real prospects for scale-up. This conclusion can be drawn because the issues outlined above can be addressed through electrode design improvements. SIBs can thus be expected to drop-in replace incumbent technologies in myriad battery energy storage applications, in particular the stationary applications of peak shaving, time-shifting, and congestion relief. This complementary feature of SIBs will further alleviate Li supply shortage risk and facilitate the integration of intermittent energy sources in electricity grids.

References

- [1] T. Broux, F. Fauth, N. Hall, Y. Chatillon, M. Bianchini, T. Bamine, J.-B. Leriche, E. Suard, D. Carlier, Y. Reynier, L. Simonin, C. Masquelier, L. Croguennec, High Rate Performance for Carbon-Coated $\text{Na}_3\text{V}_2(\text{PO}_4)_2\text{F}_3$ in Na-Ion Batteries, *Small Methods* **3** (2019) 1800215. <https://doi.org/10.1002/smtd.201800215>.
- [2] J. Ayre, 18650 Sodium-Ion Battery Developed At RS2E, CleanTechnica. (2015). <https://cleantechnica.com/2015/12/01/18650-sodium-ion-battery-developed-at-rs2e/> (accessed April 14, 2020).
- [3] J. Barker, M.Y. Saidi, J.L. Swoyer, A sodium-ion cell based on the fluorophosphate compound NaVPO_4F , *Electrochemical and Solid-State Letters* **6** (2003) A1–A4.
- [4] M. Bianchini, N. Brisset, F. Fauth, F. Weill, E. Elkaim, E. Suard, C. Masquelier, L. Croguennec, $\text{Na}_3\text{V}_2(\text{PO}_4)_2\text{F}_3$ Revisited: A High-Resolution Diffraction Study, *Chem. Mater.* **26** (2014) 4238–4247. <https://doi.org/10.1021/cm501644g>.
- [5] M. Bianchini, F. Fauth, N. Brisset, F. Weill, E. Suard, C. Masquelier, L. Croguennec, Comprehensive Investigation of the $\text{Na}_3\text{V}_2(\text{PO}_4)_2\text{F}_3$ – $\text{NaV}_2(\text{PO}_4)_2\text{F}_3$ System by Operando High Resolution Synchrotron X-ray Diffraction, *Chem. Mater.* **27** (2015) 3009–3020. <https://doi.org/10.1021/acs.chemmater.5b00361>.
- [6] R.K.B. Gover, A. Bryan, P. Burns, J. Barker, The electrochemical insertion properties of sodium vanadium fluorophosphate, $\text{Na}_3\text{V}_2(\text{PO}_4)_2\text{F}_3$, *Solid State Ionics*. **177** (2006) 1495–1500. <https://doi.org/10.1016/j.ssi.2006.07.028>.
- [7] J. Barker, R.K.B. Gover, P. Burns, A.J. Bryan, Hybrid-Ion A Lithium-Ion Cell Based on a Sodium Insertion Material, *Electrochem. Solid-State Lett.* **9** (2006) A190–A192. <https://doi.org/10.1149/1.2168288>.
- [8] N. Eshraghi, S. Caes, A. Mahmoud, R. Cloots, B. Vertruyen, F. Boschini, Sodium vanadium (III) fluorophosphate/carbon nanotubes composite (NVPF/CNT) prepared by spray-drying: good electrochemical performance thanks to well-dispersed CNT network within NVPF particles, *Electrochimica Acta* **228** (2017) 319–324. <https://doi.org/10.1016/j.electacta.2017.01.026>.
- [9] R. A. Shakoor, D.-H. Seo, H. Kim, Y.-U. Park, J. Kim, S.-W. Kim, H. Gwon, S. Lee, K. Kang, A combined first principles and experimental study on $\text{Na}_3\text{V}_2(\text{PO}_4)_2\text{F}_3$ for rechargeable Na batteries, *Journal of Materials Chemistry* **22** (2012) 20535–20541. <https://doi.org/10.1039/C2JM33862A>.
- [10] P. Serras, V. Palomares, A. Goñi, P. Kubiak, T. Rojo, Electrochemical performance of mixed valence $\text{Na}_3\text{V}_2\text{O}_{2x}(\text{PO}_4)_2\text{F}_{3-2x}/\text{C}$ as cathode for sodium-ion batteries, *Journal of Power Sources* **241** (2013) 56–60. <https://doi.org/10.1016/j.jpowsour.2013.04.094>.
- [11] K. Chayambuka, G. Mulder, D.L. Danilov, P.H.L. Notten, Sodium-Ion Battery Materials and Electrochemical Properties Reviewed, *Advanced Energy Materials* **8** (2018) 1800079. <https://doi.org/10.1002/aenm.201800079>.
- [12] D.A. Stevens, J.R. Dahn, High Capacity Anode Materials for Rechargeable Sodium-Ion Batteries, *J. Electrochem. Soc.* **147** (2000) 1271–1273. <https://doi.org/10.1149/1.1393348>.
- [13] S. Qiu, L. Xiao, M.L. Sushko, K.S. Han, Y. Shao, M. Yan, X. Liang, L. Mai, J. Feng, Y. Cao, X. Ai, H. Yang, J. Liu, Manipulating Adsorption–Insertion Mechanisms in Nanostructured Carbon Materials for High-Efficiency Sodium Ion Storage, *Adv. Energy Mater.* **7** (2017) n/a-n/a. <https://doi.org/10.1002/aenm.201700403>.

- [14] P. Tsai, S.-C. Chung, S. Lin, A. Yamada, Ab initio study of sodium intercalation into disordered carbon, *Journal of Materials Chemistry A* **3** (2015) 9763–9768. <https://doi.org/10.1039/C5TA01443C>.
- [15] C. Bommier, T.W. Surta, M. Dolgos, X. Ji, New Mechanistic Insights on Na-Ion Storage in Nongraphitizable Carbon, *Nano Lett.* **15** (2015) 5888–5892. <https://doi.org/10.1021/acs.nanolett.5b01969>.
- [16] B. Zhang, C.M. Ghimbeu, C. Laberty, C. Vix-Guterl, J.-M. Tarascon, Correlation Between Microstructure and Na Storage Behavior in Hard Carbon, *Adv. Energy Mater.* **6** (2016) n/a–n/a. <https://doi.org/10.1002/aenm.201501588>.
- [17] N. Jin, D.L. Danilov, P.M.J.V. den Hof, M.C.F. Donkers, Parameter estimation of an electrochemistry-based lithium-ion battery model using a two-step procedure and a parameter sensitivity analysis, *International Journal of Energy Research* **42** (2018) 2417–2430. <https://doi.org/10.1002/er.4022>.
- [18] C.M. Doyle, Design and Simulation of Lithium Rechargeable Batteries, Lawrence Berkeley National Laboratory. (1995). <http://escholarship.org/uc/item/6j87z0sp> (accessed April 11, 2017).
- [19] C.-H. Chen, F.B. Planella, K. O'Regan, D. Gastol, W.D. Widanage, E. Kendrick, Development of Experimental Techniques for Parameterization of Multi-scale Lithium-ion Battery Models, *J. Electrochem. Soc.* **167** (2020) 080534. <https://doi.org/10.1149/1945-7111/ab9050>.
- [20] K. Chayambuka, G. Mulder, D.L. Danilov, P.H.L. Notten, Determination of state-of-charge dependent diffusion coefficients and kinetic rate constants of phase changing electrode materials using physics-based models, *Journal of Power Sources Advances* **9** (2021) 100056. <https://doi.org/10.1016/j.powera.2021.100056>.
- [21] EU H2020 Program, Naiades, Sodium ion batteries, (2020). <http://www.naiades.eu/> (accessed August 29, 2017).
- [22] Naiades | Sodium ion batteries, (n.d.). <https://www.naiades.eu/> (accessed April 15, 2020).
- [23] K. Chayambuka, G. Mulder, D.L. Danilov, P.H.L. Notten, From Li-Ion Batteries toward Na-Ion Chemistries: Challenges and Opportunities, *Advanced Energy Materials* **10** (2020) 2001310. <https://doi.org/10.1002/aenm.202001310>.
- [24] R. Dugas, J.D. Forero-Saboya, A. Ponrouch, Methods and Protocols for Reliable Electrochemical Testing in Post-Li Batteries (Na, K, Mg, and Ca), *Chem. Mater.* **31** (2019) 8613–8628. <https://doi.org/10.1021/acs.chemmater.9b02776>.
- [25] J. Conder, C. Villevieille, How reliable is the Na metal as a counter electrode in Na-ion half cells?, *Chemical Communications* **55** (2019) 1275–1278. <https://doi.org/10.1039/C8CC07852A>.
- [26] D.I. Iermakova, R. Dugas, M.R. Palacín, A. Ponrouch, On the Comparative Stability of Li and Na Metal Anode Interfaces in Conventional Alkyl Carbonate Electrolytes, *J. Electrochem. Soc.* **162** (2015) A7060. <https://doi.org/10.1149/2.0091513jes>.
- [27] New separator for PAT insulation sleeves | EL-CELL, (n.d.). <https://el-cell.com/new-separator-for-pat-insulation-sleeves/> (accessed March 5, 2021).
- [28] R. Dugas, B. Zhang, P. Rozier, J.M. Tarascon, Optimization of Na-Ion Battery Systems Based on Polyanionic or Layered Positive Electrodes and Carbon Anodes, *J. Electrochem. Soc.* **163** (2016) A867–A874. <https://doi.org/10.1149/2.0051605jes>.

- [29] X. Chen, Y. Zheng, W. Liu, C. Zhang, S. Li, J. Li, High-performance sodium-ion batteries with a hard carbon anode: transition from the half-cell to full-cell perspective, *Nanoscale* **11** (2019) 22196–22205. <https://doi.org/10.1039/C9NR07545C>.
- [30] W.H. Smyrl, J. Newman, Current Distribution at Electrode Edges at High Current Densities, *J. Electrochem. Soc.* **136** (1989) 132. <https://doi.org/10.1149/1.2096572>.
- [31] A. Verma, K. Smith, S. Santhanagopalan, D. Abraham, K.P. Yao, P.P. Mukherjee, Galvanostatic Intermittent Titration and Performance Based Analysis of LiNi_{0.5}Co_{0.2}Mn_{0.3}O₂ Cathode, *J. Electrochem. Soc.* **164** (2017) A3380. <https://doi.org/10.1149/2.1701713jes>.
- [32] C.-J. Bae, C.K. Erdonmez, J.W. Halloran, Y.-M. Chiang, Design of Battery Electrodes with Dual-Scale Porosity to Minimize Tortuosity and Maximize Performance, *Advanced Materials* **25** (2013) 1254–1258. <https://doi.org/10.1002/adma.201204055>.
- [33] The impact of particle size and shape on battery electrode slurry formation | Malvern Panalytical, (n.d.). <https://www.malvernpanalytical.com/en/learn/knowledge-center/application-notes/AN170103BatterySlurryParticleSizeShape> (accessed March 9, 2021).
- [34] J. Maurath, B. Bitsch, Y. Schwegler, N. Willenbacher, Influence of particle shape on the rheological behavior of three-phase non-brownian suspensions, *Colloids and Surfaces A: Physicochemical and Engineering Aspects* **497** (2016) 316–326. <https://doi.org/10.1016/j.colsurfa.2016.03.006>.
- [35] Y. Sumiyama, N. Sakai (Sumitomo Bakelite Co.), JP2016136452 (A), 2016. https://worldwide.espacenet.com/publicationDetails/biblio?FT=D&date=20160728&DB=EPODOC&locale=en_EP&CC=JP&NR=2016136452A&KC=A&ND=4 (accessed March 5, 2018).
- [36] E. Berg, C. Villevieille, D. Streich, S. Trabesinger, P. Novak, Rechargeable Batteries: Grasping for the Limits of Chemistry, *J. Electrochem. Soc.* **162** (2015) A2468–A2475.
- [37] G. Hasegawa, K. Kanamori, N. Kannari, J. Ozaki, K. Nakanishi, T. Abe, Hard Carbon Anodes for Na-Ion Batteries: Toward a Practical Use, *ChemElectroChem.* **2** (2015) 1917–1920. <https://doi.org/10.1002/celec.201500412>.
- [38] K.-H. Chen, V. Goel, M.J. Namkoong, M. Wied, S. Müller, V. Wood, J. Sakamoto, K. Thornton, N.P. Dasgupta, Enabling 6C Fast Charging of Li-Ion Batteries with Graphite/Hard Carbon Hybrid Anodes, *Advanced Energy Materials* **11** (2021) 2003336. <https://doi.org/10.1002/aenm.202003336>.
- [39] C.F. Armer, M. Lübke, M.V. Reddy, J.A. Darr, X. Li, A. Lowe, Phase change effect on the structural and electrochemical behaviour of pure and doped vanadium pentoxide as positive electrodes for lithium ion batteries, *Journal of Power Sources* **353** (2017) 40–50. <https://doi.org/10.1016/j.jpowsour.2017.03.121>.
- [40] C. Delmas, H. Cognac-Auradou, J. Cocciantelli, M. Menetrier, J. Doumerc, The Li_xV₂O₅ system: An overview of the structure modifications induced by the lithium intercalation, *Solid State Ionics* **69** (1994) 257–264. [https://doi.org/10.1016/0167-2738\(94\)90414-6](https://doi.org/10.1016/0167-2738(94)90414-6).
- [41] N. Kazemi, D.L. Danilov, L. Haverkate, N.J. Dudney, S. Unnikrishnan, P.H.L. Notten, Modeling of all-solid-state thin-film Li-ion batteries: Accuracy improvement, *Solid State Ionics* **334** (2019) 111–116. <https://doi.org/10.1016/j.ssi.2019.02.003>.
- [42] D. Danilov, R. a. H. Niessen, P.H.L. Notten, Modeling All-Solid-State Li-Ion Batteries, *J. Electrochem. Soc.* **158** (2011) A215–A222. <https://doi.org/10.1149/1.3521414>.

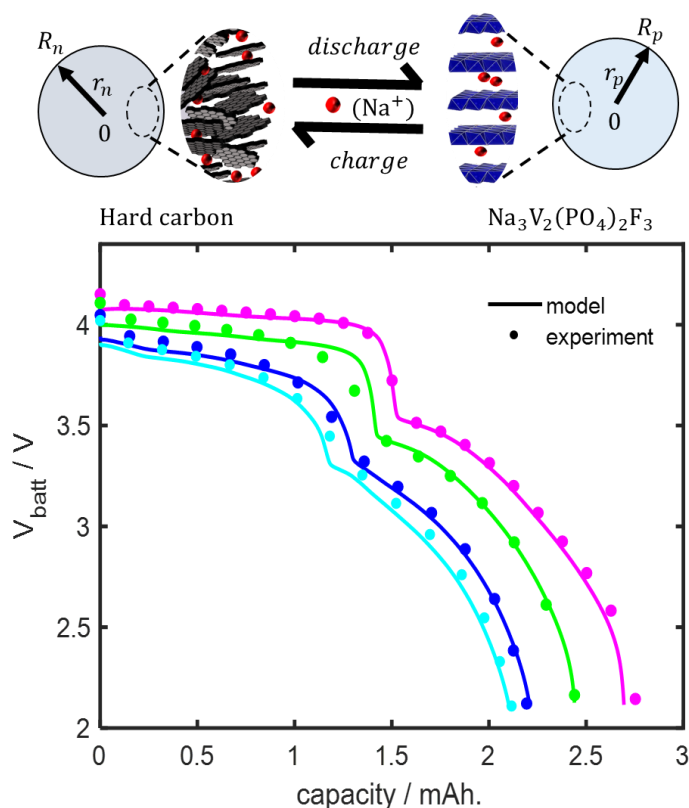
- [43] D. Li, D. L. Danilov, L. Gao, Y. Yang, P.H.L. Notten, Degradation Mechanisms of C6/LiFePO₄ Batteries: Experimental Analyses of Cycling-induced Aging, *Electrochimica Acta* **210** (2016) 445–455. <https://doi.org/10.1016/j.electacta.2016.05.091>.
- [44] E. Irisarri, A. Ponrouch, M.R. Palacin, Review—Hard Carbon Negative Electrode Materials for Sodium-Ion Batteries, *J. Electrochem. Soc.* **162** (2015) A2476–A2482. <https://doi.org/10.1149/2.0091514jes>.
- [45] A. Ledovskikh, D. Danilov, P.H.L. Notten, Modeling of hydrogen storage in hydride-forming materials: Equilibrium gas-phase kinetics, *Phys. Rev. B* **76** (2007) 064106. <https://doi.org/10.1103/PhysRevB.76.064106>.
- [46] R.B. Smith, E. Khoo, M.Z. Bazant, Intercalation Kinetics in Multiphase-Layered Materials, *J. Phys. Chem. C* **121** (2017) 12505–12523. <https://doi.org/10.1021/acs.jpcc.7b00185>.
- [47] J. Li, F. Yang, X. Xiao, M.W. Verbrugge, Y.-T. Cheng, Potentiostatic intermittent titration technique (PITT) for spherical particles with finite interfacial kinetics, *Electrochimica Acta* **75** (2012) 56–61. <https://doi.org/10.1016/j.electacta.2012.04.050>.
- [48] A. Hess, Q. Roode-Gutzmer, C. Heubner, M. Schneider, A. Michaelis, M. Bobeth, G. Cuniberti, Determination of state of charge-dependent asymmetric Butler–Volmer kinetics for Li_xCoO₂ electrode using GITT measurements, *Journal of Power Sources* **299** (2015) 156–161. <https://doi.org/10.1016/j.jpowsour.2015.07.080>.
- [49] K. Chayambuka, G. Mulder, D.L. Danilov, P.H.L. Notten, A Hybrid Backward Euler Control Volume Method to Solve the Concentration-Dependent Solid-State Diffusion Problem in Battery Modeling, *Journal of Applied Mathematics and Physics* **8** (2020) 1066–1080. <https://doi.org/10.4236/jamp.2020.86083>.
- [50] M. Doyle, J. Newman, A.S. Gozdz, C.N. Schmutz, J.-M. Tarascon, Comparison of Modeling Predictions with Experimental Data from Plastic Lithium Ion Cells, *J. Electrochem. Soc.* **143** (1996) 1890–1903. <https://doi.org/10.1149/1.1836921>.
- [51] D.E. Stephenson, E.M. Hartman, J.N. Harb, D.R. Wheeler, Modeling of particle-particle interactions in porous cathodes for lithium-ion batteries, *Journal of The Electrochemical Society* **154** (2007) A1146–A1155.
- [52] F. Sauvage, E. Quarez, J.-M. Tarascon, E. Baudrin, Crystal structure and electrochemical properties vs. Na⁺ of the sodium fluorophosphate Na_{1.5}VOPO₄F_{0.5}, *Solid State Sciences* **8** (2006) 1215–1221. <https://doi.org/10.1016/j.solidstatesciences.2006.05.009>.
- [53] S. F. Schneider, C. Bauer, P. Novák, E. J. Berg, A modeling framework to assess specific energy, costs and environmental impacts of Li-ion and Na-ion batteries, *Sustainable Energy & Fuels* **3** (2019) 3061–3070. <https://doi.org/10.1039/C9SE00427K>.
- [54] W. Wang, X. Wei, D. Choi, X. Lu, G. Yang, C. Sun, Chapter 1 - Electrochemical cells for medium- and large-scale energy storage: fundamentals, in: C. Menictas, M. Skyllas-Kazacos, T.M. Lim (Eds.), *Advances in Batteries for Medium and Large-Scale Energy Storage*, Woodhead Publishing, 2015: pp. 3–28. <https://doi.org/10.1016/B978-1-78242-013-2.00001-7>.
- [55] D. Doerffel, S.A. Sharkh, A critical review of using the Peukert equation for determining the remaining capacity of lead-acid and lithium-ion batteries, *Journal of Power Sources* **155** (2006) 395–400. <https://doi.org/10.1016/j.jpowsour.2005.04.030>.
- [56] G. Mulder, N. Omar, S. Pauwels, M. Meeus, F. Leemans, B. Verbrugge, W. De Nijs, P. Van den Bossche, D. Six, J. Van Mierlo, Comparison of commercial battery cells in relation to material properties, *Electrochimica Acta* **87** (2013) 473–488. <https://doi.org/10.1016/j.electacta.2012.09.042>.

CHAPTER 7

PHYSICS-BASED SIB MODEL AND VALIDATION

Abstract

Having described the fundamental parts needed to construct a model for SIBs, this Chapter introduces a P2D model for a full cell SIB based on HC and NVPF electrodes. Parametrization of the model is based on experimental data and global optimization methods. Validation of the model results is based on the experimental results shown in the previous Chapter. It is shown that the model is highly accurate in predicting the discharge profiles of full cell HC//NVPF SIBs. In addition, internal battery states, such as the individual electrode potentials and concentrations, can be obtained from the model at different applied currents.



Parts of this Chapter have been submitted for publication as:

K Chayambuka, G Mulder, DL Danilov, PHL Notten, Physics-Based Modelling of Sodium-ion Batteries, Part II: Model validation, *Electrochimica Acta* (2021).

7.1 Introduction

The development of a new battery chemistry, such as the SIB, and the design of control algorithms for battery management systems (BMSs) is dependent on accurate, physics-based models. Such models give reliable information regarding the performance of battery electrodes, thus enabling design improvements and performance benchmarking.

The development of physics-based models for porous insertion electrodes can be traced to the pioneering work of West *et al.* [1] in the early 1980^s. This period incidentally coincided with the 'rocking chair' battery design, in which two insertion electrodes were used in commercial cells instead of metallic lithium anodes for safety reasons [2]. West's model described the coupled transport of ionic species in the electrolyte and electrodes using the principles of porous electrode theory, a theory which had been developed by Newman *et al.* [3]. However, West's model conceptualized a porous electrode as a monolithic slab with straight pores and high conductivity. Newman *et al.* [4,5] later improved this simplified model structure by treating electrode particles as a distinct phase in intimate contact with the electrolyte. Using the principles of homogenization, the particles were treated as a macro-homogeneous phase. Newman's model, therefore, provided the basic framework for the rigorous treatment of charge transport in discrete and conceptually spherical electrode particles. This multi-phase, multi-scale coupling is often referred to as the P2D model structure because of the 1D representation of the electrode thickness and an additional pseudo-dimension, representing the spherical radius of active particles at different electrode positions.

Various P2D models have been applied to different battery chemistries, such as lead-acid and nickel-metal hydride [6,7]. Although P2D models are widely accepted and demonstrate unparalleled accuracy and reliability, there remain practical challenges to parametrize new chemistries and integrate the models in BMS microcontrollers [8]. This is because the models are based on systems of coupled PDEs, which are computationally expensive and potentially non-convergent during execution [9]. This fundamental challenge has propelled a growing trend of using reduced-order models such as single-particle models [10–12], equivalent circuit models [13,14], and data-driven semi-empirical models [15,16].

Details of the reduced-order battery models have been published in thematic reviews for the interested reader [17,18]. Nevertheless, as models become increasingly simplified, the danger is

obtaining parameters that are detached from electrochemistry and physics. In the end, the simplified models cannot be reliably used as predicting tools to improve cell design because the underlying parameters lack physical meaning and are not valid outside the conditions of model parametrization. Therefore, the development of physics-based models remains an important undertaking to understand internal battery dynamics and provide a link with experimentally derived parameters. This development should carefully consider all relevant electrochemical processes involved in the given battery chemistry to achieve accurate physical models.

In this Chapter, a physics-based P2D model of a SIB full cell is presented for the first time to understand and improve the design of this emerging battery chemistry. The experiments used to derive parameters of a SIB based on HC as the anode/negative electrode and NVPF as cathode/positive electrode are described in Chapter 6. The electrolyte is composed of 1 kmol m^{-3} NaPF_6 salt dissolved in equal weight mixtures of EC and PC, $\text{EC}_{0.5}:\text{PC}_{0.5}$ (w/w) solvent. Based on experimental evidence, the SIB electrode and electrolyte parameters are concentration-dependent. As a result, concentration-dependent diffusion coefficients, kinetic rate constants, and conductivity are introduced to the P2D model.

The full cell SIB model is scripted in MATLAB, which uses a global optimization toolbox to determine parameters that could not be experimentally deduced. Using the genetic algorithm for the optimization procedure, the SIB model is validated by comparing the simulation results with experimental voltage data for the positive and negative electrode potentials. Analyses of the model results reveal mass transport limitations in the 1 kmol m^{-3} NaPF_6 $\text{EC}_{0.5}:\text{PC}_{0.5}$ (w/w) electrolyte and in the HC and NVPF active electrode particles. These results can further guide the design of SIB systems, which are expected to operate in power-demanding applications.

7.2 Description of the system components

Fig. 7.1 shows a detailed layout of a three-electrode SIB setup composed of an HC negative electrode, a separator, an NVPF positive electrode, and a metallic Na-RE. These are assembled in a PAT-Cell (EL-Cell GmbH). HC and NVPF electrodes, in this case, act as two working electrodes, and the Na-RE acts as a reference electrode of the first kind. The Na-RE is carefully positioned between the two working electrodes for accurate potential measurements while being electronically isolated from either electrode by the separator.

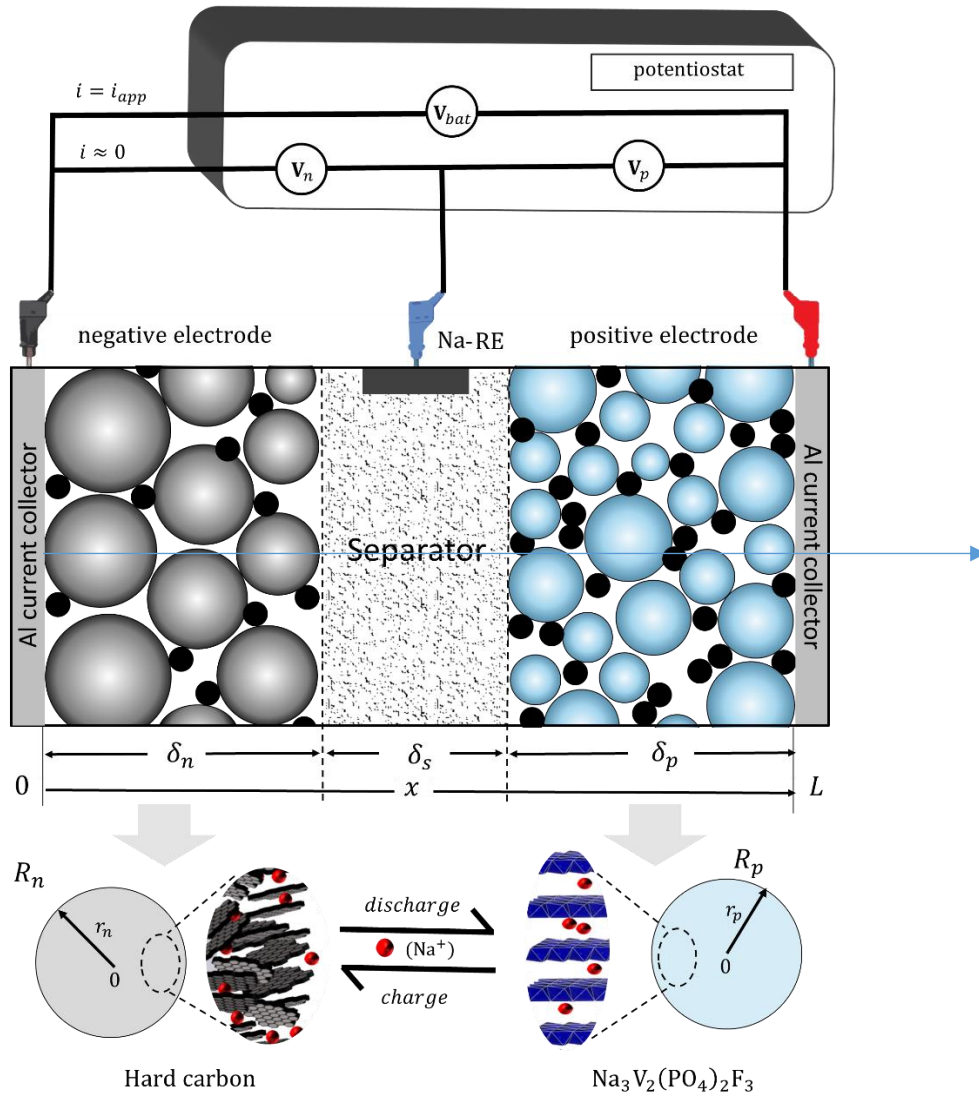


Fig. 7.1. HC/NVPF full cell configuration and potentiostat connections to the microporous battery SIB electrodes.

Based on the experimental characterizations in Chapter 6, the thickness of the negative electrode, the separator, and the positive electrode are $\delta_n = 64$, $\delta_s = 25$ and $\delta_p = 68$ μm , respectively. In addition, the average radii of the HC and NVPF electrode particles are $R_n = 3.48$ and $R_p = 0.59$ μm , respectively [19]. R_n is, therefore, 6 times larger than R_p on average. Both electrodes additionally contain graphitic conductive additives in order to enhance the electrical conductivity of the composite electrodes. These are represented in **Fig. 7.1** by black spheres. More

conductive additives are needed in the NVPF positive electrode because of the low electronic conductivity of the NVPF material [20,21].

Fig. 7.1 also shows the cable connections from the potentiostat to the three electrodes for automated cycling and cell voltage measurements. A current I_{app} [A] is specified in the potentiostat program to either charge or discharge the SIB. The Na-RE is connected to a high impedance lead of the potentiostat, which ensures a very low current passes through the RE. The three-electrode setup, therefore, allows for the accurate determination of individual electrode potentials *vs.* Na-RE. As a result, positive electrode potential (V_p), and the negative electrode potential (V_n), can be deconvoluted from the full cell voltage (V_{bat}) at different values of I_{app} .

From a modeling perspective, this knowledge of the individual electrode potentials is important for two reasons. First, the parameters for both electrodes can be independently optimized instead of relying only on V_{bat} , which is a combination of the two electrode potentials. In this way, parameters for the individual electrodes can be independently optimized. Second, the number of simultaneously optimized parameters is reduced, which increases optimization speed and model fidelity. Care, however, must be exercised on the position of the reference electrode to minimize overpotentials and voltage crosstalk between the anode and cathode.

7.3 Model description

In the isothermal P2D model described in this Chapter, the active particles are considered spherical. Another assumption is that the particle sizes are homogeneous and represented by the average particle radius. The model variables include the Na-concentration ($c_{\theta,m}$), the potential ($\varphi_{\theta,m}$), and current ($i_{\theta,m}$). The subscript θ symbolizes the phase of the variable, which can either be the solid phase ($\theta = 1$) or the liquid/electrolyte phase ($\theta = 2$), subscript m symbolizes the domain inside the battery stack, which can either be the negative electrode ($m = n$), the positive electrode ($m = p$) or the separator ($m = s$).

7.3.1 Mass transport in electrode particles

Fick's second law expresses the time-dependent radial transport of intercalated Na^+ inside the electrode active particles as

$$\frac{\partial c_{1,m}}{\partial t} = \frac{1}{r_m^2} \frac{\partial}{\partial r_m} \left(D_{1,m} r_m^2 \frac{\partial c_{1,m}}{\partial r_m} \right), \quad \forall t, m = \{n, p\}, 0 \leq r_m \leq R_m, \quad (7.1)$$

where $c_{1,m}$ is the concentration of the intercalated Na^+ [mol m^{-3}], $D_{1,m}$ is the solid-state diffusion coefficient [$\text{m}^2 \text{s}^{-1}$], r_m is the particle radius [m], and t is time [s]. At the particle surface ($r_m = R_m$) and at the center ($r_m = 0$), the flux/Neumann boundary conditions are applied to Eq. (7.1), implying

$$-D_{1,m} \frac{\partial c_{1,m}}{\partial r_m} \Big|_{r_m=R_m} = j_m, \quad m = \{n, p\} \quad (7.2)$$

$$\frac{\partial c_{1,m}}{\partial r_m} \Big|_{r_m=0} = 0, \quad m = \{n, p\} \quad (7.3)$$

where j_m is the interfacial flux of species [$\text{mol m}^{-2} \text{s}^{-1}$]. The boundary conditions in Eqs. (7.2) and (7.3) express the surface reaction flux and spherical symmetry, respectively. An initial condition is further required for the particle phase concentrations, which is defined as

$$c_{1,m}(r, t = 0) = c_{1,m}^0, \quad m = \{n, p\} \quad (7.4)$$

where $c_{1,m}^0$ is the initial Na^+ concentration inside the electrode particles. $c_{1,m}^0$ depends on the initial SOC of the active materials.

In the case of Na^+ intercalation with constant $D_{1,m}$ and R_m , Eqs. (7.1)-(7.4) can be solved by fast analytical methods [22,23]. R_m changes in intercalation active materials are generally very low. In the case of NVPF and HC electrode materials, unit cell volume changes of approximately 2 % have been reported [24]. However, experimental and modeling GITT results have shown that $D_{1,m}$ is strongly dependent on $c_{1,m}$ [19,25,26]. In other studies, $D_{1,p}$ has also been shown to vary by two orders of magnitude [25]. For these reasons, a concentration-dependent $D_{1,m}$ is used for the NVPF//HC SIB. As a result, the numerical method of the HBECV is applied instead of the analytical methods. The HBECV obtains fast and accurate solutions and has been described in Chapter 4 [27].

7.3.2 Electrode kinetics model

At the particle surface, the electrode kinetics can be described by the Butler-Volmer expression [28]

$$j_m = j_{0,m} \left[\frac{c_{1,m}^s}{\bar{c}_{1,m}} \exp\left(\frac{\alpha F}{RT} \eta_m^{ct}\right) - \frac{c_{1,m}^{max} - c_{1,m}^s}{c_{1,m}^{max} - \bar{c}_{1,m}} \frac{c_2}{\bar{c}_2} \exp\left(-\frac{(1-\alpha)F}{RT} \eta_m^{ct}\right) \right], \quad m = \{n, p\} \quad (7.5)$$

where $j_{0,m}$ is the exchange flux density of Na-ions across the electrode surface of the electrode particles [$\text{mol m}^{-2} \text{s}^{-1}$], α is the anodic transfer coefficient [-], R the gas constant [$8.314 \text{ J mol}^{-1} \text{ K}^{-1}$], T the temperature [K], F Faraday's constant $95485 \text{ [C mol}^{-1}\text{]}$, η_m^{ct} the charge transfer overpotential, $c_{1,m}^s$, $c_{1,m}^{max}$ and $\bar{c}_{1,m}$ the surface, maximum and average concentrations of intercalated Na^+ in the electrode particles, respectively [mol m^{-3}], and c_2 and \bar{c}_2 are the instantaneous and average concentrations of Na^+ in the electrolyte phase, respectively, [mol m^{-3}]. $j_{0,m}$ can be expressed as

$$j_{0,m} = F k_m (c_{1,m}^{max} - \bar{c}_{1,m})^{\alpha_a} (\bar{c}_2)^{\alpha_a} (\bar{c}_{1,m})^{\alpha_c}, \quad m = \{n, p\} \quad (7.6)$$

where k_m is the charge transfer rate constant [$\text{m}^{2.5} \text{ mol}^{-1.5} \text{s}^{-1}$]. The charge transfer overpotential, η_m^{ct} can then be expressed as

$$\eta_m^{ct} = \varphi_{1,m} - \varphi_{2,m} - U_m(c_{1,m}^s, T), \quad m = \{n, p\} \quad (7.7)$$

where $\varphi_{1,m}$, $\varphi_{2,m}$ and U_m are the electrode, electrolyte, and the EMF, respectively [V]. The EMF potentials for both the HC and NVPF electrodes were experimentally determined in Chapter 6.

7.3.3 Current distribution

Throughout the separator and porous electrode regions, the current is distributed between the electronic current density ($i_{1,m}$) and the ionic current density in the solid and electrolyte phases ($i_{2,m}$). Both $i_{1,m}$ and $i_{2,m}$ are related to the total applied current density $i_{app} = I_{app}/A_{cc}$ as

$$i_{app} = i_{1,m} + i_{2,m}, \quad \forall m. \quad (7.8)$$

Eq. (7.8) is a form of charge conservation law. Since $i_{1,s} = 0$ in the separator region (where $m = s$) this implies

$$i_{app} = i_{2,s}. \quad (7.9)$$

At the current collector boundaries of the porous electrodes

$$i_{2,n}|_{x=0} = i_{2,p}|_{x=L} = 0. \quad (7.10)$$

The boundary condition in Eq. (7.10) specifies that only an electronic current is present at the current collectors. Applying Eq. (7.8) therefore results in

$$i_{app} = i_{1,n}|_{x=0} = i_{1,p}|_{x=L}. \quad (7.11)$$

In the porous electrodes where $m = \{n, p\}$, $i_{1,m}$ can be modeled by Ohm's law

$$i_{1,m} = -\sigma_m^{eff} \frac{\partial \phi_{1,m}}{\partial x}, \quad m = \{n, p\} \quad (7.12)$$

where σ_m^{eff} is the effective electronic conductivity in the porous electrode [$\Omega^{-1} \text{ m}^{-1}$]. In addition, the derivative of $i_{2,m}$ is proportional to j_m in Eq. (7.5). This relation is expressed as

$$\frac{\partial i_{2,m}}{\partial x} = a_m F j_m, \quad m = \{n, p\} \quad (7.13)$$

where a_m is the specific surface area per unit volume of electrode [m^{-1}]. a_m is calculated from the particle radius and the electrode porosity as

$$a_m = \frac{3(1 - \epsilon_m^{el} - \epsilon_m^{filler})}{R_m}, \quad m = \{n, p\} \quad (7.14)$$

where ϵ_m^{el} and ϵ_m^{filler} are the electrolyte and additive filler volume fractions, respectively. ϵ_m^{filler} includes the binder and conductive filler additives.

7.3.4 Electrolyte potential and mass distribution

The dilute solution theory governs the electrolyte potential distribution in the liquid electrolytes. This theory is based on the Nernst-Planck equation, a classical description of the transport of charged ionic species in electrolyte media [29]. The dilute solution theory essentially considers binary interactions between ionic species and the solvent and neglects ion-ion pairing effects [30].

Because the $\text{NaPF}_6 \text{ EC}_{0.5} \text{ PC}_{0.5}$ (w/w) electrolyte does not show extensive ion-pairing effects in the concentration range of 0 to 2 mol kg^{-1} as earlier determined [31], electrolyte potential can thus be modeled by the following expression [32]

$$i_{2,m} = -\kappa_m^{eff} \frac{\partial \phi_{2,m}}{\partial x} + \frac{\kappa_m^{eff} RT}{F} (1 - 2t_+) \cdot \nabla \ln c_2, \quad \forall m \quad (7.15)$$

where κ_m^{eff} is effective ionic conductivity in the electrolyte in cell domain m [$\Omega^{-1} \text{ m}^{-1}$], and t_+ is the cationic transference number [-], defined as the fraction of $i_{2,s}$ due to cationic migration in the

absence of diffusion and convection forces. The definition of $\varphi_{2,m}$ results in the multiplier $(1 - 2t_+)$, which is different from the multiplier $2(1 - t_+)$ used in other works [33].

A Dirichlet boundary condition is thus defined for the electrolyte potential at the anode

$$\varphi_{2,n}|_{x=0} = 0 \quad (7.16)$$

Eq. (7.16) sets $\varphi_{2,n}$ as the reference potential for all potential difference measurements. Another option is to set $\varphi_{1,n}|_{x=0} = 0$, which is equivalent to grounding the anode. In either case, the position and choice of the reference potential do not affect the overpotentials and the overall cell voltage [4]. However, the convenience of the boundary condition in Eq. (7.16) is that electrode potentials $\varphi_{1,n}$ and $\varphi_{1,p}$ have values similar to those obtained experimentally using a reference electrode of the first kind. This property makes the model validation based on individual electrode potentials using the Na-RE straightforward.

The electrolyte concentration mass balance in the porous electrode region is expressed as

$$\frac{\partial c_2}{\partial t} = \frac{\partial}{\partial x} \left(D_{2,m}^{eff} \frac{\partial c_2}{\partial x} \right) + (1 - t_+) a_m j_m, \quad \forall t, m = \{n, p\} \quad (7.17)$$

and in the separator region as

$$\frac{\partial c_2}{\partial t} = \frac{\partial}{\partial x} \left(D_{2,s}^{eff} \frac{\partial c_2}{\partial x} \right), \quad \forall t \quad (7.18)$$

where $D_{2,m}^{eff}$ is the effective diffusion coefficient in the electrolyte based on thermodynamic driving forces [m^2s^{-1}]. $D_{2,m}^{eff}$ is a function of c_2 , the electrolyte concentration and therefore should not be factored out of the brackets. For a binary electrolyte, $D_{2,m}^{eff}$ is equal to the harmonic mean of the anionic and cationic diffusion coefficients [32].

Two symmetrical Neumann boundary conditions are needed to resolve the concentration profiles. These are expressed at the negative electrode/current collector boundary ($x = 0$) and at the positive electrode/current collector boundary ($x = L$) as

$$\frac{\partial c_2}{\partial x} \Big|_{x=0} = 0, \quad (7.19)$$

$$\frac{\partial c_2}{\partial x} \Big|_{x=L} = 0. \quad (7.20)$$

Boundary conditions Eqs. (7.19) and (7.20) state that there is no flux of ionic species at the current collector/electrode interface. These are identical in the case of a full cell battery with two porous electrodes.

In addition, an initial condition is needed for c_2 , which is defined as

$$c_2(x, t = 0) = c_2^0, \quad (7.21)$$

where c_2^0 is the initial concentration at rest/equilibrium, equal to 1 kmol m^{-3} . Based on experimental conductivity studies, the conductivity of NaPF_6 in $\text{EC}_{0.5}:\text{PC}_{0.5}$ (w/w) electrolyte is also highest around this concentration [31].

7.3.5 Relation between bulk transport properties and porous electrode properties

Bulk properties such as the diffusion coefficients and the electrode conductivity need to be related to the volume fraction of the bulk material in the porous electrode. The Bruggeman correlation [34] is herein used to define the effective electrolyte transport properties of conductivity and diffusion coefficient

$$\kappa_m^{\text{eff}} = (\epsilon_m^{\text{el}})^{1.5} \cdot \kappa, \quad \forall m, \quad (7.22)$$

$$D_{2,m}^{\text{eff}} = (\epsilon_m^{\text{el}})^{1.5} \cdot D_2, \quad \forall m \quad (7.23)$$

where κ and D_2 represent the bulk electrolyte conductivity and diffusion coefficient, separately determined by conductivity experiments in Chapter 3 and the AEM version 2.19.1 [31, 35–37].

A brief discussion on the Bruggeman exponent value of 1.5 in Eq. (7.22) and (7.23) is necessary. This exponent includes a hidden factor of 1, which correlates the bulk electrolyte concentration to the porous media concentration

$$c_{2,m} = \epsilon_m^{\text{el}} \cdot c_2, \quad (7.24)$$

where $c_{2,m}$ is the electrolyte concentration, which includes the volume of the solid phases in porous media [mol m^{-3}]. It is equally valid to use the Bruggeman exponent of 0.5, in which case, the correlated $c_{2,m}$ is used in the model equations. The advantage, however, of using the uncorrelated concentration c_2 is that electrolyte concentrations in different cell domains can be treated as continuous functions.

The Bruggeman correlation was nevertheless not used for σ_m^{eff} since there was no prior knowledge of the bulk electrode conductivity and the electrode porosity was not fixed. Therefore, the optimization of the electrode conductivity was performed for the effective property without including a correlation.

7.3.6 Modeling interfaces

The first-order and second-order PDEs in the electrolyte were discretized by an FDM. Because of porosity differences in the battery domains, the transport properties can change across the interface. Thus the FDM mass balance may be inaccurate across the interface. To overcome this, some authors have proposed an effective interfacial diffusion coefficient [4]. However, in the model described in this Chapter, a CVM is used to discretize the interfacial boundary of the separator and porous electrode. Detailed descriptions of the CVM have been published [38]. For the interested reader, Botte *et al.* [39,40] compared the FDM and the CVM in battery modeling applications. In general, the CVM results in perfect mass conservation across the interface. To obtain the concentration at the interface node, an imaginary control volume is defined across the interface node, and fluxes across the faces of the imaginary volume are calculated, assuming a linear concentration profile. **Fig. 7.2** illustrates the elements of the CVM herein used to derive the interfacial concentration.

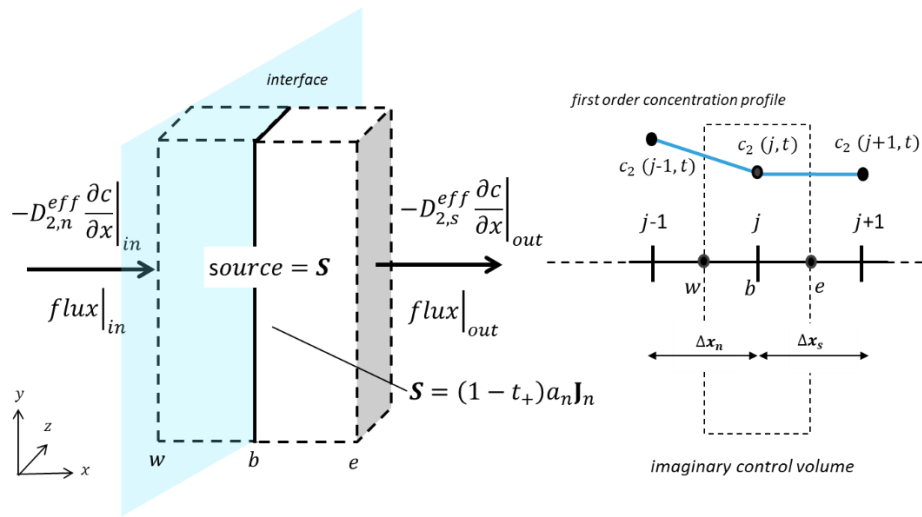


Fig. 7.2. Control volume method showing the microscopic mass balance and interface discretization for the boundary of the separator and porous electrode.

The interfacial concentration at the negative electrode/separator interface can therefore be determined as

$$\left. \frac{\partial c}{\partial t} \right|_b = \frac{1}{(\epsilon_n \Delta x_n + \epsilon_s \Delta x_s)} \left[2D_{2,s}^{\text{eff}} \left. \frac{\partial c}{\partial x} \right|_e - 2D_{2,n}^{\text{eff}} \left. \frac{\partial c}{\partial x} \right|_w + a_n j_n \Delta x_n (1 - t_+) \right], \quad (7.25)$$

where Δx_n and Δx_s are the node spacings in the negative electrode and separator [m], respectively, while b , e , and w are representing the interface, the outermost east boundary, and the west outer boundary of the imaginary control volume, respectively. A similar mass balance based on the control volume formulation can be derived at the positive electrode/separator interface.

7.3.7 Battery voltage

Finally, a Dirichlet boundary condition for the electrode potential on each electrode must be considered [41]. Suppose that the electrode potentials at the left boundary of each porous electrode ($\varphi_{1,n}|_{x=0}$ and $\varphi_{1,p}|_{x=\delta_{neg}+\delta_{sep}}$) are set to some arbitrary values. These values influence the ionic current densities at the opposing electrode end at $i_{1,n}|_{x=\delta_{neg}}$ and $i_{2,p}|_{x=L}$, respectively. To ascertain if the imposed boundary conditions are correct, Eq. (7.9) and the boundary conditions of Eqs. (7.10) and (7.11) all have to be satisfied. The functions to be solved at the negative electrode and the positive electrode can therefore be expressed by

$$I_{1,n} \left(\varphi_{1,n}|_{x=0} \right) / A_{cc} = i_{1,n}|_{x=\delta_{neg}} = 0 \quad (7.26)$$

and

$$I_{2,p} \left(\varphi_{1,p}|_{x=\delta_{neg}+\delta_{sep}} \right) / A_{cc} = i_{2,p}|_{x=L} = 0, \quad (7.27)$$

where $I_{1,n}$ represents electronic current at the interface between the anode and separator, while $I_{2,p}$ represent the ionic current at the interface with the cathode current collector. These currents are considered as generated by coupled PDEs for the negative and positive electrodes, respectively.

Eqs. (7.26) and (7.27) can be solved by various iterative root-finding methods, in which an approximate value of the electrode potential is supplied as an initial guess. In the literature, such a method is also called 'shooting' [42,43]. In this model, a combination of the dichotomy method

and the secant method is applied to optimize the solution convergence [44]. Because the system of equations in porous battery electrodes is nonlinear, it is possible to obtain intermediate solutions of extreme magnitude for minor deviations in the initial guess. A robust root finding method is therefore needed in the first iterations. To our knowledge, the dichotomy method is the only method capable of finding the root in cases where solutions on the right-hand side of the equation can have infinite values. The dichotomy method uses two guess values of the electrode potential, an overestimate and an underestimate, and then reduces the estimated range until the solution is found within the error tolerance. In this case, the tolerance is set at 0.01 % of i_{app} . However, the dichotomy method requires many iterations and is therefore slow to converge to the root. For faster root finding, the solution method switches to the secant method after 5 iterations of the dichotomy method, when the right-hand side value is for sure finite.

Once the solution is found within the error tolerance, the full cell battery voltage can then be determined by

$$V_{bat} = \varphi_{1,p}|_{x=L} - \varphi_{1,n}|_{x=0} - (R_{contact,n} + R_{contact,p}) i_{app} \quad (7.28)$$

where $R_{contact,n}$ and $R_{contact,p}$ [$\Omega \text{ m}^2$] are the negative and positive electrode current collector/porous electrode contact specific resistances, respectively. The importance of contact resistance is revealed at high currents [5,45]. In this model, the contact resistances of individual electrodes were calculated from the Na-RE measurements in Chapter 6.

It is worth highlighting that the validation of the model vs. experimental data is done based on the individual electrode potentials and not the full cell voltage, V_{bat} . This scheme is applied because, from Eq. (7.28), it is possible to have wrong values of both $\varphi_{1,p}$ and $\varphi_{1,n}$ and yet still manage to have a correct V_{bat} . The Na-RE electrode deconvolutes the individual electrode potentials from V_{bat} and thereby allows model validation on two separate electrodes.

The electrode potentials used for validation of the model vs. experimental data can thus be expressed as

$$V_p = \varphi_{1,p}|_{x=L} - A_{cc} R_{contact,p} i_{app} \quad (7.29)$$

and

$$V_n = \varphi_{1,n}|_{x=0} + A_{cc} R_{contact,n} i_{app} \quad , \quad (7.30)$$

where V_p and V_n [V] are the positive and negative electrode potentials, respectively.

7.4 Parameter identification and optimization

For the developed model to provide physically meaningful results, the model parameters should be inferred from an extensive experimental data set. Because of the minimal assumptions in P2D models, experimentally derived parameters should ideally result in a fitting model. However, this is seldom the case due to the disparity in the definitions of key parameters, such as the diffusion coefficients and transference number between experimental and modeling techniques. Another challenge is that experimentally derived parameters are technique-dependent. There is, therefore, a great need to bridge the gap between model and experimental parameters. Nevertheless, experimental parameters are an ideal starting point and provide insight into the order of magnitude of the model parameters.

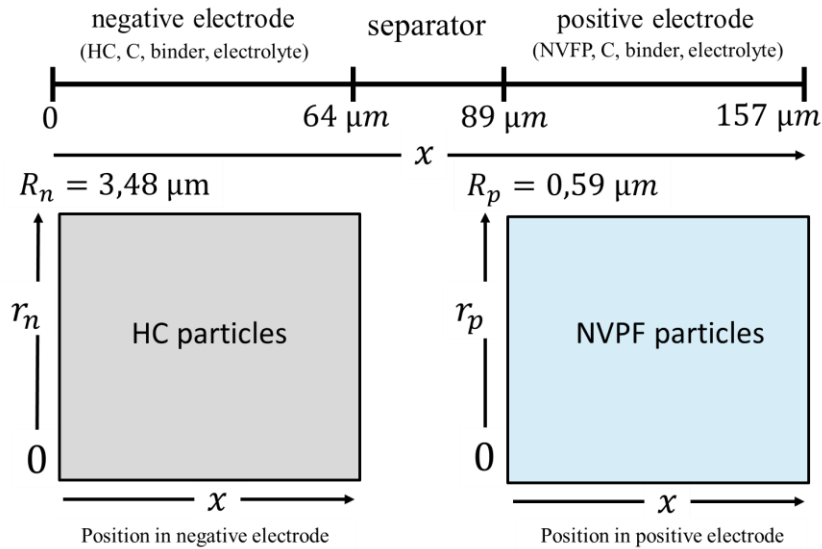


Fig. 7.3. P2D model setup and dimensions of the studied HC//NVPF SIB.

In the SIB model herein described, the experimental geometric parameters of the SIB determined in the previous Chapter are used without modification [19]. These include the thicknesses of the electrodes and separator as well as the particle radii of the positive and negative

electrodes. **Fig. 7.3** shows the cell dimensions of the HC//HVPF SIB, concluded from the experiments.

The negative electrode is therefore defined between $0 \leq x \leq 64 \mu\text{m}$, the separator in the $64 \leq x \leq 89 \mu\text{m}$ region, while the positive electrode is defined in the $89 \leq x \leq 157 \mu\text{m}$ region. The HC and NVPF electrode particles are separately modeled in a homogenous P2D domain, in which the r_m - and x -axis represents the particle radii and particle positions in the porous electrode, respectively. Having fixed cell dimensions allows the mesh of the cell components to be defined in the model. Changes in cell dimensions during optimization require a new mesh to be determined, which may inadvertently affect parameters with length scale, such as the conductivity and diffusion coefficients. This complication can also lead to numerical instabilities and inconsistent model results. It is therefore advised to maintain constant cell dimensions unless experimental evidence proves otherwise.

The experimental EMF of the NVPF and HC electrodes were also determined in Chapter 6, based on the extrapolation-to-zero-current method [28,46,47]. The particle-phase diffusion coefficients, $D_{1,m}$ and kinetic rate constants, k_m were determined at different electrode SOC points from a combination of experimental GITT data and half-cell P2D GITT model optimization as described in Chapter 5 [26]. As a result, concentration-dependent $D_{1,n}(c_{1,n})$, $D_{1,p}(c_{1,p})$, $k_n(c_{1,n})$ and $k_p(c_{1,p})$ were thus obtained. On the other hand, electrolyte properties such as $D_2(c_2)$, $\kappa(c_2)$ and t_+ were determined in Chapter 3 based on the AEM modeling and experiments [31]

The root-mean-square error between the model and the experimental results was selected as the objective function for optimizing the unknown model parameters. The MATLAB genetic algorithm (GA) was used to obtain the global error minimum for multiple discharge curves at different rates [48]. The GA is necessary due to the nonlinearity of the P2D model equations and parameter identification complexity. A two-step optimization procedure was designed because of the availability of two experimentally determined electrode potentials for each discharge curve. The parameters for the positive electrode were optimized in the first step, separate from the parameters of the negative electrode, which were then optimized in the second step.

Table 7.1 lists the constant value parameters for the HC negative electrode, NVPF positive electrode and NaPF₆ EC_{0.5}:PC_{0.5} (w/w) electrolyte. Parameters that could not be obtained experimentally were obtained by optimization. The concentration-dependent parameters were

optimized through a scaling factor. This strategy resulted in improved optimization results at high rates.

Table 7.1. Parameters used in the model.

Parameter	Unit	Description	value	Reference
δ_n	μm	Anode thickness	64	[19]
δ_p	μm	Cathode thickness	68	[19]
δ_s	μm	Separator thickness	25	[19]
R_n	μm	HC particle radius	3.48	[19]
R_p	μm	NVPF particle radius	0.59	[19]
A_{cc}	cm^2	Electrode cross-section area	2.54	[19]
T	K	Cell temperature	298.15	[27]
$c_{1,n}^{max}$	kmol m^{-3}	Max. concentration of Na^+ in HC	14.54	[19]
$c_{1,p}^{max}$	kmol m^{-3}	Max. concentration of Na^+ in NVPF	15.32	[19]
$c_{1,n}^0$	kmol m^{-3}	Initial concentration of Na^+ in HC	14.52	[19]
$c_{1,p}^0$	kmol m^{-3}	Initial concentration of Na^+ in NVPF	3.32	[19]
c_2^0	kmol m^{-3}	Initial concentration of NaPF_6	1	[19]
α	-	Charge transfer coefficient	0.5	optimization
t_+	-	Transference number	0.45	[31]
σ_n^{eff}	$\Omega^{-1} \text{m}^{-1}$	Anode electronic conductivity	256	optimization
σ_p^{eff}	$\Omega^{-1} \text{m}^{-1}$	Cathode electronic conductivity	50	optimization
ϵ_n^{el}	-	Electrolyte volume fraction in anode	0.51	optimization
ϵ_p^{el}	-	Electrolyte volume fraction in cathode	0.23	optimization
ϵ_s^{el}	-	Electrolyte volume fraction in separator	0.55	[49]
ϵ_n^{filler}	-	Filler volume fraction	0.001	optimization
ϵ_p^{filler}	-	Filler volume fraction	0.22	optimization
$R_{contact,n}$	$\text{m}\Omega \text{m}^2$	Contract resistance	2	[19]
$R_{contact,p}$	$\text{m}\Omega \text{m}^2$	Contract resistance	8.5	[19]

Fig. 7.4 compares the concentration-dependent parameters, $D_{1,m}$ and k_m obtained from the P2D GITT model (symbols) [26] to the parameters used in the optimized full cell P2D model (solid line). **Fig. 7.4** (a) and (b) show HC parameters while **Fig. 7.4** (c) and (d) show NVPF parameters. In all cases, the optimized full cell model parameters are higher than the P2D GITT model parameters, although the same qualitative trend is maintained. These differences could result from

model uncertainties and/or temperature effects at high discharge rates since the P2D GITT model parameters are obtained at comparatively very low currents (approximately C/30).

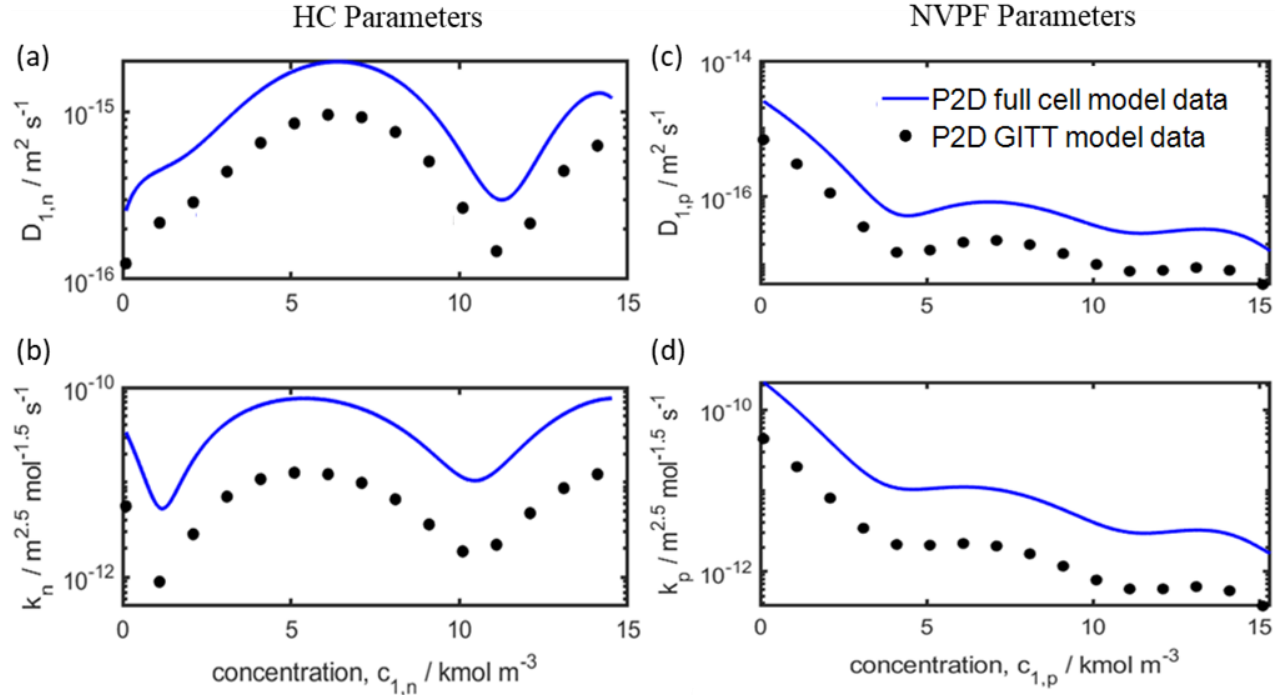


Fig. 7.4. HC and NVPF electrode parameters from the P2D GITT model (symbols) and from the optimized full cell P2D model (solid line) as function of the intercalated Na⁺ concentration, $c_{1,n}$. The diffusion coefficient in HC, $D_{1,n}$ (a) and the kinetic rate constant, k_n (b). The diffusion coefficient in NVPF, $D_{1,p}$ (c) and kinetic rate constant, k_p (d).

Fig. 7.5 compares the electrolyte properties, D_2 and κ obtained from the AEM version 2.19.1 (symbols) to the optimized parameters from the full cell P2D model (solid line). The values of κ were the same in both cases. Additional experimental measurements have validated the AEM electrolyte conductivity results [31]. Although the D_2 values obtained in the optimized P2D model are qualitatively similar, they are quantitatively lower than those obtained from the AEM. Because two model results are used to determine these parameters, further experimental investigations are necessary to investigate the origin of the differences in D_2 .

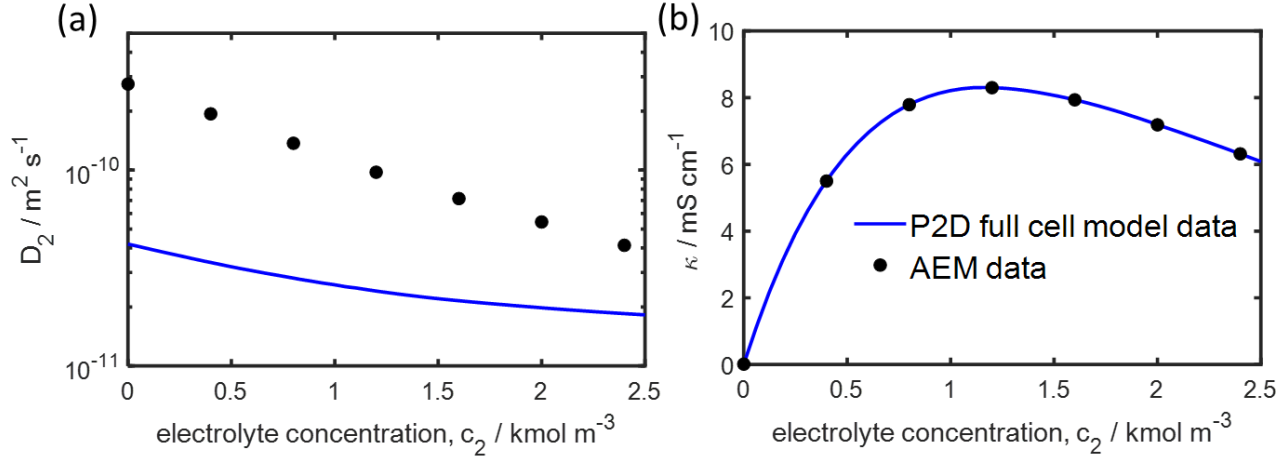


Fig. 7.5. Electrolyte properties of NaPF₆ salt dissolved in EC_{0.5}:PC_{0.5} (w/w) solvent from the AEM (symbols) and from the optimized P2D model (solid line) as function of the salt concentration, c_2 . The diffusion coefficient in the electrolyte, D_2 (a) and the electrolyte conductivity, κ (b).

7.5 Results and discussion

Fig. 7.6 shows the measured (symbols) and simulated (solid lines) SIB discharge voltage profiles as a function of transferred charge during discharge. The model results are obtained using a single set of optimized parameters for all discharge rates. Discharge current densities of 1, 5, 10, and 12 A m² were applied, corresponding to 0.1, 0.6, 1.2, and 1.4 C-rate, respectively.

Fig. 7.6 (a) shows the measured and simulated voltage profiles of an HC//NVPF, full cell SIB. The fully-charged cell voltage starts at 4.2 V and terminates at the cutoff voltage of 2 V. Note that the practically recommended cutoff voltage is 2.5 V [50]. As the current increases, the battery voltage and the maximum transferred charge decrease. This feature is caused by an increase in mass transport and charge transfer overpotentials at higher currents. Therefore, an accurate physics-based model is the only way to account for the various kinetic and mass transport effects at different rates.

Fig. 7.6 (b) and (c) show the measured and simulated voltage profiles of the NVPF positive electrode (V_p vs. Na-RE) and the HC negative electrode (V_n vs. Na-RE), respectively. At the different discharge rates, V_p varies between 4.3 – 3.4 V vs. Na-RE while V_n varies between 0.1–1.5 V vs. Na-RE. Therefore, based on the potential range and the current dependence of the

voltage profiles, both electrodes contribute significantly to the overpotential losses in the full cell and consequently to the capacity losses at high currents. In both cases, however, the P2D model is in good agreement with the experimental voltage profiles of V_p and V_n vs. Na-RE.

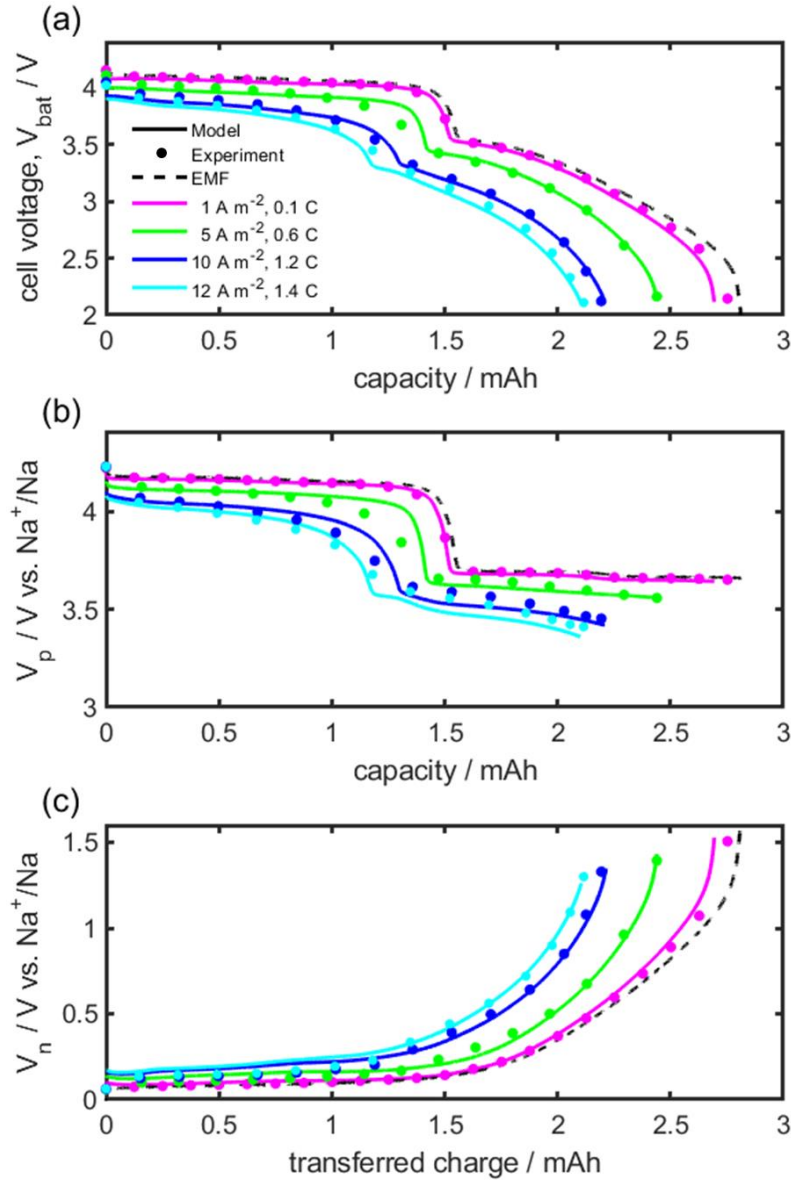


Fig. 7.6. Simulated (solid lines) and experimental (symbols) results of an optimized P2D model for an HC//NVPF SIB. Battery voltage (a) and potential of the positive electrode (b) and negative electrode vs. Na-RE (c). Dashed lines show the corresponding EMF curves.

Table 7.2 shows the percentage error in V_{bat} and the mean absolute errors in V_{bat} , V_p and V_n at different rates. The largest percentage error in V_{bat} is 1.47 %, corresponding to 48.1 mV in absolute

error terms. Therefore, the model results quite well match the experimental full cell voltage and the individual electrode potentials at different discharge rates. The accurate P2D model herein presented goes beyond the current density and terminal voltage data by providing additional information on internal battery states. In the subsequent figures, the Na^+ electrolyte concentration, the Na^+ concentration in the active particles, and the ionic current distribution are compared for the applied current of 1 and 12 A m^{-2} , to investigate how different discharge rates influence the battery performance.

Table 7.2. Simulation errors obtained at different (dis)charging rates.

i_{app} [A m^2]	V_{bat} error [%]	Mean absolute voltage error [mV]		
		V_{bat}	V_p	V_n
1	0.70	19.9	8.6	12.4
5	0.96	34.6	33.5	27.7
10	0.95	32.2	37.6	35.2
12	1.47	48.1	37.8	32.6

Fig. 7.7 (a) and (b) show 3D simulation results of the electrolyte concentration, $c_2(x, t)$ at 1 A m^{-2} and 12 A m^{-2} discharge rates, respectively. Here, $c_2(x, t)$ is shown at different cell positions, x and discharge time, t . In the negative electrode region ($0 \leq x \leq 64 \mu\text{m}$), c_2 increases as a function of time due to Na^+ deintercalation in the HC negative electrode, while in the positive electrode region ($89 \leq x \leq 157 \mu\text{m}$), c_2 decreases due to Na^+ intercalation in NVPF. This ionic transport in the electrolyte is driven by migration and diffusion mechanisms, as expressed in Eq. (7.15). Note that due to electroneutrality condition, at any given time, the average of c_2 remains constant and equal to the equilibrium and initial concentration of 1 kmol m^{-3} . While the results in **Fig. 7.7** (a) do not appreciably deviate from the equilibrium concentration of 1 kmol m^{-3} , the results in **Fig. 7.7** (b) reveal a severe depletion of Na^+ ions in the positive electrode during fast-discharge. This depletion is pronounced toward the positive current collector boundary ($x = 157 \mu\text{m}$).

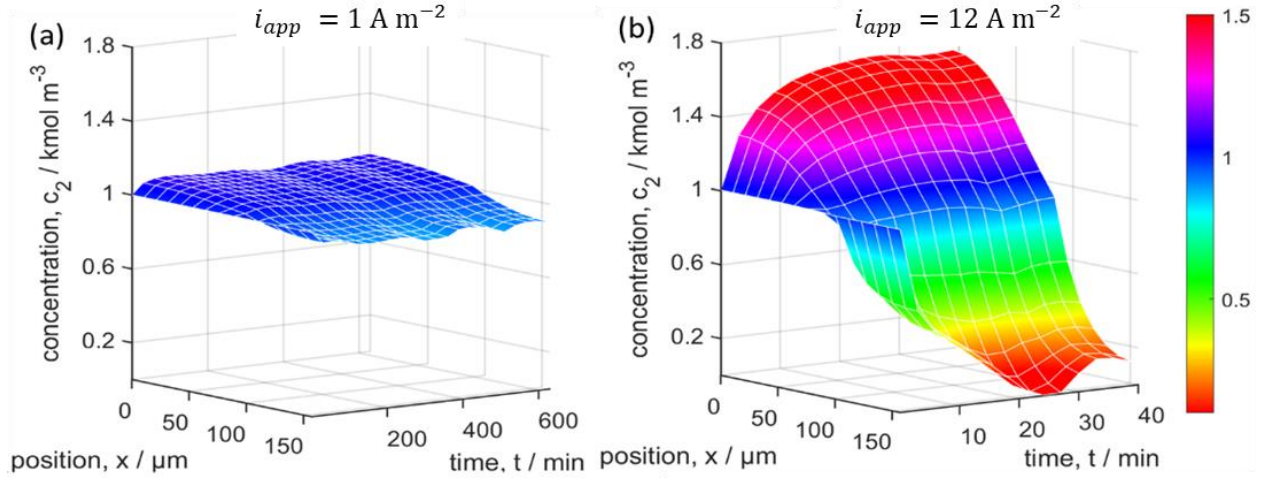


Fig. 7.7. Evolution of the electrolyte concentration (c_2) profiles as a function of position (x) and discharge time (t) upon discharging at 1 (a) and 12 A m⁻² (b).

Fig. 7.8 (a) to (c) shows the time-dependent profiles of c_2 , ϕ_2 and η_p^{ct} at different positions of the positive electrode during the fast 12 A m⁻² constant current discharge. Profiles at the separator boundary, $x = 89 \mu\text{m}$ at the middle of the positive electrode ($x = 123 \mu\text{m}$) and at the current collector boundary ($x = 157 \mu\text{m}$) are shown in red, blue and green color lines, respectively. After 25 minutes, c_2 attains a very low value 3.7 mol m⁻³ at the positive current collector boundary. This sharply reduces both ϕ_2 and η_p^{ct} for a given interfacial flux, j_p (see results in **Fig. 7.8** (b) and (c)). The relationship between j_p , c_2 and η_p^{ct} is expressed by Eq. (7.5) while the relationship between ϕ_2 and η_p^{ct} is expressed by Eq. (7.7). A negative value of η_p^{ct} indicates that the electrochemical reaction is cathodic. High values of η_p^{ct} are undesirable because they lower the voltage of the full cell SIB and generate excess heat. This phenomenon, therefore, amounts to significant energy losses.

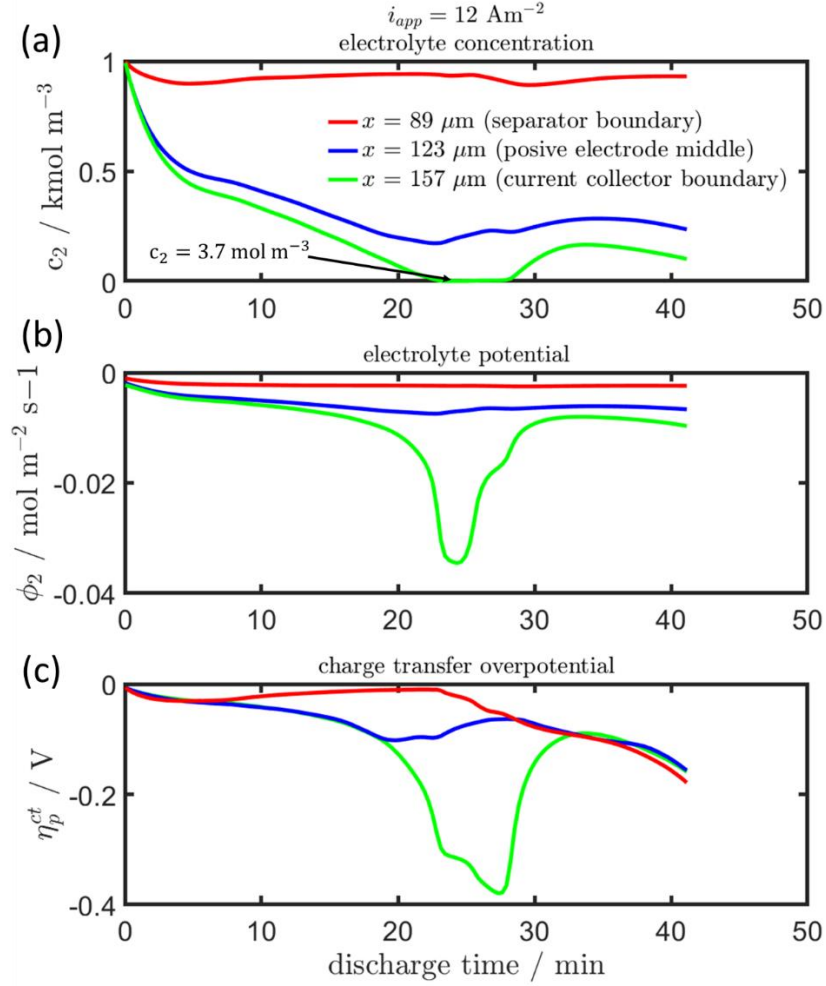


Fig. 7.8. Development of the electrolyte concentration, c_2 (a), electrolyte potential, ϕ_2 (b) and charge transfer overpotential η_p^{ct} (c) at different indicated positions in the positive electrode as a function of time during high current (12 A m^{-2}) discharge.

Fig. 7.9 shows 1D plots of the simulated results of the intercalated concentration of Na^+ ions, $c_{1,m}$ in the negative and positive electrode active particles. Note that profiles of $c_{1,m}(x, r_m, t)$ develop along the dimension of the particle radius, r_m and positions along with the porous electrode coating thickness, x . In order to analyze the profiles along x only, it is therefore necessary to plot the average and surface concentrations, $\bar{c}_{1,m}(x, t)$ and $c_{1,m}^s(x, t)$, respectively, at specific times. The results are shown at discharge times, defined as 20, 40, 60, and 80% of the maximum discharge time (t_{max}), where $t_{\text{max}} = 10.92 \text{ h}$ and 41.39 min for the 1 and 12 A m^{-2} discharge rates, respectively. The $\bar{c}_{1,m}$ plots are shown in dashed lines, while the $c_{1,m}^s$ plots are shown in

solid lines. During discharge, the negative electrode concentrations, $\bar{c}_{1,n}$ and $c_{1,n}^s$ decrease (Fig. 7.9 (a) and (c)), while the positive electrode concentrations, $\bar{c}_{1,p}$ and $c_{1,p}^s$ increase (Fig. 7.9 (b) and (d)).

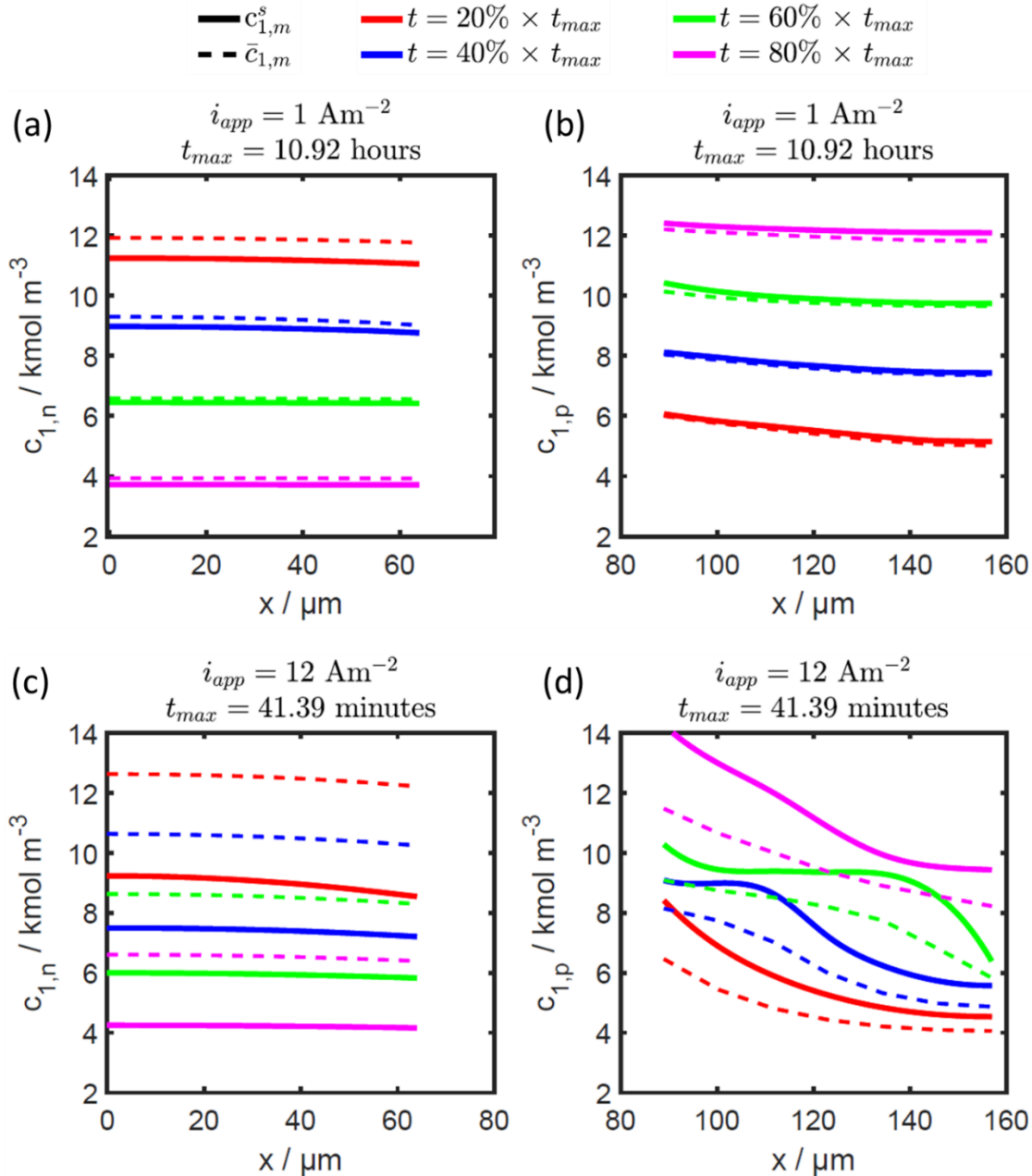


Fig. 7.9. Simulated intercalated Na^+ concentration at the active particle surface, $c_{1,m}^s$ (solid lines) and the average concentration in the active particles, $\bar{c}_{1,m}$ (dashed lines) in the porous HC negative electrode ($m = n$) (a),(c) and the NVPF positive electrode ($m = p$) (b),(d) as a function of position (x) and various indicated discharge times related to t_{max} during discharging at 1 (a),(b) and 12 A m^2 (c),(d).

Fig. 7.9 (a) and (b) show the simulated results of the intercalated concentration of Na^+ ions during a 1 A m^{-2} discharge, in the negative and positive electrode active particles, respectively. For the slow-discharge rate operation, $\bar{c}_{1,m}$ and $c_{1,m}^s$ profiles are shown to evolve uniformly along x . In addition, the profiles remain very close at all times. This indicates that slight concentration gradients develop in the electrode active particles during the slow discharge rate. From a modeling perspective, such concentration profiles can be simulated quite accurately using computationally efficient analytical methods [22].

Fig. 7.9 (c) and (d) show the simulated results during 12 A m^{-2} discharge in the negative and positive electrodes, respectively. In contrast to the results shown in **Fig. 7.9** (a) and (b), the fast-discharge exhibits non-uniform $\bar{c}_{1,m}$ and $c_{1,m}^s$ profiles along x . This behavior is most apparent in the positive electrode (**Fig. 7.9** (d)), where the active particles close to the separator receive 58% higher average concentration as compared to particles at the current collector (compare $\bar{c}_{1,p}$ at $x = 89$ and $x = 157 \text{ } \mu\text{m}$ in the dashed curves of **Fig. 7.9** (d)). These profiles can only be obtained accurately using numerical methods because of the concentration dependence of $D_{1,n}$ and $D_{1,p}$.

An analysis of the concentration difference $c_{1,m}^s - \bar{c}_{1,m}$ shows that at slow discharge rates $c_{1,m}^s - \bar{c}_{1,m}$ is not large. The maximum differences are about 0.8 and 0.25 kmol m^{-3} in the negative and positive electrodes, respectively. Such a small concentration difference is desirable and indicates the absence of mass transport limitations in the solid electrode active particles. At fast discharge rates, however, $c_{1,m}^s - \bar{c}_{1,m}$ is significantly larger. The maximum differences are about 3.5 and 2 kmol m^{-3} in the negative and positive electrodes, respectively. This indicates diffusion mass transport limitations in the electrode particles at fast rates [19].

Fig. 7.10 shows profiles of the interfacial flux, j_m at discharge rates of 1 (**Fig. 7.10** (a) and (b)) and 12 A m^{-2} (**Fig. 7.10** (c) and (d)). To analyze the distribution of the flux, the profiles are averaged over quarterly intervals of t_{max} . It can be observed that the initial stages (red lines) are characterized by high j_m rates at the electrode/separator boundary. Another observation is that profiles in the negative electrode at 1 and 12 A m^{-2} are nearly identical and scaled versions of each another (compare **Fig. 7.10** (a) and (c)). This indicates that the distribution of j_m in the negative electrode is not altered by the increase in the discharge rate. In contrast, profiles in the positive electrode (**Fig. 7.10** (b) and (d)), show considerable differences, especially in the intermediate periods $0.25 t_{max} < t \leq 0.5 t_{max}$ (blue line) and $0.5 t_{max} < t \leq 0.75 t_{max}$ (green

line). This indicates that high discharge rates are influencing the distribution of j_m in the positive electrode.

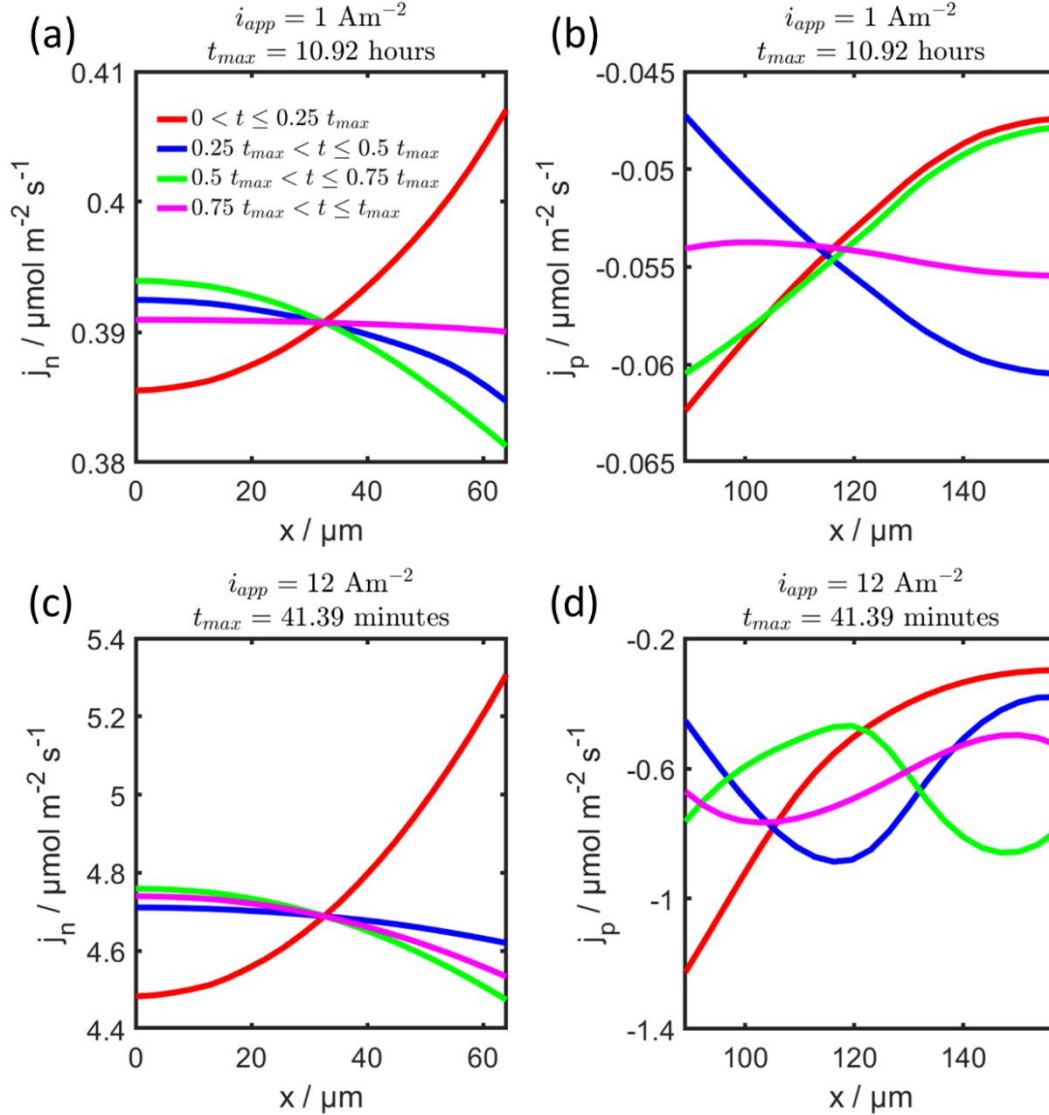


Fig. 7.10. Profiles of j_n in the negative electrode and positive electrode. Average j_n in negative. (a) and positive electrode (b) at the discharge rate of 1 A m^{-2} . Average j_n in the negative (c) and positive electrode (d) at the discharge rate of 12 A m^{-2} . The average j_n is calculated over quarterly intervals of the maximum discharge time, t_{max} .

Fig. 7.11 shows 2D simulation results of the intercalated Na^+ concentration in the negative (**Fig. 7.11** (a) to (d)) and positive (**Fig. 7.11** (e) to (h)) electrode at a 1 A m^{-2} discharge rate. For an illustration of the relationship between 1D and 2D coordinates, refer to **Fig. 7.3**. The 2D results

in **Fig. 7.11** show in more detail the 1D profiles shown in **Fig. 7.9** (a) and (b). The 2D concentrations are, however, expressed as SOC, which is defined for the negative and positive electrodes as

$$SOC_n(r, t) = \frac{c_{1,n}(r, t)}{c_{1,n}^{max}} \quad (5.15)$$

$$SOC_p(r, t) = 1 - \frac{c_{1,p}(r, t)}{c_{1,p}^{max}} \quad (5.15)$$

The SOC-scale is convenient for a side-by-side comparison of the 2D concentration profiles in two battery electrodes because the SOC is scaled between 0 and 1 or 0 and 100%.

At low discharge rates, the SOC is uniformly distributed within the active particles (along the r_m -axis) and for particles located at different positions in the electrodes (along the x -axis). In addition, toward the end of discharge (**Fig. 7.11** (d) and (h), $t = 80\% t_{max}$), the SOC is low and uniformly distributed in both electrodes. This observation signifies that the intercalated Na^+ is optimally utilized and that the maximum extractable capacity is attained. The electrode thickness can also be safely increased without harming the discharge performance of the cell at this discharge rate.

Fig. 7.12 shows the 2D SOC profiles in particles of the HC (**Fig. 7.12** (a) to (d)) and NVPF (**Fig. 7.12** (e) to (h)) electrodes at a discharge rate of 12 A m^{-2} . The results in **Fig. 7.12** further elaborate the 1D profiles shown in **Fig. 7.9** (c) and (d). In contrast to the uniform concentration profiles observed in **Fig. 7.11**, the fast discharge rate reveals non-uniform SOC distribution in both the x - and r_m -axis.

Fig. 7.12 (a) to (d) show the evolution of SOC profiles in the HC negative electrode at the various indicated times. Compared to slow-discharge profiles (**Fig. 7.11** (a) to (d)), the SOC is non-uniformly distributed during the fast-discharge rate. It can also be observed that, for the negative electrode, the differences in SOC mainly develop inside the particles (along the r_n -axis) compared to the electrode thickness (along the x -axis). For example, toward the end of discharge in **Fig. 7.12** (d), although the SOC at the surface ($r_n = 3.48 \text{ } \mu\text{m}$) is low, approximately 0.2, it remains high at the center of the HC particles ($r_n = 0$), approximately 0.8. In fact, the changes in SOC at the center of HC particles are insignificant at all times shown. This behavior implies that the HC particles are too large for efficient charge transfer at fast and continuous discharge rates.

Nevertheless, because of the high $D_{1,n}$ [19], this SOC at the center of the particles can still be recovered by putting the SIB in relaxation.

Fig. 7.12 (e) to (h) shows the evolution of SOC profiles in the NVPF positive electrode along both the x - and r_p -axis at various indicated times. During the fast-discharge rate, and similar to the SOC profiles shown in the negative electrode **Fig. 7.12** (a) to (d)), the SOC profiles are also non-uniformly distributed. However, in contrast to the negative electrode profiles in **Fig. 7.12** (a) to (d), differences in SOC develop both inside the particles (along the r_p -axis) and along with the electrode thickness (along the x -axis). In addition, there are significant changes of the SOC at the center of the particles ($r_p = 0$) during discharge. Therefore, the small NVPF particle radius (0.59 μm) compared to the HC particle radius (3.48 μm) therefore results in more efficient charge insertion in the positive electrode.

The SOC profiles along the x -axis in **Fig. 7.12** (e) to (h) also mirror the electrolyte concentration profiles shown in **Fig. 7.7** (b). The low electrolyte concentration close to the positive electrode current collector ($x = 157 \mu\text{m}$), means the NVPF particles in this region are underutilized compared to the active material close to the separator. Such a variation of SOC along the electrode thickness is detrimental to the battery's performance because intercalated Na^+ cannot diffuse between adjacent particles. This issue is analogous to a cell balancing problem in a battery module, although we are talking here of imbalances occurring along the electrode thickness. Consequently, increasing the electrode coating thickness without improving the electrolyte mass transport will result in greater imbalances and a huge penalty in terms of capacity loss for the HC//NVPF SIB.

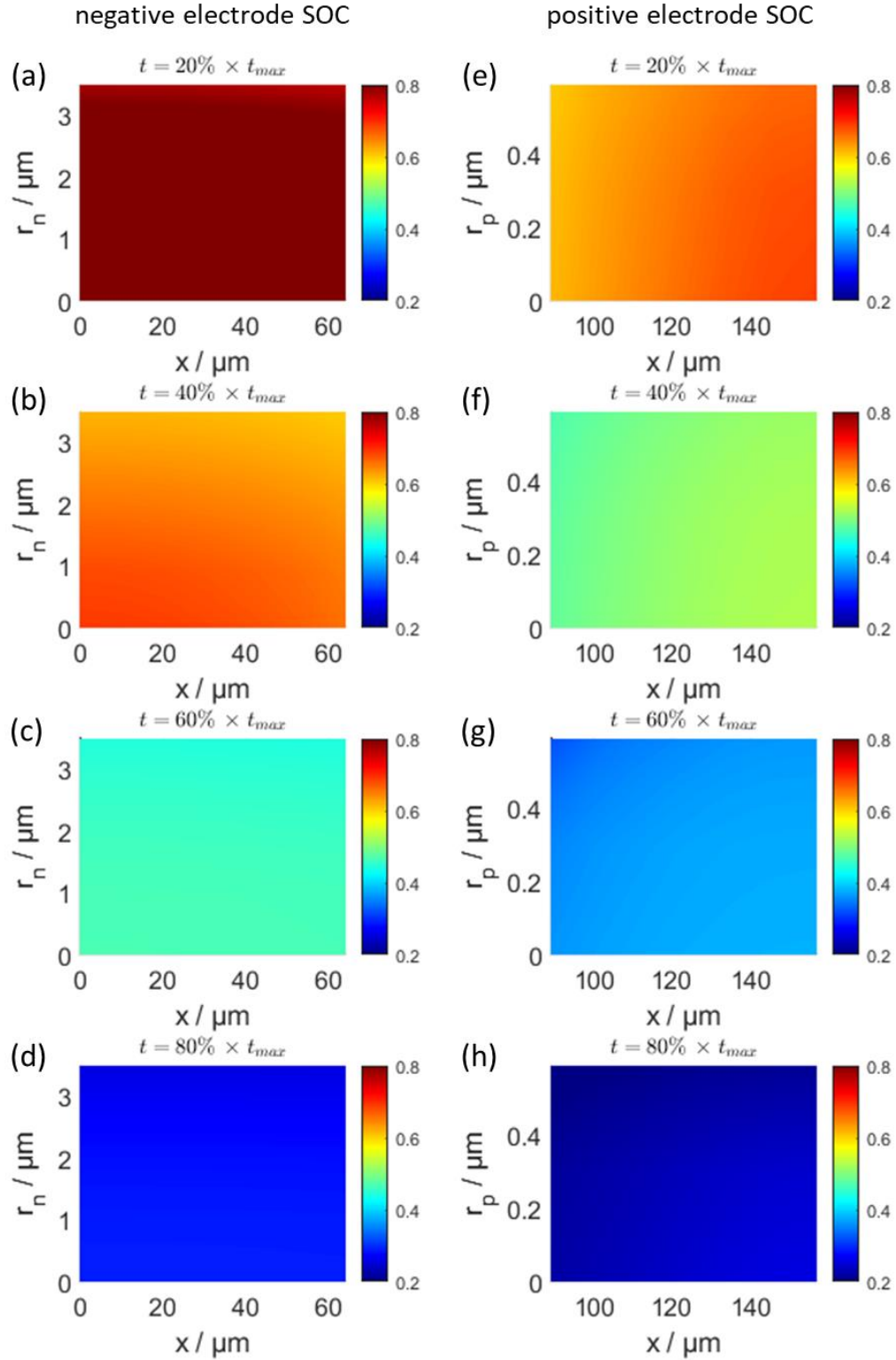


Fig. 7.11. SOC profiles along active particle radii, r_m and active particles position, x in the negative electrode ($m = n$) (a) to (d), and in the positive electrode ($m = p$) (e) to (h). Profiles are obtained at 1 A m^{-2} for which $t_{max} = 10.92$ hours.

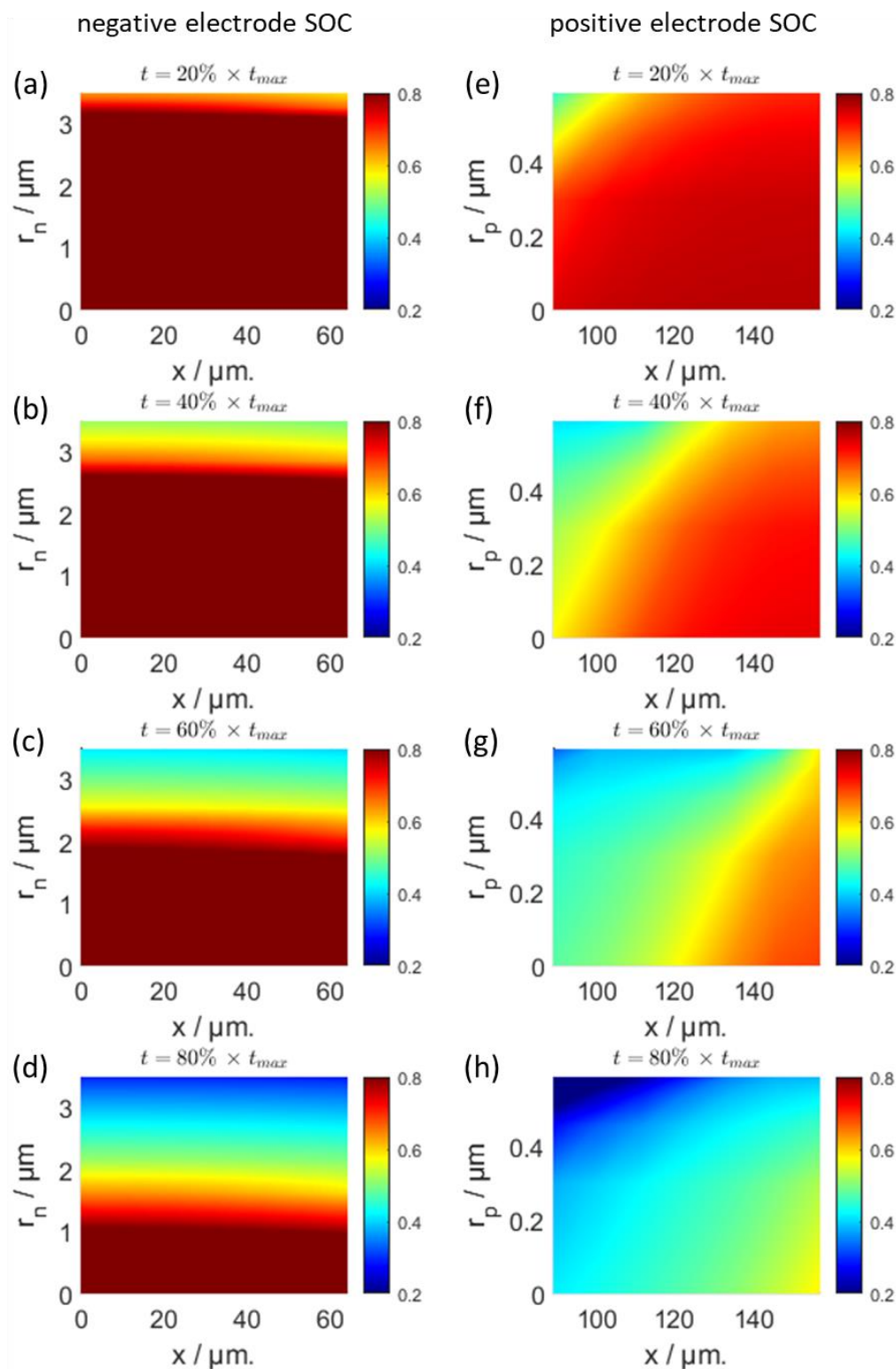


Fig. 7.12. SOC profiles along active particle radii, r_m and active particles position, x in the negative electrode ($m = n$) (a) to (d), and in the positive electrode ($m = p$) (e) to (h). Profiles are obtained at 12 A m^{-2} for which $t_{max} = 41.39$ minutes.

Fig. 7.13 shows the simulated results of ionic current density, i_2 in 2D color plots and the EMF of the positive electrode, U_p in 1D plots as a function of the discharge time t (expressed as a percentage of t_{max}). The results of i_2 are also shown as a function of position x , and they are normalized with respect to i_{app} , as indicated in the color code at the right-hand side of **Fig. 7.13** (a) and (c). Here, i_2 represents the flux of Na^+ due to migration and diffusion in the electrolyte phase, as expressed by Eq. (7.15). The results show that $i_2 = 0$ at the current collector ($x=0$ and $x=157 \mu\text{m}$) and $i_2 = i_{app}$ at the separator ($64 \leq x \leq 89 \mu\text{m}$). This is in accord with the boundary conditions and thus validates the solution method in Eq. (7.26) and (7.27).

Fig. 7.13 (a) and (b) show i_2 profiles and the corresponding U_p at a 1 Am^{-2} discharge rate, respectively, while **Fig. 7.13** (c) and (d) show i_2 and U_p during 12 Am^{-2} discharge rate, respectively. It can be observed that i_2 profiles are linear in the negative electrode and nonlinear in the positive electrode, irrespective of the discharge rate. In addition, based on the side-by-side comparison of i_2 and U_p , it can be observed that the nonlinear i_2 profiles in the positive electrode align with the step changes in the corresponding EMF of the NVPF. Therefore, the 'staircase' NVPF EMF results in nonlinear i_2 in the positive electrode. Results in **Fig. 7.13** demonstrate that even in the cases of a slow discharge rate, the profiles of i_2 can be quite dynamic, which is a potential challenge for reduced-order models to be accurate in the case of SIBs.

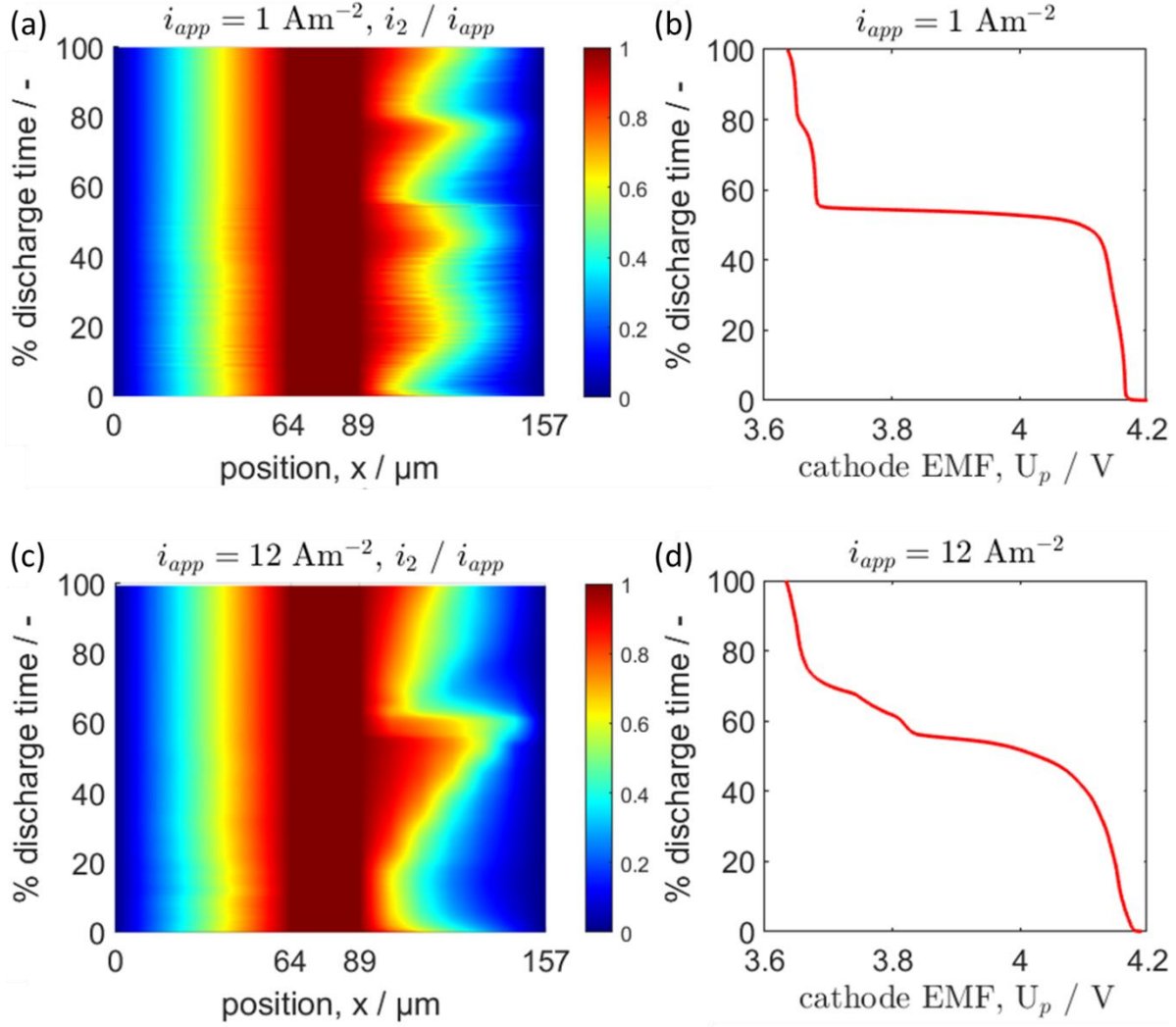


Fig. 7.13. Profiles of the electrolyte current density, i_2 at different positions x and % discharge time. The i_2 profiles are normalized with respect to the applied current i_{app} and compared with the voltage profile of the NVPF cathode. (a) and (b) i_2/i_{app} and NVPF voltage profiles at 1 A m^{-2} respectively. (c) and (d) i_2/i_{app} and NVPF voltage profiles at 12 A m^{-2} respectively. The staircase voltage profile of the NVPF electrode results in the nonlinear i_2 profile in the cathode.

Fig. 7.14 shows a comparison of the experimental and simulation results of the HC//NVPF SIB in a Ragone plot. This figure compares the energy and power characteristics of the SIB. The simulation results are very close to the experimental results up to the 1-hour discharging rate. At higher rates, deviations appear, which can be explained by phase changes in the NVPF active material, which are not included in the solid-solution model. To improve accuracy at higher rates, a multi-phase diffusion mechanism is therefore needed to model phase transformations in the

NVPF active material [51,52]. Nevertheless, the improvements brought by concentration-dependent $D_{1,m}$ and k_m result in a close match between the experiment and model predictions while maintaining a single set of parameters for all rates.

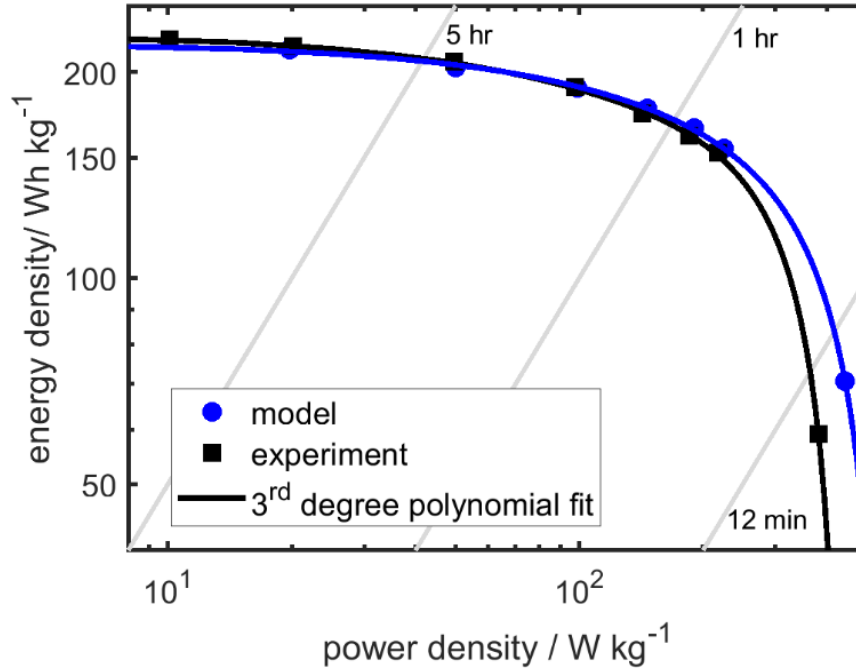


Fig. 7.14. Ragone plot of the HC//NVPF SIB showing the simulation (blue) and experimental (black) results.

Often, in battery design, increasing the battery's energy density results in decreased power density. As a result, optimizing battery performance is nontrivial. However, the model herein presented can be used to determine design parameters, such as electrode thickness and porosity, based on the accuracy shown in the Ragone plot. At the same time, battery manufacturing costs should not be neglected, which can also be part of a multi-objective optimization procedure [53]. For example, increasing the coating thickness reduces the cost but simultaneously reduces the battery's power [54,55]. These factors can be combined and investigated using this SIB P2D model as a strategy and tool to avoid the often-expensive experimental trial and error methods.

7.6 Conclusions

A pseudo-two-dimensional (P2D) model is shown in this Chapter to model the voltage of a sodium-ion battery (SIB) composed of $\text{Na}_3\text{V}_2(\text{PO}_4)_2\text{F}_3$ (NVPF) and hard carbon (HC) as positive and negative electrodes, respectively. The HC/NVPF SIB model uses a coupled set of partial differential equations (PDEs) for the current and concentration profiles. An iterative root finding method is applied to determine the solution of the coupled system of PDEs. The model parameters are optimized by a genetic algorithm, which determines the global minimum. The negative and positive electrode parameters are optimized separately as a strategy to reduce the number of simultaneously optimized parameters and improve accuracy. It is shown that the model is least accurate by 1.47 % at a 1.4 C-rate, using a constant set of parameters.

The developed P2D model can be rapidly parametrized using experimentally derived data. The voltage profiles for individual electrodes were obtained at different C-rates using a reference electrode. They were further used to determine parameters for each electrode. Using the validated P2D SIB model, more information concerning internal cell dynamics was obtained, which allowed an analysis of the limiting factors. It is shown that the high C-rate performance of the HC/NVPF SIB is limited by the poor mass transport in the HC and NVPF electrodes and in the electrolyte. Mass transport in HC electrodes can be improved by reducing the particle sizes. In contrast, the NVPF particles suffer from a low diffusion coefficient.

The model shown in this Chapter can be used as a design tool to improve the performances of SIBs, starting with the limiting factors already identified. Future work will thus focus on multi-objective optimization of the cell design, including electrode thickness and material costs as additional design considerations. In addition, the model accuracy can be improved by including temperature effects in large format cells and multi-phase intercalation dynamics in the NVPF electrode material.

References

- [1] K. West, T. Jacobsen, S. Atlung, Modeling of Porous Insertion Electrodes with Liquid Electrolyte, *J. Electrochem. Soc.* **129** (1982) 1480–1485. <https://doi.org/10.1149/1.2124188>.
- [2] B. Scrosati, Lithium Rocking Chair Batteries: An Old Concept?, *J. Electrochem. Soc.* **139** (1992) 2776–2781. <https://doi.org/10.1149/1.2068978>.
- [3] J. Newman, W. Tiedemann, Porous-electrode theory with battery applications, *AIChE Journal* **21** (1975) 25–41. <https://doi.org/10.1002/aic.690210103>.
- [4] C.M. Doyle, Design and Simulation of Lithium Rechargeable Batteries, PhD. Thesis, University of California at Berkeley (1995).
- [5] T.F. Fuller, M. Doyle, J. Newman, Simulation and Optimization of the Dual Lithium Ion Insertion Cell, *J. Electrochem. Soc.* **141** (1994) 1–10. <https://doi.org/10.1149/1.2054684>.
- [6] W.B. Gu, C.Y. Wang, B.Y. Liaw, Numerical Modeling of Coupled Electrochemical and Transport Processes in Lead-Acid Batteries, *J. Electrochem. Soc.* **144** (1997) 2053. <https://doi.org/10.1149/1.1837741>.
- [7] B. Paxton, J. Newman, Modeling of Nickel/Metal Hydride Batteries, *J. Electrochem. Soc.* **144** (1997) 3818–3831. <https://doi.org/10.1149/1.1838098>.
- [8] W. Li, D. Cao, D. Jöst, F. Ringbeck, M. Kuipers, F. Frie, D.U. Sauer, Parameter sensitivity analysis of electrochemical model-based battery management systems for lithium-ion batteries, *Applied Energy* **269** (2020) 115104. <https://doi.org/10.1016/j.apenergy.2020.115104>.
- [9] K.A. Smith, C.D. Rahn, C.-Y. Wang, Control oriented 1D electrochemical model of lithium ion battery, *Energy Conversion and Management* **48** (2007) 2565–2578. <https://doi.org/10.1016/j.enconman.2007.03.015>.
- [10] M. Guo, G. Sikha, R.E. White, Single-Particle Model for a Lithium-Ion Cell: Thermal Behavior, *J. Electrochem. Soc.* **158** (2010) A122. <https://doi.org/10.1149/1.3521314>.
- [11] J.M. Reniers, G. Mulder, S. Ober-Blöbaum, D.A. Howey, Optimal Control of Grid-Connected Li-Ion Batteries to Maximise Revenue and Minimise Degradation, Meet. Abstr. MA2017-02 (2017). <https://doi.org/10.1149/MA2017-02/1/40>.
- [12] S.J. Moura, F.B. Argomedeo, R. Klein, A. Mirtabatabaei, M. Krstic, Battery State Estimation for a Single Particle Model With Electrolyte Dynamics, *IEEE Transactions on Control Systems Technology* **25** (2017) 453–468. <https://doi.org/10.1109/TCST.2016.2571663>.
- [13] X. Lai, Y. Zheng, T. Sun, A comparative study of different equivalent circuit models for estimating state-of-charge of lithium-ion batteries, *Electrochimica Acta* **259** (2018) 566–577. <https://doi.org/10.1016/j.electacta.2017.10.153>.
- [14] B. Yann Liaw, G. Nagasubramanian, R.G. Jungst, D.H. Doughty, Modeling of lithium ion cells—A simple equivalent-circuit model approach, *Solid State Ionics* **175** (2004) 835–839. <https://doi.org/10.1016/j.ssi.2004.09.049>.
- [15] M. Schimpe, M.E. von Kuepach, M. Naumann, H.C. Hesse, K. Smith, A. Jossen, Comprehensive Modeling of Temperature-Dependent Degradation Mechanisms in Lithium Iron Phosphate Batteries, *J. Electrochem. Soc.* **165** (2018) A181. <https://doi.org/10.1149/2.1181714jes>.
- [16] K.A. Severson, P.M. Attia, N. Jin, N. Perkins, B. Jiang, Z. Yang, M.H. Chen, M. Aykol, P.K. Herring, D. Fraggadakis, M.Z. Bazant, S.J. Harris, W.C. Chueh, R.D. Braatz, Data-

- driven prediction of battery cycle life before capacity degradation, *Nature Energy* **4** (2019) 383–391. <https://doi.org/10.1038/s41560-019-0356-8>.
- [17] B. Wu, W.D. Widanage, S. Yang, X. Liu, Battery digital twins: Perspectives on the fusion of models, data and artificial intelligence for smart battery management systems, *Energy and AI* **1** (2020) 100016. <https://doi.org/10.1016/j.egyai.2020.100016>.
- [18] A. Jokar, B. Rajabloo, M. Désilets, M. Lacroix, Review of simplified Pseudo-two-Dimensional models of lithium-ion batteries, *Journal of Power Sources* **327** (2016) 44–55. <https://doi.org/10.1016/j.jpowsour.2016.07.036>.
- [19] K. Chayambuka, M. Jiang, G. Mulder, D.L. Danilov, P.H.L. Notten, Physics-based Modeling of Sodium-ion batteries Part I: Experiments, (Unpublished).
- [20] Y. Cai, X. Cao, Z. Luo, G. Fang, F. Liu, J. Zhou, A. Pan, S. Liang, Caging Na₃V₂(PO₄)₂F₃ Microcubes in Cross-Linked Graphene Enabling Ultrafast Sodium Storage and Long-Term Cycling, *Advanced Science* **5** (2018) 1800680. <https://doi.org/10.1002/adv.201800680>.
- [21] Z.-Y. Gu, J.-Z. Guo, Z.-H. Sun, X.-X. Zhao, W.-H. Li, X. Yang, H.-J. Liang, C.-D. Zhao, X.-L. Wu, Carbon-coating-increased working voltage and energy density towards an advanced Na₃V₂(PO₄)₂F₃@C cathode in sodium-ion batteries, *Science Bulletin* **65** (2020) 702–710. <https://doi.org/10.1016/j.scib.2020.01.018>.
- [22] K. Chayambuka, G. Mulder, D.L. Danilov, P.H.L. Notten, A modified pseudo-steady-state analytical expression for battery modeling, *Solid State Communications* **296** (2019) 49–53. <https://doi.org/10.1016/j.ssc.2019.04.011>.
- [23] H.S. Carslaw, J.C. Jaeger, *Conduction of heat in solids*: Oxford Science Publications, Oxford, England, 1959.
- [24] R. A. Shakoor, D.-H. Seo, H. Kim, Y.-U. Park, J. Kim, S.-W. Kim, H. Gwon, S. Lee, K. Kang, A combined first principles and experimental study on Na₃V₂(PO₄)₂F₃ for rechargeable Na batteries, *Journal of Materials Chemistry* **22** (2012) 20535–20541. <https://doi.org/10.1039/C2JM33862A>.
- [25] Z. Liu, Y.-Y. Hu, M.T. Dunstan, H. Huo, X. Hao, H. Zou, G. Zhong, Y. Yang, C.P. Grey, Local Structure and Dynamics in the Na Ion Battery Positive Electrode Material Na₃V₂(PO₄)₂F₃, *Chem. Mater.* **26** (2014) 2513–2521. <https://doi.org/10.1021/cm403728w>.
- [26] K. Chayambuka, G. Mulder, D.L. Danilov, P.H.L. Notten, Determination of state-of-charge dependent diffusion coefficients and kinetic rate constants of phase changing electrode materials using physics-based models, *Journal of Power Sources Advances* **9** (2021) 100056. <https://doi.org/10.1016/j.powera.2021.100056>.
- [27] K. Chayambuka, G. Mulder, D.L. Danilov, P.H.L. Notten, A Hybrid Backward Euler Control Volume Method to Solve the Concentration-Dependent Solid-State Diffusion Problem in Battery Modeling, *Journal of Applied Mathematics and Physics* **8** (2020) 1066–1080. <https://doi.org/10.4236/jamp.2020.86083>.
- [28] D. Danilov, R. a. H. Niessen, P.H.L. Notten, Modeling All-Solid-State Li-Ion Batteries, *J. Electrochem. Soc.* **158** (2010) A215. <https://doi.org/10.1149/1.3521414>.
- [29] M.K. Das, P.P. Mukherjee, K. Muralidhar, *Modeling Transport Phenomena in Porous Media with Applications*, Springer, 2017.
- [30] J. Newman, K.E. Thomas-Alyea, *Electrochemical systems* 3rd Ed., John Wiley & Sons, 2012.
- [31] K. Chayambuka, R. Cardinaels, K.L. Gering, L.H.J. Raijmakers, G. Mulder, D.L. Danilov, P.H.L. Notten, An experimental and modeling study of Sodium-ion battery electrolytes,

- Journal of Power Sources **516** (2021) 230658.
<https://doi.org/10.1016/j.jpowsour.2021.230658>.
- [32] D. Danilov, P.H.L. Notten, Mathematical modelling of ionic transport in the electrolyte of Li-ion batteries, *Electrochimica Acta* **53** (2008) 5569–5578.
<https://doi.org/10.1016/j.electacta.2008.02.086>.
- [33] R. Ranom, Mathematical modelling of Lithium ion batteries, University of Southampton, 2014.
- [34] D. a. G. Bruggeman, Berechnung verschiedener physikalischer Konstanten von heterogenen Substanzen. I. Dielektrizitätskonstanten und Leitfähigkeiten der Mischkörper aus isotropen Substanzen, *Ann. Phys.* **416** (1935) 636–664. <https://doi.org/10.1002/andp.19354160705>.
- [35] K.L. Gering, Prediction of electrolyte viscosity for aqueous and non-aqueous systems: Results from a molecular model based on ion solvation and a chemical physics framework, *Electrochimica Acta* **51** (2006) 3125–3138. <https://doi.org/10.1016/j.electacta.2005.09.011>.
- [36] K.L. Gering, Prediction of Electrolyte Conductivity: Results from a Generalized Molecular Model Based on Ion Solvation and a Chemical Physics Framework, *Electrochimica Acta* **225** (2017) 175–189. <https://doi.org/10.1016/j.electacta.2016.12.083>.
- [37] E.R. Logan, E.M. Tonita, K.L. Gering, L. Ma, M.K.G. Bauer, J. Li, L.Y. Beaulieu, J.R. Dahn, A Study of the Transport Properties of Ethylene Carbonate-Free Li Electrolytes, *J. Electrochem. Soc.* **165** (2018) A705. <https://doi.org/10.1149/2.0981803jes>.
- [38] S. Patankar, Numerical heat transfer and fluid flow, CRC press, 2018.
- [39] G.G. Botte, V.R. Subramanian, R.E. White, Mathematical modeling of secondary lithium batteries, *Electrochimica Acta* **45** (2000) 2595–2609. [https://doi.org/10.1016/S0013-4686\(00\)00340-6](https://doi.org/10.1016/S0013-4686(00)00340-6).
- [40] G.G. Botte, J.A. Ritter, R.E. White, Comparison of finite difference and control volume methods for solving differential equations, *Computers & Chemical Engineering* **24** (2000) 2633–2654. [https://doi.org/10.1016/S0098-1354\(00\)00619-0](https://doi.org/10.1016/S0098-1354(00)00619-0).
- [41] Sandip Mazumder, Numerical Methods for Partial Differential Equations, Academic Press (2016) 1-49, <https://doi.org/10.1016/B978-0-12-849894-1.00001-9>.
- [42] A nonlinear shooting method for two-point boundary value problems, *Computers & Mathematics with Applications*. **42** (2001) 1411–1420. [https://doi.org/10.1016/S0898-1221\(01\)00250-4](https://doi.org/10.1016/S0898-1221(01)00250-4).
- [43] A. Granas, R. Guenther, J. Lee, Nonlinear boundary value problems for ordinary differential equations, (1985). <https://eudml.org/doc/268365> (accessed March 5, 2021).
- [44] D.J. Wilde, Optimum seeking methods, Englewood Cliffs, NJ : Prentice-Hall, (1964).
- [45] D.E. Stephenson, E.M. Hartman, J.N. Harb, D.R. Wheeler, Modeling of particle-particle interactions in porous cathodes for lithium-ion batteries, *Journal of The Electrochemical Society* **154** (2007) A1146–A1155.
- [46] N. Kazemi, D.L. Danilov, L. Haverkate, N.J. Dudney, S. Unnikrishnan, P.H.L. Notten, Modeling of all-solid-state thin-film Li-ion batteries: Accuracy improvement, *Solid State Ionics* **334** (2019) 111–116. <https://doi.org/10.1016/j.ssi.2019.02.003>.
- [47] D. Li, D. L. Danilov, L. Gao, Y. Yang, P.H.L. Notten, Degradation Mechanisms of C6/LiFePO4 Batteries: Experimental Analyses of Cycling-induced Aging, *Electrochimica Acta* **210** (2016) 445–455. <https://doi.org/10.1016/j.electacta.2016.05.091>.
- [48] A. Chipperfield, P. Fleming, H. Pohlheim, A genetic algorithm toolbox for MATLAB, *Proceedings of the International Conference on Systems Engineering* (1994) 200–207.

- [49] New separator for PAT insulation sleeves EL-CELL, <https://el-cell.com/new-separator-for-pat-insulation-sleeves/> (accessed March 5, 2021).
- [50] T. Broux, F. Fauth, N. Hall, Y. Chatillon, M. Bianchini, T. Bamine, J.-B. Leriche, E. Suard, D. Carlier, Y. Reynier, L. Simonin, C. Masquelier, L. Croguennec, High Rate Performance for Carbon-Coated $\text{Na}_3\text{V}_2(\text{PO}_4)_2\text{F}_3$ in Na-Ion Batteries, *Small Methods* **3** (2019) 1800215. <https://doi.org/10.1002/smtd.201800215>.
- [51] R.B. Smith, E. Khoo, M.Z. Bazant, Intercalation Kinetics in Multiphase-Layered Materials, *J. Phys. Chem. C* **121** (2017) 12505–12523. <https://doi.org/10.1021/acs.jpcc.7b00185>.
- [52] G.K. Singh, G. Ceder, M.Z. Bazant, Intercalation dynamics in rechargeable battery materials: General theory and phase-transformation waves in LiFePO_4 , *Electrochimica Acta* **53** (2008) 7599–7613. <https://doi.org/10.1016/j.electacta.2008.03.083>.
- [53] S. F. Schneider, C. Bauer, P. Novák, E. J. Berg, A modeling framework to assess specific energy, costs and environmental impacts of Li-ion and Na-ion batteries, *Sustainable Energy & Fuels* **3** (2019) 3061–3070. <https://doi.org/10.1039/C9SE00427K>.
- [54] E. Berg, C. Villevieille, D. Streich, S. Trabesinger, P. Novak, Rechargeable Batteries: Grasping for the Limits of Chemistry, *J. Electrochem. Soc.* **162** (2015) A2468–A2475.
- [55] G. Patry, A. Romagny, S. Martinet, D. Froelich, Cost modeling of lithium-ion battery cells for automotive applications, *Energy Science & Engineering* **3** (2015) 71–82.

CHAPTER 8

SUMMARY AND OUTLOOK

SIBs are rapidly emerging as frontrunner complementary technology to the ubiquitous LIBs. This emergence is due to an extensive repertoire of candidate electrode materials, constituted mainly of sustainable, earth-abundant elements. This thesis focused on the experimental and modeling procedures necessary to construct a validated electrochemical battery model for a new battery chemistry.

Chapter 2, therefore, began by introducing the SIB chemistry and showcasing the different electrode materials currently available. It became apparent that SIBs are not a new technology relative to LIBs, as evidenced by the shared history between the two technologies. The decline of interest in SIB research, which occurred in the early 1990s, resulted from the breakthrough commercialization of LIBs, and the lack of suitable anode materials for SIBs. The role of technological drivers in the development of emerging battery chemistries, was equally highlighted. As an example, the concurrent rise of portable electronic applications in those days, which thrive on relatively small, single-cell batteries and the high energy density afforded by LIBs, resulted in a lack of incentives to justify the further development of SIBs.

Contrary to the widely held opinion that the discovery of hard carbon anode material for SIBs in the year 2000, was the turning point for the SIB technology, it is pretty clear that nearly a decade passed after this discovery, before considerable research attention returned to the SIB technology. Without the large-scale demand for battery energy storage, due to e-mobility and grid-scale applications and the potential challenges related to LIB raw materials, SIBs would have remained in obscurity. Therefore, the future success of the SIB technology is mainly dependent on the technology's ability to respond to the critical demands of these emerging applications. This can be viewed as an opportunity to redesign the room temperature rechargeable battery technology to meet the scalability and sustainability requirements of such large-scale electrical energy storage applications. SIBs therefore need to distinguish themselves not only as performance equivalents but also as the environmentally friendly choice in a society that is becoming increasingly conscious about climate change.

As revealed by the historical development of both LIBs and SIBs, commercialization is a key milestone for emerging battery technologies. In the case of LIBs, this resulted in the industrial production scale-up and a drop in price due to the economies of scale. In the case of SIBs, the commercialization effort in the last decade is largely thanks to the impressive groundwork done by start-up companies, such-as Faradion, Tiamat and HiNa. There are further encouraging signs of the imminent commercialization of SIBs based on recent pronouncements from established battery manufacturers.

In order to develop a robust electrochemical model of SIBs, it was necessary to first understand each of the battery's main components from an experimental and modeling perspective. These components include the electrolyte phase, the individual electrode active materials, and current collectors, together constituting the full battery cell. Chapter 3, therefore, explored the conductivity and viscosity properties of SIB electrolytes. This work was also fundamental in providing a comparative basis between SIB and LIB electrolytes. In this study, the combined use of the Advanced Electrolyte Model and experiments allowed the investigation of extensive electrolyte properties, which are not easily obtainable through experimental techniques. It became apparent that the cationic preferential ion solvation is an important factor to consider, which impacts the stability of hard carbon anodes in SIB mixed solvents. Further studies on this topic are indeed necessary to optimize solvent blends, systematically investigate SIB and LIB electrolytes and compare the experimental results with the statistical mechanics approach.

The determination of electrochemical mass transport parameters in SIB electrode particles was elucidated in Chapters 4 and 5. In Chapter 4, the modeling of diffusion mass transport mechanism using the modified pseudo steady-state method and the hybrid backward Euler control volume method was introduced. This study showed the importance of the functional form of the diffusion coefficient and the effect of the diffusion length on the node distribution. In Chapter 5, the P2D GITT method was used to determine the diffusion coefficient and kinetic rate constants for an active material contained in a porous battery electrode. These two Chapters demonstrate the use of electrochemical models and experiments to derive validated electrochemical parameters for porous battery electrodes. The P2D GITT method was shown to be quite promising to replace the analytical "Weppner-style" method. In order to promote further adoption and wider use of the P2D GITT method, it is therefore necessary to develop open access models and apps, which will allow experimentalists to independently compare the P2D GITT method with other methods.

The study of full cell SIBs was finally introduced in Chapters 6 and 7. In Chapter 6, the experimental work done on SIBs based on hard carbon anodes and $\text{Na}_3\text{V}_2(\text{PO}_4)_2\text{F}_3$ cathodes was shown, in order to derive parameters to be used in the SIB P2D model. Through this work, some of the key challenges in improving the performance of SIBs became apparent. These include the voltage differences between (dis)charge cycles, the rate-dependent capacity decrease of hard carbon and the low mass transport rate in NVPF active particles. In Chapter 7, the full cell electrochemical model of SIBs was presented for the first time. The model was validated by the experimental results obtained in Chapter 6. In order to obtain accurate voltage profiles for the different discharge rates while maintaining the same parameters, it was necessary to include concentration dependent parameters for the diffusion coefficient and the kinetic rate parameters. Because the P2D model was validated based on the voltage response of the two individual electrodes, the model can thus reliably predict the internal battery states. This ability is useful in fast charging applications, for example the model can be used to determine the battery state-of-charge and avoid the sodium plating potential at the anode.

In conclusion, the SIB system based on HC anode and NVPF cathode has been systematically investigated through electrochemical models and experiments. This work enhances the understanding of the electrochemical properties and performance of SIBs as they position themselves alongside LIBs. Through in-depth reviews, the SIB state-of-the-art and future roadmap challenges toward commercialization were herein unraveled. Electrochemical experiments then allowed model parameters to be deduced. Finally, a validated SIB P2D model was presented which can be used as a design and optimization tool. The optimization objective is therefore to determine the optimum electrode thickness, porosity, and particle size and minimize manufacturing costs for a given target application. The methods presented herein, are therefore useful for investigating and developing electrochemical models for a new battery chemistry.

Future work in the modeling of SIBs should address issues which arise due to the increasing scale of the batteries. At the individual cell level, thermal effects are expected to be significantly high considering the high Ohmic resistance in the SIB electrodes. In addition, physics-based models are required to manage and predict the thermal runaway and aging behavior of SIBs. These aspects are becoming increasingly important with respect to battery safety and lifetime prediction. At the SIB module level, there is need to work on model order reduction, to enable low computational cost simulations in imbedded systems. This will result in battery management

systems and battery emulators with improved reliability in battery state estimation. In this work, guidelines for SIB cell design have been described which should allow design improvements and performance enhancement of SIBs. Given that the remaining challenges toward SIB commercialization are cost related, and since battery cost can be minimized through battery design, the developed model can therefore be instrumental toward the commercial success of SIBs.

ACKNOWLEDGEMENTS

It is befitting to dedicate this last segment of this thesis to give special thanks to the many people who made this study a success. Each PhD study has its peculiar challenges and this was no exception. I could not have overcome these challenges were it not for the selfless individuals, friends and colleagues, some of whom it is my pleasure and honor to mention briefly.

First and foremost, I would like to give special thanks to my first promotor Prof. Peter Notten. Peter, you have never doubted me from our first interview and then later on you helped me prepare a PhD proposal to obtain funding from VITO which was successfully granted. I have learnt a lot under your guidance, through the many papers we have written together and your meticulous analysis of experimental results. I also remember our regular follow-up meetings which you always made the effort to attend in person in EnergyVille. There was one such meeting on the 2nd of January and we had trouble finding lunch because everything in Genk was closed. However, such was your dedication and commitment to the success of this PhD for which I am forever grateful. Although we have not had physical encounters since the start of the COVID outbreak, you have remained a constant pillar of support. When my daughter was born you gave me support that I can never repay and I speak on behalf of my family that we are forever indebted to you. Thank you Professor Notten for being a champion promotor, mentor and friend.

Special heartfelt thanks also goes to my first co-promotor Dr. Dmitri Danilov whose relentless support made this study the success that it is. I remember how we worked hard together, going through every line of the MATLAB code to increase the model speed which was taking hours to run. By working together, we managed to reduce the runtime to only a few seconds! Our collaboration became more efficient when I moved closer to Jülich and I am very proud of the work we did to modify the pseudo-steady-state method. I do not think the related paper has received the attention that it deserves, maybe with time it will. All this was possible because of your mathematical skills which are truly remarkable. This thesis further benefited from your attention to detail and careful analysis of the text. For all this I am indebted and I want to thank you Dmitri for your support.

I also had the fortune and pleasure to have the guidance of Grietus Mulder who was my second co-promotor. Grietus, I always look back to the time you sent me an email asking if I was still interested in pursuing a PhD on battery modeling. I was back home in Zimbabwe at the time and you helped me to prepare a well-written proposal for the VITO Jury which was accepted. I have fond memories of the time we spent at EnergyVille which was made comfortable by your presence. We always made an effort to sit near each other and this enhanced our collaboration. In all the follow-up meetings, you helped with prior preparations and enriched the discussions. Thank you so much Grietus for your valuable mentorship.

Turning to the other esteemed members of the defense committee: Prof. Dr. R.-A. Eichel, Dr. M. Safari and Prof. Dr. Ir. J.G. Slootweg. Thank you so much for setting aside your valuable time to diligently assess the thesis. It is no understatement that this work greatly improved as a result of your constructive feedback. I also wish thank Prof. Dr. K. A Williams for chairing the defense ceremony.

When I needed assistance with experiments, I could always rely on the assistance of Dr. Luc Raijmakers. Thank you so much Luc, you never refused to help and no task was too big for you. Even when we faced obstacles, you always had a positive mindset that eventually we will get it done. Because of your intelligence, tenacity and work ethic, we would always succeed. You displayed in-depth knowledge of the experimental setups and it was reassuring to have your support. I also valued our friendship and discussions on general topics and you always listen to what the others say. My arrival and stay in Jülich was made easy by your presence and I want to thank you for helping me reach this stage of my scientific development.

One of the unique challenges of this PhD was the need to commute between the Netherlands, Belgium and Germany. In the first years I did not have neither a car nor a drivers' license and this meant I had to rely on public transport. However, I was very fortunate to find colleagues who were willing to carpool which greatly made the commutes time efficient, interactive and enjoyable. I cannot forget Dr. Georgi Yordanov for the carpool between Genk and EnergyVille. You had a unique understanding of the problems faced by PhD Students in a foreign country and you were always a phone call away. The book you gave me "Writing for scholars" really helped me and I would recommend it to any aspiring PhD students. You then drove me to Aachen when I relocated there and without your help this would have been a difficult task. Thank you so much for being always willing to help. I was again very fortunate to come in contact with Dr. Georg Jung who offered to

carpool whenever I needed to travel to Energyville from Aachen. I will forever cherish our discussions on topics which ranged from spirituality to Star Wars while I was ‘‘riding shotgun’’. I shall continue to cherish these conversations your wise council and as well as our friendship.

To my colleagues in EnergyVille, I want to thank you for making this PhD experience memorable. I am particularly grateful for the support that I got from Dr. Jeroen Büscher who worked very hard to get parameters for the battery from Naiades project partners and crucially managed to secure the all-important sodium-ion battery electrodes - not once, but twice after the first set somehow disappeared. I also want to thank Dr. Fekriasl Sajjad who has been more than a colleague and a friend. Although I met Sajjad in the later stages of my PhD, he took keen interest in my work and it was a pleasure to implement some of your ideas. I am confident the best is yet to come and the ‘‘peanut butter and jelly’’ will taste good. Special thanks also goes to the team manager Hans Rymenants for the approval of the conference trips and organizing for my apartment in Aachen. I also want to thank Sarah for always making it comfortable to work at EnergyVille, be it through organizing meetings or just a friendly chat. I finally also want to thank the other members of the SEED team: Peter, Khiem, Klaas, Odile, Carlo, Geert, Reinhilde, Dominique, Jan, Da Wang, Meraj and Filip. Thank you for the kindness you showed in our various engagements and I am grateful for your commitment to science in general and thus helping me succeed.

In the same breath, I want to express heartfelt gratitude to the members of Forschungszentrum Jülich IEK-9 who enriched my PhD experience. Many thanks to Dr. Bert De Haart, whose help was instrumental in organizing the group and assistance in our orders. To Prof. Dr. Rüdiger-A. Eichel, I am particularly grateful for allowing me access to the Forschungszentrum Jülich research facilities as a visiting researcher during my PhD and approving for the purchase of the AEM software. We have managed to get some interesting results with this software which has helped the quality of this thesis. I extend my gratitude to Achim Weber for your assistance in our orders for chemicals and for providing safety instructions and training when I first arrived. I was also honored and fortunate to have worked with quite a number of Chinese colleagues who were pursuing their PhDs at the time. I learnt a lot from their intelligence, hard work and generosity and I got to appreciate their food and culture. I want to thank Ming Jiang for your unwavering support and organizing our get-togethers and presents for our group members. You also helped me with the SEM micrographs and general organizations in the lab. I also wish to thank Dr. Chungang Chen who was instrumental in many of our group activities and was always willing to help. I also

want to acknowledge Lei Zhou and Zhiqiang Chen whose were always willing to help in all matters. I was fortunate to have you as Colleagues and I hope we continue to collaborate on future topics. I want to thank the organizers of the electrochemistry days which was a good opportunity to interact with many colleagues. Special thanks goes to our secretaries Michaela, Chantal, Sandra and Birgit for their administrative support.

Although I did not spend a lot of time in TU/e where I was officially registered in the Control Systems group, I want to thank the group members for creating a conducive environment for research. I would like the thank Dr. Ruth Cardinaels who assisted me with rheological measurements in a very short space of time. I am very proud of the outcome of the work we did. I also received a lot of administrative support from the control systems secretary Ms. Diana Heijnerman and I want to thank her for the timely assistance.

To the many family and friends who helped and made my stay in Belgium memorable, I am forever indebted to you generosity. I first came to Belgium through the helping hand of Dr. Xochitl Dominguez who was my first mentor during my Master's thesis. Just like other giants, she allowed me to see further than I could by allowing me to step on her shoulders and planted the seeds in me to pursue a PhD. Later on, I met Prof. Jan Fransaer who left an impression on me for scientific rigor and thus grew my passion for scientific research. To both Xochitl and Jan, I want to thank you from the bottom of my heart for your steadfast support and encouragement which kept lifting me up when the chips were down. You truly went out of your way to make Belgium a home away from home for me. I also count myself fortunate to have met Dennis Cardoen and his wife Poonam whose friendship toward me left an indelible mark. I remember the times we went for rock climbing activities and I also cherish the time you invited me to spend Christmas at your mother's house. Later on we would exchange visits when my wife came to Belgium and thanks to you I never felt like I was on my own. Thank you so much Dennis and Poonam for the warmth of friendship. It was also an honor to meet Mbuwir Brida during my stay in Genk as a friend and colleague it was nice to have another African friend nearby. Thank you Brida for being a good friend during my PhD. When my wife arrived in Belgium, she brought many good things with her and one of these was a chance encounter with Claude and Dennis and we became friends. I remember Denise helping me to buy flowers for my wife as I was preparing to welcome my wife in Belgium. She reasoned it was not proper for Yemurai to arrive without a vase of flowers in the

house, it would have been a grave mistake indeed! Claude and Denise, words fail to describe your love and friendship to us which is more than family, I can only say thank you for being kindhearted.

Finally I want to thank my immediate family. Starting with my wife Yemurai, the one who was equally yoked and burdened throughout this PhD journey, it is only appropriate that you equally share in the success of this PhD. Thank you for all the hard work you did quietly and diligently behind the scenes. You have experienced first-hand, the worst of the late working hours and sometimes coming home late when I have to meet deadlines. Even though it has been hard to spend quality time together, you have remained loving and supportive in spite of all the challenges. I am proud of this PhD because we achieved it together. Thank you for the love and support, for being a good wife and mother to our daughter Ropafadzo. Dear Ropa my co-author, you arrived into our lives and brought contagious joy. I know that one day you will reach great academic heights of your own and my only hope is to guide you to reach your full potential. To my dear mother, I hope I have made you proud amai. I know of all the sacrifices you made for me to reach this stage and I owe it to your love to me and prayers. It would have been my pleasure to have you here present but travel restrictions have scattered our plans. I want to say a special thanks to my dear brother Farai who kept encouraging me to study hard during my formative years. I do not know what you saw in me then but you spared no expense to make sure I went to the best schools and got the best books. Thank you so much Baba matwins. To the Tevedzai family, I could not have asked for better in-laws. You have treated me as a son and I know you have kept me in your thoughts and prayers and I want to thank you for your unwavering love and encouragement. Many thanks as well to the family and friends in Duren, the Samuriwo family, thank you for being present at our moments of need. I will finish in loving memory of my dear father, Conrad Maja who passed away while I was in Algeria. In his last words to me, he said I should continue pursuing my studies. I am happy to have reached this stage and I know you would have been proud and overjoyed on this occasion. May your legacy live on.

LIST OF PUBLICATIONS

1. **K. Chayambuka**, G. Mulder, D.L. Danilov and P.H.L. Notten,
“Sodium-ion battery materials and electrochemical properties reviewed”,
Advanced Energy Materials **8** (2018) 1800079. <https://doi.org/10.1002/aenm.201800079>
2. **K. Chayambuka**, G. Mulder, D.L. Danilov and P.H.L. Notten,
“A modified pseudo-steady-state analytical expression for battery modeling”,
Solid State Communications **296** (2019) 49-53. <https://doi.org/10.1016/j.ssc.2019.04.011>
3. **K. Chayambuka**, G. Mulder, D.L. Danilov and P.H.L. Notten,
“A Hybrid Backward Euler Control Volume Method to Solve the Concentration-Dependent Solid-State Diffusion Problem in Battery Modeling”,
Journal of Applied Mathematics and Physics **8** (2020), 1066-1080.
<https://doi.org/10.4236/jamp.2020.86083>
4. **K. Chayambuka**, G. Mulder, D.L. Danilov and P.H.L. Notten,
“From Li-ion Batteries toward Na-ion Chemistries: Challenges and Opportunities”,
Advanced Energy Materials **10** (2020) 2001310. <https://doi.org/10.1002/aenm.202001310>
5. **K. Chayambuka**, G. Mulder, D.L. Danilov and P.H.L. Notten,
“Determination of state-of-charge dependent diffusion coefficients and kinetic rate constants of phase changing electrode materials using physics-based models”,
Journal of Power Sources Advances **9** (2021) 100056.
<https://doi.org/10.1016/j.powera.2021.100056>

6. **K. Chayambuka**, R. Cardinaels, K.L. Gering, L. Raijmakers, G. Mulder, D.L. Danilov and P.H.L. Notten,
“An experimental and modeling study of sodium-ion battery electrolytes”,
Journal of Power Sources **516** (2021) 230658.
<https://doi.org/10.1016/j.jpowsour.2021.230658>
7. **K. Chayambuka**, M. Jiang, G. Mulder, D.L. Danilov and P.H.L. Notten,
“Physics-based Modeling of Sodium-ion Batteries Part I: Experimental parameter determination”,
Electrochimica Acta, **404** (2022) 139726. <https://doi.org/10.1016/j.electacta.2021.139726>
8. **K. Chayambuka**, G. Mulder, D.L. Danilov and P.H.L. Notten,
“Physics-based Modeling of Sodium-ion Batteries Part II. Model and validation”,
Electrochimica Acta, **404** (2022) 139764. <https://doi.org/10.1016/j.electacta.2021.139764>
9. Z. Chen, D.L. Danilov, L. Raijmakers, **K. Chayambuka**, M. Jiang, L. Zhou, J. Zhou, R. -
A. Eichel, and P.H.L. Notten,
“Overpotential analysis of graphite-based Li-ion batteries seen from a porous electrode modeling perspective”,
Journal of Power Sources **509** (2021) 230345.
<https://doi.org/10.1016/j.jpowsour.2021.230345>
10. V. van Vught, **K. Chayambuka**, G. Pozo, S. Eggermont, J. Fransaer and X. Dominguez-Benetton,
“Synthesis of material libraries using gas diffusion electrodes”,
Journal of Materials Chemistry A **8** (2020), 11674-11686.
<https://doi.org/10.1039/d0ta00633e>
11. **K. Chayambuka**, J. Fransaer and X. Dominguez-Benetton,
“Modeling and design of semi-solid flow batteries”,
Journal of Power Sources **434** (2018) 226740.
<https://doi.org/10.1016/j.jpowsour.2019.226740>

Conference contributions

12. Sodium-ion Battery Technology Transition – Poster.

K. Chayambuka, G. Mulder, D. L. Danilov and P. H. L. Notten, 5th International Conference on Sodium Batteries, St Malo, France (2018).

13. Modeling of Sodium-ion Batteries – Oral presentation.

D. L. Danilov, **K. Chayambuka**, G. Mulder and P. H. L. Notten, 5th International Conference on Sodium Batteries, St Malo, France (2018).

14. Modeling of Sodium-ion Batteries – Oral presentation.

K. Chayambuka, G. Mulder, D. L. Danilov and P. H. L. Notten, 6th International Conference on Sodium Batteries, Chicago, USA (2019).

15. Concentrated Solution Theory vs Dilute Solution Theory – Poster.

K. Chayambuka, G. Mulder, D. L. Danilov and P. H. L. Notten, Oxford Battery Modelling Symposium, Oxford, UK (2020).

16. Modeling Diffusion in Spherical Electrode Particles – Poster.

K. Chayambuka, G. Mulder, D. L. Danilov and P. H. L. Notten, Oxford Battery Modelling Symposium, Oxford, UK (2020).

CURRICULUM VITAE

Kudakwashe Hilary Chayambuka was born on 31-01-1987 in Harare, Zimbabwe. After finishing high school in 2005 at St Johns Secondary School in Zimbabwe, he was awarded a government scholarship for tertiary studies in Algeria. Subsequently, he enrolled at the University of Béjaïa where he successfully completed a Bachelor's degree in Process engineering in 2010, and a Master's Degree in Chemical Engineering in 2012. He then enrolled at Paul Sabatier University (Toulouse III) in France where he studied for a Master's degree in Process Engineering specializing in electrochemistry and graduated in 2014. He then worked as a research assistant at VITO in Belgium, and collaborated in EU projects in the development semi-solid flow batteries. From 2016 he started a PhD trajectory at Eindhoven University of Technology (TU/e) in the group of Prof. dr. Peter H.L. Notten of which the results are presented in this dissertation. During this study, he published a total of 8 peer reviewed publications as first author. The first review article from this study was awarded 2018-2019 top 10 % most downloaded papers in Wiley. Most of the research` work was conducted at EnergyVille in Belgium and at the Forschungszentrum Jülich (IEK-9) in Germany. Since 2020 he is employed at the Forschungszentrum Jülich (IEK-9).

